Free-Space Optical Communications with Retro-reflecting Acquisition and Turbulence Compensation

Pithawat Vachiramon

Balliol College

A thesis submitted in partial fulfilment of the requirements for the degree of Doctor of Philosophy at the University of Oxford

Department of Engineering Science

Parks Road, Oxford OX1 3PJ, UK

October 2009

Abstract

Free-space optics (FSO), or wireless optical communications, has received extensive research due to its promise of practically limitless bandwidths. However, FSO has challenges yet to be met for a cost effective realisation. This D.Phil thesis explores a solution using a ferro-electric liquid crystal spatial light modulator (FLC SLM) and binary phase holograms to significantly reduce the hardware complexity of an FSO system with auto-alignment and turbulence compensation.

The theory of binary phase hologram is presented and extended to obtain a new algorithm that is suitable for a FLC SLM. The algorithm is able to be used in a demonstration system to broadcast data streams to multiple receivers, showing the capability of using FLC SLM to form any beam configuration. An FSO transmitter is then developed that uses retro-reflectors as markers for the receivers. The transmitter combines an imaging system with the FLC SLM as a reconfigurable beam steering system for acquiring the retro-reflector location. The FLC SLM is also used to reduce aberrations in the optics, resulting in a significant increase in the transmitted beam power density. The accuracy of the acquisition is measured to give a small steering error without the use of a closed loop controller.

An optical turbulence simulator, using the principals of binary phase hologram, is constructed to simulate optical beam propagation in turbulent conditions. The simulator accurately produces aberrations that have the same statistics with the theoretical prediction. Analysis of the phase distortion due to turbulence is performed and a wavefront sensorless turbulence compensation method based on the FLC SLM gives significant reduction in calculated bit error rates. New scintillation index derivation for multiple optical beams is described and then used to demonstrate further decrease in bit error rates.

Acknowledgements

I would like to express my gratitude to each person for their contribution to the completion of this thesis:

To my supervisor Dr. Dominic O'Brien for his support and expert guidance.
I will always remember his invaluable insights, as well for his endless patience with this thesis.

To Grahame Faulkner for his generosity in helping with any and all technical problems
that naturally arises in research.

To the Communications Group and especially to my colleagues:
Sashigaran Sivathasan, Jing Jing Liu and Wei Wen Yuan for their collaborations with the base station.

To Prof. Paul Buckley for his advice on College related topics.

To my friends, Shashank, Daniel and Daniele for their input, company, and endless positivity.
They have transformed my time in Oxford to more than just an experience. Thanks guys.

To Aee for her never-ending love and devotion, without whom
this journey would not have been possible. Thank you na.

And finally, I would like to dedicate this thesis to my parents, my brothers and my family.
They have given me so much love and support.

Tan Vachiramon

8th October 2009

List of publications

Journal Publications

[1] **P. Vachiramon**, G. E. Faulkner, D. C. Obrien, "Direct current balancing algorithm for FLCOS binary phase holograms", Optics Letters, Volume 32, Issue 22, November 2007, Pages 3275-3277. (Accepted)

[2] D. C. O'Brien, J. Liu, G. E. Faulkner, **P. Vachiramon**, S. Sivathasan, W. Yuan, S. Collins, S. J. Elston, "Design and Implementation of Optical Wireless Communications with Optically Powered Smart Dust Motes", IEEE Journal on Selected Areas in Communications, Volume 27, No. 9, December 2009. (Submitted)

Conference Proceedings

[3] **P. Vachiramon**, G. E. Faulkner, D. C. Obrien, "A DC balancing algorithm for complex binary phase holograms", Proc. SPIE, *Unmanned/Unattended Sensors and Sensor Networks V*, October 2008, Article No. 711208

Contents

List of Figures

List of Tables

List of abbreviations and symbols

Abbreviations

AO	Adaptive Optics
DC	Direct Current
BER	Bit Error Rates
FLC	Ferro-electric Liquid Crystal
FOV	Field Of View
FSO	Free-Space Optics
OTS	Optical Turbulence Simulator
PRBS	Pseudo-Random Bit Stream
SLM	Spatial Light Modulator
SNR	Signal to Noise Ratio

Symbols

A	Aperture averaging factor
C_n^2	Refractive index structure constant
D_n	Refractive index structure function
F	Focal length
I	Electric field intensity
k	Wave number
L	Propagation path length
r	Radial scalar variable
r_0	Atmospheric coherence width (Fried's parameter)
U	Scalar electric field

W	Gaussian beam width
κ	Spatial frequency
Θ_0, Λ_0	Gaussian beam parameters at the transmitter
Θ, Λ	Gaussian beam parameters at the receiver
ψ	Phase shift/distribution
Φ_n	Three dimension spatial power spectrum of refractive index
σ_R^2	Rytov variance
σ_I^2	Scintillation index
Γ	Gamma function
$\langle\ \rangle$	Expected value / ensemble average

1 Introduction

1.1 Free space optics

Optical wireless communications, or free-space optics (FSO), has received much interest in the past 30 years [1]. Recently, the need for medium range wireless communications technology has reinvigorated the field, particularly for solving the 'last mile' connectivity problem; the majority of homes and businesses are located within one mile of a major telecommunications exchange [2][3][4]. This is contributed to by the explosive rise in demand for Internet access and fast local area networks. Wired solutions have existed for a long time, including dedicated fibre optic or coaxial cables, with capacity of up to 600Mb/s for passive fibre networks [5], and gigabits per second or more for active networks [6]. However, the prohibitive costs of rewiring buildings have made this an unpopular solution, unless mass-rewiring is undertaken [7]. With the advent of asynchronous digital subscriber lines (ADSL) to reuse the voice telephone network, this is somewhat alleviated. The demand for faster links will not be met by this technology, since the physical limit for ADSL technology has already been reached [8]. Current wireless radio networks such as the UMTS, IEEE 802.11 (Wireless LAN), and IEEE 802.16 (WiMAX) standards offer relatively low maximum capacity of up to 100 megabits per second [9], mainly due to the limited availability of licensable spectrum.

Free-space optics is an attractive technology to overcome the bandwidth problems faced with wireless radio communications. It uses laser sources with wavelengths from 2μm to 640nm as the carrier wave. The most important aspect of using FSO is the unrestricted access to an extremely wide spectrum. Moreover, the necessary optoelectronic devices, such as high speed laser modulators and photodetectors, are already commercially available for use in optical fibres. High powered lasers can also output large optical power with small mass and space, and the beams can easily be collimated, allowing high antenna gain [10]. There are challenges, however, that need to be addressed for FSO to be widely deployed.

A typical FSO system is shown in Figure 1, consisting of three subunits: the transmitter, the atmosphere, and the receiver. The transmitter contains a laser that is modulated by the binary data stream, which is then collimated by the beam expander. The emitted optical beam then propagates though the earth's atmosphere to the receiver. A lens focuses the optical beam onto a detector that converts the intensity fluctuations back to data. The narrow optical beam poses a problem for receiver alignment and transmission to multiple receivers. Coupled with the limited power output for eye safety, the optical beams cannot be expanded to cover large transmission areas and sophisticated beam steering and receiver position tracking system is required.

There is also the problem of optical beam propagation through the atmosphere. Precipitation [11] and clear air or atmospheric turbulence [12] can deteriorate the link quality significantly. Simply selecting a wavelength that falls within the atmospheric window of low absorption can help with precipitation [11]. However, turbulence causes fluctuations in the beam intensity, or scintillation, that exists at all wavelengths [13]. An adaptive optics system can be used to compensate for turbulence, which has been shown to work well for imaging systems [14]. Progress has been made to use this technique for FSO; however, they tend to require extra complexity that will increase the initial cost of link deployment.

In this thesis, some of these challenges are met by using a relatively new type of optical wavefront modulator, or spatial light modulator (SLM). These devices are used to control the spatial phase distribution of the transmitted beam, which can produce wide ranging of optical beam configurations when the beam reaches the receiver [15][16]. The flexibility of an SLM reduces the number of parts needed for a FSO transmission system, which can potentially reduce the initial cost of the link and allowing FSO to be used for wide range of applications.

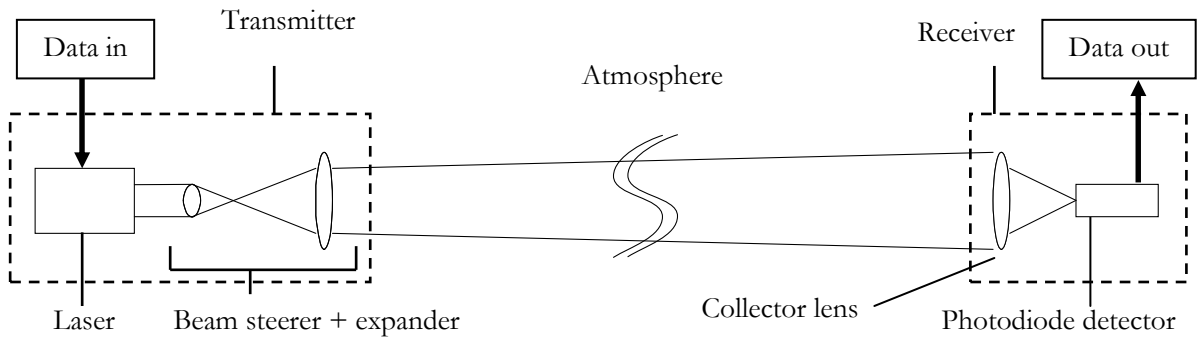

Figure 1: A Typical free space point-to-point optical configuration

1.2 Overview

The thesis is split into three parts. The first introduces holographic beam steering from first principles. It is then extended to the case of binary phase holograms. Two algorithms are described to find optimal binary phase holograms and their performances compared. A number of approaches to improve existing methods are then tested numerically and in practice on an optical system. A point-to-multipoint transmission is then tested to confirm the method's effectiveness.

The second part consists of implementing an FSO transmission system with automatic receiver acquisition using retro-reflecting targets. Holographic beam steering is used to implement optical aberration correction and also as a beam expansion system. Software processing is then used to isolate these targets and to reduce interference from ambient lighting. Its acquisition performance is then measured.

The final part evaluates the use of binary phase holograms for atmospheric turbulence simulation, as well as a compensation system without the use of a wavefront sensor. A theoretical overview of electromagnetic wave propagation in turbulence is presented using the Kolmogorov spectrum and the Rytov approximation. These are used to obtain parameters needed to accurately simulate Gaussian optical beams with a binary phase only system. A numerical simulation and physical measurements are compared for a number of receiver aperture sizes. The system is then extended to wavefront sensorless estimation of Zernike modes, which is then used to compensate for the effects of turbulence. Bit error rates are then calculated from the scintillation results with and without aperture averaging effects. A multi-beam transmission is then numerically evaluated for three different beam geometries, and the bit error rates are numerically evaluated for the case of compensated multi-beam configuration.

2 Holographic beam steering for binary phase holograms

2.1 Ferroelectric Spatial Light Modulators

A spatial light modulator (SLM) consists of an array of electrically controllable pixels. Each pixel is able to modulate the complex amplitude of a light beam incident upon it [17]. An ideal SLM has an infinite modulation range for both phase (from 0 to $2m\pi$), and amplitude (from -1 to 1) as show in Figure 2A.

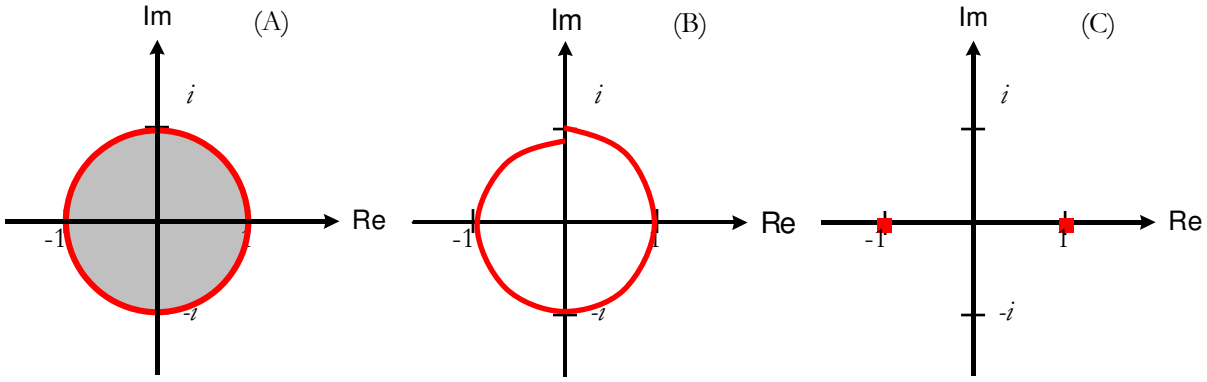

Figure 2. (A) Ideal SLM modulation space. (B) Phase only modulation. (C) Binary Phase only

There are a number of spatial phase modulation devices that are available [18]. Their advantages and disadvantages are listed below:

1. Twisted Nematic liquid crystal display (TNLCD) based SLMs can have very large number of modulation states. However, it has been shown that the phase modulation is not uniform, due to the amplitude-phase coupling [19]. A diagram of the phase modulation states of a TNLCD is shown in Figure 2B. Despite this, its performance as a phase modulator has been demonstrated to be good [20], but commercially available products are limited to video rates of 10s of Hertz [21], which may be too slow for some purposes.
2. Micromirrors can also be used as SLMs [22]. Phase modulation is achieved by physical movement of mirror pixels, such that the extra distance produces phase modulation. It has been shown that

in certain configurations the bandwidth of the mirrors is in the region of 60kHz [22]. However, they generally have low spatial resolution relative to TNLCD SLMs.

3. Ferroelectric liquid crystal (FLC) based SLMs have resolutions similar to TNLCD devices [23]. They are bistable devices, and can only produce binary phase modulation as shown in Figure 2C. Because the ferroelectric liquid crystal molecules are driven with polar voltages, unlike TN liquid crystals, they can be driven to high refresh rates. Commercially available devices can operate at 1 kHz and higher [24]. The drawback from their bipolar molecules is the absence of a defined zero voltage state [25]. Each FLC cell needs to have either positive or negative electric field, and this will unavoidably cause liquid crystal cell ionisation [17]. A prolonged DC current degrades the cells' switching characteristic permanently.

Of the current commercial devices available at the time of this project, only FLC based devices have both the high spatial resolution for beam steering [26] and high refresh rates suitable for atmospheric turbulence compensation. These are the main factors for the decision to choose FLC SLM for this Thesis.

The FLC SLM that is used throughout the project is a SXGA F-LCOS (Ferroelectric Liquid Crystal on Silicon) manufactured by 4th Dimension Displays, which was commercially available in 2008. It is capable of displaying an SXGA video signal at 1280x1024 pixel resolution. It is a high refresh rate binary phase modulation device. Table 1 shows its specifications.

Spatial Resolution	1280 x 1024 pixels (SXGA)
Display area dimensions (width x height)	17.43mm x 13.95mm
Pixel dimensions (width x height)	13.62μm x 13.62μm
Refresh rate (binary phase modulation)	1.44kHz
Maximum single video frame display time	100ms

Table 1. Specifications for SXGA F-LCOS ferroelectric SLM used in this thesis.

2.2 Holographic beam steering

The process for calculating the required complex amplitude distribution from a required intensity pattern can be derived from the equation governing light propagation. The chief mechanism for diffraction is the Fresnel diffraction [27]. The Fresnel diffraction integral can be expressed as:

:

$$U_{Fresnel}(x,y,z)=\frac{e^{(jkz)}}{j\lambda z}e^{j\frac{\pi}{\lambda z}(x^2+y^2)}\iint_{-\infty}^{\infty}\left\{U(\xi,\eta,0)e^{j\frac{\pi}{\lambda z}(\xi^2+\eta^2)}\right\}e^{-j\frac{2\pi}{\lambda z}(x\xi+y\eta)}d\xi\,d\eta \qquad (2.2.1)$$

Where $U(\xi,\eta,0)$ is the complex amplitude at one plane, $U_{Fresnel}(x,y,z)$ is the complex amplitude at a plane a distance z from this plane as shown in Figure 3, and λ is the wavelength of the illumination.

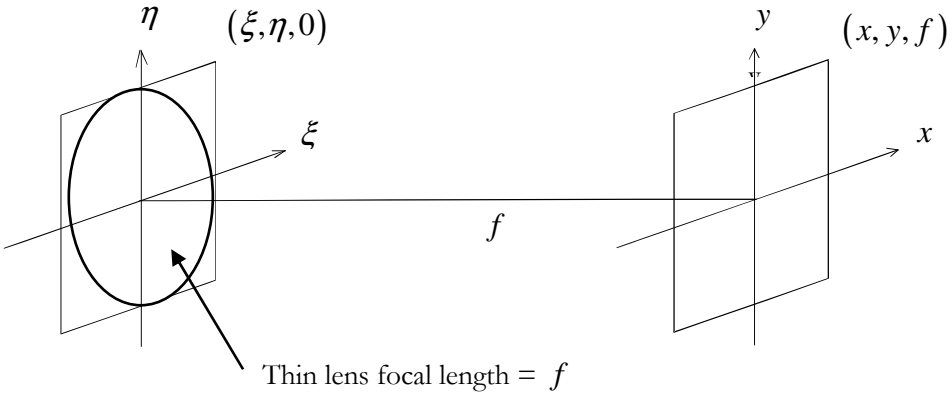

Figure 3. The optical layout of an optical Fourier Transform.

Ignoring the constant phase factor outside the integral, the Equation (2.2.1) is a Fourier transform of the input plane, multiplied by a quadratic phase factor and scaled relative to the wavelength. An important observation can be made concerning the quadratic phase factor; it is the inverse of a positive lens at its focus. Therefore, if one places a lens in front of the input plane, the quadratic terms cancel, and this reduces the relation to a Fourier transform between the two complex planes (shown here without the constant phase factor):

$$U(x,y,f)=\iint_{-\infty}^{\infty}U(\xi,\eta,0)e^{-j\frac{2\pi}{\lambda f}(x\xi+y\eta)}d\xi\,d\eta \qquad (2.2.2)$$

Therefore, the focal plane of the setup is exactly the Fourier plane of the complex amplitude pattern present at the aperture of the lens. The result also allows the intensity distribution in the focal plane $U(x, y)$ to be calculated by taking the inverse transform of the required amplitude distribution:

$$U(\xi,\eta) = \mathcal{F}^{-1}\left(U(x, y)\right) \tag{2.2.3}$$

Where $\mathcal{F}^{-1}$ denotes the inverse Fourier transform. This complex input pattern $U(\xi,\eta)$ is typically called a hologram. For instance, to shift a beam of light to a position (x', y');

$$\mathcal{F}^{-1}\left(\delta(x-x', y-y')\right) = e^{j\frac{2\pi}{\lambda f}(\xi x'+\eta y')} \tag{2.2.4}$$

This is a linear phase tilt, with the phase value proportional to the sum of $(\xi x', \eta y')$. The Fourier transform planes are scaled by $(\lambda f)^{-1}$. It has been shown that on spatially sampled devices such as the SLM, the sampling theorem determines the maximum size of the Fourier plane [27]. The maximum first order diffraction angle is derived to be:

$$\theta_{Max} \simeq \frac{\lambda}{d_{pixel}} \tag{2.2.5}$$

Where θ_{Max} is the maximum first order diffraction angle and d_{pixel} is the pixel spacing distance. The maximum size of the Fourier plane, given a focal length of the lens to be f:

$$D_{Max} \simeq \frac{\lambda f}{d_{pixel}} \tag{2.2.6}$$

Where D_{Max} is the maximum dimension of the Fourier plane. The smallest beam size at the Fourier plane can be shown to follow a similar relation:

$$D_{Min} \simeq \frac{\lambda f}{d_{SLM}} \tag{2.2.7}$$

Where D_{Min} is the minimum beam width at the Fourier plane and d_{SLM} is the maximum dimension of the SLM.

The physical properties of the SLM are then used to estimate the expected dimensions of the Fourier plane. Equations(2.2.5), (2.2.6) and (2.2.7) are used to calculate these estimates, and they are shown in Table 2, using λ = 650nm.

Maximum beam divergence angle (rad)	0.0477 rad / 2.7°
Minimum beam divergence at 1m	47.7mm
Minimum beam size at 1m	37.3μm x 46.6μm

Table 2. Estimates of the beam properties at the focal plane.

Although the relationship between the Fourier and the aperture plane of the lens is relatively simple, there is a problem representing the complex amplitudes on the SLM, since the majority of SLMs can only modulate the phase of the amplitude distribution. Taking the inverse Fourier transform of the desired Fourier plane amplitudes and displaying only the phase is not generally insufficient [27]. To make matter worse, the FLC SLM device can only display binary phase states of 0 and π. However, a special case of single beam steering can be implemented with the limited modulation states. The next section analyses this special case, and the implications of binary phase only modulation on the Fourier plane.

2.3 Single beam steering

To steer a beam of light in the focal plane, the hologram at the input plane can be calculated from inverse Fourier transforming an impulse at the required beam location. This results in the simplest case of single beam steering, which is shown in Equation (2.2.4) to be a continuous phase ramp. Because the phase ramp only has varying phase values, binary phase quantisation can be used. Figure 4 shows both the continuous and binary quantised phase holograms with their simulated replay intensities.

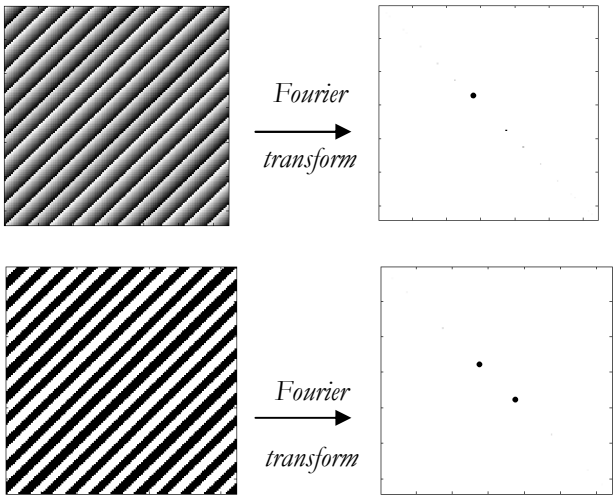

Figure 4. Comparison between simulated continuous phase and binary phase holograms, showing their respective intensities at the focal plane.

The Fourier transform was implemented by using a 2D Fast Fourier transform algorithm built into Matlab. The quantisation is performed numerically by assigning all complex values on the right half of the argand diagram to have a phase value of 0, and the left to be π;

$$\psi_{\text{binary}} = \begin{cases} 0 & \text{if } \cos\psi > 0 \\ \pi & \text{otherwise} \end{cases} \tag{2.3.1}$$

Where ψ is the phase angle of the continuous hologram.

As shown in Figure 4, the replay of the binary phase hologram has produced another copy of the beam with half rotation around the origin. This is due to the ambiguity of the two binary phase states

(Appendix A). This effect is inherent in all binary phase holograms, and only half of the addressable beam locations can be used without interference from this effect.

In addition, although not visible in the diagram due to their low intensities, the replay has produced higher diffraction orders. This reduces the power density of the desired beam. Taking average values of the intensities at the routed location, the simulated replay produces a beam with an overall efficiency of 0.81 compared to the continuous hologram. Taking into account beam duplication, this reduces the efficiency further to approximately 0.4.

The higher diffraction orders can be accounted for the harmonics produced by the quantisation (Appendix A). If $U(x,y) = \exp\left[j\xi(x,y) \right]$ is a continuous phase distribution at the aperture plane, a quantisation gives:

$$U_B(x,y) = 2\sum_{n=odd}^{\infty} A_n \left(\exp\left[jn\xi \right] + \exp\left[-jn\xi \right] \right) \qquad (2.3.2)$$

where $A_n = \dfrac{2(-1)^{\frac{n-1}{2}}}{n\pi}$. A binary hologram therefore loses much of its diffracted power to these extra harmonics. These can be suppressed by using optimisation techniques such as Direct Binary Search and the Iterative Fourier Transform. These are described in the next section.

2.4 Direct binary search algorithm

It has not been demonstrated that an analytical solution exists for producing an optimised binary phase hologram for an arbitrary intensity pattern. However, there exists a family of algorithms that search for the optimal solution numerically. One popular implementation is the direct binary search algorithm [28]. The algorithm starts with a random distribution of binary phase pixels, and using trial and error, flips a pixel one at a time such that its Fourier transform converges to the desired intensity pattern. The convergence is calculated by comparing the desired Fourier plane amplitude distribution to the simulated replay of the hologram. The details of the algorithm can be seen in Figure 5.

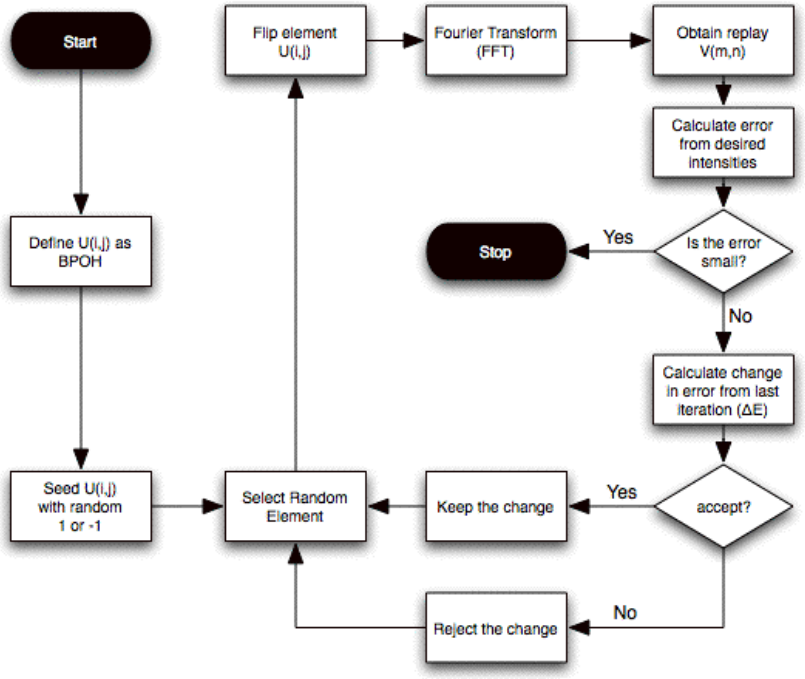

Figure 5. Flow chart of the direct binary search algorithm

Central to the algorithm is the acceptance criterion $accept$ and the differential error ΔE. The acceptance criterion is a function that decides to accept or reject the changes based on ΔE. Normally, the acceptance criterion is to reduce the error, and has the form

$$accept = \begin{cases} true & \Delta E < 0 \\ false & otherwise \end{cases} \tag{2.4.1}$$

The quantity ΔE is calculated by the differential error function to give an estimate of the error change between the new and the old hologram replay. Given that the phase of the amplitude distribution in the Fourier plane is unimportant, only the intensity information is used as basis for the error calculation. The root mean square of the difference in intensities is normally chosen:

$$\Delta E = \sqrt{\sum_m \sum_n \left(V_{new}(m,n)^2 - V_{req}(m,n)^2 \right)^2} - \sqrt{\sum_i \sum_j \left(V_{old}(m,n)^2 - E_{req}(m,n)^2 \right)^2} \qquad (2.4.2)$$

The sign of the differential error function determines if the noise has been reduced after the pixel has changed. This decision process is repeated many times while the algorithm cycles though the hologram's pixels. Eventually, the algorithm terminates when the change in error is less than a preset amount, or if the number of iterations is too large. Although the algorithm does not search the solution space globally, hence it can give results that are trapped within a local minima, it is surprisingly effective [29]. Using this algorithm, arbitrary beam shaping is now possible. Figure 6 shows the hologram that produces an array of beams that might be used for beam shaping applications.

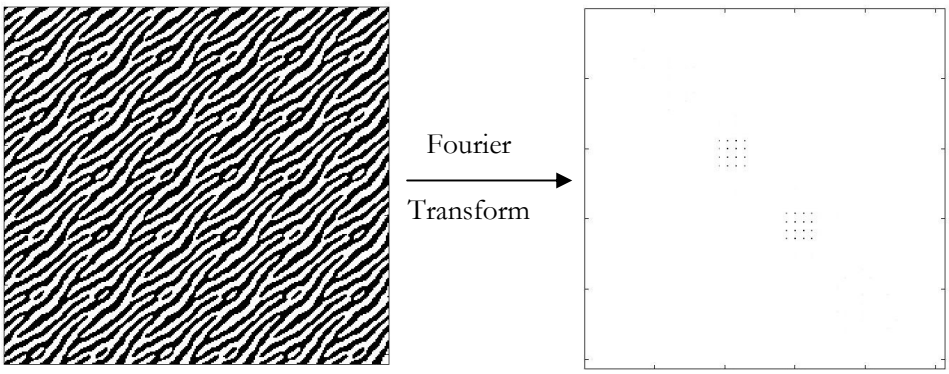

Figure 6. An example of a binary phase only hologram for an array of beams and its simulated replay. For the holograms, white and black pixels indicates 0 and π phases respectively.

2.5 DC balancing for binary phase only holograms

Although the binary phase representation problem has successfully been solved with the direct binary search algorithm, the DC balancing required by the choice of FLC SLM has not been satisfactorily addressed.

In order for a set of holograms to be DC balanced, it must have an equal number of 0 and π phase states for every pixel location in a fixed amount of time. A conceptually simple DC balancing scheme takes the spatial distribution of pixels and display its inverse in an alternating configuration. They are displayed for the same amount of time and average the phase values to zero. This scheme is shown in Figure 7.

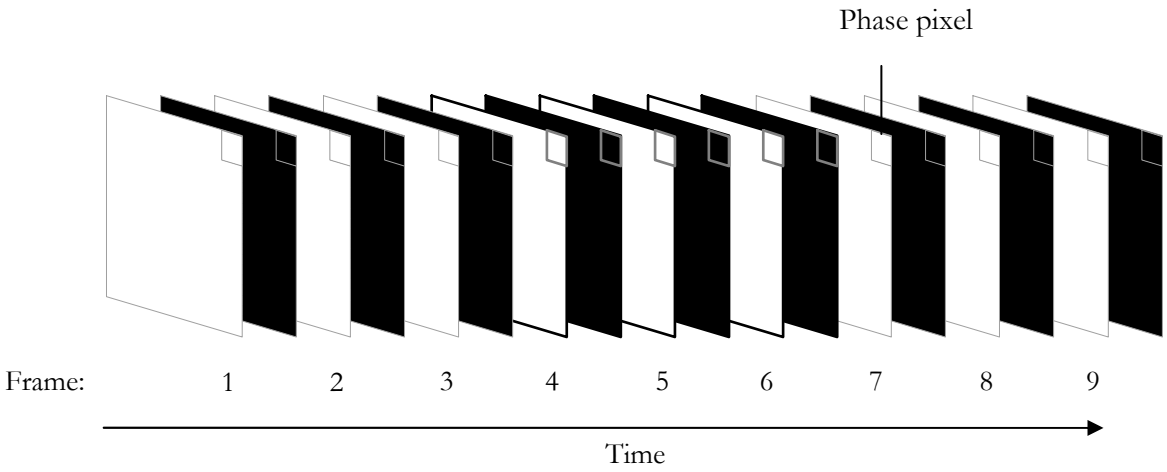

Figure 7. Schematic diagram of a frame-inverse frame DC balanced input. A video frame (white) is immediately followed by its inverse (black).

Although the phase inversion does not cause any differences in the hologram replay due to Babinet's principle [30], closer inspection reveals that the scheme causes drops in the beam's intensity during the switching between a frame and its inverse. During this transitional period, as each pixel moves from 0 to π or vice versa, it goes through an intermediate state. As this happens, the SLM has a uniform phase profile, and it loses the phase modulation properties for a short period of time [24][17]. Without spatial phase variations, the light modulated by the SLM falls inside the zero order, and the beam steering capability is lost. This is demonstrated in Figure 8. Some phase modulation capability can be retained by

increasing the number of frames in the hologram set. This reduces the number of pixel changes between each frame. Figure 9 shows a schematic view of a 4 frames DC balancing scheme. Two half inversions are used to produce a balanced set, which requires 4 frames to complete.

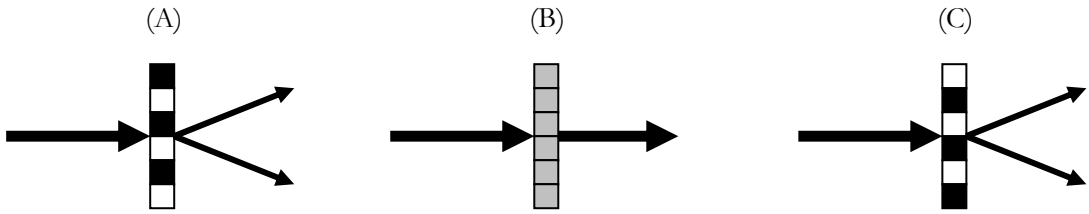

Figure 8. Simple frame inverse-frame scheme.
(A) Side on view of the SLM and the diffracted light. (B) During the transition to frame's inverse, the SLM assumes uniform phase distribution, and the modulation is lost. (C) Modulation is restored during the inverse frame.

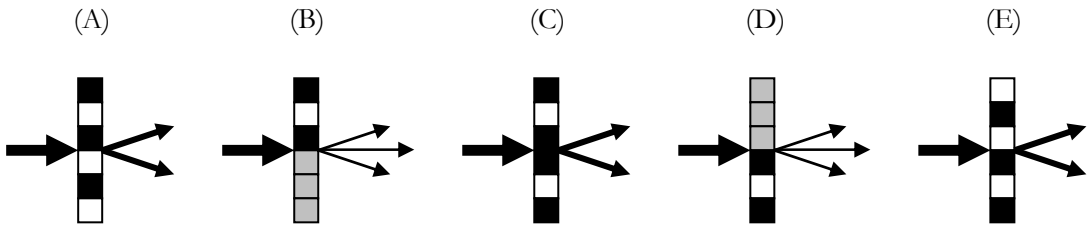

Figure 9. A more complex DC balancing scheme.
(A) Non-inverting frame. (B)-(E) shows the transition with half number of pixels at a time. The transition period (B) & (C) allows some phase information to be retained.

2.5.1 Numerical simulation of a simple DC balancing scheme

A Matlab model was developed to simulate the decrease in diffraction loss during a frame transition. The model compares two adjacent frames and determines the pixels that undergo changes. It then inserts a transitional hologram with the changing pixels set to zero. The zero emulates the loss of modulation in the real FLC SLM. The model then Fourier transforms the hologram frames, plus the transitional holograms, in a sequential order. For each frame, the intensity of the beam at the routed location is measured. A simple 4 frames DC balanced set is tested with the model. Figure 10A-G shows a test set of holograms and the replay results.

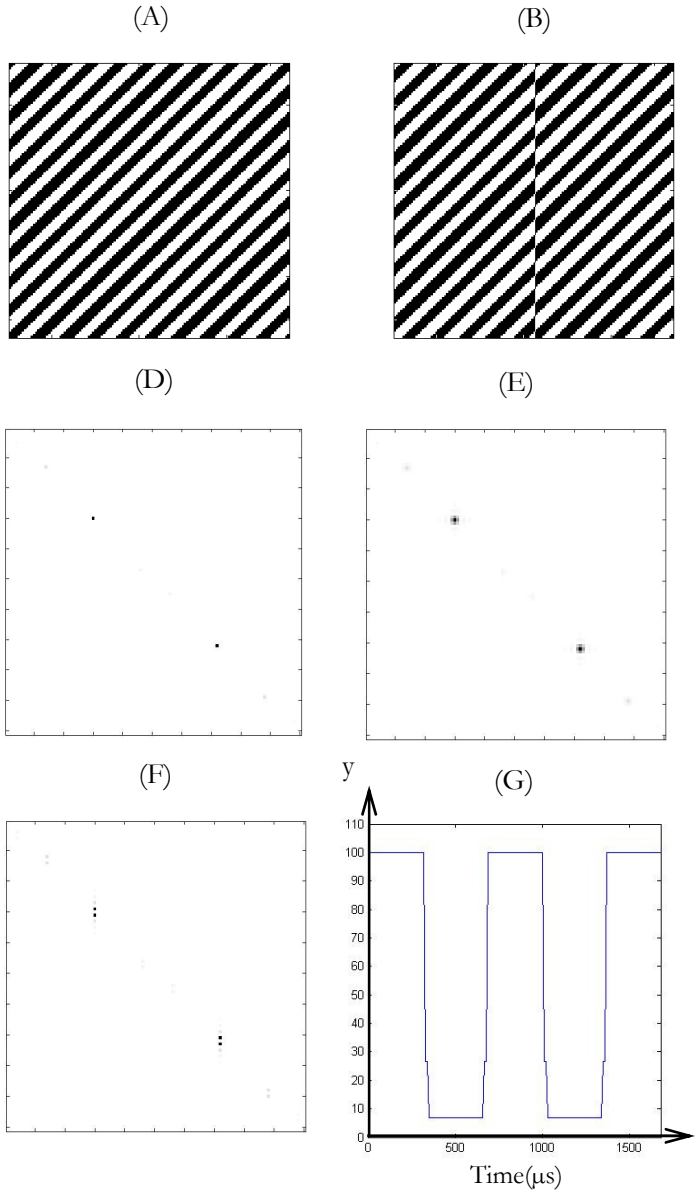

Figure 10. Simulated intensity fluctuation for a windowing scheme.

(A) Hologram to be inverted.

(B) Half window inversion.

(C) Full inversion.

(D) Simulated replay of hologram A.

(E) Simulated replay of transitional period between hologram A and B.

(F) Simulated replay of hologram B.

(G) The plot of the simulated output power of the routed spot as the hologram progresses from A to C. Vertical axis is normalised to percentage

The effect of this simple 4 frames 'windowing' scheme on the original beam can be seen in Figure 10D-F. It can be seen that the discontinuity in the phase pattern in Figure 10B causes distortion to the intended beam shape in Figure 10F. The plot of the simulated output power of the routed beam in Figure 10G shows drops in the intensity due to this distortion. In this case, the loss of modulation due to the transitional period of the frames is less than the inefficiency due to balancing holograms, which causes the intensity to drop to 5%. The windowing scheme can be shown to be a sub-optimal by analysing the effect of the inversion window on the Fourier plane. Using the convolution theorem, when the hologram is projected onto the Fourier transformed plane:

$$U'(x,y) = \mathcal{F}\left(\Pi_{win} \times H(\xi,\eta)\right) = \mathcal{F}\left(\Pi_{win}\right) * U(x,y) \qquad (2.5.1)$$

where $U'(x,y)$ is the amplitude in the Fourier plane, Π_{win} is the window function and $H(\xi,\eta)$ is the hologram. The spots are convolved with the point-spread function of the windowing function, and in this case, causes spot splitting.

Because the windowing function does not have to be a rectangular window, other windowing shapes can be used, as long as they satisfy the DC balancing criterion. However, this analysis can be extended further to these windowing schemes, which suffer from the same fundamental problem. These schemes have their own sets of point spread functions that are not optimised for the hologram being displayed. Therefore, the focus now turns to finding an algorithm that can generate an optimised scheme such that the beam shape and power density remains close to the original during the transitions.

2.5.2 Optimised schemes

An algorithmic approach based on direct binary search that tailors the balancing scheme to a particular hologram was considered in order to solve the problems encountered from using a fixed window balancing scheme. The direct binary search belongs to a family of search algorithms that can be adapted to varying types of problems. However, it can only optimise a problem with simple constraints that can be expressed in the differential error function. Initially, the DC balancing condition could not be applied directly to the algorithm. However, by applying the constraint indirectly, it was possible to ensure that every hologram in the set generated by the search algorithm remains DC balanced. The DC balance constraint was implemented by using an inversion mask, as shown in Figure 11.

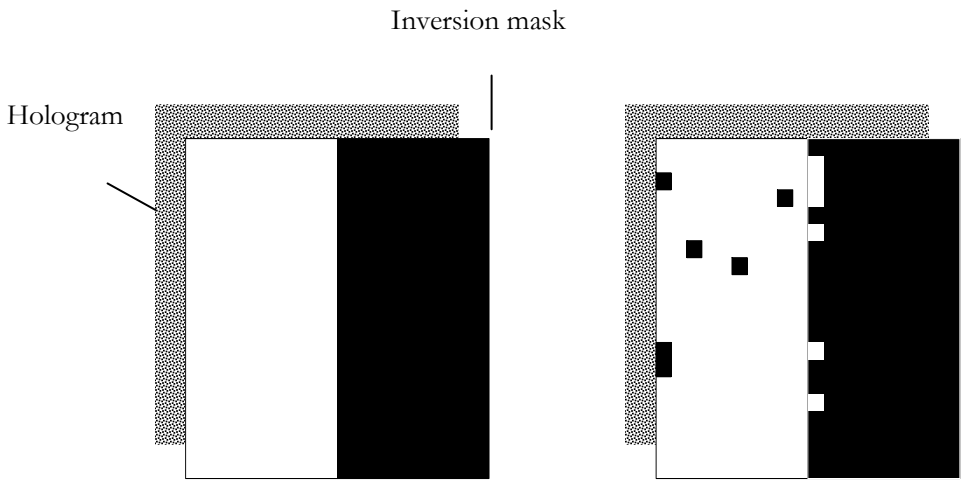

Figure 11. A graphical representation of the search algorithm initialising, and in progress of the first pass. White and black pixels represent 1 and -1 respectively.

A pre-generated base hologram is produced by using direct binary search. The algorithm then applies the mask, and relocates the inversion pixels to produce a second hologram that forms a part of a balanced set. The algorithm steps are outlined below:

1. Initialisation of a rectangle inversion mask. An inversion mask is an array of (1,-1) that has the same dimensions as the hologram, as shown in Figure 11. The numbers of 1 and -1 pixels are exactly equal. Multiplying the mask with the hologram gives the next hologram to be displayed in

a balanced set. A list of -1 pixel locations is then generated, which is used as a queue for the inversion pixels.

2. Multiply the mask with the hologram, and Fourier transform. Calculate the differential error function, based on the same RMS of intensity difference as Equation (2.4.2). This gives a measure of the mask's optimality.
3. Take the location of the first -1 pixel in the list, and randomly swap with a 1 pixel.
4. Calculate the replay and the cost function again. If the cost decreases, which means the mask is now more optimal, retain the swap and push the new -1 pixel location into the back of the queue. Otherwise, reverse the swap, push the old -1 pixel into the back of the queue and pick a new -1 pixel.
5. Jump to (3), until a predefined number of iterations have exceeded.

By starting with half of the mask inverted, once the algorithm halts, the rest of the set can be simply computed from the inverse of the first two frames.

The hologram set produced by this algorithm were then tested on the Matlab model of the SLM. Figure 12A-C shows Fourier transforms of a single routed beam balanced by this algorithm. Figure 12D-F shows the simulated replay of the hologram, including the transitional period between the holograms. Figure 12G shows the intensity of the beam as the hologram progresses though the set. The search algorithm has retained the beam shape unlike the windowing scheme. The minimum intensity has now increased to 38% of peak intensity value.

The search algorithm has successfully produced a DC balanced hologram set that improved on the simple windowing scheme. The holograms were then tested on a laboratory setup to verify both the Matlab model of the SLM and the new hologram set produced by the search algorithm.

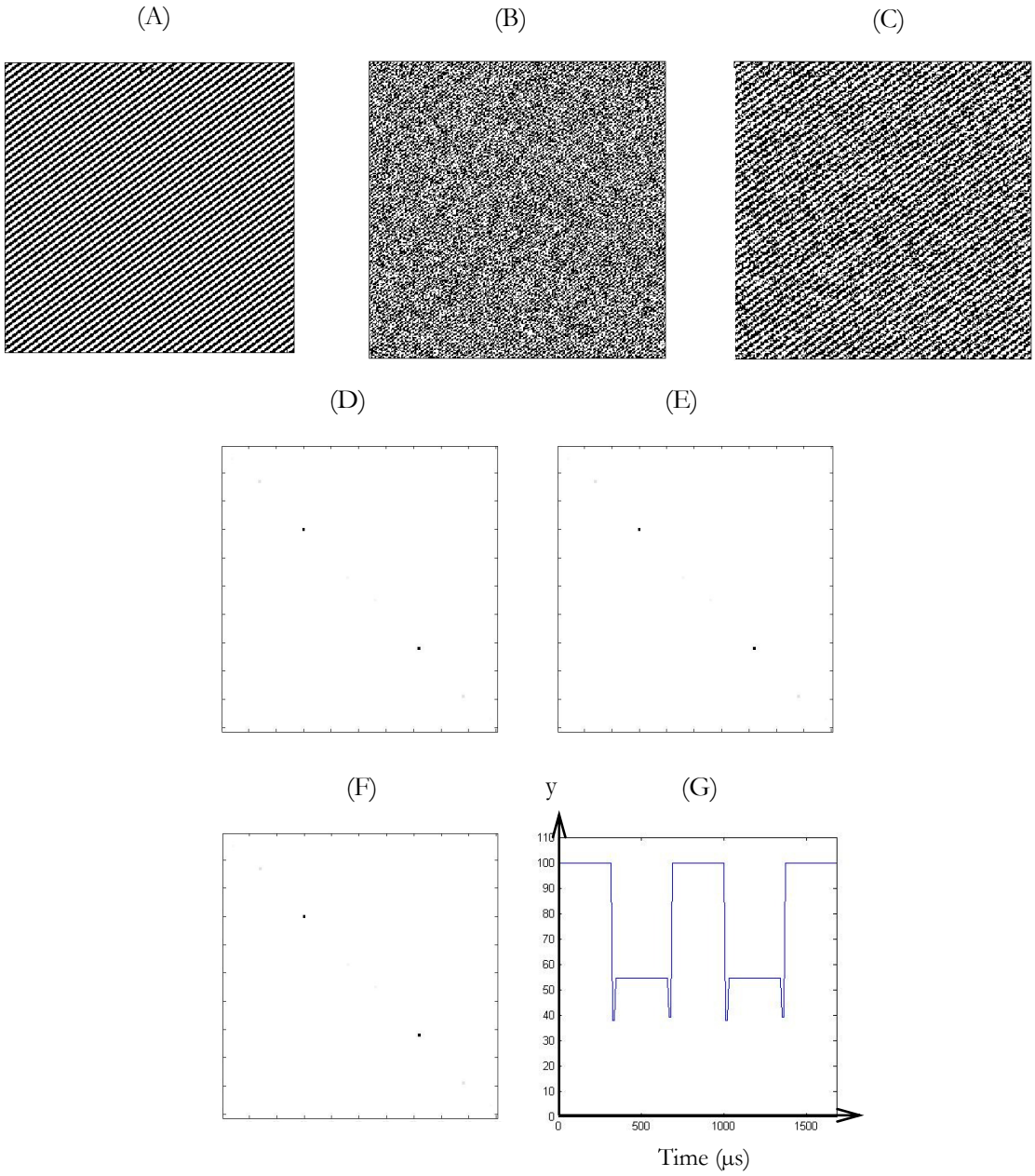

Figure 12. Simulated intensity fluctuation for a scheme derived using binary search.

(A) The original hologram.

(B) Inversion mask.

(C) Generated half inversion pattern

(D) Simulated replay of hologram A.

(E) Simulated replay of transitional period between Hologram A and C.

2.5.3 Experimental Verification

The optimised hologram set was then tested on the FLC SLM. Figure 13 shows the setup used. The illumination is provided by a Helium Neon laser with wavelength of 633nm. The laser beam is then expanded using a beam expander to illuminate the SLM. The SLM is mounted at an angle, such that the beam is reflected on to a Fourier transform lens with 6cm focal length. The beam is then split using a beam splitter, such that a copy of the beam is captured by the CCD camera. The remaining beam falls inside the aperture of the photodiode detector, the output of which is connected to an oscilloscope. This, and the CCD camera was placed at the focal plane of the SLM. The photodiode produces a voltage output that is proportional to the light intensity incident on to its sensor. The CCD camera was used to verify the intensity pattern at the focal plane.

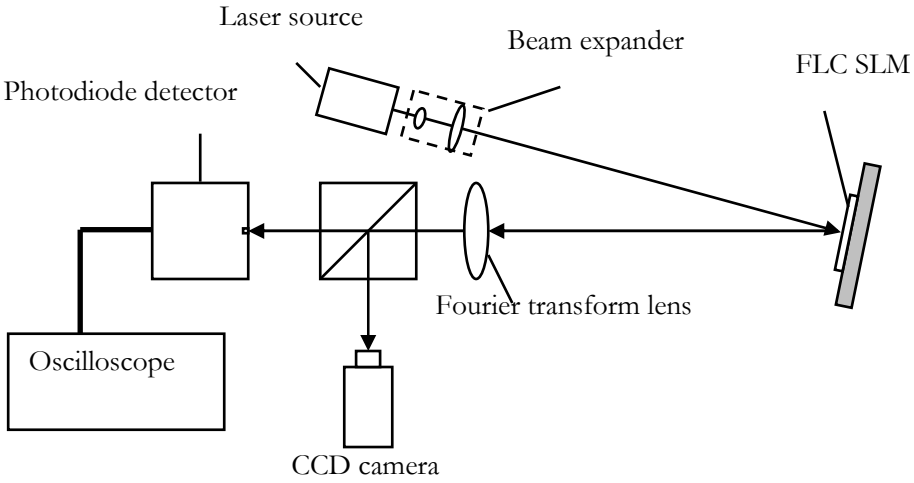

Figure 13. Schematic diagram of an experimental setup for testing DC balancing.

The optimised phase pattern produced by the algorithm was designed to shift a single beam 3mm from the zero order and was then displayed on the SLM. The photodiode detector is then placed such that the aperture coincides with the routed beam 3mm from the zero order.

Figure 14 shows the oscilloscope trace of the beam intensity from the photodiode detector when a frame inverse-frame is used for DC balancing. The intensity dips periodically to zero during the transitional period of the frame inversion. Using an optimised scheme generated from the search

algorithm, it is possible to reduce the fluctuations significantly. The output of the photodiode in Figure 15 shows the intensity fluctuations are now improved using the optimised hologram set. The lowest intensity during the transitional period was measured to be 39% of the maximum. However, the algorithm also produces frames that are 56% efficient. The average power falling within the photodiode aperture has therefore decreased by this scheme.

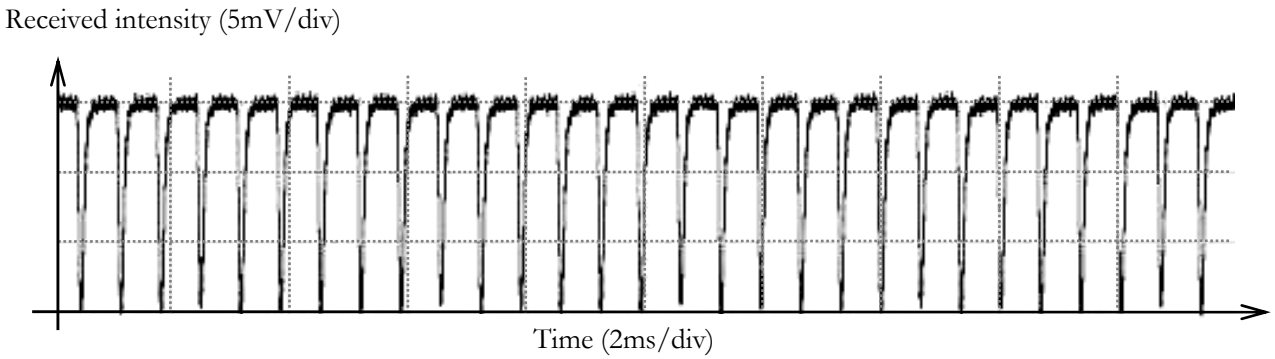

Figure 14. Trace of the output of the photodiode detector for frame inverse-frame scheme.

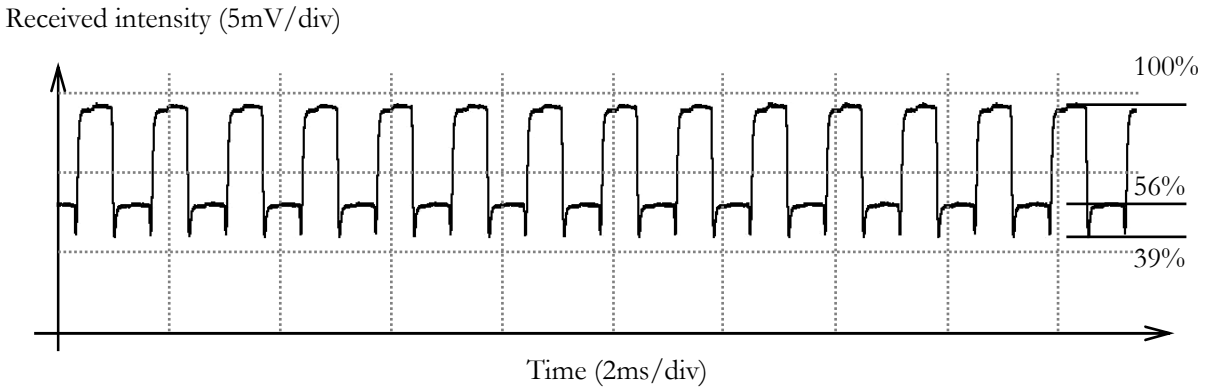

Figure 15. Trace of the output of the photodiode detector for the optimised scheme. The percentages show the drops in intensity relative to the maximum value.

The algorithm has been demonstrated to work both in the Matlab model and in a laboratory setup. It produces hologram sets that significantly improves the intensity fluctuations observed by the frame inverse-frame balancing scheme. However, the search algorithm produces hologram frames that are half as efficient as the original hologram. This is found to be due to the large amount of time needed for the algorithm. It was necessary to stop the algorithm short of total completion. The next section gives an analysis of the algorithm, and possible ways to over come this inefficiency.

2.5.4 Time estimation of the search algorithm

Although the search algorithm improved the beam shape during the balancing, it was observed that the additional iteration steps introduced by the search require a large computation time. Because the efficiency of the hologram increases with the number of iterations undergone by the algorithm, an efficient hologram requires longer computation time. The ability for the algorithm to scale with the increase in hologram size also depends heavily on the algorithm. It is therefore necessary to analyse the search algorithm such that for slow section of the code can be optimised.

The computation time for an algorithm depends on both the input hologram dimensions and the actual implementation of the algorithm. An estimate of the time required can be computed by analysing the general structure of the code. This approach is generally called time complexity analysis.

Time complexity is a function that maps an algorithm's input data size to the upper bound of computation time. It is desirable to have low complexity order, because high complexity order quickly requires impractical computation power as the input size increases. In this specific case, the number of hologram pixels is likely to determine the time complexity. The algorithm can be broken down into three independent sections. For each pixel, where n is the number of pixels and O is defined as the order operator:

1. Keeping track of the inversion pixels. This involves the retrieval and reinsertion of pixel locations from the queue. This step can be efficiently coded with a linked list, requiring $O(1)$ computation steps per iteration.
2. Calculating the Fourier transform plane. The most simplified version of the algorithm uses a Fast Fourier transform to obtain the diffraction pattern for each iteration. The transform requires $O(n\log(n))$ steps. However, a more complex scheme using pre-calculated vectors of complex angle values uses $O(n)$ multiplications. Later refinements to the code included this optimisation.
3. Calculating the error value between the desired diffracted image, and the resulting image from the new hologram. This step requires all the pixels to be computed, resulting in $O(n)$ computations steps.

By adding the computational steps, the upper bound of a single pass of the algorithm becomes $O(n)$. Therefore, for each hologram pixel to be calculated, the algorithm requires of the order of the total number of pixels in the hologram. The overall computation time will therefore depend on the number of hologram pixels the algorithm requires before it can produce reasonable solution. Since it is ideal to have a fixed running time, such that it guarantees to have finished before the next required frame begins, a good compromise for the number of iterations was found experimentally to be 4 times the number of pixels. The final complexity is therefore $n \times O(n)$ or $O(n^2)$.

The decision to have the algorithm iterate a fixed amount of times per hologram produces the inefficiency seen in the laboratory setup. Despite the compromise, the analysis shows that this approach will quickly be unable to cope with increasing hologram size, if the computational power available were to stay the same. For example, timed runs on an Athlon X2 4800+, 2GB RAM yielded a quickly growing computation time. Table 3 shows the runtimes of the search algorithm as the hologram scales from 32x32 to 1280x1024 pixels.

32x32 Pixels	0.41s
64x64 Pixels	3.5s
128x128 Pixels	51s
256x256 Pixels	803s (estimated)
1280x1024 Pixels	3.2×10^5s (estimated)

Table 3. Run times for the DC balancing search algorithm of various hologram resolutions. The algorithm was implemented in Matlab and ran on an Athlon X2 4800+, 2GB ram.

The projected run time for a full resolution hologram of 1280x1024 pixels is 3.2×10^5s, or 3.7 days, which is clearly not feasible in practice. The resolution of holograms used in the experiment were therefore reduced to 256x256, and then tiled to fill the SLM.

To further increase the efficiency of the holograms, a parallel algorithm approach was then proposed to decrease the computational time. This approach splits the computation task into smaller pieces, such that the number of computations can be concurrently computed by parallel hardware. This approach is discussed in the next section.

2.5.5 Parallel algorithm

A parallel implementation of the search algorithm is described in this section. The approach uses multiple CPUs to process the data concurrently, thus obtaining increasing improvements to the computation time with the additional CPUs.

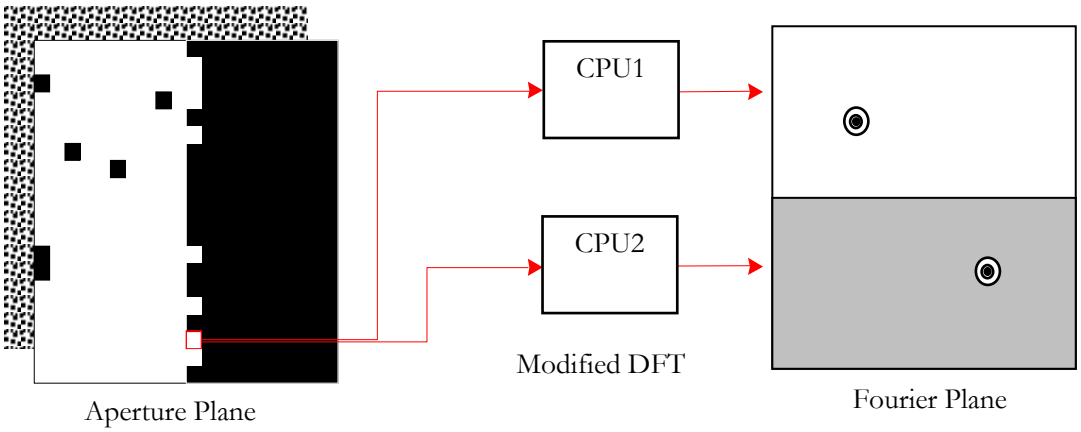

Figure 16. The parallel algorithm splits the task by assign CPUs for processing a portion of the Fourier plane.

One area of the algorithm that gains parallel computation improvement is in the repeated application of the Fourier transform. Without parallel processing, one CPU calculates the changes in the Fourier plane due to the pixel update. A modification to this step calculates the Discrete Fourier transform in two halves, each of which can be processed independently. This is shown in Figure 16. To improve this further, the cost function calculation is also divided in the same fashion.

In order to calculate the speed up offered by parallel processing, the upper bound is calculated by using Amdahl's law [31]:

$$SpeedUp = \frac{1}{(1-F)+\frac{F}{N}} \qquad (2.5.2)$$

Where F is the fraction of the parallel part in terms of the processing usage, and N is the number of parallel processors. For the Amdahl's law to apply, *F* and *N* must be independent, and this is true in the case of the modified Discrete Fourier transform and the cost function calculations. Using the MATLAB

profile command, the Fourier transform and cost function calculations are shown in Figure 17 to use 83% of the CPU. The speed up can be calculated to have an upper bound of 1.71 times faster for 2 processors system, and 2.65 times faster for 4 processors.

Lines where the most time was spent

Line Number	Code	Calls	Total Time	% Time	Time Plot
76	`Af_new = Af + (dA.*far_row_mat...`	6621	13.172 s	50.6%	
85	`Error = norm(If_new(:) - If);`	6621	5.016 s	19.3%	
70	`Af = Af + (dA.*far_row_mat(:,m...`	1663	3.313 s	12.7%	
82	`If_new = real(Af_new).^2 + ima...`	6621	3.141 s	12.1%	
104	`invPixelsVect = [invPixelsVect...`	1651	0.516 s	2.0%	
Other lines & overhead			0.859 s	3.3%	
Totals			26.016 s	100%	

Figure 17. A time profile of the original binary search algorithm.
The CPU spends 83% calculating the Fourier transform and the error function.

The concept was then implemented in the search algorithm. Because Matlab does not support parallel algorithms, a hybrid implementation using C and Matlab was used. The parallel portion is written with an OpenMP construct [32] and compiled with Intel C++ 9.0 compiler [33] for Windows as a dynamically linked library for Matlab (.mex file). The Pthreads model [34] was also investigated; however OpenMP performance was significantly better, possibly due to its smaller parallelisation overhead.

To gain more computation power from the CPUs, further parallelisation was performed using Intel's SSE2 instruction sets. SSE2 belongs to Single Instruction, Multiple Data (SIMD) parallelisation, or vector calculations. SIMD allows highly repetitive computation structures to be processed in large chunks, and are usually used in calculating vectors and matrices [35]. SSE2 specification allows up to 4 single precision floating-point multiplications in one clock cycle. To implement the algorithm using SSE2, the data structure of the hologram had to be processed explicitly in a non-overlapping manner, which was achieved by rearranging the inner loops and specifying #pragma tags in the source code. The appropriate compiler flags [36] were also expressed at compile time. For maximum performance, the Matlab and the C code was converted to single precision only. The compiler was chosen to be Intel C++ 9.0, with

optimisation flags turned on. The run times are given in Table 4 (average of 10 runs for a 256x256 pixels hologram).

1 CPU standard	1 CPU SSE2	2 CPU SSE2 + OpenMP
688s	399s	257s

Table 4. Average runtimes of DC balancing search algorithms on parallel hardware.

Although the time for the algorithm has improved significantly, it remains too slow for real time DC balancing. Beyond a hologram size of 256x256, the underlying scheme converges too slowly for large holograms. Further ways to improve computation time were investigated, such as running the search on highly parallelised super computers [37], to using graphic units to calculate the required FFT [38]. Both of these approaches were too complex to implement reliably. Therefore, this class of algorithm is currently too costly to run on current generation of computers. A new algorithm was then proposed to reduce this computational cost.

2.6 Phase redundant DC Balancing

A different approach to DC balancing was taken by observing the results produced by the direct search algorithm. There were clear patterns that can be seen from the search algorithm's output. Shown in Figure 18, the search algorithm appears to find the pixels to invert in areas where the structure of the hologram is kept intact. Figure 18A and B show two holograms for comparison. Hologram (A) and (B) suggests that there is a slight shift of the general grating structure. The shift causes phase shift in the Fourier plane, while retaining the same intensity distribution.

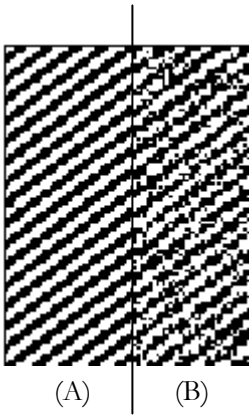

Figure 18. Comparison of DC balanced phase holograms from binary search algorithm

(A) An enlargement of a beam steering hologram.

(B) Binary searched optimal inversion mask. The mask retains the original general structure of the phase ramp, but shifted in a direction perpendicular to the grating.

For a single beam steering, the balancing scheme produced by the algorithm is similar to a phase scrolling scheme [39][40][41]. Scrolling has been demonstrated as a good scheme for FLC devices by retaining the beam shape and produces small modulation loss. It works by spatially shifting the grating perpendicular to its direction, and relying on its periodic structure to guarantee an equal number of phase states per pixel. Figure 19 shows an example of a 4 frames scheme. However, in principle, scrolling only works with phase ramps, since the scrolling direction remains fixed and perpendicular to the grating direction. It has not been demonstrated to work in other types of binary holograms.

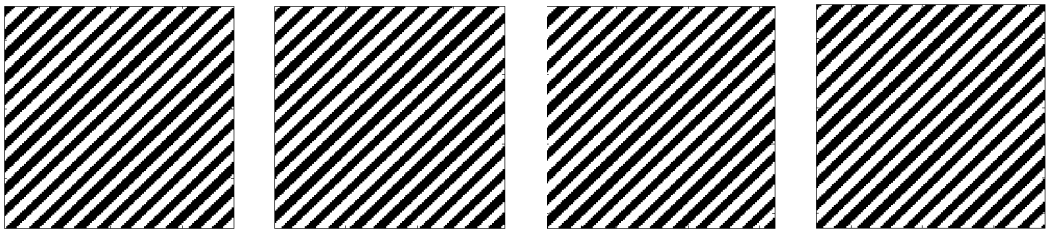

Figure 19. An example of a phase scrolling scheme. The grating is shifted in the perpendicular direction.

By observing these behaviours, it is apparent that the most optimal balancing scheme should perform the changes around the fringe edges, such that the general structure of the hologram remains the same. The new fringe shape would then slowly change into the inverted version of the hologram over a number of cycles. Each step needs to ensure that the inverting pixels will account for a balanced sequence.

A simpler approach to produce the same result can be considered by reversing the process:

1. Generate phase ramp for a particular beam location.
2. Apply a phase shift of ϕ to the hologram.
3. Quantise the hologram, and increase ϕ.
4. Repeat until the phase shift reaches 2π.

Where ϕ is:

$$\phi = \frac{2\pi}{m} \tag{2.6.1}$$

And m is the total number of frames in the scheme.

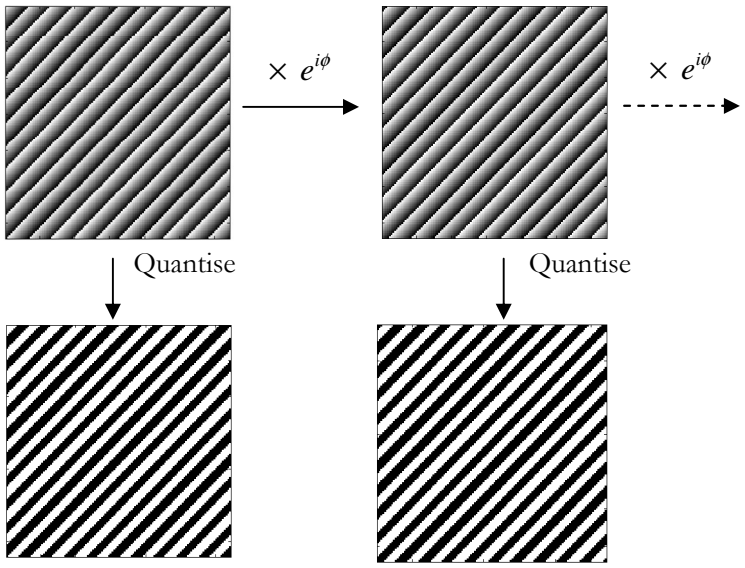

Figure 20. Diagram showing a simpler method for producing scrolling scheme.

This approach assumes that a continuous phase hologram exists that produces an efficient binary phase hologram after quantisation. If this is to be assumed true for the moment, the scheme guarantees both optimal replay and a DC balanced hologram set. This can be proven by considering a pixel in the continuous hologram.

Figure 21 is an argand diagram of a single phase pixel *A*. The pixel has a starting phase of θ. The phase of the pixel is then shifted by ϕ to *B*. If ϕ is calculated using Equation(2.6.1), pixel *A* can be shifted $m-1$ times before the phase value circles back to *A*. Therefore, there are in total m unique phase values. If m is an even number, the symmetry would force equal numbers of phase values in the left side of the diagram as the right. If the shift is applied throughout the hologram and then quantised into binary phases, the resulting hologram set will have the same number of negative as the positive pixels in each pixel location. This proves that the DC balancing is achieved using this technique.

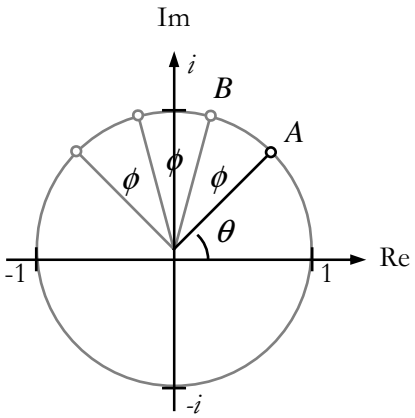

Figure 21. An argand diagram of a phase pixel in the continuous hologram undergoing phase shifting of ϕ.

Point *A* represents the original phase of θ. Point *B* represents shifted phase of $\theta+\phi$.

Because the shifting is applied throughout the hologram by multiplying the hologram with a complex number, the Fourier transform of the hologram will also be multiplied by the same constant. Therefore, the hologram set will also produce constant intensity in the Fourier plane.

The assumption of an existence of a continuous hologram that can be quantised to binary phases is fulfilled by adopting a different class of binary hologram generation algorithm: the Iterative Fourier Transform (IFT). There are many variations of IFT algorithms, with different convergence performances [42][43], but the one based on the Gerchberg-Saxton algorithm [44] was chosen due to its simple implementation.

Figure 22 shows a flow chart of an IFT algorithm. The basic IFT algorithm works by starting with a hologram of an inverse Fourier transform of the desired intensity distribution. It then forces constraints onto the hologram, in this case, binary phase quantisation, and setting the amplitude to unity. It then Fourier transforms the binary hologram to obtain the complex amplitude distribution in the Fourier plane. To complete the iteration, the algorithm replaces the amplitudes of the Fourier plane to the

desired intensity. This leaves the phase of the Fourier plane intact. The next iteration can then start. During the iterations, a differential error function is calculated to determine the halting point. This algorithm has been shown to produce reasonable binary phase holograms [42].

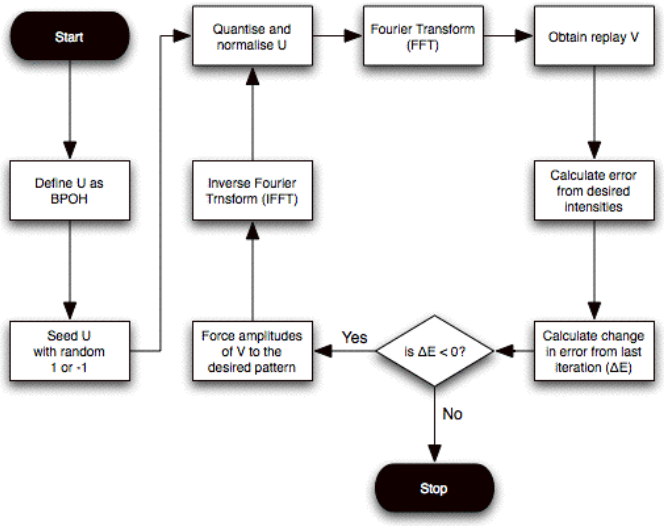

Figure 22. A flow chart of Gerchberg-Saxton based Iterative Fourier Transform Algorithm

The algorithm is useful in this balancing scheme because it retains the continuous phase information before the binary quantisation step. This satisfies the assumption that there exists a continuous phase hologram that can be quantised to binary phase effectively. A modification is then made to allow phase shifting at the final stage of the algorithm.

The application of phase shifts is computationally much quicker than calculating the frames explicitly using the method described in Section 2.5.2. This allows the algorithm to be evaluated using varying number of hologram frames. For a full resolution of 1280x1024 pixels, using the IFT algorithm requires only 17s on an Athlon X2 4800+. Figure 23 shows the power fluctuations due to new the DC balancing scheme. The 4 frames scheme in Figure 23A is shown for comparison with the simple windowing scheme and search algorithm in the previous section. Figure 23B shows the simulated power output using a 24 frames scheme. The fluctuation is now significantly less compared to both window and search algorithm schemes.

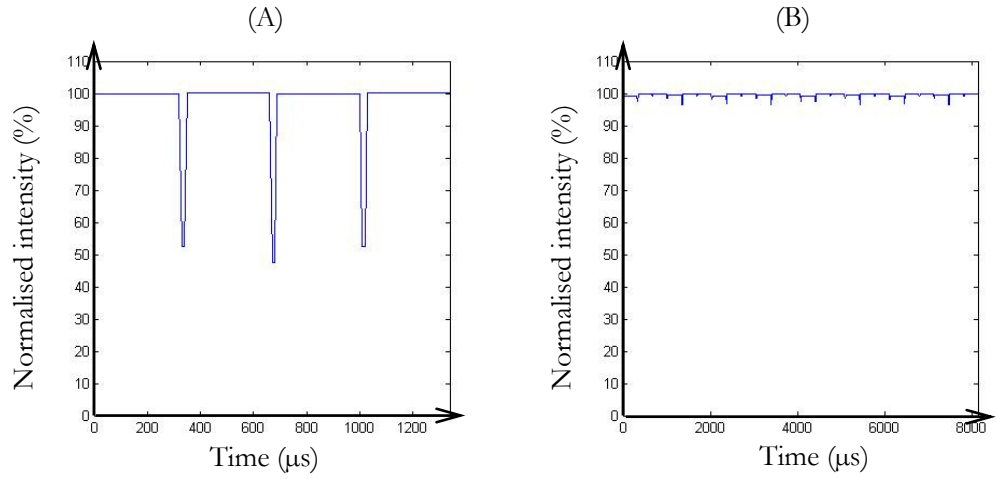

Figure 23. Simulated power fluctuation of the phase redundant balancing scheme. (A) 4 frames phase redundant balancing scheme. (B) 24 frames phase redundant balancing scheme.

As the number of frames in a balancing scheme increases, the number of pixel transitions decreases, therefore the ripple can be minimised by increasing the number of frames. To test this argument, the scheme is extended to a 24 frames scheme. Figure 23B shows a plot of the simulated replay's light intensity for a 24 frames scheme. The beam intensity dips are now almost completely suppressed. There is a reduction in refresh rate, however, as one hologram now takes 24 frames to display. This reduces the refresh rates to 60Hz.

In order to test the scheme, the holograms were displayed on the optical setup shown in Figure 13. The trace of the oscilloscope in Figure 24 shows the beam drops to 89% of its peak intensity. The trace also shows no fluctuations in intensity due to hologram efficiencies.

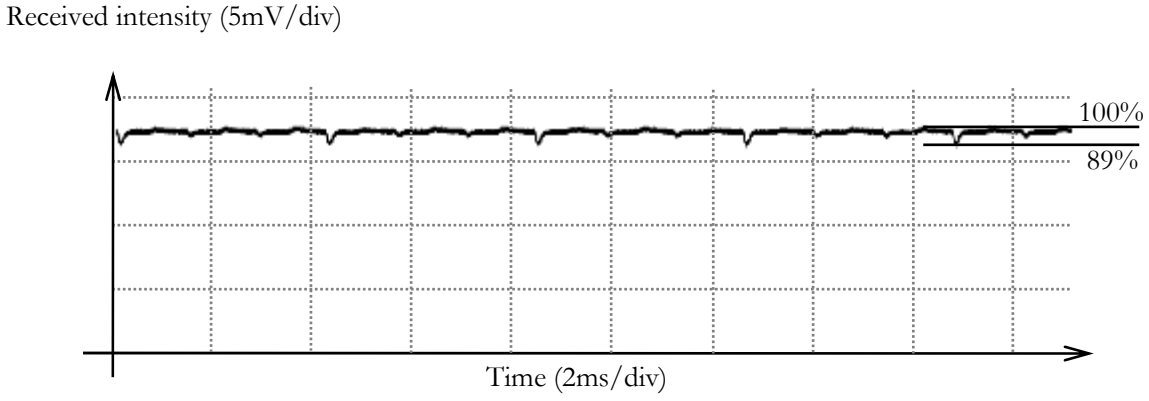

Figure 24. Voltage output from the photodiode detector for a 24 frames phase redundant scheme. The percentages show the drops in intensity relative to the maximum value.

The result shows that the phase redundant scheme is suited for DC balancing binary phase holograms. The IFT algorithm provides the necessary continuous phase hologram that can be quantised to an efficient hologram. It also requires significantly less computation time than previous approaches. With the beam intensity now within acceptable fluctuation levels, it is now possible to send data through the steered beam. The next section describes the laboratory setup to test data transmission.

2.7 Point-to-point data transmission

A laboratory setup to test data transmission using the new DC balancing scheme is shown in Figure 25. The illumination is provided by a single mode fibre coupled HL6501MG GaAs laser, operating at 650nm. The laser operating conditions are set by a laser driver, which provided a constant 60mA direct current. This sets the output laser power to 3.2mW. A data stream is provided HP 81130A pseudorandom bit stream (PRBS) generator. The two signals are combined by a bias-T, before connecting to the laser. A beam expander expands the beam to 10mm diameter, centred on the FLC SLM. The reflected beam then passes through a 5m focal length lens with 25mm diameter.

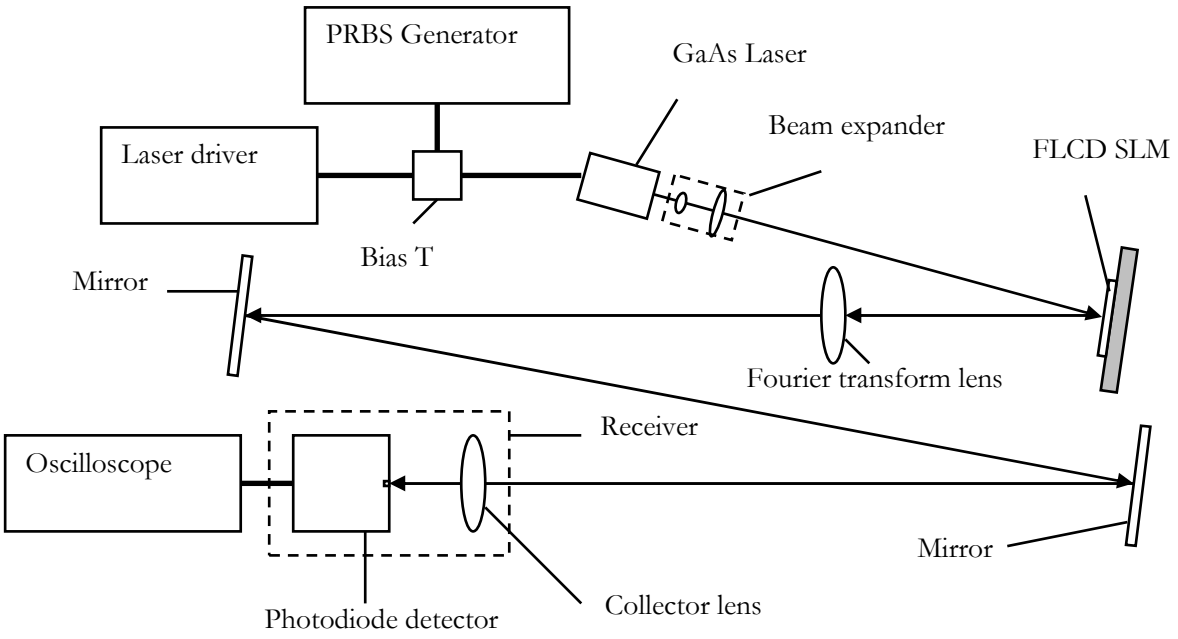

Figure 25. A diagram of the point-to-point data transmission system.

The Fourier transform lens transforms the beam onto a receiver with a 2cm diameter aperture. The two mirrors are configured to extend distance between the Fourier lens and the receiver to 5m. The maximum Fourier plane dimension is calculated to be 24cm at this distance. The focused beam diameter is measured to be 1mm. The routed location is 80mm from the optical axis. The receiver is then connected to an oscilloscope. The setup is designed to be a 1:20 scaled model of a diffraction limited 100m link.

A frame inverse-frame and a 24 frames phase redundant balancing scheme were tested. Figure 26A shows the oscilloscope trace of the receiver's output for the frame-inverse frame scheme. A large drop in optical power can be seen due to the transitions between two successive frames. In contrast, the phase redundant DC balancing in Figure 26B has small power fluctuations by comparison. The PRBS rate is set to 10Mbps in both cases.

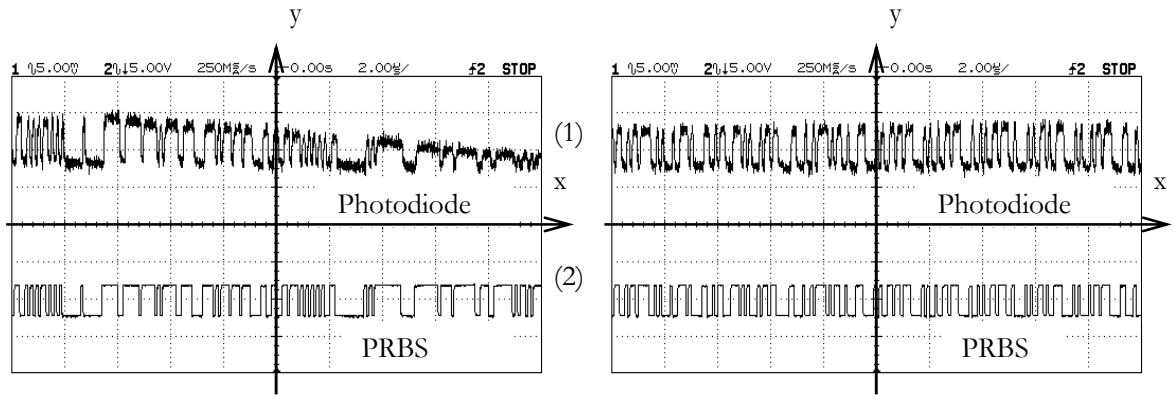

Figure 26. Oscilloscope trace of the output of point-to-point transmission system.

The time axis scale: 2μs/div. (1) the signal output of the photodiode at 5mV/div. (2) the data signal directly from the PRBS generator.

The two traces shows (A) With frame inverse-frame DC balancing. (B) With 24 frames phase redundant DC balancing. The PRBS rate is set to 10Mbps.

The experiment successfully demonstrated the FLC SLM's ability to establish and route stable free-space optical data transmission for data rate of 10Mb/s. In the next section, the SLM is reconfigured to display a beam splitting hologram to test a point-to-multipoint transmission system.

2.8 Point-to-Multipoint Transmission

Another receiver is placed in the focal plane to allow multipoint reception. Figure 27 shows the additional receiver. The laser source is provided by a 850nm GaAs vertical-cavity surface-emitting laser (VCSEL), which allows modulation up to 1.25Gbps. A collimator is attached to the front of the laser, and provides a collimated beam of 10mm diameter, illuminating the centre of the SLM. The optical power output was measured to be 1.5mW at the output of the collimator. The PRBS generator and the laser driver are connected directly to the VCSEL. A new balanced set of beam splitting holograms were created using the phase redundant algorithm and displayed on the SLM. The routed locations are 80mm and 40mm from the optical axis.

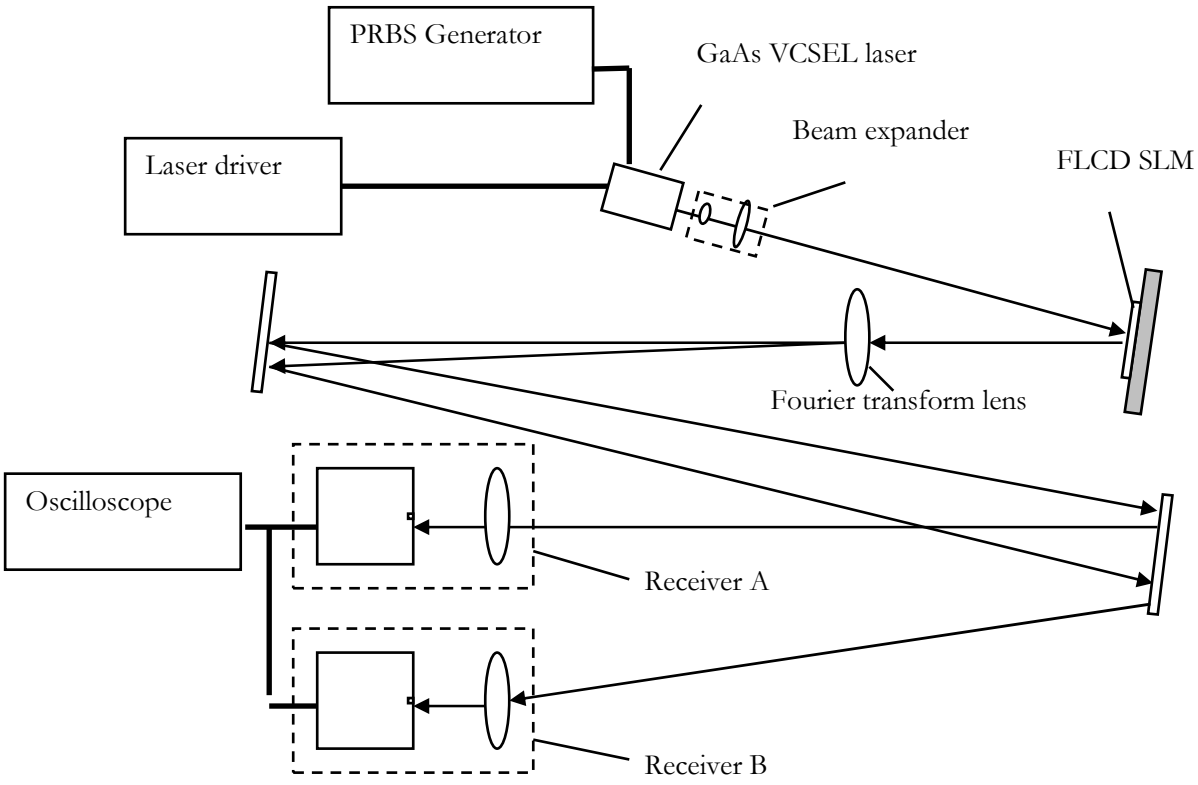

Figure 27. A diagram of a point-to-multipoint data transmission system

Figure 28 shows the output from the two receivers at 15Mbps. The two detectors were able to receive the data successfully. The setup was then tested for the maximum bandwidth of the receivers by

increasing the bit rate of the PRBS generator to 100Mbps. Figure 29 shows the eye diagrams at the outputs of the receivers. The open eyes suggest good reception for both receivers at 100Mbps.

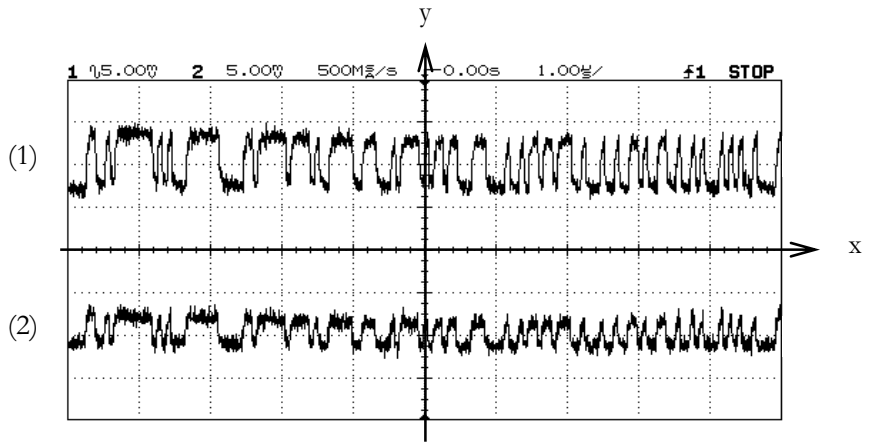

Figure 28. Output of the two receivers in the point-to-multipoint system at 15Mbps. Time axis scale: 1µs/div. (1) Output from receiver A (5mV/div). (2) Output from receiver B (5mV/div).

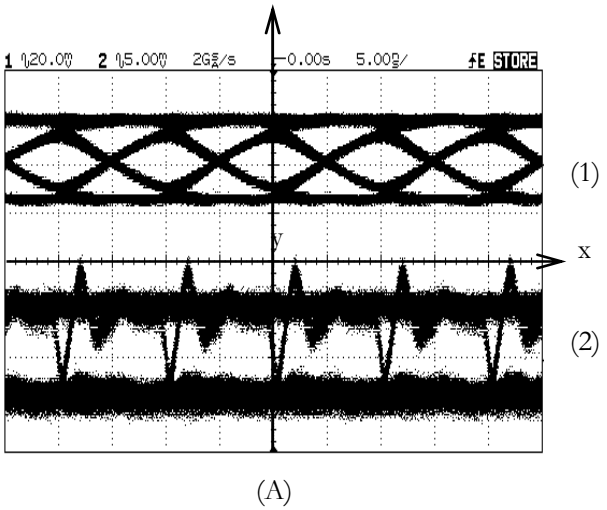

(A)

Figure 29. Eye diagram from the point-to-multipoint system. Time axis scale: 5ms/div. (1) Output from receiver A (5mV/div). (2) Output from receiver B (5mV/div). The two traces shows data stream at 100Mbps.

2.9 Conclusion

The requirement for a high refresh rate SLM device narrowed the available choices to a FLC SLM. Its high refresh rate is suited to atmospheric wave front compensation as described in [26]. Because of ferroelectric liquid crystal's inherent properties, the FLC can only operate as a binary phase modulation device. It also requires a special DC balancing routine to prolong its lifetime. The direct binary search algorithm has been demonstrated to solve the binary phase representation problem. The algorithm can generate a general intensity pattern at the Fourier plane by directly search the solution space using trial and error.

Using an FLC device to represent binary phase hologram, DC balancing is a key issue for long term stability of the liquid crystal cells. Using a modified binary search algorithm, an optimal DC balancing method was found by using phase redundancy in the intensity measurements. Computer simulation of the diffracted beam showed significantly reduced intensity fluctuation compared to a simple DC balancing method.

Point to multipoint data transmission using FLC has now been demonstrated for optical wireless transmission over a simulated 100m path length. A link transmission speed of 100Mbps was achieved in the laboratory, and likely to be much higher using faster receivers.

The new DC balancing technique can now be used in conjunction with an FLC SLM in any holographic beam steering system that requires more complex phase pattern. The next chapters reuse this result for the implementation of a retro-reflecting acquisition system and an optical turbulence simulator.

3 Retro-reflecting location acquisition

FSO communications is an attractive technology to implement wireless point-to-point communications for distances up to a kilometre. Because optical signals from a laser source can be transmitted with smaller angular divergence than radio frequencies, high optical power density can be achieved. A theoretical evaluation shows that a narrow beam is potentially more secure from detection and interception [45]. The signal levels can also be designed to provide power to the receiving devices themselves [46][47]. However, the small beam divergence limits the spread of the optical power, requiring the receiver to be positioned in line of sight to the transmitter. The acquisition of the receiver position is therefore necessary. Automatic receiver position acquisition poses an interesting challenge for most practical FSO systems [48][49][50][51].

For short to medium range FSO systems, a simplification to the acquisition process is possible by taking advantage of the narrow beam. Using a passive device that reflects the beam back to the transmitter would allow the transmitter fitted with an imaging system to detect large intensity that has high likelihood of being a receiver. These are called retro-reflectors, and the system would be suitable for areas with low ambient lighting. However, since background illumination is also imaged, further software processing is necessary.

In this chapter, an acquisition system based on a holographic beam steering is described. The system is designed for locating receivers fitted with retro-reflecting targets, by means of their retro-reflected optical return. The holographic beam steering system was also used to correct for optical aberrations present in the system to maximise the optical power density in the beam. Software processing is then used to obtain likely locations of the retro-reflectors. To calculate the acquisition performance, a gradient search algorithm is then used to measure any acquisition errors using an array of retro-reflectors.

3.1 Acquisition

Acquisition involves accurately determining the two dimensional coordinates of a receiver relative to the transmitter. The optical beam divergence angle in an FSO system is generally much smaller than radio frequency antenna radiation pattern. A small pointing error can result in large reduction in optical power received, therefore sophisticated methods are needed to acquire and steer to the precise location of the receiver [52]. There have been two main approaches that are used to autonomously acquire a transceiver position: absolute measurement [53] and beam scanning [54]. An absolute measurement of the receiver can be made via a positioning system such as a Global Positioning System (GPS). This information is then sent to other transceivers via a secondary communication channel, such as a low speed radio link. The relative coordinates can then be calculated by subtracting the two absolute positions. This method suffers from large errors in absolute position measurements, due to insufficient resolution provided by the current generation of GPS devices. There has been work in suppressing this initial error by using a feedback control system and a raster scan [53]. Another approach is to use Real-Time-Kinematic GPS and data from local accelerometers to provide greater absolute position measurement accuracy [48]. The main drawback of this approach is that GPS devices can not be placed indoors.

Beam scanning uses an optical beam to scan across the transmitter's field-of-view. A detection mechanism differentiates the return signal from a receiver from surrounding object, which is fed back to the transmitter. One method is to apply a coded signal to the beam as it scans, such as the transmitter's bearings [55]. Another is to attach a passive optical device such as a retro-reflector to each receiver, and image the transmitter's field of view as shown in Figure 30.

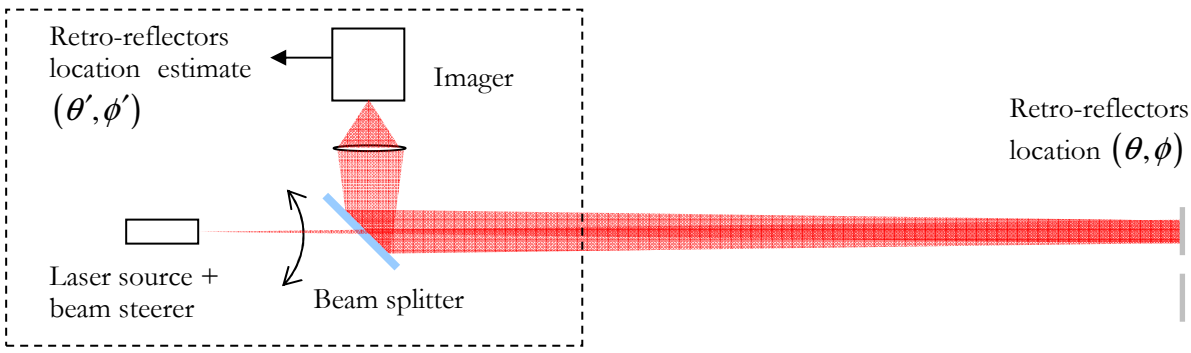

Figure 30. Optical layout of retro-reflecting target acquisition system.

During a scan, a large optical power return indicates a likely receiver position. The advantage of the system is a large simplification in the acquisition process. Figure 31 summarises this acquisition process. There are two intrinsic problems that need to be considered; the determination of retro-reflected from ambient light sources, and the non-ideal imager noise and optical characteristics. These are investigated in this Chapter.

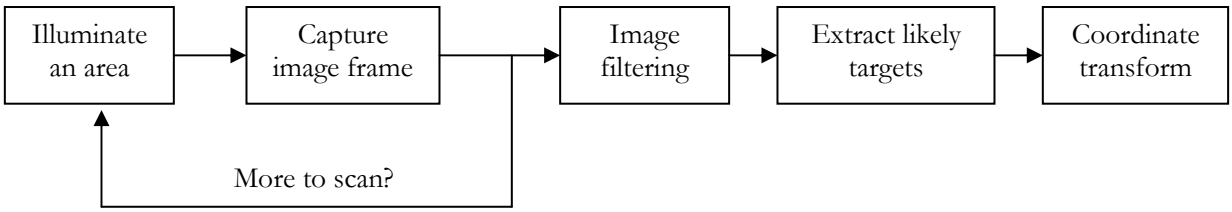

Figure 31. Flow chart of the retro-reflecting target acquisition process

3.1.1 Beam steering coordinates system

In Section 2.2, the Fresnel integral is used to describe diffraction using the paraxial approximation, which is then subsequently simplified to Fourier relations by using a positive lens. The coordinates used in a beam steering system are not spatial (x, y) but angular (θ, ϕ), since the absolute spatial positions would depend on the exact propagating distance L. By using radians, within the paraxial approximation:

$$x \simeq \theta L \tag{3.1.1}$$

The diffraction equation becomes a Fourier transform with an angular form:

$$U(\theta, \phi) = \iint_{-\infty}^{\infty} U(\xi, \eta, 0) e^{-j\frac{2\pi}{\lambda}(\theta\xi + \phi\eta)} \, d\xi \, d\eta \tag{3.1.2}$$

This form does not change the form of the algorithms used to steer the optical beam. Since the pixel size of the SLM is finite, a Fourier angular pixel is a convenient normalisation for measuring the angular deviation:

$$\Delta\varphi = \frac{2\theta_{\max}}{M} \tag{3.1.3}$$

where M is the number of pixels in a linear dimension of the SLM. This is the angular size corresponding to a pixel in the Fourier plane when an FFT is used.

3.1.2 Retro-reflecting target scanning

Figure 32 shows a schematic of the beam steering and acquisition system under consideration. The particular design considered was used in a project to transmit data to a small sensor node [46][47]. Each node has a retro-reflector and in this chapter, the target acquisition using a retro-reflector is used to locate their positions. The same system can be used for any FSO system, by appropriately selecting the maximum angular divergence and imaging system to match the design distance.

The system can be further divided into three sub-systems; the holographic beam steering, the angular magnifier, and the imager. The power budget of the system is analysed in this section.

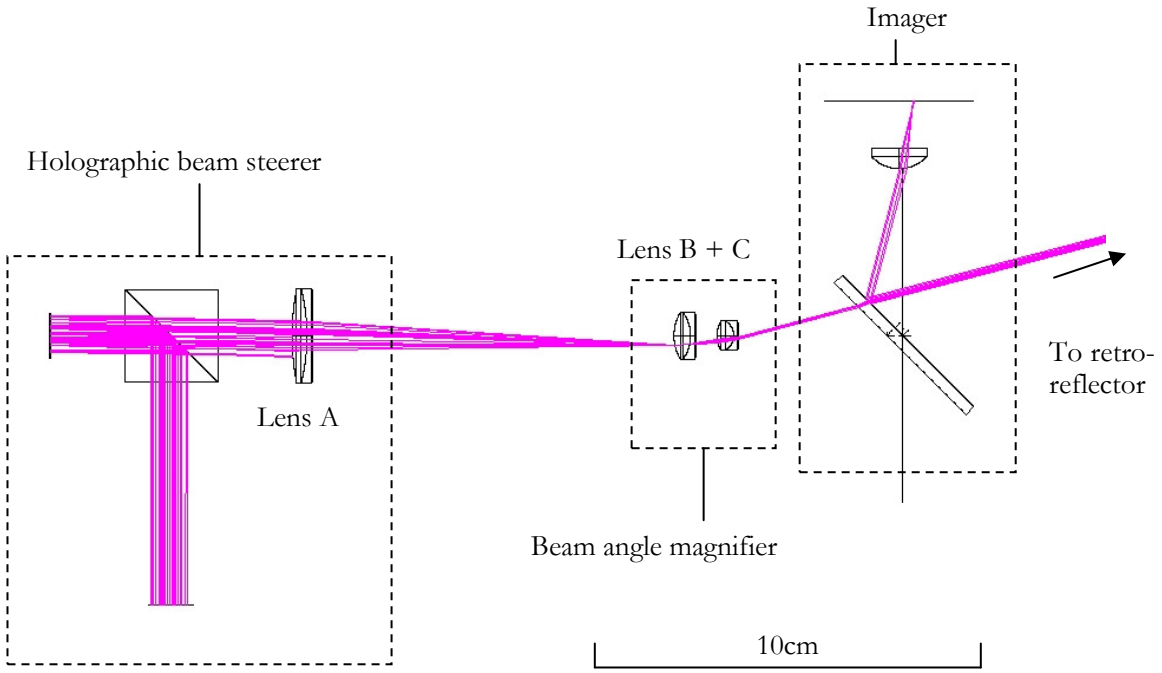

Figure 32. A model of the transmitter with holographic beam steering and angular magnifier

The beam steering subsystem uses an expanded, collimated coherent optical beam from a laser source. The beam passes though a beam splitter, and illuminates an SLM, which modulated the spatial phase profile of the beam. The beam then passes through a positive Lens A to form the holographic beam steering unit. The beam can be steered or shaped using binary phase hologram described in Chapter 2.

Lenses B and C form a beam angle magnifier to greatly increase the transmitter's field of view. The beam then passes through another beam splitter and propagates to a retro-reflector at the receiver.

The beam is then retro-reflected, and returns to the beam splitter where it is diverted to an imager. This is used to digitise spatial optical intensities coming back to the base station.

The transmitter illuminates a retro-reflector by scanning an optical beam across the field-of-view (FOV), defined as the angular range accessible by the beam steerer. An imager images any returning illumination reflected by the retro-reflectors plus any ambient illumination. The size of the output beam is measured in terms of the angular spread. The size is a compromise between the power output levels and the sensitivity of the imager. The scanning time can be estimated by considering the power density of a uniform retro-reflected beam p_r :

$$p_r = \frac{a_r p}{4} \tag{3.1.4}$$

where p is the transmitted beam power density and a_r is the retro-reflecting coefficient. Ideally a_r is 1 if the reflected beam is reflected back without causing further beam spreading. The factor of 4 is caused by loss from the beam splitter in Figure 32. The amount of energy in the static return falling on a sensor pixel with an imaging lens diameter of D and an exposure time of *t* is therefore:

$$E = \frac{\pi}{16} D^2 a_r p t \tag{3.1.5}$$

The sensitivity σ of a sensor pixel is measured as the minimum energy density J/m² to produce the smallest measurable change in its output, usually one bit value. Accounting for quantum efficiency η_q and pixel area A_p, the minimum exposure time needed to measure the retro-reflected beam becomes:

$$t = \frac{16\sigma A_p}{\pi D^2 a_r p \eta_q} \tag{3.1.6}$$

A sensitive fast frame rate imager that is used in the system is a Photonfocus MV-D1024-160-CL-8 with 45mm focal length lens f/0.95. The imager's parameters are shown in Table 5.

Pixel size	10.6μm × 10.6μm
Pixel area (A_p)	$1.1236\times10^{-10}m^2$
Responsivity	120×10^3 DN/(J/m²)
Sensitivity (σ)	8.33×10^{-6} J/m²/DN
Quantum efficiency @ 650nm (η_q)	70%
Lens Diameter (D)	2.6×10^{-2}m
Retro-reflecting coefficient (a_r)	~10%

Table 5. Imager optical and electrical parameters

The retro-reflecting coefficient is estimated to be 10%, although this value can fluctuate with different retro-reflector types. Using these values, the exposure time required is related to the power density of the outgoing beam as follows:

$$t = \frac{1.01\times10^{-10}}{p} \tag{3.1.7}$$

The exposure time is therefore inversely proportional to the power density of the optical beam. To minimise signal to noise ratio, the power density required has to saturate the imaging sensor. For 8bit sensor, this saturation amount is 256 times the minimum power density. The numerical values required are shown in Table 6.

Exposure time	Optical power density (J/m²)	Optical power density (J/m² saturating 8 bit sensor)
1 ms	1.01×10^{-7}	2.58×10^{-5}
10 ms	1.01×10^{-8}	2.58×10^{-6}
100 ms	1.01×10^{-9}	2.58×10^{-7}

Table 6. Transmitted optical power density needed as a function of imager exposure time.

With the exposure time set to 10ms and a beam total power of 20μW for an eye safe power level [56], the required beam angular size at different distances can be calculated. Assuming the transmitter total field of view of 30° full angle FOV, the percentage of angular coverage per beam is shown in Table 7.

Distance	Maximum beam diameter (m)	Angular spread (degrees, full angle)	Percentage of coverage (30° FOV)
1 m	3.14	145°	480%
10 m	3.14	35°	117%
100 m	3.14	3.6°	12%

Table 7. Beam angular spread as a function of retro-reflector distance.

Even for lower powered beams, the optical power density needed to saturate the imager is relatively small. This allows a large beam size to be used for scanning the full FOV quickly for short distances. However, at distances near to 100m, the required search beam spread needs to be small. Increasing the exposure time or transmitter power density would allow broader beams to be used.

The returned beam is imaged by the imager, and the positions of the returned beams are recorded in two dimensional coordinates. The steering angle uses a different coordinate based on the beam angular position. These are in general on a different plane to the steering coordinates; therefore a coordinate transformation between the two is needed. It is assumed in this chapter that a linear transform would be sufficient to map the two. A coordinate transformation between the two based on the perspective transform is described in the next section.

3.1.3 Imaging and steering coordinates transform

Retro-reflectors are imaged onto spatially separated pixel locations [47] on the imager. Once the retro-reflectors are visible and detected, the locations of these pixels are transformed into steering angles for the beam steerer. These can be calculated by finding the perspective transformation between the pixel coordinates and the steering angular coordinates [57].

Letting the angular coordinates of the retro-reflectors be (θ,ϕ) and the imager's pixel coordinates to be (X,Y), their respective homogeneous coordinates can be written as $(\theta,\phi,1)$ and $(X,Y,1)$. In general, the two coordinates are related by a homography matrix $\mathbf{H}$:

$$\begin{pmatrix} W\theta \\ W\phi \\ W \end{pmatrix} = \mathbf{H}\begin{pmatrix} X \\ Y \\ 1 \end{pmatrix} = \begin{pmatrix} a & b & c \\ d & e & f \\ g & h & 1 \end{pmatrix}\begin{pmatrix} X \\ Y \\ 1 \end{pmatrix} \tag{3.1.8}$$

Where all elements in $\mathbf{H}$ are real valued. $\mathbf{H}$ represents a linear transform between the imager and beam steerer planes, which maps the required transformation from the imager plane to the steering angular plane. W is the scale of the matrix. Recognising that W is calculated by the last three elements of $\mathbf{H}$, it can be factored out by dividing the right hand side [57]:

$$\begin{pmatrix} \theta \\ \phi \\ 1 \end{pmatrix} = \frac{\begin{pmatrix} a & b & c \\ d & e & f \\ g & h & 1 \end{pmatrix}\begin{pmatrix} X \\ Y \\ 1 \end{pmatrix}}{\begin{pmatrix} g & h & 1 \end{pmatrix}\begin{pmatrix} X \\ Y \\ 1 \end{pmatrix}} \tag{3.1.9}$$

(θ,ϕ) can then be separated into individual components to give:

$$\begin{aligned} \theta &= \frac{aX+bY+c}{gX+hY+1} \\ \phi &= \frac{dX+eY+f}{gX+hY+1} \end{aligned} \tag{3.1.10}$$

Rearranging and including zero terms:

$$\begin{aligned}\theta &= aX + bY + c + 0d + 0e + 0f - gX\theta - hY\theta \\ \phi &= 0a + 0b + 0c + dX + eY + f - gX\phi - hY\phi\end{aligned} \tag{3.1.11}$$

Reforming these two equations into matrix form:

$$\begin{pmatrix}\theta \\ \phi\end{pmatrix} = \begin{pmatrix}X & Y & 1 & 0 & 0 & 0 & -g\theta & -h\theta \\ 0 & 0 & 0 & X & Y & 1 & -g\phi & -h\phi\end{pmatrix}\begin{pmatrix}a \\ b \\ c \\ d \\ e \\ f \\ g \\ h\end{pmatrix} \tag{3.1.12}$$

More points can be added by stacking matrices into a larger matrix:

$$\begin{pmatrix}\theta_1 \\ \phi_1 \\ \theta_2 \\ \phi_2 \\ \dots\end{pmatrix} = \begin{pmatrix}X_1 & Y_1 & 1 & 0 & 0 & 0 & -g\theta_1 & -h\theta_1 \\ 0 & 0 & 0 & X_1 & Y_1 & 1 & -g\phi_1 & -h\phi_1 \\ X_2 & Y_2 & 1 & 0 & 0 & 0 & -g\theta_2 & -h\theta_2 \\ 0 & 0 & 0 & X_2 & Y_2 & 1 & -g\phi_2 & -h\phi_2 \\ & & & & \dots & & & \end{pmatrix}\begin{pmatrix}a \\ b \\ c \\ d \\ e \\ f \\ g \\ h\end{pmatrix} \tag{3.1.13}$$

There are 8 degrees of freedom, requiring a minimum of 4 unique reference points (calibration points) with known coordinates in both imager and beam steerer planes. More points can be used by using a pseudo-inverse using singular value decomposition as a solution to $\mathbf{H}$, giving a least squares estimate for the matrix elements [58]. This is needed if the coordinates of the reference points have uncertainty.

The homography matrix determination, or calibration, process can be summarised with a flow chart, as in Figure 33. The process is needed once as long as the transmitter's optical configuration remains fixed.

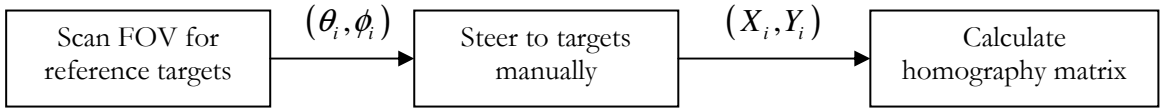

Figure 33. Flow chart of imager to beam steering calibration process

3.2 Transmitter implementation

The transmitter consists of three main subsystems: a holographic beam steerer, a beam angle magnifier and an imager as previously shown in Figure 32. Figure 34 shows an image of the transmitter.

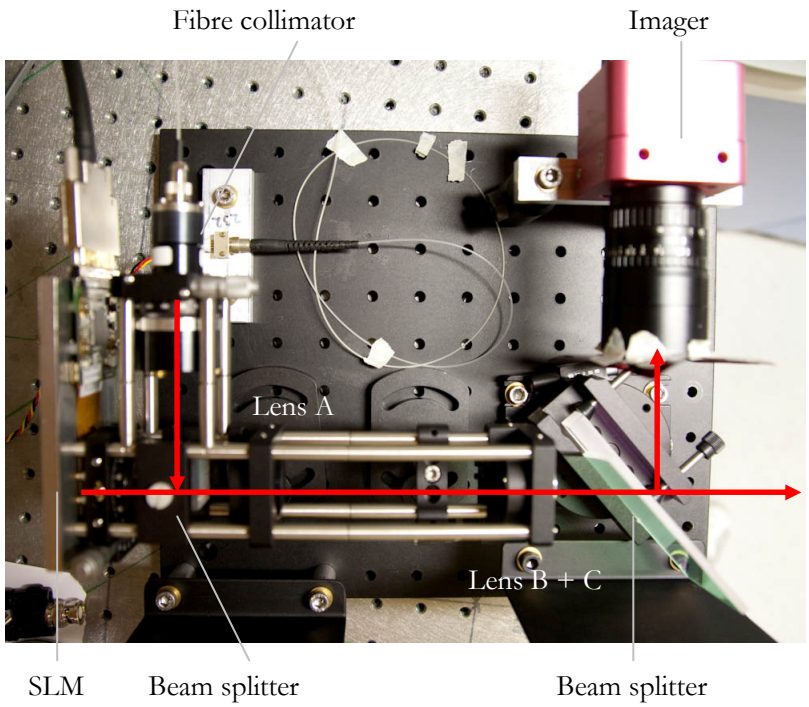

Figure 34. A photograph of the transmitter and its components

The base station measures 250mm by 300mm. The designed propagating path length is 15m. The hardware, software controller and image processing routines are described in the following sections.

3.2.1 Holographic beam steerer

Figure 35 shows the holographic beam steering unit. A collimated coherent beam is formed from a single mode fibre coupled PTLD655G50-SMFC pigtail laser diode, emitting 10mW at 650nm using a modulating current of 70mA. The fibre is attached to a beam expander to provide a large coverage over the SLM. The expanded beam shape was measured to be approximately Gaussian, with a beam radius of 15mm, covering 73% of the active area. The SLM is positioned to provide on axis spatial phase modulation using a polarising beam splitter and a half-wave plate.

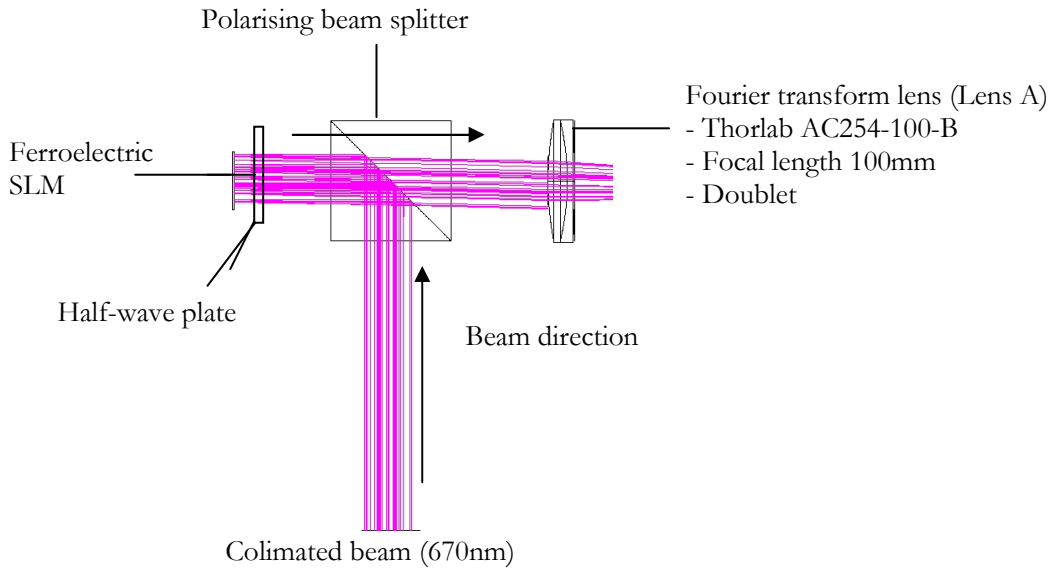

Figure 35. Details of holographic beam steering unit

A 4th Dimension Display SXGA-R2 is used for the SLM. A square area of 1024x1024 pixels is used in the system. Using the results from Section 2.2, the device maximum steering angle is:

$$\theta_{\max} \simeq \frac{\lambda}{d_{pixel}} = 2.7° \qquad (3.2.1)$$

Where λ is 650nm and d_{pixel} is the pixel linear dimension. For convenience, the angular resolution of θ and ϕ are expressed in multiples of single Fourier pixel, $\Delta\varphi$ equalling to:

$$\Delta\varphi = \frac{2\theta_{\max}}{1024} = 5.1\times10^{-4} \text{ rads} \qquad (3.2.2)$$

3.2.2 Imager and control system

Figure 36 shows a chart illustrating the connections between the transmitter electronic components. The imager consisted of a Photonfocus MV-D1024-160-CL-8 CMOS sensor module (Table 5). The sensor is then connected to a Matrox PCI-E frame grabber card. The card is housed in a Pentium 4 3GHz workstation with 2GB of available RAM (Workstation). This is used to control all aspects of the transmitter, except for the SLM. The SLM is connected to a display server (Server) on a DVI bus. The two computers are connected using an Ethernet network. The server runs a custom application to serve display requests from the Workstation.

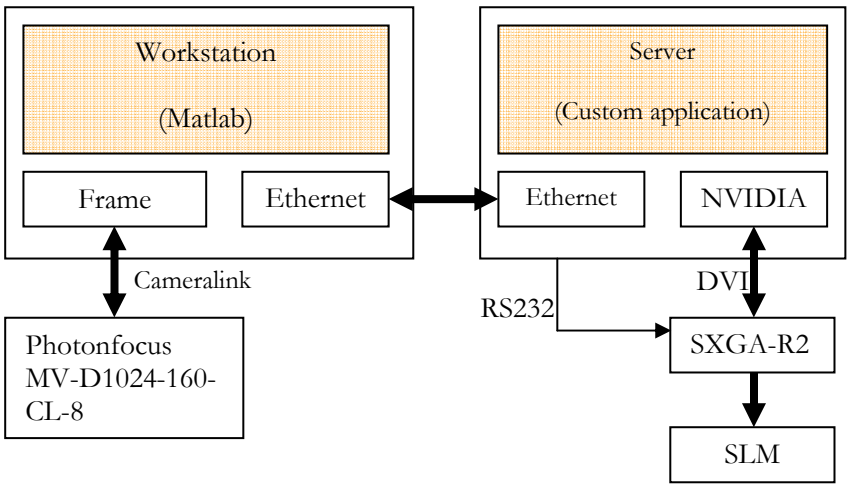

Figure 36 Schematic diagram of the components used to drive the transmitter.

The Matrox frame grabber's application programming interface (API) used is based on the Camera Link standard [59]. This standard allows software control of the imager's parameters, such as the exposure time and frame rates. A wrapper was written in C++ to interface MATLAB functions to the imager. The exposure time is set according to the required lighting condition, ranging from 3ms to 20ms.

3.2.3 Angular magnifier and optimisation

Two positive lenses B and C positioned in a Keplerian telescope configuration are used to increase the maximum steering angle to match the imager's field of view of 30°, chosen to correspond to the area covered by receivers at 15m. The design process in this section can be used for greater distances.

The choice for these two lenses affects the minimum beam size due to aberrations. A Zemax simulation is used to find an optimal spacing between the two lenses. The SLM is simulated by a continuous phase grating with varying spatial frequency. The distances between the Fourier transform lens and the angle magnifier lenses are each optimised with a Damped Least Square algorithm to find the best values for these two distances. A manual selection of possible lens combinations resulted in a choice of Edmund optics AC127-019-B and AC080-010-B for lens B and C (Figure 37A) for a maximum beam angular deflection of 30.2°. The optimised distances are found to be D_f = 92.12mm and D_m = 9.96mm, producing RMS spot angular sizes of 0.028° on-axis and 0.020° at the maximum for beams propagating 15m.

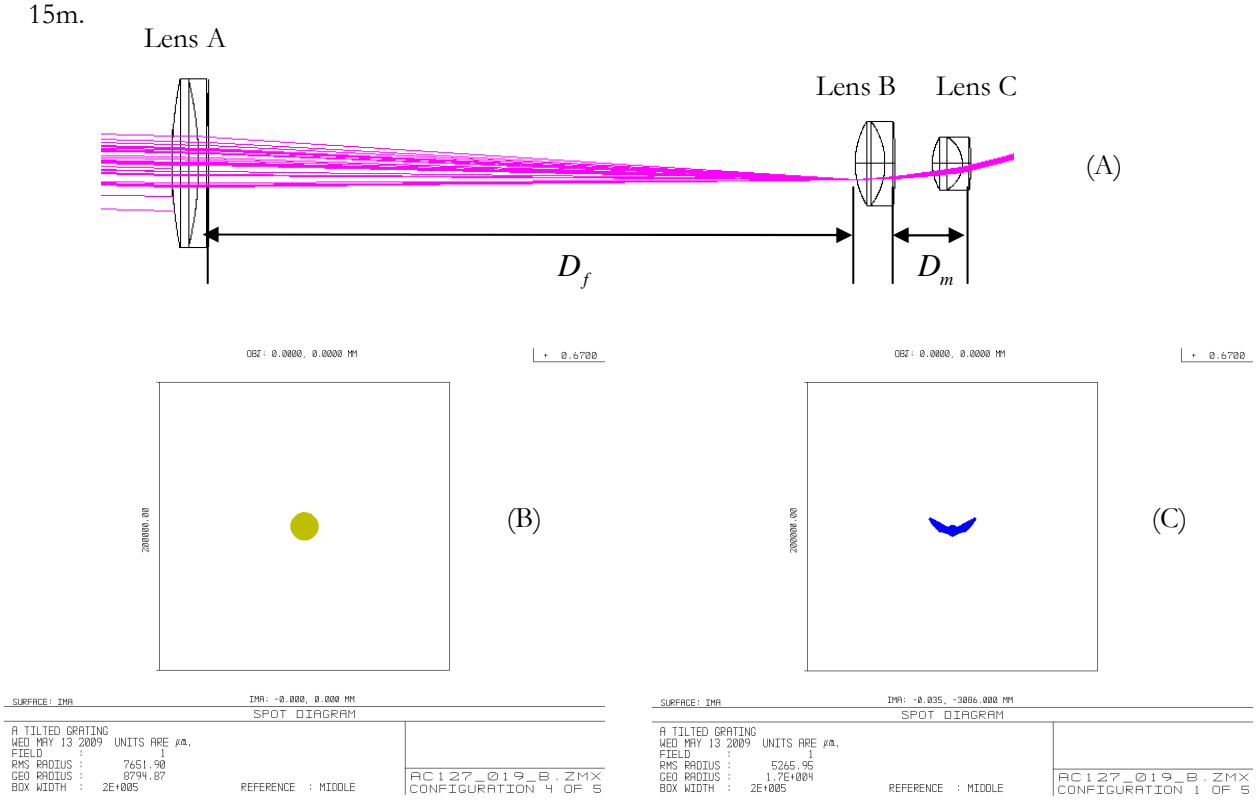

Figure 37. Retraced diagram of the angular magnifier and the spot diagrams.
(A) Distances between three lenses were optimised using Zemax optimisation tool.
(B) Spot diagram of on-axis beam at 15m.
(C) Spot diagram of maximum deflection at 15m.

To maximise the beam power density, it is necessary to design the angle magnifier such that a small beam radius is maintained across the transmitter's field of view. There has been recent research using deformable mirrors to correct for aberrations in wide field-of-view imaging systems to the point of diffraction limited performance. Wick and Martinez [60][61] found that spatial distribution of phase corrections are necessary for the whole field of view, since the aberration is spatially dependent. A similar method is investigated here to optimise the transmitter beam shape using the SLM in the holographic beam steerer.

It is observed that by optimising the distances to only consider the maximum deflection beam, giving D_f = 97.312mm and D_m = 5.620mm, the beam size can be improved significantly. Table 8 shows the simulated beam properties for this case.

	On axis beam	Maximum deflected beam
Spot radius	21mm	1.871mm
Power density	0.02μW/mm²	2.89μW/mm²
Deflection	0°	30.2°

Table 8. Simulated beam measurements for maximum-deflection optimised angle magnifier at 15m

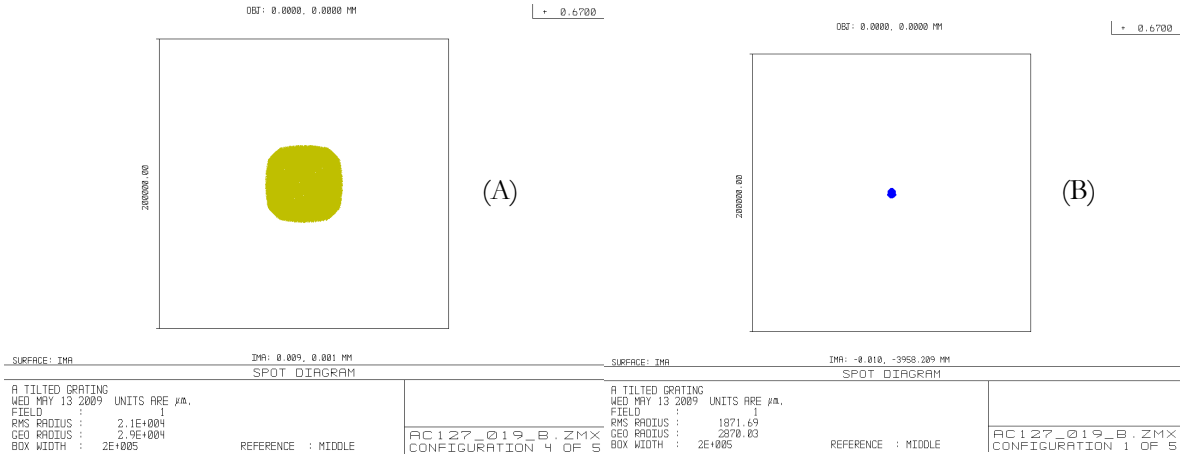

Figure 38. Spot diagrams for (A) on-axis beam (B) max-deflection beam for maximum-deflection optimised angle magnifier at 15m propagating distance

The optimisation is then run using a merit function that uses the on axis beam only, i.e. a beam with zero deflection. The new optimal distances becomes D_f = 92.509mm and D_m = 9.713mm. Table 9 shows the new simulated beam properties and the spot diagrams in Figure 39.

	On axis beam	Maximum deflected beam
Spot radius	7.651mm	5.265mm
Power density	0.16μW/mm²	0.34μW/mm²
Deflection (full angle)	0°	23.6°

Table 9. Simulated beam measurements for on-axis optimised angle magnifier at 15m

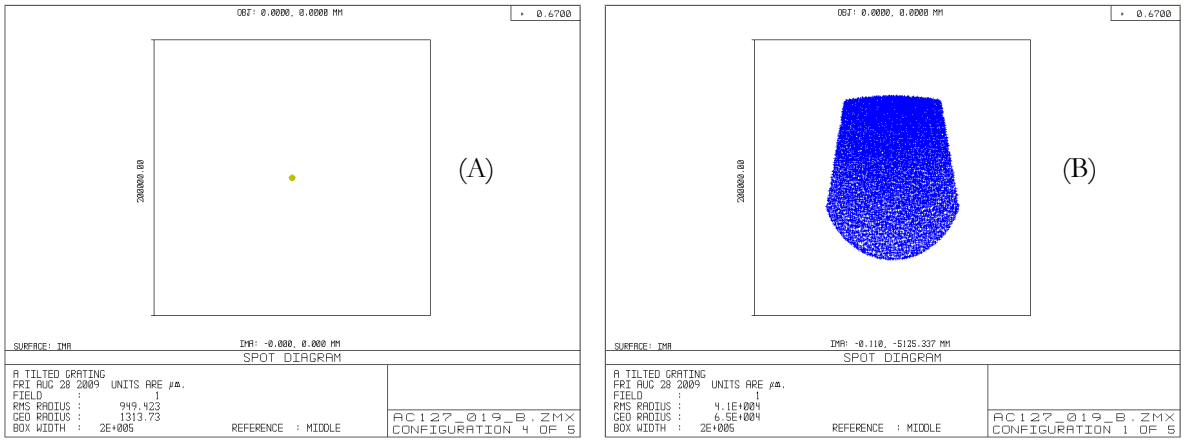

Figure 39. Spot diagrams for (A) on-axis beam (B) max-deflection beam for maximum-deflection optimised angle magnifier at 15m

A simulation was carried out to calculate exactly the aberration compensation was required. The model is modified to include a paraxial lens component in contact with the SLM, and its focal length F is set as a variable. F is then optimised for different values of beam deflection. This configuration simulates focusing power applied on to the SLM. Values of D_f and D_m are set to be 97.312mm and 5.620mm, giving a good spot radius at maximum deflection. Figure 40A shows a plot of the corrective radius of curvature ($1/F$) versus SLM grating frequency S, while the corrected beam radius is plotted in Figure 40B.

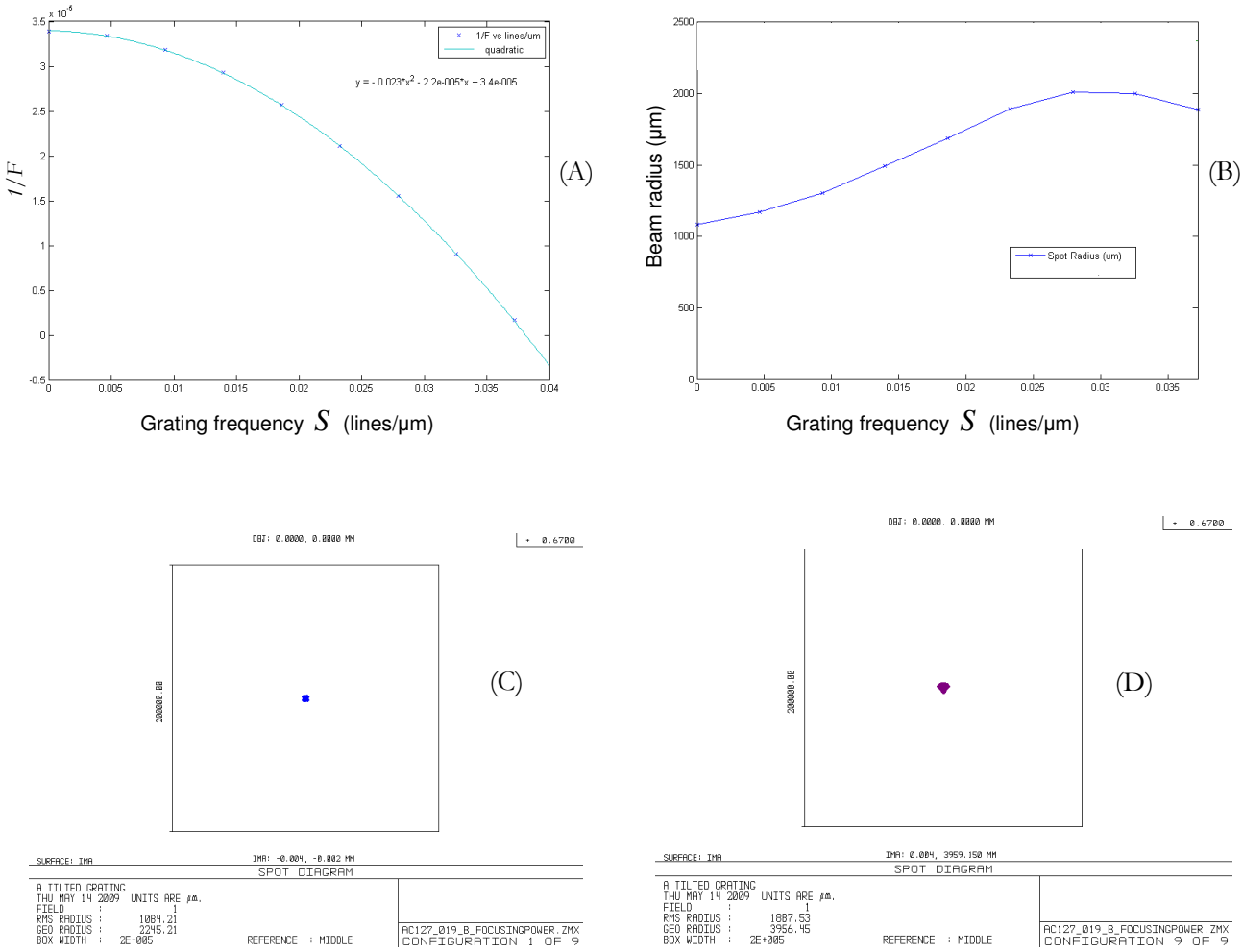

Figure 40. Plots of maximum-deflection optimised angle magnifier at 15m

(A) Plot of the required $1/F$ correction per grating frequency to minimise beam radius.
(B) Corrected beam radius per grating frequency.
(C) Spot diagram of corrected on-axis beam
(D) Spot diagram of corrected maximum-deflection beam

The RMS spot radius has now been significantly reduced compared to Figure 37A-B. The spot diagrams are shown in Figure 37C-D. The focusing power $1/F$ is fitted very closely by a quadratic function of the grating frequency. D_f is then readjusted to assess the defocus correction for a system focused for on-axis beams, giving value of D_f = 97.651mm. Figure 41A shows the $1/F$ versus grating frequency S, and the RMS spot sizes and simulated beam radius is plotted in Figure 41B.

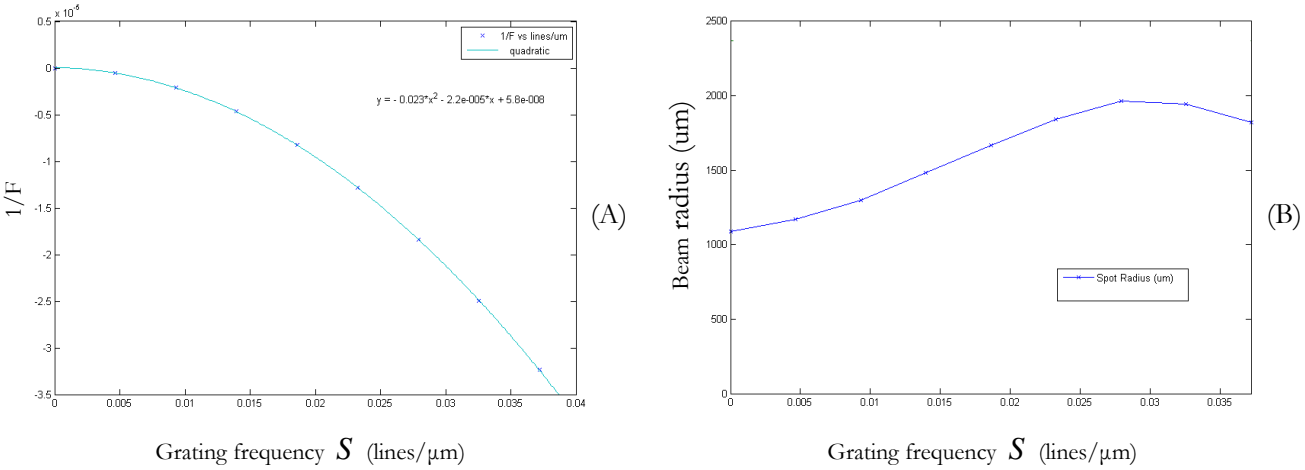

Figure 41. Plots of on-axis optimised angle magnifier at 15m

(A) Plot of the required 1/F correction per grating frequency to minimise beam radius.
(B) Corrected beam radius per grating frequency.

There are no appreciable differences between the two systems in terms of RMS spot sizes and absolute value of defocus. Pre-focusing the on-axis beam had the advantage of requiring no defocus correction near the axis, where most beam power density was available. The beam RMS radius at distances smaller than 15m was then simulated by reducing distance to the surface in Figure 42. The defocus adjustment F was kept at values optimal for 15m distance.

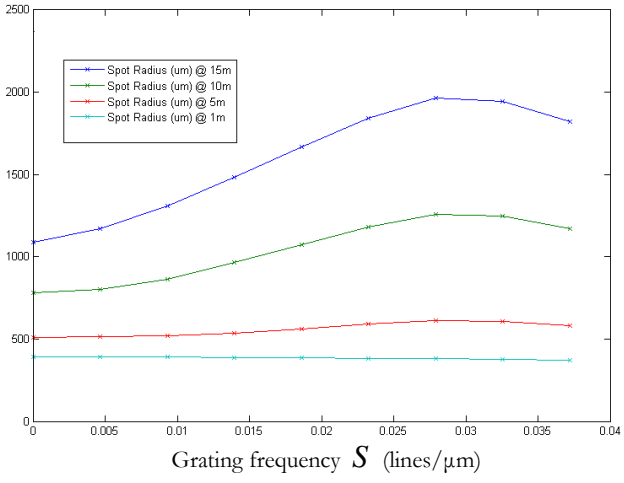

Figure 42. Simulated beam radius for various propagating distances

In order to generate the defocus correction on the SLM, the same Zernike focusing term is used:

$$focus(S) = \exp\left(\frac{2i\pi d(S)}{N^2}\left(j^2 + k^2\right)\right) \qquad (3.2.3)$$

Where N is the dimension of the SLM in pixels, parameter d is related to the paraxial focal length F and grating frequency S by using the quadratic fit from Figure 41A:

$$d(S) = \frac{k}{F(S)} = k\left(-0.0229S^2 - 2.22\times10^{-5}S + 5.76\times10^{-8}\right) \qquad (3.2.4)$$

The constant k is found by measuring the relationship between the optimal simulated defocus values to actual measured defocus values from the transmitter. The measurement of this constant was made by manually selecting values of d to find minimum spot radius produced by the transmitter. A number of points were recorded then plotted against the grating frequency S in Figure 43.

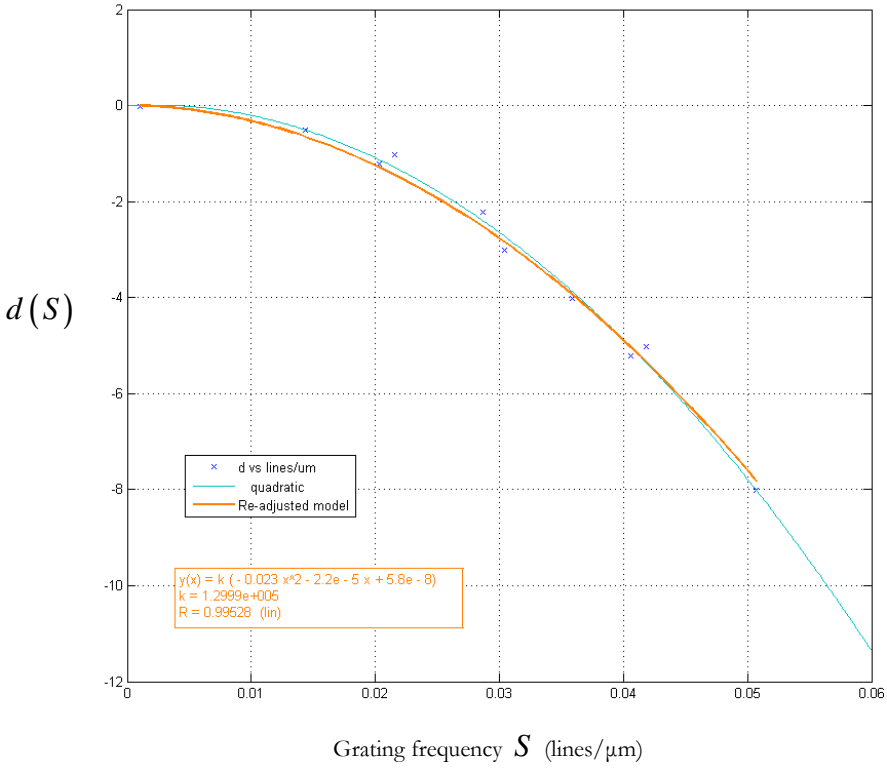

Figure 43. Plot of manually measured focus correction, fitted with a quadratic fit and best fit obtained from simulation.

The measured defocus values compare favourably to those simulated. The constant of proportionality k could be estimated by fitting equation (3.2.4) to the data, giving value of:

$$k = 1.30\times10^5 \qquad (3.2.5)$$

Thus the defocus parameter d is described by:

$$d = -2.99\times10^3 S^2 - 2.89\times S + 7.5\times10^{-3} \qquad (3.2.6)$$

Converting the spatial grating frequency to a more convenient unit of angular displacement in multiples of $\Delta\varphi$ or 5.1x10^{-4} rads, d becomes:

$$d = -0.214(m\Delta\varphi)^2 - 2.07\times10^{-4}(m\Delta\varphi) + 7.5\times10^{-3} \qquad (3.2.7)$$

where m is the pixel location in the Fourier plane. This function was then incorporated into equation (3.2.3) to be applied during SLM grating calculation. The SLM ia then DC balanced as described in the previous section. Measurements of the beam power density improvement are described in the next section.

3.2.4 Beam power density measurements

The defocus correction is implemented in the holographic beam steering routine. A DC balancing routine was applied afterwards to ensure long term stability of the liquid crystal cells. Figure 44 shows uncorrected first order beams illuminating a white screen at a distance 3.5m from the transmitter, with varying deflection from the optical axis. A scale was placed near the beam as reference, and the final image was adjusted to the same scale. At each steering angle, the total power within the beam was measured using a 10mm diameter aperture optical power meter. Total optical power was increased by roughly 1μW.

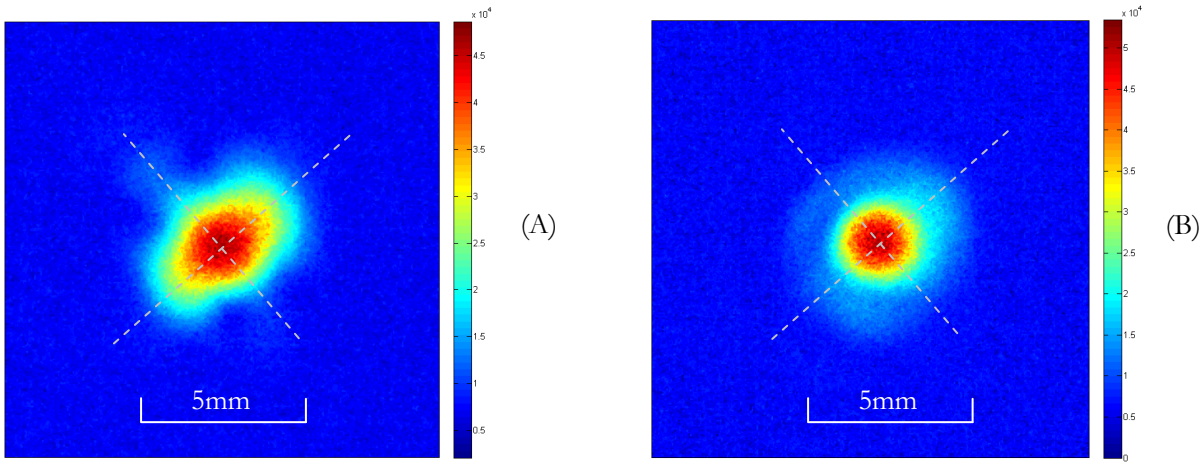

Figure 44. (A) Beam intensity profile close to on-axis. (B) Corrected intensity profile.

Pixel location	Uncorrected	Power	Corrected	Power
(50,50) $m = 50\sqrt{2}$	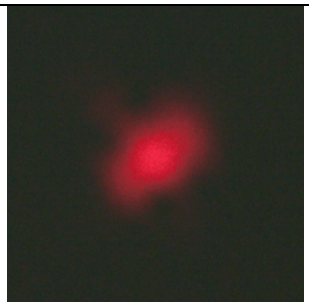	28.2μW	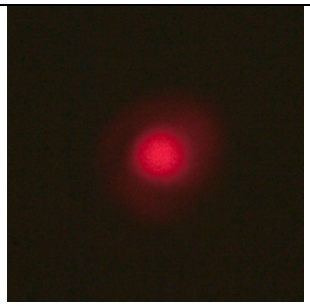	29.25μW
(100,100) $m = 100\sqrt{2}$	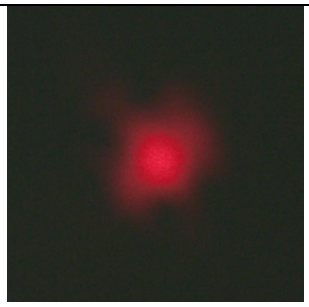	28.4μW	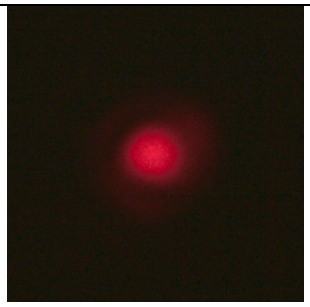	29.0μW
(200,200) $m = 200\sqrt{2}$		24.2μW	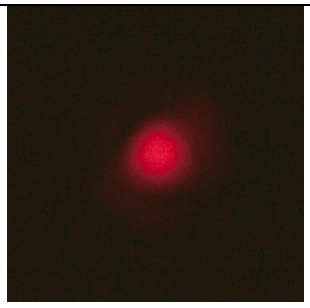	25.6μW
(300,300) $m = 300\sqrt{2}$	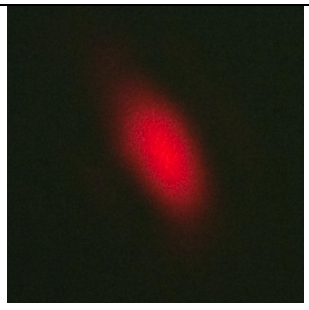	20.4μW	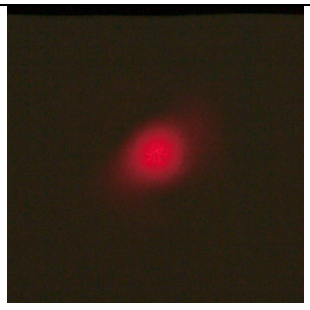	21.6μW

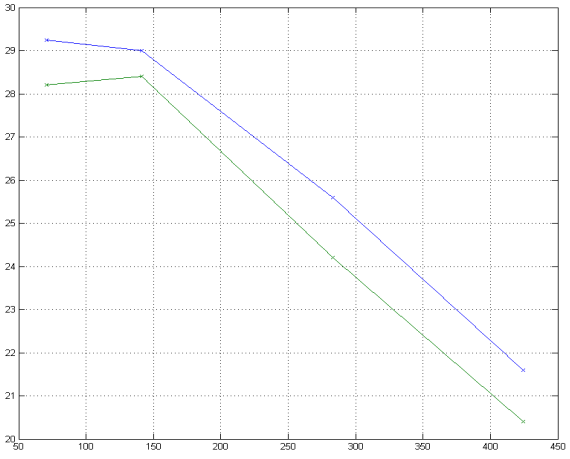

(B)

Figure 45. Comparison of uncorrected and corrected beam power densities.

(A) Images of beam profile at various distances from optical axis with and without correction.

(B) Intensity measurements for uncorrected (green) and corrected (blue) beams

The improvement in power density can be calculated by finding an estimated beam waists in longest (ω_l) and shortest axes (ω_s) as shown in Figure 44A-B and Figure 46. The power p is calculated using:

$$p(\omega_l, \omega_s) = 2Erf\left(\frac{1}{\sqrt{2}}\right)Erf\left(\frac{1}{\sqrt{2}}\right)\frac{P_0}{\pi\omega_l\omega_s} \tag{3.2.8}$$

where P_0 is the total power measured in Figure 45A. The power densities are tabulated in Table 10, showing approximately 65% improvement with a corrected beam, over the uncorrected case.

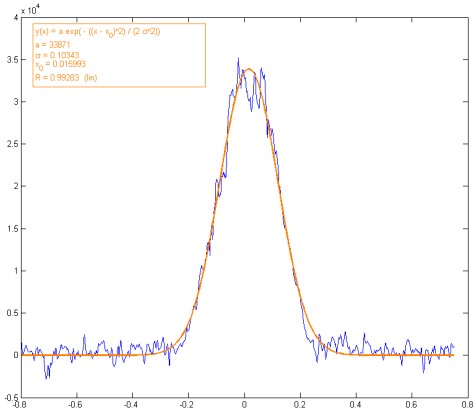

Figure 46. Example of Gaussian curve fitting for a beam intensity profile.

	Beam waists (ω_l, ω_s) mm	Beam total Power (P_0)	Beam power density (D=2mm)
(50,50) $m = 50\sqrt{2}$	3.74, 2.84	28.2 μW	1.49 μW/mm²
	2.86, 2.16	**29.25 μW**	**2.43 μW/mm²**
(100,100) $m = 100\sqrt{2}$	3.54, 3.27	28.4 μW	1.40 μW/mm²
	2.61, 2.27	**29.0 μW**	**2.51 μW/mm²**
(200,200) $m = 200\sqrt{2}$	2.79, 4.13	24.2 μW	1.18 μW/mm²
	2.52, 2.14	**25.6 μW**	**2.38 μW/mm²**
(300,300) $m = 300\sqrt{2}$	2.15, 4.88	20.4 μW	1.05 μW/mm²
	2.89, 2.07	**21.6 μW**	**1.83 μW/mm²**

Table 10. Beam power density at various angular positions. Figures in bold are for corrected beams.

3.2.5 Beam expansion

The transmitter moves the beam to illuminate retro-reflectors across the field of view. The power calculations in Section 3.1.2 suggests that a large beam can be used to speed up the scanning process. The beam expansion is then implemented by adding defocus power used in the previous section. The focusing power is calculated from the Zernike focus mode in equation (3.2.3). A relationship between the focusing power and the beam angular spread is found by physically measuring the beam spread as a function of d.

A white sheet of paper was placed 20 cm away from the transmitter to provide a screen for the diffused beam. The imager was refocused to image on the screen, and different values of d were used to expand the beam. A 4th order polynomial was then used to interpolate the data. The half power points were recorded as a measure of the beam sizes. Figure 47A-B shows two examples, for $d = 100$ and $d = 300$. The measurements are then plotted with respect to d, as shown in Figure 48. It could be seen that the relationship is roughly linear, which led to good linear regression fitting.

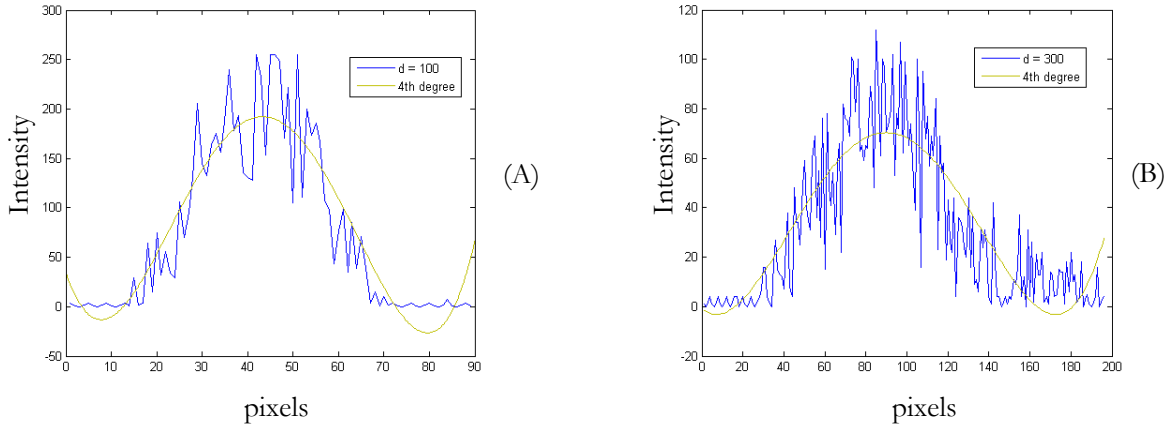

Figure 47. Expanded beam intensity profile with defocus parameter d of (A) 100 (B) 300

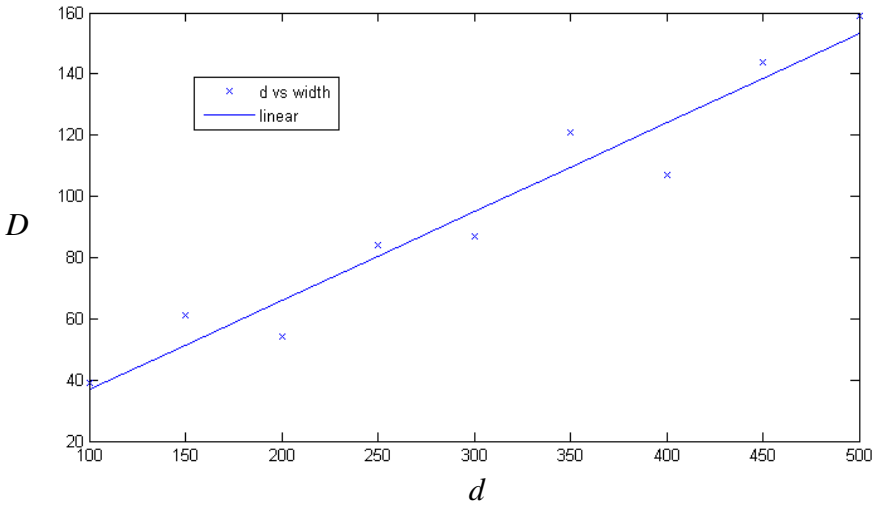

Figure 48. Plot of beam diameter D against defocus parameter d, fitted with a linear curve.

The expanded beam is split into multiple beams covering scanning regions of the transmitter's field of view. The beam diameter D can be calculated by assuming a square region and considering the size and number of scanning regions required:

$$D = \frac{L\sqrt{2}}{n} \tag{3.2.9}$$

Where L is the imager's linear dimension (in this case 1024) and n is the number of beams used for the scan in one axis (Figure 49). The total number of beams is therefore n^2. The factor of $\sqrt{2}$ is required due to the diagonal gaps between the beams. When $n = 4$, D was calculated to have a value of 362.0 pixels, which corresponds to d of 115. This value was chosen to provide sufficient power density while minimising the number of scanning regions. When n is even, the point-reflection symmetry observed in using binary phase holograms effectively scan the transmitter's field of view twice, as shown in Figure 49. To detect multiple targets with multiple beams, the frames are integrated to give a single frame for further processing.

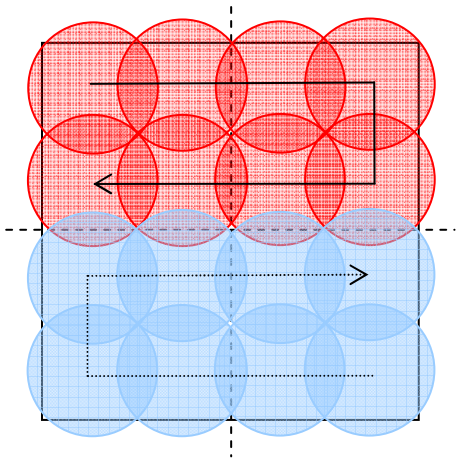

Figure 49. Schematic diagram of a beam scanning across half of the field of view (red) with $n = 4$. Because of point reflection symmetry, the second half plane is also scanned (blue).

3.2.6 Imager noise measurements

The noise sources from the imager can be modelled as a single Gaussian noise souce $n_t(t)$ [62]. Figure 50 shows a schematic diagram of the noise sources with respect to the pixel amplifier. $p(\mathbf{r},t)$ is the idealised photo voltage generated from one pixel, and $p'(\mathbf{r},t)$ is the amplified voltage fed to an analogue to digital converter. The noise sources are separated into temporal and spatial components that can be measured independently.

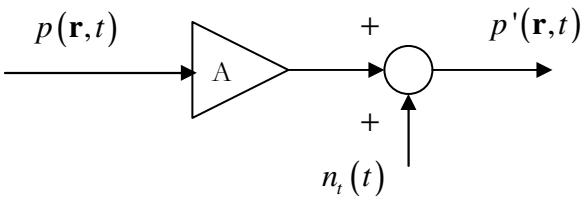

Figure 50. Noise model of a single imager pixel

Time dependent noise was measured by taking 100 image frames of a typical ambient lighting scene in the laboratory, and an exposure time of 20ms. The imager was set to obtain maximum sensitivity and the ambient lighting condition shown in Figure 51 was used for noise measurements. The temporal

pixel variance measured was 2.485, which corresponded to 0.98% of the maximum brightness level. It can be seen from Figure 51B that time dependent noise is also dependent on the luminosity.

(A) (B)

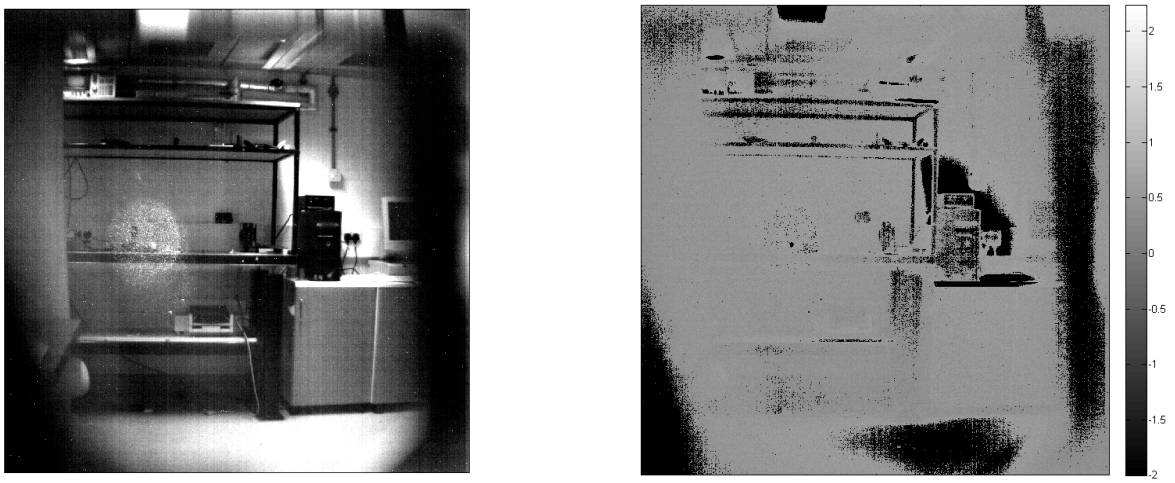

Figure 51. Output from the imager and its noise distribution.

(A) Typical well lit scene captured by the imager. (B) Temporal noise variance distribution across the same sceme. The scale is in dB.

3.3 Target acquisition

In the optical configuration under consideration, the retro-reflector itself return no temporal information that can be used to identify the targets. However, the transmitter beams can be modulated for determining likely targets. Ambient light received by the imager corrupts this information by introducing large areas of high intensity and masking the desired returned intensity. A large amount of the ambient intensity can be subtracted from the captured frame, by using the assumption that the ambient light remains the same during this time period. Therefore, the difference between two consecutive frames of ambient intensity can be assumed to be temporal noise:

$$p_{ambdiff}(\mathbf{r}) \simeq p_{amb}(\mathbf{r},t) - p_{amb}(\mathbf{r},t+\Delta t) \approx \sqrt{2}n(t) \qquad (3.3.1)$$

where $p_{amb}(\mathbf{r},t)$ is the intensity reading due to ambient light alone, $p_{amb}(\mathbf{r},t+\Delta t)$ is the intensity reading for the next frame and $n(t)$ is time dependent noise. Since the imager is close to linear, total received luminosity is a sum of retro-reflected return intensity and ambient light intensity. If the latter frame has no illumination from the transmitter, the difference directly produces only the retro-reflected return and noise:

$$p_{diff}(\mathbf{r},t) \simeq p_{amb}(\mathbf{r},t) + p_R(\mathbf{r},t) - p_{amb}(\mathbf{r},t+\Delta t) \approx p_R(\mathbf{r},t) + \sqrt{2}n(t) \qquad (3.3.2)$$

where $p_R(\mathbf{r},t)$ is the intensity from the retro-reflector. The return must be large enough to differentiate it from the temporal noise. The result of taking the difference between frames can be seen in Figure 52A-D, showing a scene with a narrow search beam illuminating scattered retro reflector targets under typical ambient light. A grating with no phase variation was used to steer the search beam to the 0th order. The imager's exposure time was set to 20ms. The total scan time was measured to be 20 seconds, including the image processing time. The retro-reflectors are 1cm^2 pieces of commercially available retro-reflecting tape placed 2m away from the transmitter. They can be seen to produce a large difference between the frames, having pixel values of 237 and 171. By applying a threshold value of 128, any pixels above this has high probability of being a retro-reflector.

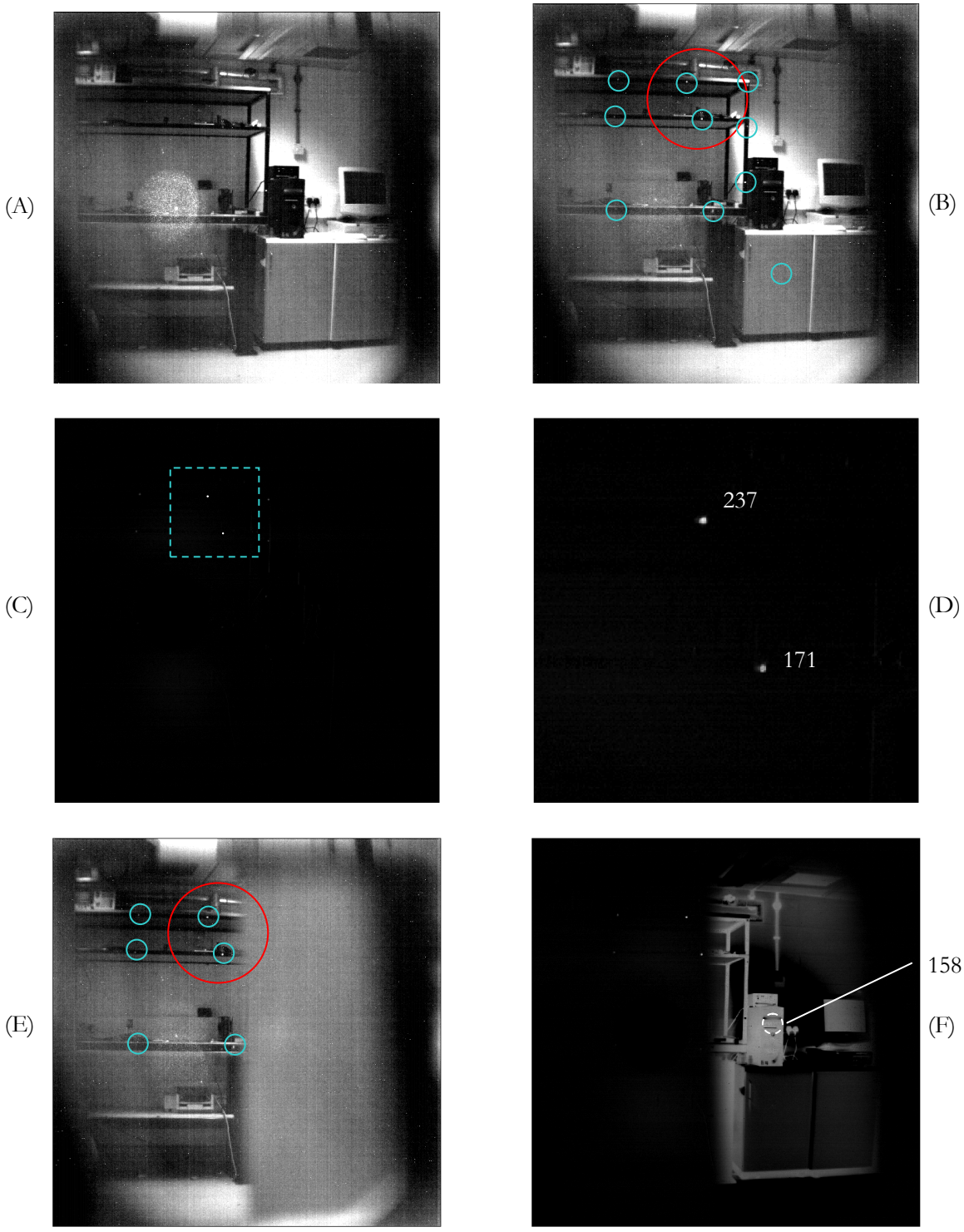

Figure 52. Retro-reflected return with beam illumination.

(A) Scene with no beam.
(B) Scene with a Gaussian beam illuminating within the circular region. The blue circles indicate the location of the retro-reflectors.
(C) Image from subtracting (A) from (B)
(D) Magnifying (C) shows retro-reflectors. Their associated maximum pixel values are also shown.
(E) Same scene as (B) but with white object obscuring the view.
(F) Subtracted image using (E). Pixel value of large white area is shown.

This method fails when the ambient luminosity changes with time. Figure 52E shows a frame obstructed by a white sheet of paper. In this scenario, the second frame is partially blocked. Subtracting from the dark frame results in Figure 52F. White regions can be seen clearly. A pixel sampled from a large white region has value of 152, thus the threshold value of 128 would not distinguish between the two areas. At increasing higher threshold levels, unintended areas are reduced, although with a loss of one retro reflector (Figure 53A-C). Using pixel values alone is not enough to distinguish the retro-reflectors from the ambient light. A method for distinguishing between these two types of luminosity was then investigated, by using morphological filters and knowledge of the shape of retro-reflected return.

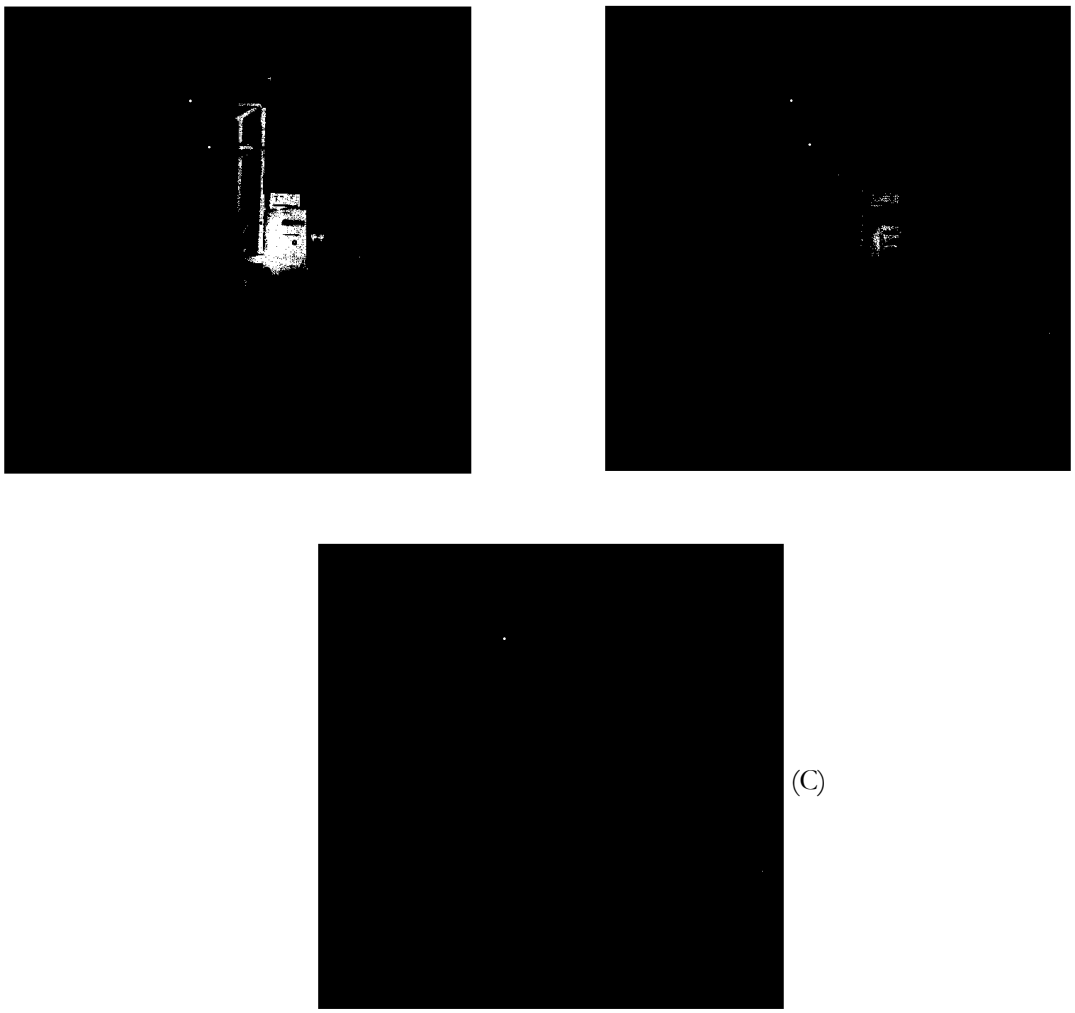

(C)

Figure 53. Thresholding image obtained from Figure 52.
(A) At pixel value of 128 (B) At pixel value of 153 (C) At pixel value of 179 has only one retro-reflector visible

3.3.1 Morphological filter

Non-linear filters are useful in cases where feature extraction is required. A simple example of this is the *median* filter, which is effective for extracting an image from a noisy source. Maragos [63] showed that Ordered Statistic filters such as a median filter can be represented as a larger non-linear class called mathematical morphological filters. A morphological filter is a set of mathematical transformations that operates on a signal's geometrical features locally. It is based on four operators, dilation, erosion, open and close, which are used to process a signal with a structuring element. They are spatial non-linear operators that can be represented mathematically as Minkowski addition and subtraction [64]:

$$\begin{aligned}
&\text{Minkowski addition}: \quad A \oplus B = \{a + b \mid a \in A, b \in B\} \\
&\text{Minkowski subtraction}: \quad A \ominus B = \{x \mid x - b \in A, b \in B\} \\
&\text{Symetric Reflection}: \quad B^S = \{-b \mid b \in B\} \\
&\text{Dilation of A by B}: \quad A \oplus B^S \\
&\text{Erosion of A by B}: \quad A \ominus B^S \\
&\text{Opening of A by B}: \quad A \circ B = \left(A \ominus B^S\right) \oplus B \\
&\text{Closing of A by B}: \quad A \bullet B = \left(A \oplus B^S\right) \ominus B
\end{aligned} \tag{3.3.3}$$

Where A is usually the signal to be filtered, and B the structuring element. The reflection operator is needed, in some way similar to time or space reflection of linear convolution filters. It is possible to express these filters in terms of a linear filter kernel [65], but it is more useful to consider their geometrical properties. Figure 54 shows the effect of these operators on a binary image, using a structuring element 5x5 pixels square. The original image contains bright areas with varying geometrical sizes. Dilation and erosion are operators that expand light or dark areas with an amount specified by the structuring element. Opening and closing reverses these operators as much as possible, except for areas that have been dilated or eroded 'too much'.

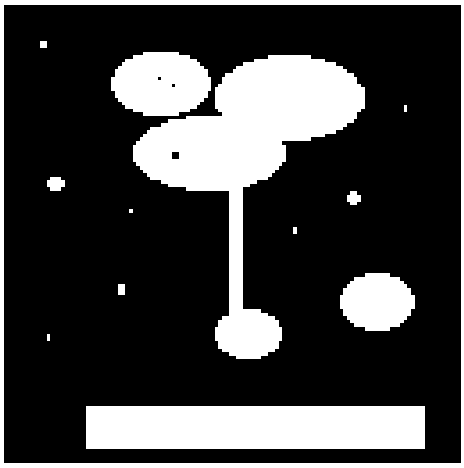

(A)

Figure 54. Examples of morphological operations on a 5x5 square pixel structuring element.

(A) Original image
(B) Dilation
(C) Erosion
(D) Opening
(E) Closing

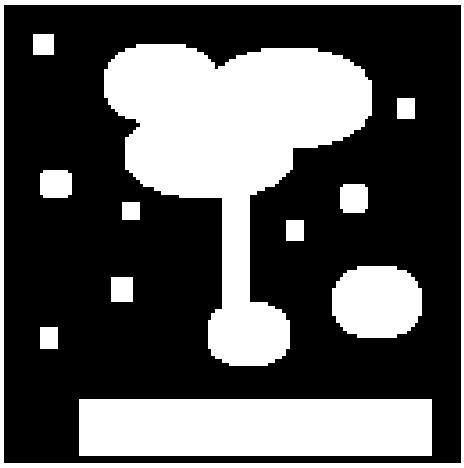

(B)

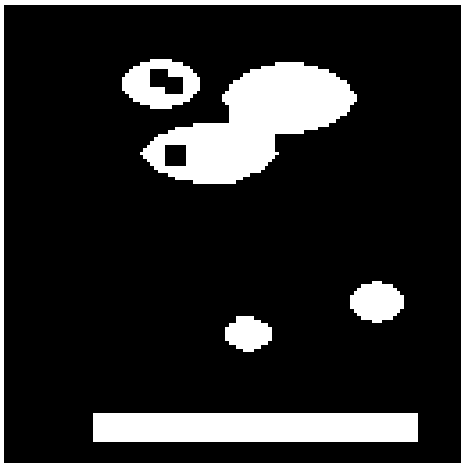

(C)

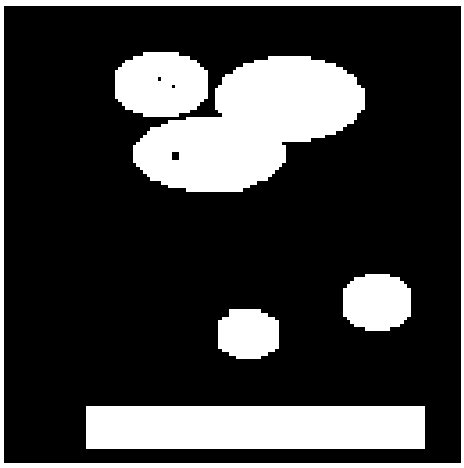

(D)

(E)

The desired effect is to retain areas that are larger than the structuring element (opening leaves dark areas unchanged, while closing retains the light areas). It is observed that the opening operator has also removed the light line in the middle of the image. Although the examples used are black and white, morphological operators are adapted to grey scale images by applying them on the grey scale levels [66].

The large background luminosity can be removed by using an opening operation by a structuring element that is slightly larger than static returns from retro-reflectors. Once the background luminosity distribution is obtained, this is subtracted from the original image:

$$L_{SR}(\mathbf{r}) = L_{diff}(\mathbf{r}) - L_{diff}(\mathbf{r}) \circ B(\mathbf{s}) \tag{3.3.4}$$

Where $B(\mathbf{s})$ is the structuring element. At distance of 5m and a 45mm focal length lens used with the Photonfocus imager, a 10mm x 10mm retro-reflector gave a static return size of 5 pixels in diameter. Various sizes for $B(\mathbf{s})$ are used to determine the optimal structuring element. Morphological filtering was performed in MATLAB using the strel function to generate $B(\mathbf{s})$ and imopen for morphological opening. A sample of pixels with the highest value from four different regions are used to determine the effectiveness of the filter with respect to two static returns, one area with large light background and areas with lines. The plot of these values is shown in Figure 55.

There are some single pixel artefacts from morphological filtering, shown in Figure 56. These can be removed by applying a median filter with 3 x 3 sampling size after the background extraction Figure 57:

$$L_{SR}(\mathbf{r}) = medianfilter_{3\times3}\left(L_{diff}(\mathbf{r}) - L_{diff}(\mathbf{r}) \circ B(\mathbf{s})\right) \tag{3.3.5}$$

The median filter reduces both the peak pixel values for static returns and background pixel levels; therefore it does not affect the relative values of these quantities.

Morphological filtering has been shown to significantly improve the contrast of the imaged retro-reflectors. The intensity values of the retro-reflectors are now different from the background intensities, allowing them to be identified by a threshold in intensity value. These can now be segmented into potential target coordinates.

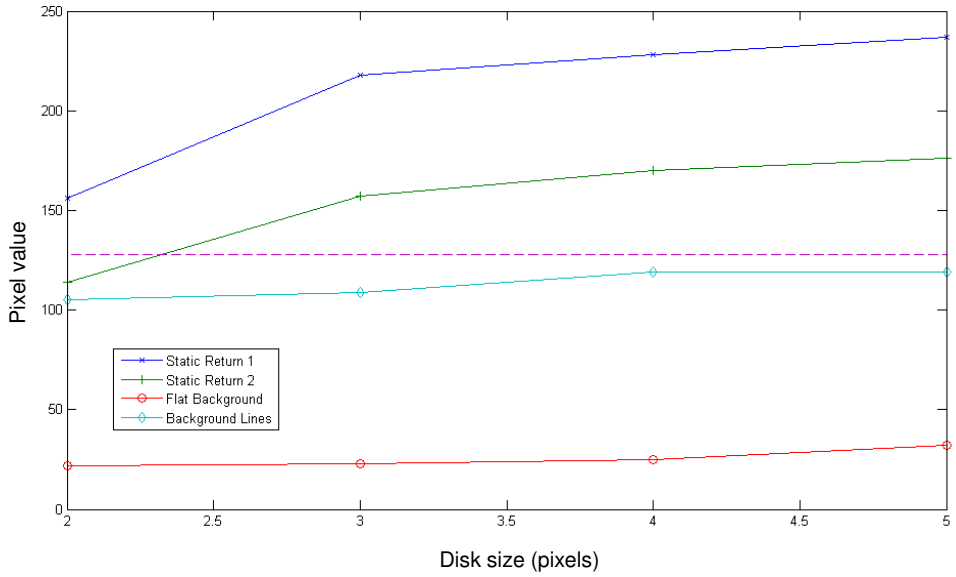

Figure 55. Outputs from background subtraction. The plot shows pixel values at different locations as a function of the structuring element size 2,3,4, and 5.

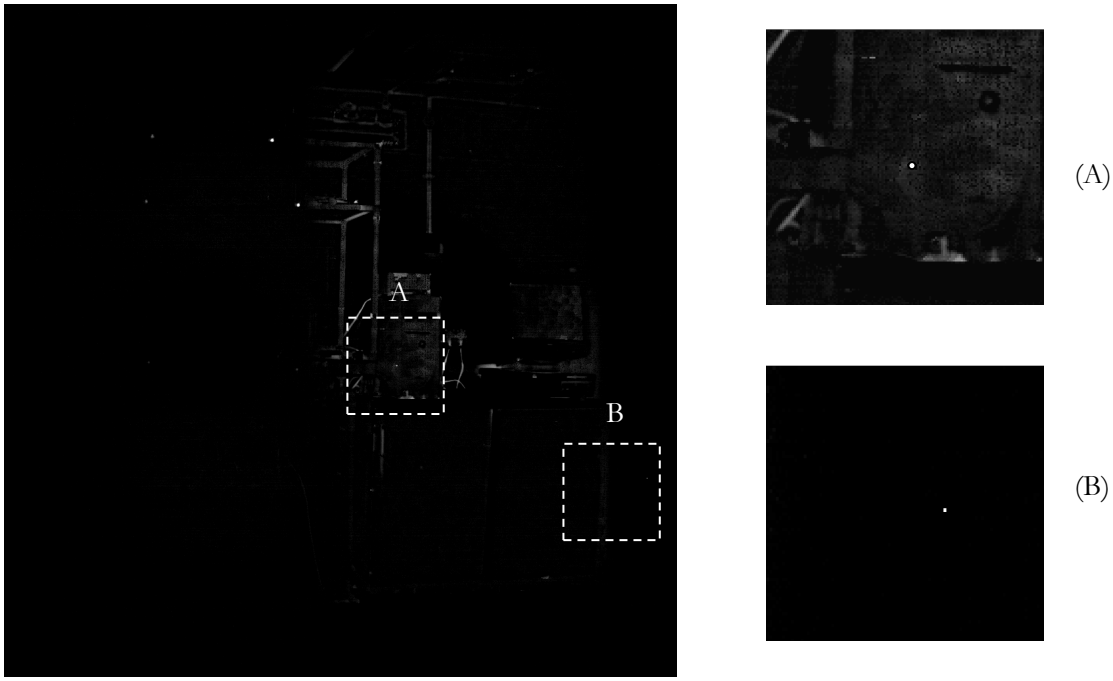

Figure 56. Outputs from background subtraction, showing pixels that do not correspond to retro-reflectors. Evidence of unwanted large valued pixels due to processing. Two areas are enlarged to show these pixels.

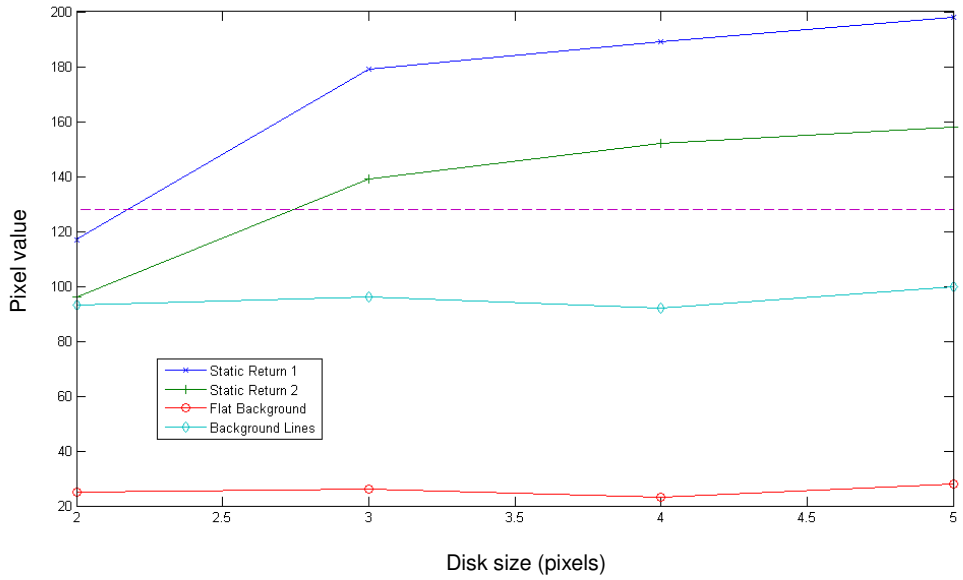

Figure 57. Outputs from background subtraction with a median filter applied. The plot shows pixel values at different locations as a function of the structuring element size 2,3,4, and 5.

3.3.2 Target extraction and labelling

Once the filtering has been applied, the target detection could then proceed using a segmentation algorithm to find clusters of light pixels. The algorithm uses a run-length encoding to find connected regions as described in [67]. The algorithm outputs groups of 3 coordinates, corresponding to different clusters of light pixels: top-left, bottom-right, and the centroid. The centroid was chosen to be the best estimation for the centre of the target. An image of the detected static returns is also displayed on the computer screen and the user can identify the targets quickly.

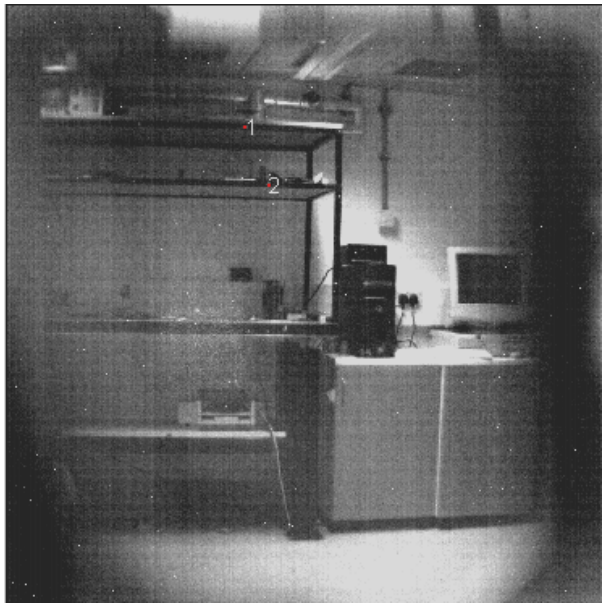

Figure 58. Image of processed and labeled retro-reflector targets.

An example of having the field of view blocked during the 'dark frame' is shown in Figure 58. A morphological filter with structuring element of size 5 pixels is used. Figure 59 shows the detected targets with this example.

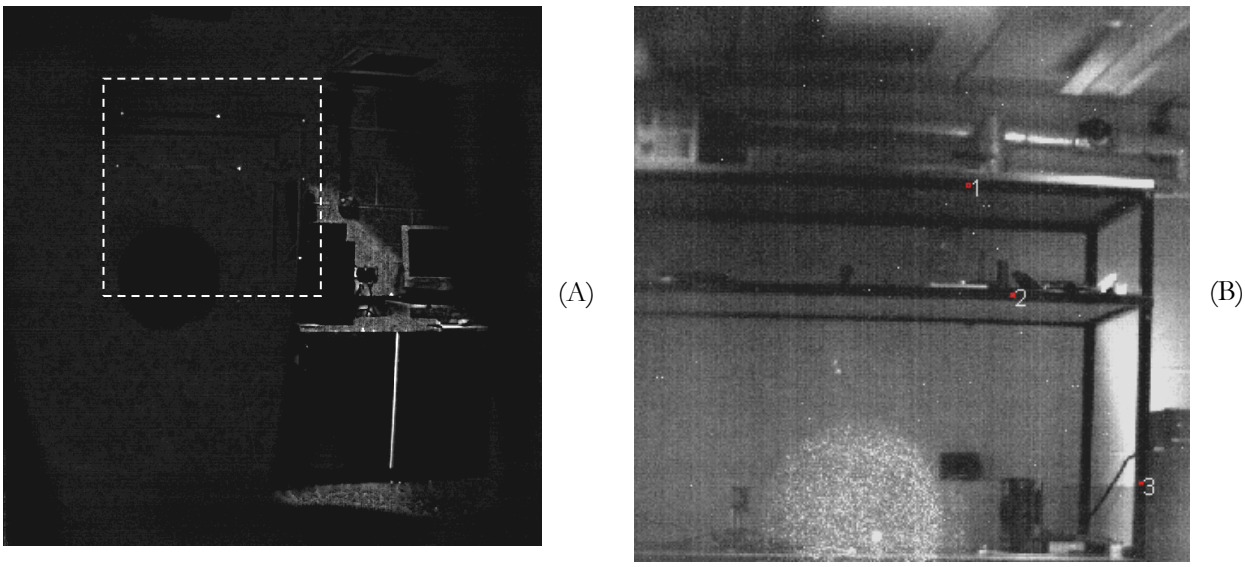

Figure 59. Image of: (A) Subtracted frame partially blocked with a white paper. (B) Detected retro-reflector locations with partially blocked view.

To simulate a time varying ambient light, a white sheet of paper was used to block the view of the imager during beam scanning, producing large areas of luminosity which would have caused the transmitter to produce false positives as in Figure 59A. By applying suitable morphological filter to suppress unwanted luminosity as described previously, the transmitter can obtain the location of retro-reflector targets despite drastic disturbances as shown in Figure 59B.

To complete the target locating process, the transmitter is required to find targets across the whole FOV. Figure 60 shows detected retro-reflecting targets scattered across the FOV under normal ambient lighting condition.

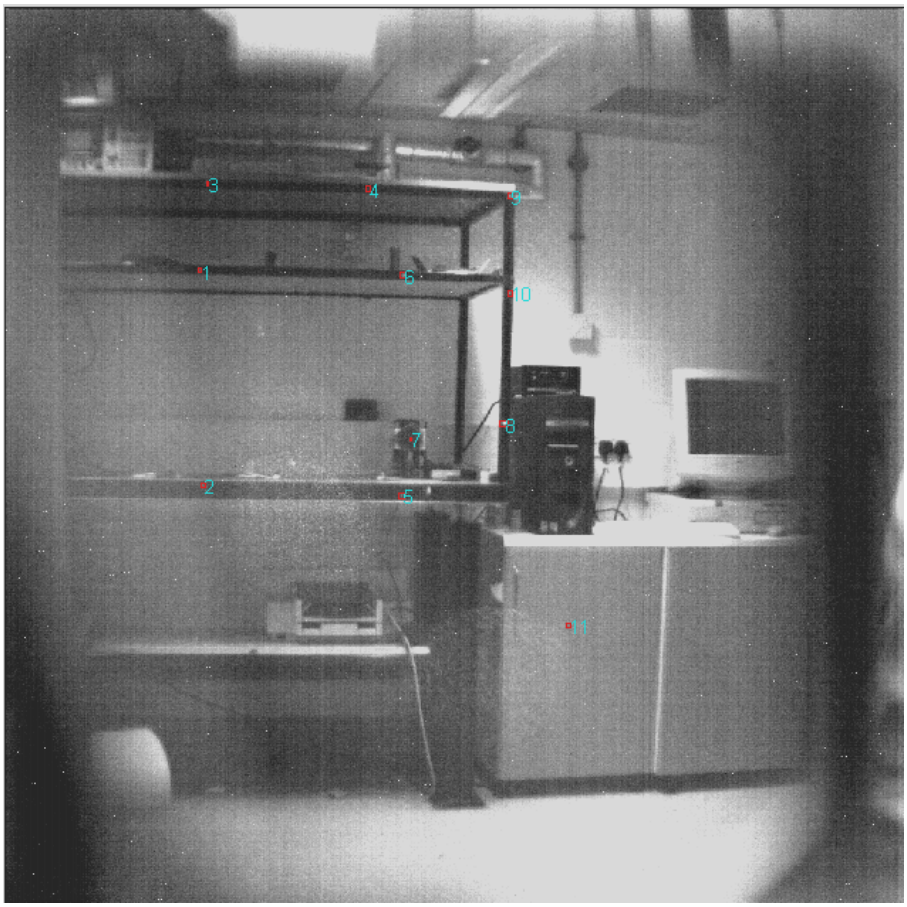

Figure 60. Image of acquired retro-reflecting targets using a full field of view scan under ambient lighting.

3.3.3 Perspective transform calibration

In order to correctly steer an optical beam to a detected target, a linear transformation from the imager's plane to the SLM plane was required to map the SLM steering plane from the imager plane. The transformation described in section 3.1.3 required at least four reference points to determine the homography matrix relating between the two planes. Figure 61 summarises the calibration process.

Eight retro-reflecting targets were distributed uniformly across the transmitter field of view. The locations of the targets were acquired using the method described in the previous section. Manual beam steering was then used to visually direct the optical beam onto the targets. Once the user confirms the coordinates, the script then asks for the next target to be steered to. A matrix inversion is then performed to obtain the homography matrix

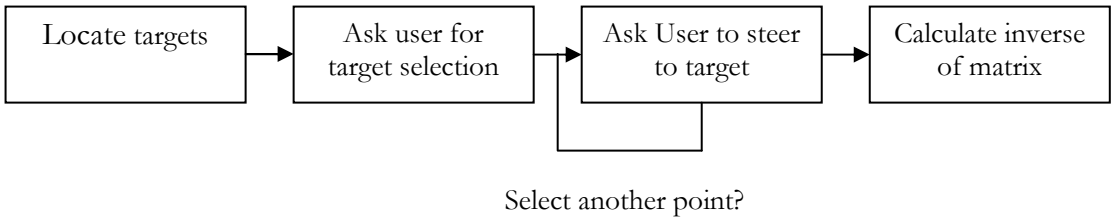

Figure 61. Flow chart of perspective transform calibration

The matrix inversion is implemented with MATLAB's pseudo-inverse pinv function, which computes the Moore-Penrose pseudo-inverse using singular value decomposition. With eight reference points, the pseudo-inverse produced an homography matrix:

$$\mathbf{H} = \begin{bmatrix} 1.2790 & -0.0020 & -426.9712 \\ 0.0203 & -1.6015 & 829.2054 \\ 0.0000 & -0.0000 & 1.0000 \end{bmatrix} \tag{3.3.6}$$

3.3.4 Acquisition error measurements

The effect of acquisition error on an optical beam is investigated to determine the acquisition performance of the system. Acquisition error ε is calculated from the Euclidian distance of the difference between the real angular coordinates of the retro-reflectors relative to the base station, and the estimated angular coordinates obtained from the acquisition:

$$\varepsilon = \sqrt{(\theta - \theta')^2 + (\phi - \phi')^2} \tag{3.3.7}$$

where (θ, ϕ) are the real steering coordinates, and (θ', ϕ') are estimated. To determine the real angular coordinates with the transmitter, a gradient ascent algorithm is implemented to optimise the beam steering after acquisition is made. The algorithm assumes that the first approximation for estimating the returned beam power is derived by considering a Gaussian beam illuminating a circular retro-reflector, as shown in Figure 62. Assuming that the retro-reflector is much larger than any speckle, the returned beam intensity is proportional to the area covered by the retro-reflector multiplied by the spatial intensity distribution of the illuminating beam. The retro-reflector has a radius of a, and the beam is offset by Δx relative to the retro-reflector's centre. R is the distance between the circumference of the retro-reflector from the beam axis.

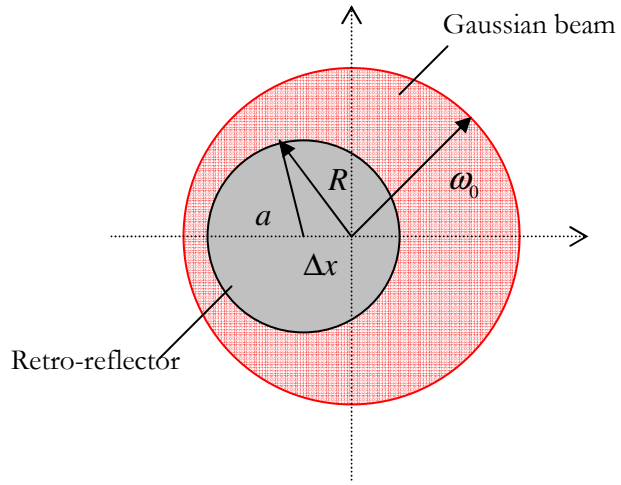

Figure 62. When a Gaussian beam is at a different centre to a retro-reflection, a fraction of the beam power is reflected.

In polar coordinates, the normalised radial intensity of the beam is given as:

$$I(r) = \frac{2}{\pi\omega_0^2}\exp\left(-\frac{2r^2}{\omega_0^2}\right) \tag{3.3.8}$$

Where ω_0 corresponds to the waist radius of the Gaussian beam and r is the radial coordinate centred on the beam axis. The total power contained within the retro-reflector given by Norman [68] for a small displacement is:

$$P \simeq 1 - \exp\left(\frac{-2a^2}{\omega_0^2}\right)\left(1 + \left(\frac{4a^2\Delta x^2}{\omega_0^4}\right)\right) \tag{3.3.9}$$

By assuming that a constant proportion of the optical power that falls within the retro-reflector gets reflected back to the base-station, the power received can be plotted as a function of Δx and $\frac{a}{\omega_0}$ (Figure 63).

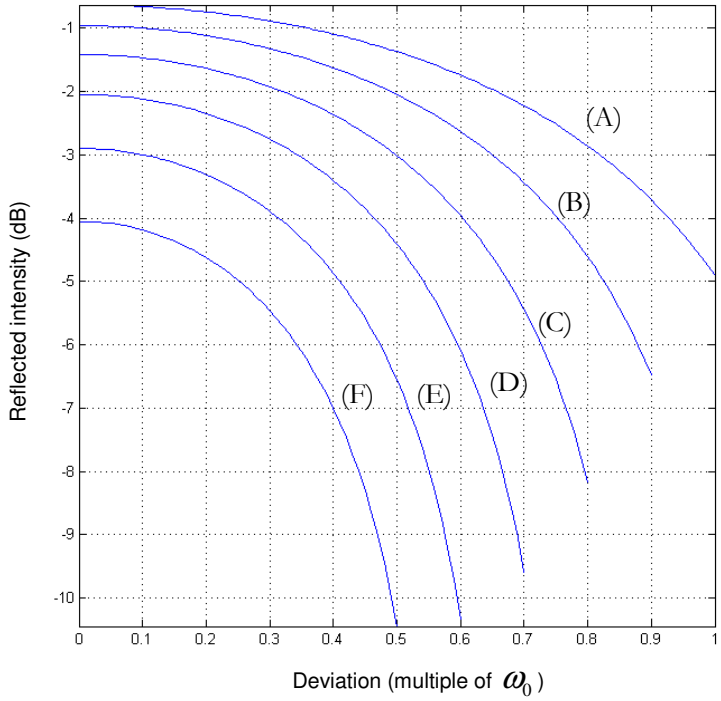

Figure 63. Ratio of intensity return from a circular retro-reflector as a function of deviation normalised to ω_0. Curve (A)-(F) corresponds to $a = \omega_0$ to $a = 0.5\omega_0$

Differentiating (3.3.9) results in a negative gradient for all values of $\frac{a}{\omega_0}$, and the function is monotonically decreasing with respect to Δx. A similar result is obtained by exchanging a circular retro-reflector with a rectangular shaped reflector [69]. Therefore, by moving the beam angular position such that the beam moves in the direction of positive intensity gradient, the position is more centred relative to the retro-reflector. Individual axis can be separately optimised since the returned intensity is symmetrical in both the vertical and horizontal axis.

An implementation of a gradient ascent control system is shown in Figure 64. The algorithm was implemented as a function in MATLAB. The amount of angular resolution per step of the loop is again normalised to a single Fourier plane pixel:

$$\Delta\varphi = \frac{2\theta_{\max}}{1024} = 5.1\times10^{-4} \text{ rads} \tag{3.3.10}$$

A regular pattern of retro-reflectors was used to provide a regular distribution of targets, covering a large proportion of the transmitter's FOV. The reflector array contained 9x10 retro-reflectors spread across a 900x1000mm square grid shown in Figure 65A. The array was then placed 2.5m away from the transmitter, covering approximately 70% of the field of view. The transmitter scans the FOV to acquire as many targets as possible, which are then optimised individually using the gradient ascent algorithm. An interpolated plot of the error values is shown in Figure 65B. The mean steering error was found to be 0.932 pixel ($4.75\text{x}10^{-4}$ rads) and the variance 0.778 pixel ($4.0\text{x}10^{-4}$ rads). The error is largest at the outer edges of the FOV, and smallest in the centre.

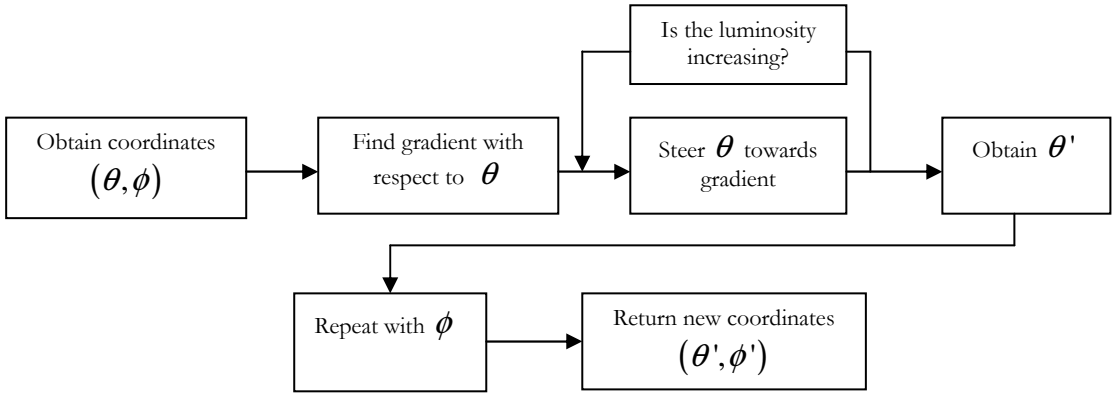

Figure 64. Gradient search loop for obtaining optimised steering angular coordinates.

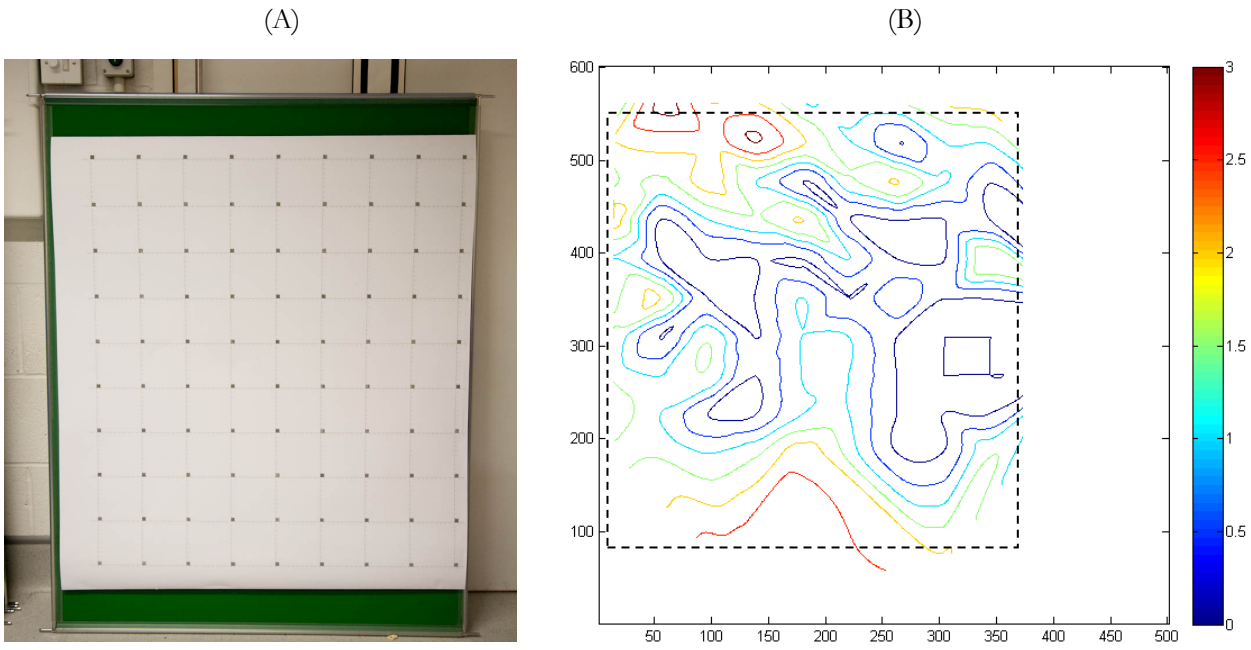

Figure 65. (A) Retro-reflecting array. (B) Contour plot of spatial distribution of acquisition error. The bounding box shows the placement of the retro reflecting array. The colour scale is in multiples of 5.1×10^{-4}

3.4 Conclusion

A retro-reflecting, optical position acquisition system has been described. The system uses an optical beam to scan the transmitter's field of view for a large optical signal. The power budget calculation shows that small optical power is required to locate the retro-reflectors, and large beams can be used to quickly scan the transmitter's field of view. Using a holographic beam steering system, the transmitted beam was able to dynamically adjust to an optimal scanning size. The system also allowed the beam to be optimised with respect to output beam density by applying spatially varying defocus correction to the spatial light modulator. An improvement of 65% in power density was demonstrated.

An imaging system is used to capture retro-reflected returns. The noise characteristics were measured to give temporal and spatial components. Using frame subtraction, spatial noise was found to be effectively removed. Temporal noise was measured to have a much smaller variance than spatial noise.

Images of illuminated retro-reflectors were then processed using frame subtraction and morphological filters to remove ambient illumination. A large disturbance such as a partially blocked beam was demonstrated to be removed effectively using this method. The performance of the acquisition system was tested using a gradient ascent algorithm and an array of regularly spaced retro-reflectors. The system has an overall mean acquisition error of 4.75×10^{-4} rads.

The use of the holographic beam steering system to correct for aberration in the optics is extended further to provide corrections for atmospheric distortions in the next chapter.

4 Optical Turbulence simulation and compensation

In this chapter, the effect of atmospheric disturbances on a propagating free-space laser beam is investigated. These disturbances can be modelled as clear air turbulence that affects the spatial distribution of the refractive index of air. A discussion of the statistical nature of turbulence is first presented. A theoretical solution to the beam propagation from the governing Maxell equation is found using a classical theory of propagation through random media. Statistical properties are then derived which are used to model the severity of fading in this channel. The theoretical limit to bit error rates are then derived for a turbulent channel. An optical turbulence simulator consisting of a binary phase SLM is constructed to simulate the turbulent atmosphere, providing a test bed for a turbulence compensation system.

An adaptive optics system using single receiver intensity measurements is then described and used in conjunction with the turbulence simulator to decrease expected fluctuation in received intensity. The system estimates the aberrations in the beam path without using a wavefront sensor. Bit error rates are then numerically calculated and compared to an uncorrected system.

Finally, a multiple beam transmission is investigated using numerical simulation. Different beam configurations are tested for the effectiveness in intensity fluctuation reduction. Bit error rates are then calculated for multiple beams with and without adaptive optical compensation systems.

4.1 Optical turbulence overview

The deterious effects of atmospheric disturbance on a propagating laser beam can be shown by a simple experiment, with a Helium Neon laser source and a hot air gun. Figure 66A shows a diagram of this set up. The hot air gun is used to create a temperature gradient sufficient enough to cause random mixing of hot and cold air, creating a region of strong turbulence. The laser beam passes though this region, and the beam is captured by an imager. Figure 66B shows the beam with the heat gun off, and Figure 66C with the heat gun on.

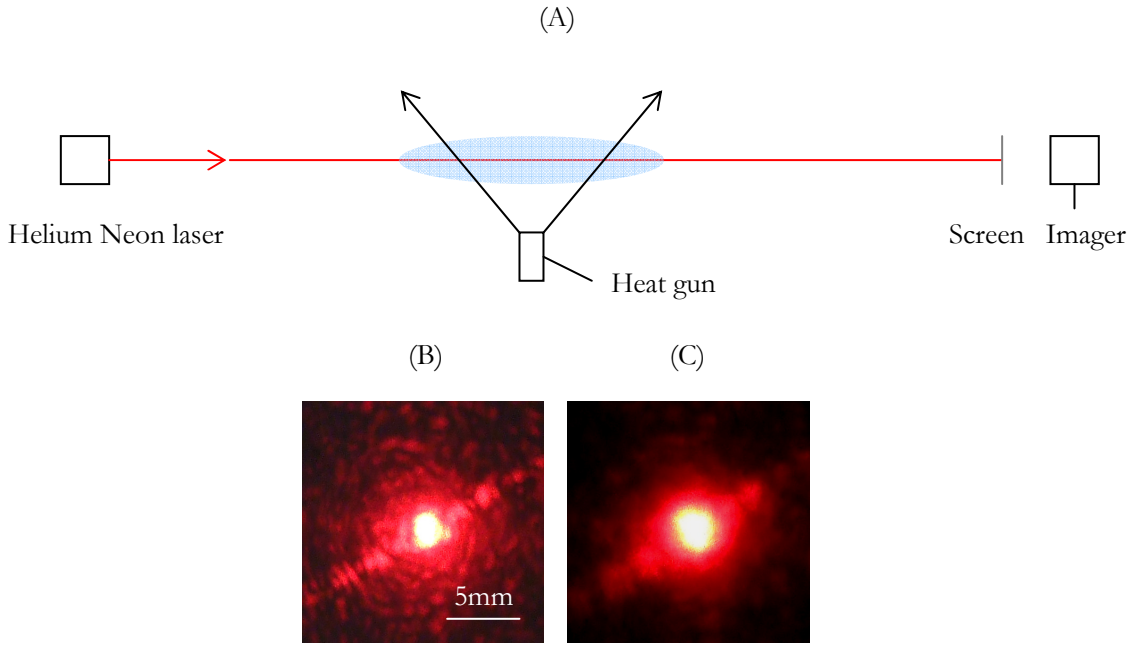

Figure 66. An optical turbulence demonstration using a hot air gun as the turbulence source. (A) The diagram of the set up. (B) Laser beam without turbulence. (C) Laser beam with turbulence.

The beam propagation though turbulence clearly shows the bradening of the beam. This broadening causes the decrease of the power density, which increses the signal to noise ratio if the beam is used for a communication link. Although it is difficult to show with images, the beam also experiences time varying fluctuations, which causes the intensity to scintillate. This scintillation causes further increase in the signal to noise ratio of the link. For a given point in the beam profile, these two quantities can be

measured to give two stochastic moments: the mean intensity $\langle I(\mathbf{r})\rangle$ and the normalised intensity variance or scintillation index $\sigma_I^2(\mathbf{r})$:

$$\sigma_I^2(\mathbf{r}) = \frac{\langle I(\mathbf{r})^2\rangle - \langle I(\mathbf{r})\rangle^2}{\langle I(\mathbf{r})\rangle^2} \tag{4.1.1}$$

These quantities can then be used to estimate the the expected bit error rates of the communication link. The aim of this chapter can be summarised as the development of a compensation system that increses the mean intensity of the beam and decreases the scintillation index. A model that can describe the random processes in an optical turbulence is therefore needed to allow the development of such system.

A typical electromagnetic wave propagation theory assumes that the Earth's atmosphere consists of a uniform medium with refractive index close to one at long wavelengths [70]. This assumption is valid since there is little interaction between the electric field and the atmospheric fluctuations on a large scale. Unfortunately at much smaller optical wavelengths, there exist three phenomena that affect propagation: absorption, scattering [71] and refractive-index fluctuation (or optical turbulence) [72][73]. At distances considered in this chapter, absorption due to gaseous molecules is considered negligible [74]. Scattering constitutes a small and constant attenuation of the intensity in the optical beam, mostly due to small dust particulates in the atmosphere [75]. Other extreme weather conditions such as heavy precipitation in forms of fog, rain and snow also increases scattering. Increasing the optical power output at the transmitter can alleviate this problem over short distances; however temporal dispersion caused by multiple scattering is still an on going area of research [76][77]. Optical turbulence on the other hand produces strong and fast intensity fluctuations [78][79]. These fluctuations are caused by local differences in air temperature in the optical wave propagation path. Various attempts at compensation, or mitigation, of atmospheric turbulence effects have been studied over the years [80][81]. Most of this effort has been in the use of wavefront sensing to conjugate the phase fluctuation effects at the link receiver.

One of the first theoretical treatments of wave propagation through such medium was carried out by Kolmogorov [82]. Although the original statistical theory was developed for the velocity field of a fluid, it was extended to turbulence caused by temperature fluctuations [83]. This was subsequently identified as the most significant mechanism for generation of refractive index fluctuations. A solution of the wave

propagation though random medium was derived initially for acoustic waves [84] and later an electro-magnetic wave solution for weak fluctuation was derived by Tatarskii using a more advanced Rytov method [73]. Using a direct approach using parabolic equations [85][86], solutions for strong fluctuation have been obtained. Since optical turbulence is a random process, various statistical moments were then deduced from these solutions. Properties such as scintillation index (a measure of beam intensity fluctuations) and beam mean intensity can then be calculated.

Recently, due to availability of spatial light modulators (SLMs), there has been a large effort in simulating turbulence in laboratories [87][88][89]. This is in the form of numerical generation of random phase distributions with Kolmogorov statistics. The advantage of this approach allows turbulence parameters to be repeated, and different tests can be made on the same turbulent conditions.

The aim of this chapter is to explore these developments and implement a turbulence mitigation system, as a proof of concept for a smart free-space optical communications link. A theoretical development of optical turbulence is presented to be used for understanding the decisions made during its development. Two different numerical generation schemes for a Kolmogorov phase screen are described and compared. The phase screen is then implemented on a computer controlled SLM. The phase modulation range of the SLM is described and a novel binary phase method is used to encode large phase shifts. Results of a laboratory simulation of laser beam propagation through artificial random medium are presented, and compared to theoretical values. Finally, a prototype of wavefront sensorless turbulence mitigation system is described and implemented. Scintillation index measurements from this system showed significant reduction in bit error rates.

4.1.1 Kolmogorov model

A turbulent flow of a viscous fluid is characterised by a non-dimensional Reynolds number:

$$\mathrm{Re} = \frac{Vl}{\nu} \tag{4.1.2}$$

Where V is the velocity of the fluid flow, l is the characteristic dimension of flow, and ν is the fluid's viscosity. Above a critical value, the flow is considered to be unstable, and turbulent flow is assumed. It can be demonstrated that the Reynolds number in a typical air flow near the ground is very large (~10^5), thus the flow is considered highly turbulent. Inside such a flow, an analytical solution can be found using Navier-Stokes equations, which describes a fluid flow with a set of partial differential equations. However, there has yet to be a report of a successful description of optical turbulence using these first principles.

Pioneering work was carried out by Kolmogorov [82] who used dimensional analysis in conjunction with a set of statistical postulates to derive a simplified statistical theory of turbulence. In this model, two length scales (L_0, l_0) exist. In between these two scales, turbulence is assumed to be statistically homogeneous and isotropic. L_0 is the largest scale which this assumption applies; any turbulent structure outside this scale is generally undefined. L_0 is assumed to grow with the height of the atmosphere. l_0 is the smallest scale, where turbulent flow begins to vanish. Within this range, a single statistical model can be used to describe the random processes using the energy cascade theory in Figure 67. The theory postulates that the kinetic energy is injected into the fluid at the largest scale. As the fluid's velocity reaches a critical Reynolds number, an unstable flow begins to form, creating large vortices that break up into independent, smaller ones. These flows generate their own unstable flow, breaking up into even smaller vortices. This process is iterated until the scale of the vortices reaches length scale l_0, where and energy is dissipated by viscous friction. Below this scale, turbulence decays rapidly into heat.

The rate of energy dissipation into smaller structures is governed by a constant ε. Kolmogorov showed this constant uniquely determines the second moment of velocity difference between two points, separated by a distance R:

$$D_V(R) = \left\langle \left(V(R) - V(0)\right)^2 \right\rangle = 2\varepsilon^{2/3} R^{2/3} \tag{4.1.3}$$

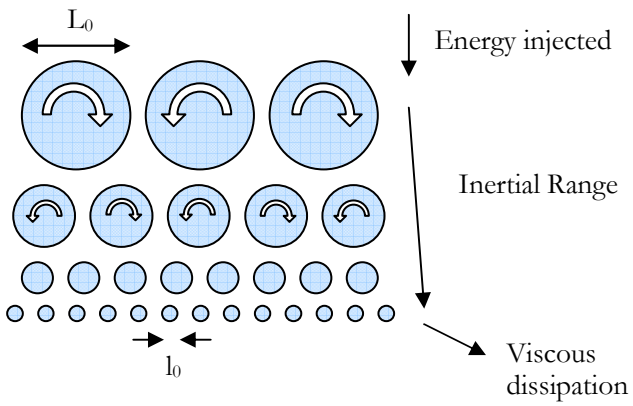

Figure 67. Diagram of the energy cascade theory.
Length L_0 represents the largest turbulence scale, and l_0 the smallest.

Where $V(R)$ is the velocity at distance R. D_V is also called the velocity structure function fluctuation. It is related to the spatial covariance B of two points separated by distance R:

$$D(R) = 2\left[B(0) - B(R)\right] \tag{4.1.4}$$

Obukhov [83] extended this theory to derive a related expression for temperature fluctuation within the fluid:

$$D_T(R) = \left\langle \left(T(R) - T(0)\right)^2 \right\rangle = C_T{}^2 R^{2/3} \tag{4.1.5}$$

Where $T(R)$ is the temperature at distance R, and $C_T{}^2$ is the temperature structure constant. Again this expression is only valid within the same inertial scale range. It was identified that temperature fluctuation is the main mechanism for changes in refractive index, i.e. the refractive index caused by pressure variation is negligible. By writing the refractive index in the form of:

$$n(R) = 1 + n_1(R) \tag{4.1.6}$$

A similar expression for the refractive index structure function with the same power law can be written as:

$$D_n(R) = \left\langle \left(n_1(R) - n_1(0)\right)^2 \right\rangle = C_n{}^2 R^{2/3} \tag{4.1.7}$$

Where $C_n{}^2$ is the refractive index structure constant that dictates the strength of optical turbulence. The physical measurement of $C_n{}^2$ is therefore important in determining the behaviour of optical propagation.

Its measurement can be made by measuring C_T^2 using two thermometers separated by a fixed distance, and estimating the value of the temperature structure function. Using a relationship given by Owens [90] and Andrew [79] it is possible to relate C_n^2 with C_T^2:

$$C_n^2 = \left(79\times10^{-6}\frac{P}{T^2}\right)C_T^2 \tag{4.1.8}$$

Where P and T are the bulk pressure and temperature of the fluid. The value of C_n^2 therefore varies depending on the atmospheric conditions. A typical value of C_n^2 varies from the "weak" condition; roughly 10^{-17} $m^{-2/3}$ at night, to the "strong" condition, 10^{-13} $m^{-2/3}$ during hot days. Height also affects the severity of turbulence, since both pressure and temperature are affected. For a ground to ground optical link with low angle of elevation, a simplification is made by assuming that C_n^2 remains a constant during propagation time, and throughout the propagation path.

4.1.2 Refractive index power spectral density

For a given a single variate random process with zero mean and well defined covariance $B(\tau)$, it is possible to express the covariance as a Fourier transform of the power spectral density (PSD) $S(\omega)$:

$$B(\tau) = \int_{-\infty}^{\infty} S(\omega)e^{i\omega\tau}d\omega \tag{4.1.9}$$

Or similarly the inverse transform is given as:

$$S(\omega) = \frac{1}{2\pi}\int_{-\infty}^{\infty} B(\tau)e^{-i\omega\tau}d\tau \tag{4.1.10}$$

The relationship is know as Weiner-Khintchine theorem [91]. The PSD describes the power distribution within the random process in the frequency domain. This relationship can then be extended into three dimensions to give the three-dimensional PSD $\Phi(\mathbf{K})$:

$$B(\mathbf{R}) = \iiint \Phi(\mathbf{K})e^{i\mathbf{KR}}d^3\kappa \tag{4.1.11}$$

Where $\mathbf{R}=(x,y,z)$ is the position vector, and $\mathbf{K}=(\kappa_x,\kappa_y,\kappa_z)$ is the spatial frequency. The three-dimensional PSD $\Phi(\mathbf{K})$ can be obtained by using the inverse transform:

$$\Phi(\mathbf{K})=\left(\frac{1}{2\pi}\right)^3\iiint B(\mathbf{R})e^{-i\mathbf{KR}}d^3R \tag{4.1.12}$$

Applying the homogeneous and isotropic condition, and using equation (4.1.4), the structure function can be expressed [78] in terms of the three-dimensional PSD, and $R=|\mathbf{R}|$:

$$D(R)=8\pi\int_0^\infty \kappa^2\Phi(\kappa)\left(1-\frac{\sin(\kappa R)}{\kappa R}\right)d\kappa \tag{4.1.13}$$

The inverse transform can be derived with homogeneous and isotropic condition [79]:

$$\Phi(\kappa)=\frac{1}{4\pi^2\kappa^2}\int_0^\infty \frac{\sin(\kappa R)}{kR}\frac{d}{dR}\left[R^2\frac{dD(R)}{dR}\right]dR \tag{4.1.14}$$

The integral can then be evaluated with Kolmogorov refractive index structure function in (4.1.7), simplifying to an integral:

$$\Phi_n(\kappa)=\frac{5C_n^{\ 2}}{18\pi^2\kappa^3}\int_0^\infty R^{2/3}\sin(\kappa R)\,dR \tag{4.1.15}$$

This can be evaluated analytically to give the well know Kolmogorov spectrum of refraction index fluctuation:

$$\Phi_n(\kappa)=\frac{5\sqrt{3}C_n^{\ 2}\Gamma\left(\frac{2}{3}\right)}{36\pi^2}\kappa^{-11/3}\simeq 0.033C_n^{\ 2}\kappa^{-11/3}\quad \frac{1}{L_0}<\kappa<\frac{1}{l_0} \tag{4.1.16}$$

The Kolmogorov spectrum is only applicable within the inertial scale range of spatial frequency $\frac{1}{L_0}<\kappa<\frac{1}{l_0}$. At higher wave numbers, Tatarskii [72] proposed a modification that truncates the spectrum, corresponding to fast decay of vortices of scale smaller than l_0. A more serious problem persists at lower wave numbers, where the PSD diverges to infinity at a spatial frequency of zero. A reasonable assumption is to allow the power to saturate to a constant value, resulting in so called the Von Kármán spectrum [92]. Recently, modifications were proposed as detailed analytical assessment and

measurements were made. Hill numerically demonstrated that at high wave numbers a small deviation to the -11/3 power is needed [93][94]. Andrew [79] demonstrated an analytical expression that approximates this effect. However, these corrections add complexity to the theoretical derivation of statistical properties, while producing relatively small correction in most scintillation index calculations. Therefore, the Kolmogorov spectrum is the only spectrum used throughout this chapter.

4.1.3 Turbulent channel model

The free-space optical propagation though a turbulent atmosphere can be viewed as a channel model consisting of a random medium with turbulence cells placed along the propagation path. These cells cause random refractive index fluctuation, with their PSD corresponding to the Kolmogorov spectrum. A transmitter and a receiver is placed between a block of turbulent medium width L, containing turbulence cells that are assumed to exist everywhere (Figure 68). The transmitter emits a Gaussian beam of a complex amplitude profile, and the receiver consists of a pin hole aperture located on the optical axis. Since the medium is extended across the whole optical propagation path, it is called the extended medium model.

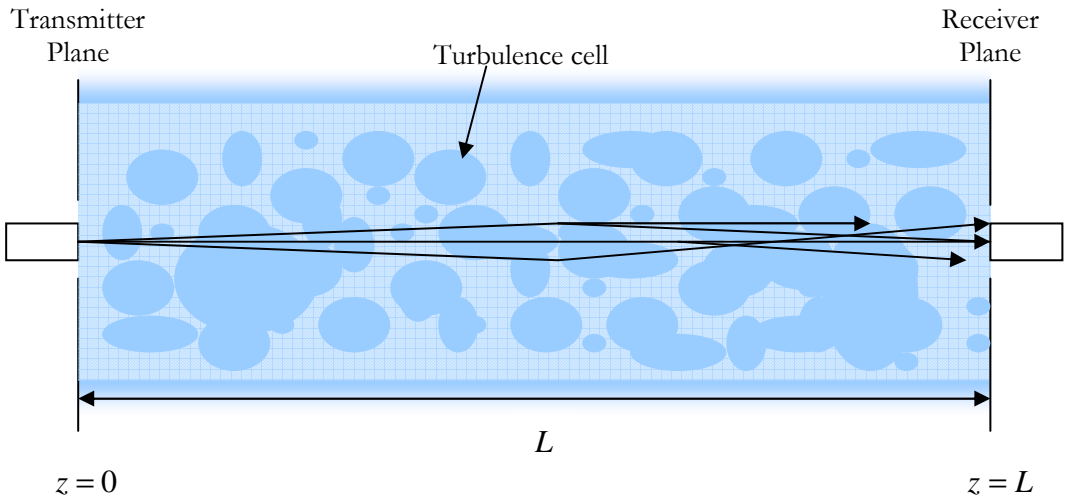

Figure 68. Turbulent channel model with extended random medium.
A Gaussian beam is propagated from the transmitter plane to the receiver plane, passing though a random medium with Kolmogorov statistics.

It is assumed that the medium has sufficiently slow time evolution within the wave propagation time that it can be viewed as static. This allows the use of a time independent partial differential equation. Also, the optical wavelength used is assumed to be much smaller than the smallest turbulence cell (i.e. $l_0 \gg \lambda$), thus back scattering is negligible.

4.1.4 Propagation theory through random medium

With assumptions outlined in the channel model, Maxwell's equation can be simplified to produce a time independent Helmholtz equation [95][79]:

$$\nabla^2 \mathbf{E} + k^2 n^2 (\mathbf{R}) \mathbf{E} = \mathbf{0} \tag{4.1.17}$$

Where $\mathbf{E}$ is the electric field vector along the propagation path, k is the wave number $2\pi / \lambda$ and $n(\mathbf{R})$ is the refractive index of the medium as a function of displacement vector $\mathbf{R}$.

There are two approaches that have been found successful in solving the Helmholtz equation with a stochastic refractive index. A classical approach was first derived using the Born approximation used in theory of quantum scattering [96]. The approximation was further improved by Rytov [79][97] to produce well known results that are applicable to weak turbulence conditions. The second approach uses a direct approach in conjunction with a parabolic approximation method to derive a result that is suitable for both the weak and strong turbulence regime [85][86]. However, the parabolic method cannot produce the fourth order statistics needed for scintillation index calculation. Different attempts at extending the Rytov method to the strong regime have been described by Andrew [79], although no single theory is valid for all regimes. Because of the multiplicity of theories available, a suitable one is used to ensure the greatest accuracy.

The strength of turbulence is normally classified using a quantitative measure known as the Rytov variance [73]:

$$\sigma_R^{\,2} = 1.23 C_n^{\,2} k^{7/6} L^{11/6} \tag{4.1.18}$$

A medium is considered to be in the weak regime when $\sigma_R^2 < 1$. At larger variance, the assumptions used by Rytov can not accurately describe the processes inside the medium. Figure 69 shows a plot of Rytov variance against distance with typical C_n^2 value of 10^{-14} and 10^{-13} $m^{-2/3}$ and wavelength of 640nm. At a high C_n^2 value corresponding to a very hot day time condition, the Rytov variance reaches one at 400 meters. As C_n^2 is reduced to 10^{-14}, the distance extends to 1400 meters. This limits Rytov theory to no more than 1400m, just suitable for modelling medium distance free-space optical links for last mile connectivity. However, measurements observed by Gracheva [98] suggest an existence of saturation as turbulence shifts towards the strong regime. The weak fluctuation theory therefore tends to over-estimate the intensity fluctuations; this was confirmed by Andrew [79] using numerical simulation and strong fluctuation theory. If the results from weak fluctuation theory are treated as an upper bound, in this case the use of weak fluctuation theory is appropriate. The rest of the chapter will briefly derive the necessary statistical moments needed from this weak fluctuation theory using the Rytov method.

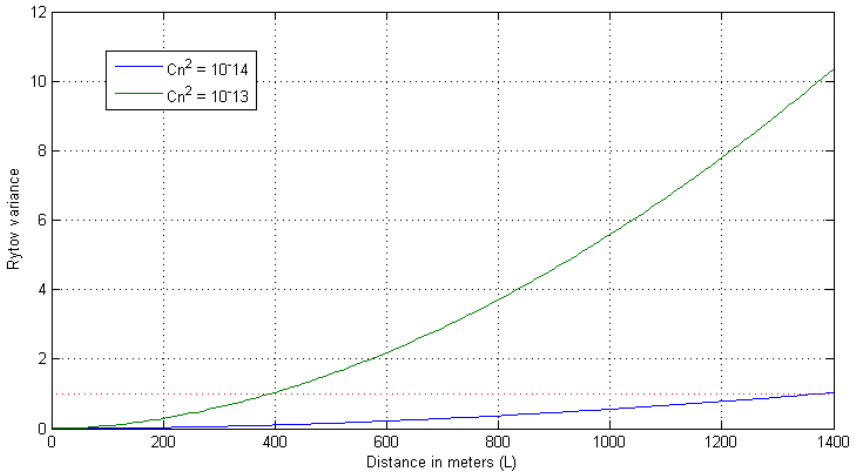

Figure 69. Rytov variance σ_R^2 as a function of propagating distance and refractive index structure constant C_n^2. The validity of Rytov approximation is within the region where $\sigma_R^2 < 1$.

4.1.5 Rytov method

The Helmholtz equation in (4.1.17) can be further simplified by ignoring any de-polarisation effects caused by the refractive index fluctuation. This allows the vector components to be separated and solved individually. A scalar Helmholtz equation in terms of an electric field component U perpendicular to the propagation path is written in the form:

$$\nabla^2 U + k^2 n^2(\mathbf{R}) U = 0 \tag{4.1.19}$$

If the refractive index is constant, the equation simply reduces to the three-dimensional wave equation for the electric field component. The spatial dependence of refractive index produces additional diffractive effects as the optical beam propagates through the medium. In air, $n(\mathbf{R})$ can be expressed as:

$$n(\mathbf{R}) = 1 + n_1(\mathbf{R}) \tag{4.1.20}$$

Where $n_1(\mathbf{R})$ is the refractive fluctuation from the nominal value of one. Squaring (4.1.19) and approximating by ignoring higher order fluctuation term:

$$n^2(\mathbf{R}) \simeq 1 + 2n_1(\mathbf{R}) \tag{4.1.21}$$

Assuming that Born approximation applies, this is equivalent to writing the scalar electric field U as summation of ever smaller fluctuations:

$$U = U_0 + U_1 + U_2 + \ldots \tag{4.1.22}$$

Using perturbation theory, each term is multiplied by corresponding perturbation parameter ε:

$$U = U_0 + \varepsilon U_1 + \varepsilon^2 U_2 + \ldots \tag{4.1.23}$$

Applying the same treatment to the refractive index:

$$n^2(\mathbf{R}) \simeq 1 + 2\varepsilon n_1(\mathbf{R}) \tag{4.1.24}$$

Inserting (4.1.23) and (4.1.24) into (4.1.19) gives an expression:

$$\begin{aligned} &\nabla^2 U_0 + \varepsilon \nabla^2 U_1 + \varepsilon^2 \nabla^2 U_2 + \cdots \\ &+ k^2 (U_0 + \varepsilon U_1 + \varepsilon U_2 + \cdots) \\ &= -2k^2 (\varepsilon n_1(\mathbf{R}) U_0 + \varepsilon^2 n_1(\mathbf{R}) U_1 + \cdots) \end{aligned} \tag{4.1.25}$$

Collecting the terms with same orders of ε, the original Helmholtz equation reduces to one homogeneous partial differential equation, and a set of inhomogeneous partial differential equations:

$$\begin{aligned}
&\nabla^2 U_0 + k^2 U_0 = 0 \\
&\nabla^2 U_1 + k^2 U_1 = -2k^2 n_1(\mathbf{R}) U_0 \\
&\nabla^2 U_2 + k^2 U_2 = -2k^2 n_1(\mathbf{R}) U_1 \\
&\cdots
\end{aligned} \tag{4.1.26}$$

The first equation is simply the free-space wave propagation without the effects of refractive index fluctuations. The solution to this equation is known for plane, spherical and Gaussian beams. The extra field contributions have been transformed to inhomogeneous equations that are of standard free-space wave propagation; with constant terms on the left hand side and the effects from refractive index have been moved to the forcing function. An equation of this form can be solved by Green's function integral. In this case, a paraxial Green's function leads to a form similar to a Fresnel integral with varying refractive index [74]:

$$U_m(\mathbf{r}, L) = \frac{k^2}{2\pi} \int_0^L dz \int_{-\infty}^{\infty} U_{m-1}(\mathbf{s}, L) \frac{n_1(\mathbf{s}, z)}{L - z} \exp\left(ik(L - z) + \frac{ik|\mathbf{s} - \mathbf{r}|^2}{2(L - z)} \right) d^2 s \tag{4.1.27}$$

Where m is the order of the perturbation. It is convenient to write the field perturbation in terms of normalised field ϕ_m:

$$\phi_m(\mathbf{r}, L) = \frac{U_m(\mathbf{r}, L)}{U_0(\mathbf{r}, L)} \tag{4.1.28}$$

The series solution was shown to deviate from the experimental data other than at very weak turbulence regime. Rytov suggested that the field perturbation is physically inaccurate, and an alternative perturbation, based on expansion of phase terms, is written instead as:

$$U(\mathbf{r}, L) = U_0(\mathbf{r}, L) \exp(\psi(\mathbf{r}, L)) \tag{4.1.29}$$

Where $\psi(\mathbf{r}, L)$ is the complex phase perturbation, consisting of high ordered phase terms:

$$\psi(\mathbf{r}, L) = \psi_1(\mathbf{r}, L) + \psi_2(\mathbf{r}, L) + \cdots \tag{4.1.30}$$

Using a first order Maclaurin approximation, the phase terms can be equated to the normalised field perturbation in the Born approximation:

$$\psi_1(\mathbf{r},L) \simeq \phi_1(\mathbf{r},L)$$
$$\psi_2(\mathbf{r},L) \simeq \phi_2(\mathbf{r},L) - \frac{1}{2}\phi_1^2(\mathbf{r},L) \tag{4.1.31}$$

However the refractive index is not an analytical function, but a statistical distribution with expected value and covariance function between two points. Using the Riemann-Stieltjes integral [74] the stochastic refractive index fluctuation can be expressed in frequency space:

$$n_1(\mathbf{s},z) = \int_{-\infty}^{\infty}\int \exp(i\mathbf{K}\cdot\mathbf{s})\, d\nu(\mathbf{K},z) \tag{4.1.32}$$

Substituting (4.1.32) into (4.1.27), the expression for phase fluctuation moments can be solved for plane and spherical waves [73]. To find a solution for a Gaussian beam, the unperturbed field can be written in the form of spot radius W_0 and field phase curvature F_0:

$$U_0(\mathbf{r},0) = U_0(r,0) = a_0 \exp\left(\frac{-r^2}{W_0^2} - \frac{ikr^2}{2F_0}\right) \tag{4.1.33}$$

Where a_0 is the initial beam amplitude. The position vector has been converted to a scalar radial term due to cylindrical symmetry. Following the approach used by Andrew [79], the transmitter plane complex beam parameters are rewritten as:

$$\Theta_0 = 1 - \frac{L}{F_0}, \quad \Lambda_0 = \frac{2L}{kW_0^2} \tag{4.1.34}$$

The beam parameter for the unperturbed field at the receiver plane can then be written as a function of these parameters:

$$\Theta = 1 - \frac{L}{F} = \frac{\Theta_0}{\Theta_0^2 + \Lambda_0^2}, \quad \Lambda = \frac{2L}{kW^2} = \frac{\Lambda_0}{\Theta_0^2 + \Lambda_0^2} \tag{4.1.35}$$

Andrew shows that, by using the framework of Rytov's solution to weak fluctuation theory, the mean intensity at the receiver is given by this radially dependent expression:

$$\langle I(r,L)\rangle = \frac{a_0^2 W_0^2}{W^2}\exp\left[H_1(r,L)\right] \tag{4.1.36}$$

H_1 is given by an integral of the refractive index power spectrum density $\Phi_n(\kappa)$:

$$H_1(r,L) = 4\pi^2 k^2 L \int_0^1 d\xi \int_0^\infty \kappa \Phi_n(\kappa) \left[I_0(2\Lambda r \xi \kappa) \exp\left(-\frac{\Lambda L \kappa^2 \xi^2}{k} \right) - 1 \right] d\kappa \quad (4.1.37)$$

Where k is spatial frequency, k is the wave number, L is the propagation distance, I_0 is the modified Bessel function. Using the Kolmogorov spectrum, the integral can be simplified greatly to a standard result [99]:

$$H_1(r,L) \simeq {\sigma_R}^2 \Lambda^{5/6} \left(2.22 \frac{r^2}{W^2} - 1.33 \right) \quad (4.1.38)$$

Where ${\sigma_R}^2$ is Rytov variance given in equation (4.1.18). Combining (4.1.36) and (4.1.38), the on axis mean intensity becomes:

$$\left\langle I(0,L) \right\rangle = \frac{{a_0}^2 {W_0}^2}{W^2} \exp\left[-1.33 {\sigma_R}^2 \Lambda^{5/6} \right] \quad (4.1.39)$$

The on-axis intensity distribution is a function of only the propagation distance, the strength of the turbulence and the unperturbed beam profile. The scintillation index ${\sigma_I}^2$ is calculated from the second intensity moment:

$${\sigma_I}^2 = \frac{\left\langle I(r,L)^2 \right\rangle - \left\langle I(r,L) \right\rangle^2}{\left\langle I(r,L) \right\rangle^2} = \frac{\left\langle I(r,L)^2 \right\rangle}{\left\langle I(r,L) \right\rangle^2} - 1 \quad (4.1.40)$$

Where the second moment is given by Andrew [79]:

$$\left\langle I(r,L)^2 \right\rangle = \left\langle I(r,L) \right\rangle^2 \exp\left[H_2(r,L) \right] \quad (4.1.41)$$

$$H_2(r,L) = 8\pi^2 k^2 L \int_0^1 d\xi \int_0^\infty \kappa \Phi_n(\kappa) \exp\left(-\frac{\Lambda L \kappa^2 \xi^2}{k} \right) \times \left(I_0(2\Lambda r \xi \kappa) - \cos\left[\frac{L\kappa^2 \xi \left(1 - (1-\Theta)\xi \right)}{k} \right] \right) d\kappa \quad (4.1.42)$$

When the Kolmogorov spectrum is used, the expression can be solved by using a Mellin transform and contour integral [100]. This method produces a solution in terms of a hypergeometric function. For the scintillation index, a solution is given in [74]:

$$\sigma_I^{\,2}\left(r,L\right)=\sigma_R^{\,2}\left(\begin{array}{c}3.86\,\mathrm{Re}\left[i^{5/6}\,{}_2F_1\left(-\frac{5}{6},\frac{11}{6};\frac{17}{6};(1-\Theta)+i\Lambda\right)\right]\\ -2.64\Lambda^{5/6}\,{}_1F_1\left(\frac{-5}{6};1;\frac{2r^2}{W^2}\right)\end{array}\right) \tag{4.1.43}$$

Where ${}_1F_1$ is the confluent hypergeometric function, and ${}_2F_1$ is the Gauss hypergeometrical function (Appendix B). The scintillation index is therefore a separable function of the Rytov variance and function of the Gaussian beam parameters and propagating distance. The $\sigma_I^{\,2}/\sigma_R^{\,2}$ ratio therefore determines the component of the scintillation index caused by the geometry of the beam propagation. For the on-axis only component, the expression reduces to:

$$\sigma_I^{\,2}\left(0,L\right)=3.86\,\mathrm{Re}\left[i^{5/6}\,{}_2F_1\left(-\frac{5}{6},\frac{11}{6};\frac{17}{6};(1-\Theta)+i\Lambda\right)-\frac{11}{16}\Lambda^{5/6}\right]\sigma_R^{\,2} \tag{4.1.44}$$

By assuming that the beam is collimated (Θ_0 = 1), the $\sigma_I^{\,2}/\sigma_R^{\,2}$ ratio for on axis detector is shown in Figure 70.

The on axis scintillation index is applicable for a point detector, i.e. a pinhole detector with aperture dimension of no significant extent. In practice, the diffraction limit allows an aperture below the first Fresnel zone $\sqrt{L/k}$ to be regarded as a point detector [101]. If an aperture is large relative to this dimension, scintillation is essentially reduced by an effect called aperture averaging. This is caused by overlapping of multiple uncorrelated 'patches' of intensity on the aperture. The effect can be modelled by calculating the scintillation index across a circular aperture with diameter D [74]:

$$\sigma_{I_a}^{\,2}\left(D,L\right)=\frac{16}{\pi D^2}\int_0^D rB_I\left(r,L\right)\left[\cos^{-1}\left(\frac{r}{D}\right)-\frac{r}{D}\sqrt{1-\frac{r^2}{D^2}}\right]dr \tag{4.1.45}$$

where $B_I\left(r,L\right)$ is the circular symmetric normalised covariance function of intensity (Appendix C):

$$B_I\left(r,L\right)=\frac{\left\langle I\left(r,L\right)I\left(0,L\right)\right\rangle}{\left\langle I\left(r,L\right)\right\rangle\left\langle I\left(0,L\right)\right\rangle}-1 \tag{4.1.46}$$

Andrews [74] showed that $B_I\left(r,L\right)$ is closely approximated by a separable function of the Rytov variance and an aperture averaging factor A, defined as a ratio of the aperture averaged scintillation index to the point detector scintillation index:

$$A = \frac{\sigma_{I_a}^{\ 2}(D,L)}{\sigma_I^{\ 2}(0,L)} \tag{4.1.47}$$

Numerical integration yields a factor as a function of the collimated beam diffraction parameter Λ_0, D and a Fresnel zone size $\sqrt{L/k}$ [74]. For a path distance L = 1000m, k = 640nm, curves for the aperture averaging factor are shown in Figure 71.

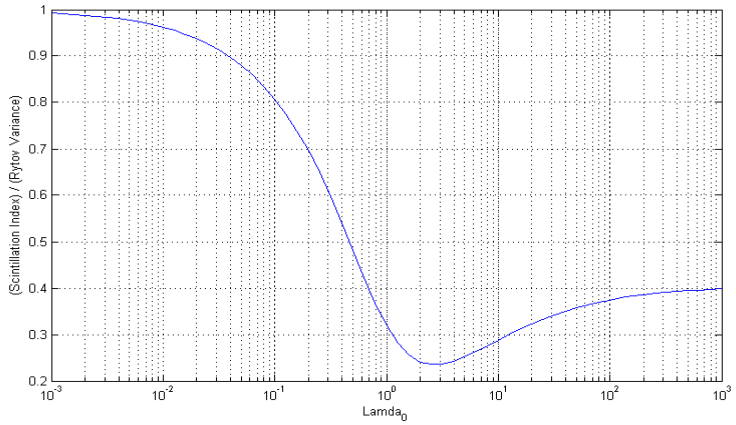

Figure 70. A plot of the ratio of on-axis scintillation index to Rytov variance varies with Gaussian beam parameter Λ_0.

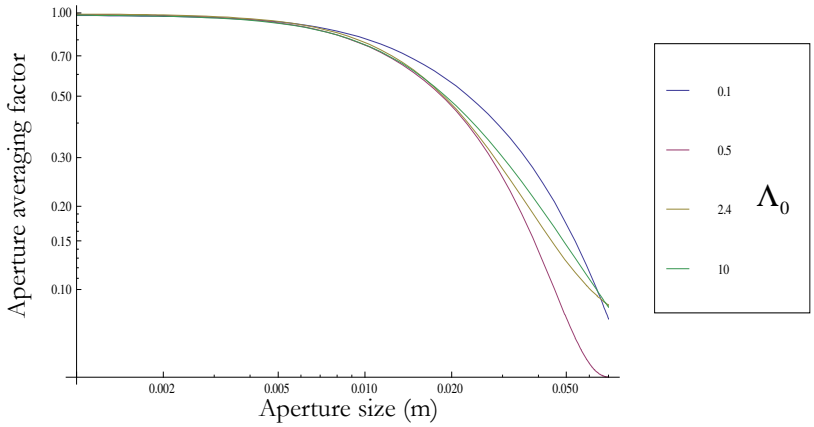

Figure 71. Aperture averaging factor A as a function of aperture size for collimated beam. Parameters are L = 1000m and k = 640nm.

There is a small dependency on the diffractive beam parameter Λ_0. As D increases the averaging factor reduces scintillation up to a factor of 10 or more.

A long beam propagation distance can be simulated with a short distance by reducing the beam radius W_0 such that the Gaussian beam parameters Θ and Λ are the same for both cases. These parameters are typically chosen to coincide with the least scintillation index. Inspecting the relationship between σ_R^2 and scintillation index σ_I^2 for a collimated Gaussian beam in Figure 70A, the ideal beam profile is achieved when $\Lambda_0 \approx 2.5$, corresponding to σ_I^2 / σ_R^2 ratio of 0.25. Using this value, the beam radius versus distance curve is plotted in Figure 72.

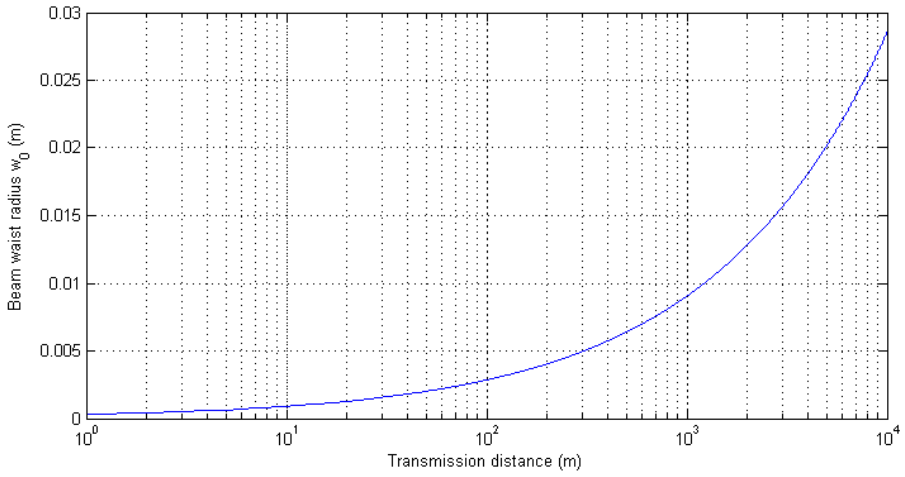

Figure 72. Beam radius as a function of propagating distance to maintain $\Lambda_0 = 2.5$ for minimum scintillation index. Wavelength is 640nm.

In a laboratory, a long distance link can be simulated by selecting propagating distance L and beam waist W_0 such that they lie along a curve of a particular value of Λ_0. The scintillation properties for both cases are then exactly identical under the assumption of weak fluctuation theory.

4.1.6 Signal to noise ratio and bit error rates

Optical scintillation causes random fluctuation in an otherwise constant optical beam. At the receiver, data modulated on the optical beam is further modulated by scintillation, causing periods of low beam power similar to a fading channel. Fading deteriorates the channel capacity by decreasing the signal to noise ratio (SNR). A relationship between the strength of turbulence and the channel capacity is therefore needed to determine the performance of a turbulence limited free-space optical link.

A typical probabilistic channel model consists of signal i_s from a photodetector, an additive noise source i_N, and a multiplicative noise source h caused by intensity fading in the turbulent channel. The combination of these signals is sent to a decoder in the form of:

$$i = hi_s + i_N \tag{4.1.48}$$

i_n is usually caused by shot and thermal noise from photodetector components, and it is assumed to have zero mean and variance of σ_N^2. i_s is assumed to be linearly proportional to the received optical power, neglecting any optical turbulence. h is the fading component by the turbulent channel, with mean of 1 and variance of σ_I^2 or the scintillation index. The probability density function (PDF) of h has been extensively studied during the early periods of optical turbulence research. The earliest model assumed only a first order phase disturbance which, under the Rytov approximation, is a Gaussian process. The resulting PDF therefore follows a log-normal function:

$$p_h(u) = \frac{1}{u\sigma_I^2\sqrt{2\pi}} \exp\left[-\frac{\left(\ln(u) + \frac{1}{2}\sigma_I^2 \right)^2}{2\sigma_I^2} \right] \tag{4.1.49}$$

where u is the normalised signal intensity $I / \langle I \rangle$. The log-normal PDF provides a good fit for very weak turbulent conditions as shown in Figure 73A. In this case, the scintillation index is below 0.4 [79]. As turbulence increases, second order processes start to contribute significantly. This likely not to be

Gaussian, and another PDF was proposed using a modification of Nakagami m distribution [102][103], called the gamma-gamma distribution:

$$p_h(u) = \frac{2(\alpha\beta)^{\frac{\alpha+\beta}{2}}}{\Gamma(\alpha)\Gamma(\beta)} u^{\frac{a+b}{2}-1} K_{a-b}\left(2\sqrt{abu}\right) \tag{4.1.50}$$

Where α and β are the distribution parameters, which are related to the scintillation index by:

$$\sigma_I^2 = \frac{1}{\alpha} + \frac{1}{\beta} + \frac{1}{\alpha\beta} \tag{4.1.51}$$

The parameters can be estimated from the scintillation index and collimated beam parameter Λ_0 using a simplification from [74]:

$$\alpha = \left\{ \exp\left[\frac{0.49\sigma_I^2}{\left(1+0.56\left(1+1/\left(1+\Lambda^2\right)\right)\sigma_I^{12/5}\right)^{7/6}} \right] - 1 \right\}^{-1}$$
$$\beta = \left\{ \exp\left[\frac{0.51\sigma_I^2}{\left(1+0.69\sigma_I^{12/5}\right)^{5/6}} \right] - 1 \right\}^{-1} \tag{4.1.52}$$

A plot of the gamma-gamma PDF is shown in Figure 73B for different valued of scintillation index.

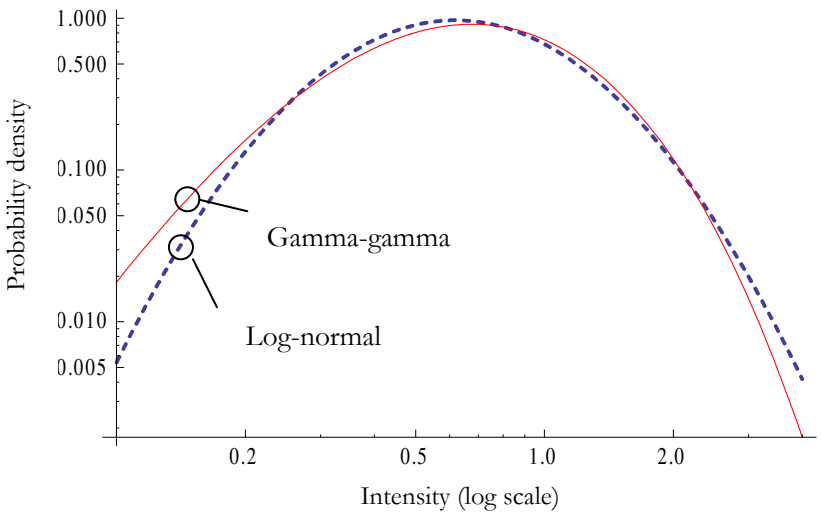

Figure 73. A plot of a log-normal and a gamma-gamma PDFs for σ_R^2 = 1.

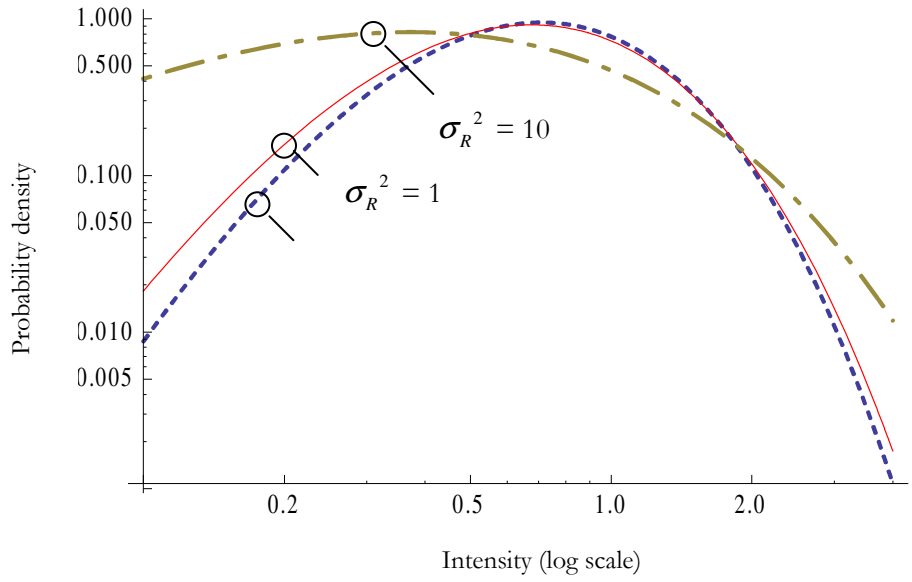

Figure 74. A plot of Gamma-gamma probability density function for normalised intensity fluctuation $I/\langle I \rangle$ at different Rytov variance.

The probability that a channel is in a fade condition is defined as the probability that the normalised intensity is below a threshold F_T. This is simply the cumulative probability of $p_h(u)$:

$$P_F(u \le F_T) = \int_0^{F_T} p_h(u)\,du \tag{4.1.53}$$

The signal to noise ratio can be calculated by first considering the signal to noise ratio of the fadeless channel:

$$SNR_0 = \frac{i_s}{\sigma_N} \tag{4.1.54}$$

By using the assumption that the noise PDF is normally distributed, the probability of error (bit error rate or BER) for an on-off keying (OOK) data stream is given by the well known result:

$$BER_0 = \frac{1}{2} erfc\left(\frac{SNR_0}{2\sqrt{2}}\right) \tag{4.1.55}$$

The detection threshold value is set to u = 0.5. Fading can be thought of a modulation of the noise source, and dynamically changes the SNR of the received signal. Multiplying the probability of fading with the BER and integrating results in the fading channel BER [104]:

$$BER_F = \frac{1}{2}\int_0^{\infty} p_h(u)\, erfc\left(\frac{\langle SNR\rangle u}{2\sqrt{2}}\right) du \qquad (4.1.56)$$

Where $\langle SNR\rangle$ is the mean or expected SNR due to turbulence. A power calculation of received intensity gives the $\langle SNR\rangle$ approximately by Andrew [74]:

$$\langle SNR\rangle = \frac{SNR_0}{\sqrt{1+5.9\sigma_I^{12/5}\left(\frac{\Lambda_0}{1+\Lambda_0^2}\right)+\sigma_I^2 SNR_0^2}} \qquad (4.1.57)$$

As SNR_0 increases to large values, $\langle SNR\rangle \approx 1/\sigma_I^2$. The minimum BER is therefore scintillation limited [105][106]. Using numerical integration, a plot of the minimum BER for OOK against scintillation index is shown in Figure 75.

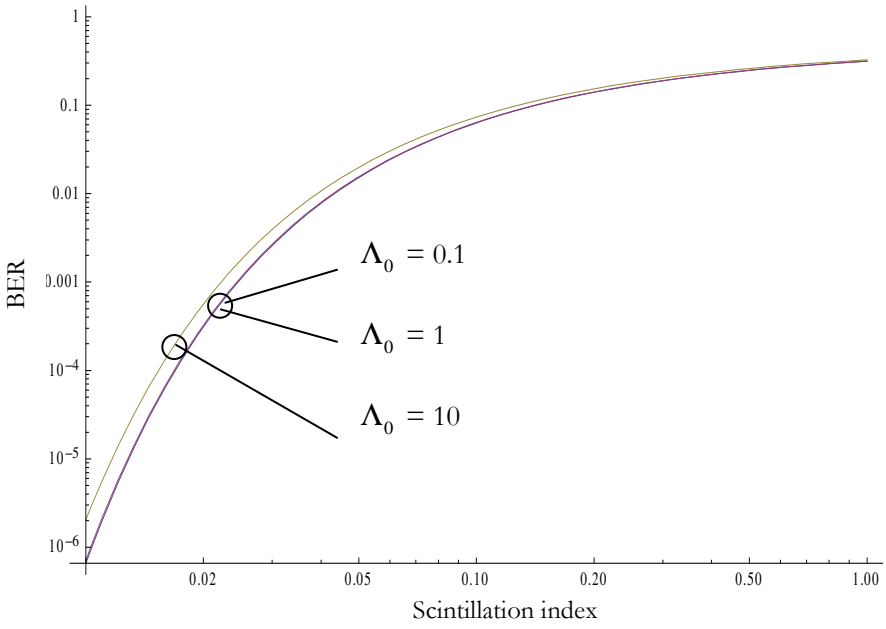

Figure 75. Maximum OOK bit error rates calculated as a function of scintillation index for Λ_0 = 0.1, Λ_0 = 1 and Λ_0 = 10.

A very low scintillation index of 0.01 is required for reliable communication of 10^{-6} or better. Note that this result applies to both a point detector and an aperture averaged signal. Improvements can be made by using a large receiver aperture to reduce scintillation as much as possible. Another possibility is the use of forward error correction codes [107] such as Reed-Solomon or convolution coding [108] to use time diversity, or by taking advantage of the statistical knowledge of the turbulent channel with maximum

likelihood sequence detection [109]. Two to four orders of BER improvements have been reported [107] using a combination of these techniques.

In this section, the turbulent channel is treated in the same way as a typical fading channel. The probability density function for such channel follows a gamma-gamma distribution. Because the maximum SNR is limited by the scintillation index, the minimum bit error rate is also limited by scintillation. Turbulence mitigation schemes are therefore necessary for reliable communication.

4.2 Turbulence simulation with phase screens

The availability of high resolution liquid crystal based SLMs has allowed a new technique for simulating turbulence with any given properties in the confine of a laboratory [87]. An SLM acts as a phase modulator that mimics the phase distortions experienced by a propagating beam. The phase profile is calculated on a computer using a number of algorithms available [110][111][112]. An advantage of using computer generated turbulence, compared to other methods such as hot air boxes [113][114] and lithographically etched dielectrics [115], is the ease of generating and storing a phase screen with any characteristics. The effects of optical turbulence can then be made temporally static. Recent work has showed great promise in using this method [87][89]. However, they have all failed to address two problems: the finite nature of the propagating beam, specifically of the Gaussian beam, and the limited phase modulation depth of a liquid crystal device.

In this section, an experimental laboratory turbulence simulation technique is described. The propagation path length used is order of magnitudes shorter than the simulated path length, while the scintillation index achieved matches closely to theoretical results. The problem of phase modulation depth is solved using a binary phase encoding, with numerical simulation to verify the accuracy of the approach. Limitations of this approach are also presented.

4.2.1 Phase screen channel model

An extended random medium can effectively be modelled by one or more phase 'screens'. A phase screen is defined as a thin piece of medium that exhibits the same Kolmogorov statistics as an extended random medium. When placing a phase screen along the optical propagation path (Figure 76) the electric field can be made to experience the same amount of fluctuations as for an extended medium. Using results from [79], the equivalent Rytov variance of an extended medium model is given by the usual definition:

$$\sigma_R^{\,2} = 1.23 C_n^{\,2} k^{7/6} L^{11/6} \tag{4.2.1}$$

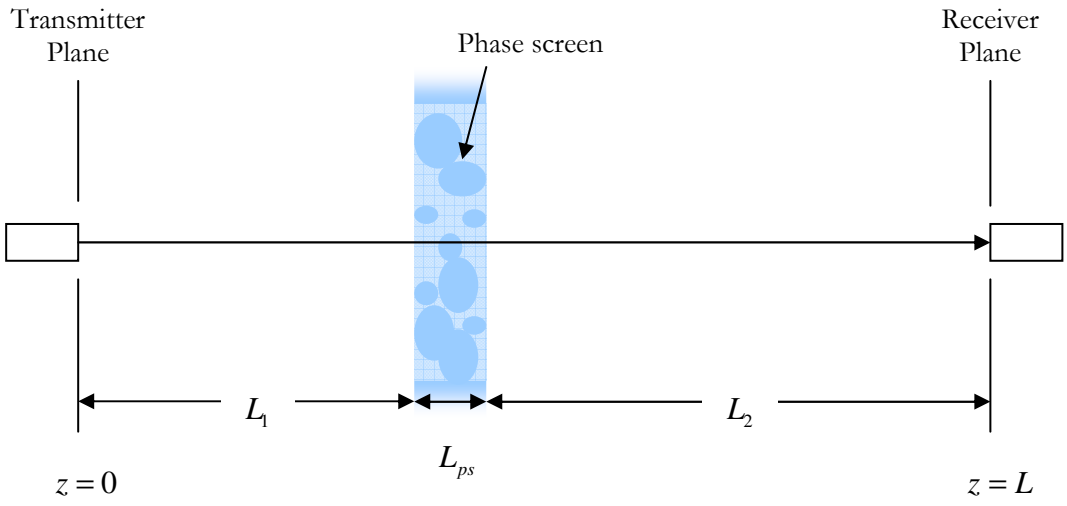

Figure 76. Phase screen channel model, containing a small slice of random medium with Kolmogorov statistics.

In the phase screen model, due to the limited extent of turbulence in a finite medium, the Rytov variance is shown to be modified to an expression [116]:

$$\sigma_{R_{PS}}^{\,2} = 2.25 C_{n_{PS}}^{\,2} k^{7/6} L^{11/6} \frac{L_{PS}}{L_2} \left(\frac{L_2}{L} \right)^{11/6} \tag{4.2.2}$$

Where $C_{n_{PS}}^{\,2}$ is the refractive index structure constant. If the phase screen is assumed to have no thickness, for example by using a very thin high refractive index material, the L_{PS} / L_2 factor can be ignored. Equating the two expressions gives:

$$C_n^{\,2} = 1.83\left(\frac{L_2}{L}\right)^{5/6} C_{n_{PS}}^{\,2} \tag{4.2.3}$$

The phase shifts can be described by a two dimensional phase structure function. This is derived directly from Rytov phase disturbances and considering the complex log amplitude of the mutual coherence function $\left\langle U(\mathbf{r}_1, L)U^*(\mathbf{r}_2, L)\right\rangle$. Using a cylindrical coordinate system, and assuming a spherical wave with negligible attenuation, this is reduced to an integral [79]:

$$D_\phi(r_1, r_2, L) = 8\pi^2 k^2 L \int_0^1 \int_0^\infty \kappa \Phi_n(\kappa)\left[1 - J_0\left(\kappa|r_1 - r_2|\right)\right] d\kappa d\xi \tag{4.2.4}$$

which simplifies to a function of separation distance r [79]:

$$D_\phi(r, L) = 1.09 C_n^{\,2} k^2 L |r|^{5/3} \tag{4.2.5}$$

Where r is the separation distance between two points. This can also be written in terms of atmospheric coherence width, or Fried's parameter r_0 [117]:

$$D_\phi(r, L) = 6.88\left(\frac{|r|}{r_0}\right)^{5/3} \tag{4.2.6}$$

Where $r_0 = \left(0.16 C_n^{\,2} k^2 L\right)^{-3/5}$. Fried's parameter is a measure of the correlation width of the phase fluctuation or the smoothness of the phase fluctuation. For a Gaussian beam wave, the phase structure function can be approximated [74] using a correction term a:

$$D_\phi(r, L) = \frac{6.88a}{\left(a + 0.62\Lambda^{11/6}\right)}\left(\frac{|r|}{r_0}\right)^{5/3} \tag{4.2.7}$$

Where a is a function of receiver plane phase curvature $a = \left(1 - \Theta^{8/3}\right)/(1 - \Theta)$. Figure 77 shows a plot of the correction factor for a collimated beam, against transmitter plane beam parameter Λ_0. The factor does not change appreciatively with Λ_0, and the phase structure was therefore approximated by simply the use of equation (4.2.6). It is convenient to normalise Fried's parameter to D/r_0, where D is the transmitter aperture diameter, giving a dimensionless metric of the strength of optical turbulence called the normalised coherence scale.

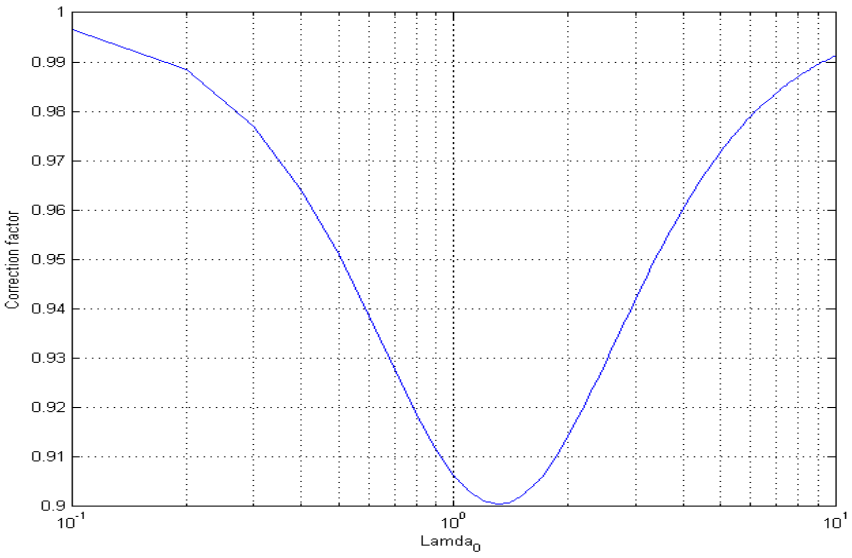

Figure 77. Phase structure correction factor $\left(a+0.62\Lambda^{11/6}\right)^{-1}$ for a collimated beam as a function of transmitter plane beam parameter Λ_0

Further constraints regarding the propagation of a Gaussian beam, and its field moments [116] enforces the location of the phase screen as a function of beam diffractive parameter Λ_0. For collimated Gaussian beams, the expression can be simplified to:

$$\frac{L_2}{L}=0.67-0.17\left[\frac{1}{1+\Lambda_0{}^2}\right] \tag{4.2.8}$$

Where $\Lambda_0=2L/kW_0{}^2$, k is the wave number and W_0 is the Gaussian beam waist radius.

4.2.2 Phase screen generation

The distribution of phase values on a phase screen is completely described by either its power spectral density (PSD) or its structure function. The PSD is essentially a Fourier transform of the spatial phase covariance between two points. Therefore, by assuming each spatial frequency is modelled well with a normally distributed variable and variance given by the PSD, the phase screen can be calculated [118]. However, since a phase screen is in practice sampled into discrete points, a Fast Fourier Transform (FFT) algorithm is needed. The periodic nature of FFT has been shown to significantly alter the phase structure function, affecting the low frequencies in the spectrum [118]. Padding alleviates the periodicity within a small region of the phase screen, but this has been found to be computationally very expensive.

Two other methods have been published that over come much of the problems with FFT method. The first method uses Zernike decomposition of a Kolmogorov spectrum [111], while the second uses spatial midpoint interpolation [110] to gradually increase the resolution of the phase screen. Both of these methods are assessed to quantitatively measure the differences in computation complexity and accuracy.

Zernike polynomials belong to an orthogonal basis of radial and angular functions, and are extensively used in wavefront interpolation. There are a number of different definitions for Zernike polynomials; however this chapter adopts the definition chosen by Noll [112]:

$$\left.\begin{aligned} Z_{even\ j} &= \sqrt{n+1}\,R_n^m(r)\sqrt{2}\cos(m\theta) \\ Z_{odd\ j} &= \sqrt{n+1}\,R_n^m(r)\sqrt{2}\sin(m\theta) \end{aligned}\right\} \quad m \neq 0$$

$$Z_j = \sqrt{n+1}R_n^0(r) \qquad m = 0 \tag{4.2.9}$$

$$R_n^m(r) = \sum_{s=0}^{(n-m)/2} \frac{(-1)^s (n-s)!}{s!\left[(n+m)/2-s\right]!\left[(n-m)/2-s\right]!} r^{n-2s}$$

Where n and m are the azimuthal and radial mode numbers as a function of an ordering number j:

$$\begin{aligned} n &= ceil\left[\frac{\sqrt{8j-1}-1}{2}\right]-1 \\ m &= ceil\left[j-\frac{n(n+1)+(n+1)(\mathrm{mod}\,2)}{2}\right]\times 2-1-(n+1)(\mathrm{mod}\,2) \end{aligned} \tag{4.2.10}$$

Zernike decomposition of Kolmogorov phase screen can be calculated by cross correlating the modes with the phase correlation function [112]:

$$\left\langle a_j a_k^{\,*} \right\rangle = \int_0^{2\pi}\int_0^{2\pi}\int_0^{1}\int_0^{1} Z_j(\rho,\theta) Z_m(\rho',\theta') B(D\rho, D\rho')\, d\rho d\rho' d\theta d\theta' \qquad (4.2.11)$$

Where D is the size of the aperture, and B is the phase covariance function. By using the relation in (4.1.12), the integrals can be evaluated exactly in Fourier space. Noll [112] and Wang [119] derived this expression exactly:

$$\left.\begin{aligned} \left\langle a_j a_k \right\rangle = & \frac{0.0144\sqrt{(n_j+1)(n_k+1)}\,(-1)^{(n_j+n_k-2n_j)/2}}{\pi} \\ & \times \int k(k^{-11/3}) \frac{J_{n_j+1}(2\pi k) J_{n_k 1}(2\pi k)}{k^2} dk \end{aligned}\right\} m_j = m_k$$
$$= 0 \qquad \text{otherwise} \qquad (4.2.12)$$

Covariance only exists for modes with the same azimuth frequency m due to orthogonality of trigonometric terms. Roddier [111] gave an exact expression for plane waves, giving a sparse covariance matrix consisting of mostly diagonal elements. A closed form expression for this matrix is given as a function of j (Appendix D). The matrix for the first 7 modes, excluding constant phase or piston is tabulated in Table 11.

j =	2	3	4	5	6	7	8
2	0.4557	0	0	0	0	0	–0.0144
3	0	0.4557	0	0	0	–0.0144	0
4	0	0	0.0236	0	0	0	0
5	0	0	0	0.0236	0	0	0
6	0	0	0	0	0.0236	0	0
7	0	–0.0144	0	0	0	0.0063	0
8	–0.0144	0	0	0	0	0	0.0063

Table 11. Zernike modes covariance matrix of a Kolmogorov phase screen.

Mode coupling exists, and Zernike polynomials do not form an orthogonal basis with respect to the Kolmogorov phase screen. A more convenient basis is in numerical Karhunen-Loève form. The

amplitudes for the Karhunen-Loève modes can be generated from the Zernike covariance matrix using the singular value decomposition outlined in [111]. A vector of normally distributed random numbers are then multiplied and transformed back to the Zernike modes. The Zernike modes are summed and scaled by $\left(D/r_0\right)^{5/3}$ to give the final phase screen.

The implementation of the Zernike method is characterised by the generation of two steps in computation: pre-generation of covariance and Zernike matrices and the Zernike mode summation. The flow chart in Figure 78 summarises these two steps. MATLAB was used to perform the computations. The resolution of the phase screen is set to 768x768 pixels, corresponding to the resolution of the SLM used. The time needed to generate the sparse covariance matrix for 50 Zernike modes are then recorded. The MATLAB SVD routine was used for singular value decomposition. Each of the 50 Zernike modes are pre-calculated and stored in a 3 dimensional matrix. The total time needed for pre-calculation is 103 seconds. Using the 50 pre-calculated modes, generation of each phase screen takes less than 1 second. A phase screen generated by using 50 modes is shown in Figure 79.

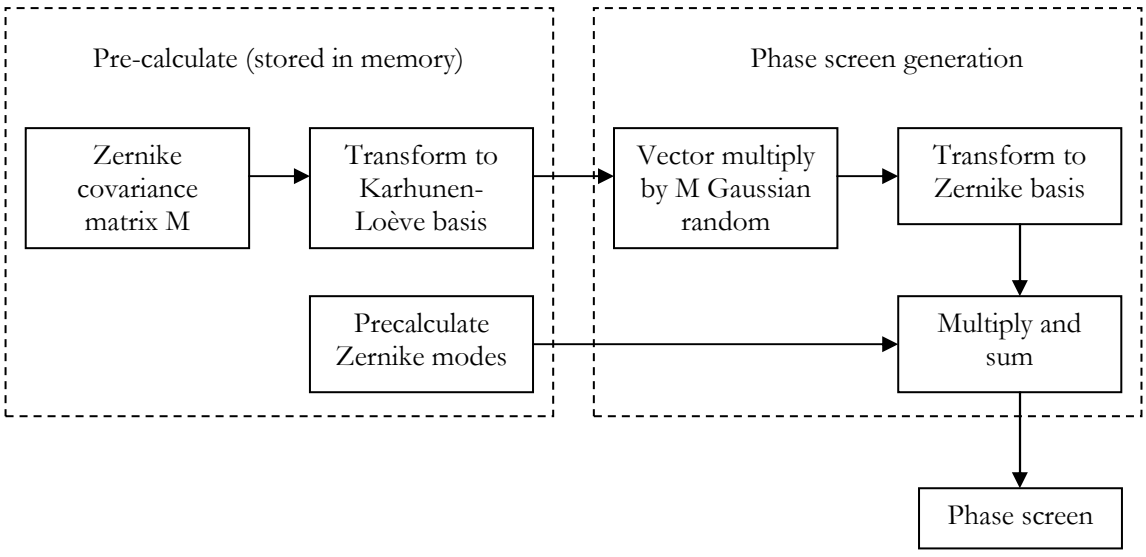

Figure 78. Flow chart of Zernike phase screen generation.

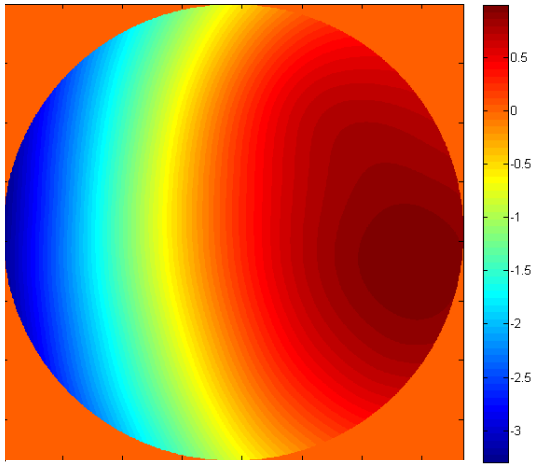

Figure 79. An example of phase screen generated with 50 modes with $D/r_0 = 1$.

There are two limitations observed using this method. By inspection, the phase screen is smooth, containing no features of scale l_0 as expected from the refractive index structure function. This is likely to be due to the limited number of Zernike modes used in the computation. The number of modes needed can be calculated by considering the residual mean squared error as an increasing number of Zernike modes are used, as given by [112]:

$$\Delta_j \approx 0.2859\, j^{-\frac{\sqrt{3}}{2}} \qquad j \gg 1 \tag{4.2.13}$$

Where Δ_j is the mean squared residuel of phase difference, j the sum of Zernike modes relative to a Kolmogorov phase screen (Figure 80). As more modes are added, the residuel will asymptotically approach zero. A large number of modes are therefore required. [87] suggests 120 modes are sufficient.

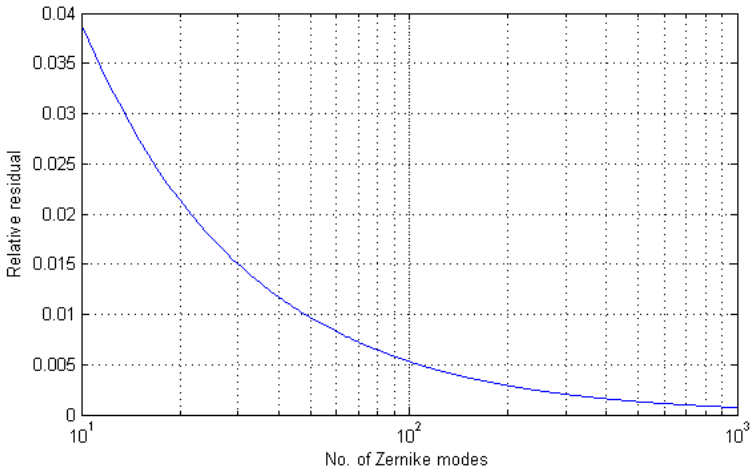

Figure 80. Mean squared residual phase error as a function total number of Zernike modes.

The second problem encountered was the memory requirement for storing pre-calculated Zernike modes. For 50 modes, total memory of $8x768^2x50/1048576 = 225$Mbytes is required. For 120 modes, the memory requirement increases linearly to 540Mbytes. Hu [89] solves this problem by brute force, implementing all Zernike calculations 'on the fly', using a graphics processing unit (GPU).

An alternative method using spatial mid point interpolation (MPI) has been shown to produce a good approximation to a Kolmogorov phase screen with a large reduction in computation effort. MPI is an iterative method for creating realistic landscapes in computer graphics by exploiting the fractal scaling of turbulence, i.e. the structure is identical at any scale [118].

An initial coarse phase screen is produced by numerically integrating the structure function from (4.2.5) to obtain a covariance matrix of a small number of points [110]. The points can directly be produced by using SVD on the covariance matrix and multiplying the orthogonal basis with a vector of normally distributed random numbers. This is numerically intensive, however, so it is pre-calculated once. The points form the edges of the phase screen (Figure 81A).

An interpolation of these coarse phase screen points can be achieved by considering 4 points (a,b,c,d) forming a square dimension d. If an interpolation point is placed in the middle (m), a linear interpolation results in:

$$m = \frac{a+b+c+d}{4} + \varepsilon \tag{4.2.14}$$

Where ε is random displacement added after the interpolation (Figure 81B). Lane [118] calculated the variance of the interpolated point, and subtracting this from the theoretical calculation using (4.2.5) gives:

$$\left\langle \varepsilon^2 \right\rangle = 0.6091(d)^{5/3} \tag{4.2.15}$$

For the special case where the new interpolation point is located along an edge, the correction term takes different variance (Figure 81C), since:

$$m_{edge} = \frac{a+b}{2} + \delta \tag{4.2.16}$$

The variance is given as:

$$\left\langle \delta^2 \right\rangle = 0.4471(d)^{5/3} \tag{4.2.17}$$

The process is iterated until desired resolution is obtained. Again, the phase screen is finally scaled with $(D/r_0)^{5/3}$.

The MPI algorithm was implemented with MATLAB. A numerical solution to the integral given in [110] was used to obtain a covariance of 15x15 points, resulting in a matrix size of 225x225 pixels. An SVD() routine was used to decompose the covariance matrix into singular values in a diagonal matrix and a transformation matrix. These calculations were needed once, and the matrix was then stored in memory. The total time required was 20 minutes. The main MPI routine consists of an interpolator and a random displacement corrector. Edge effects were corrected by producing a slightly larger phase screen than required and trimmed to the specified dimensions. The total time required for the MPI calculation is less than 1 second for a phase screen of 768x768 pixels. An example of the phase screen generated with MPI is shown in Figure 81D.

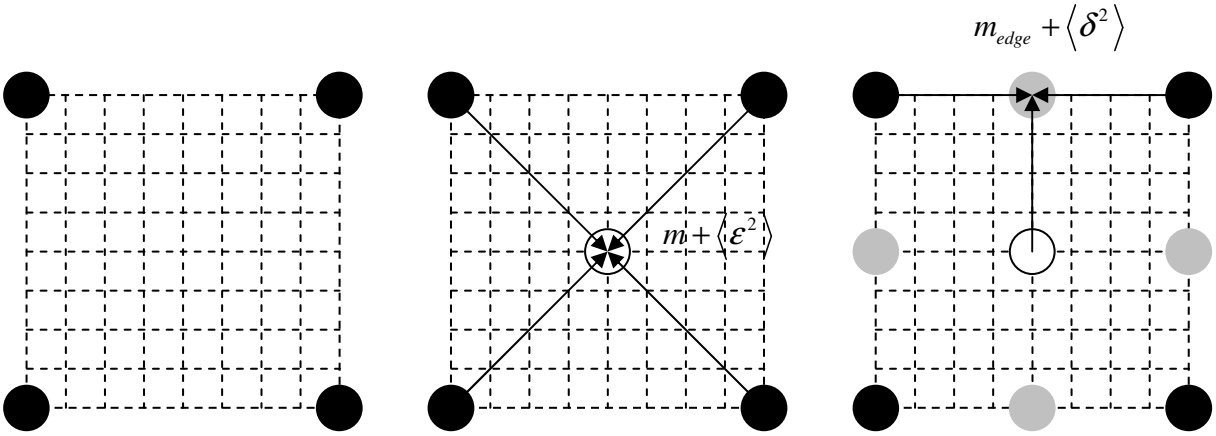

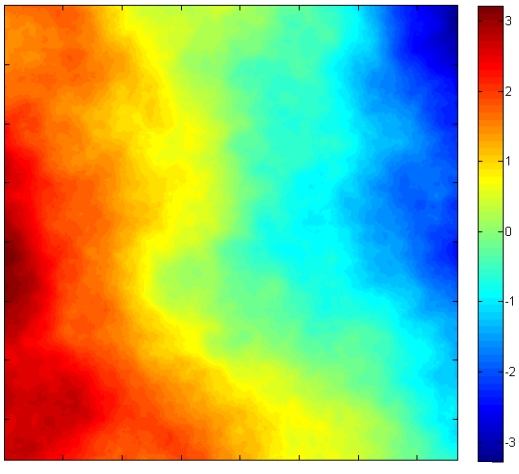

Figure 81. Diagram of the MPI algorithm and the resulting phase screen.

(A) Initial phase screen pixels calculated directly from spatial covariance function.

(B) New mid point generated by interpolation and residual addition.

(C) Edge points with edge interpolation and residual addition.

(D) An example of phase screen generated using MPI algorithm with D/r_0 = 1.

The closeness of the generated phase screen to an ideal Kolmogorov phase screen can be estimated using the phase structure function given in equation (4.2.6). Figure 82A plots the numerical value of the structure function for three different phase screens calculated using 50 Zernike modes, 120 Zernike modes, and the MPI algorithm. These were calculated for 1000 random phase screens with D/r_0 = 1. A theoretical curve (Equation (4.2.6)) is also plotted. The result shows that by more than doubling the number of Zernike modes, the expected phase structure improves only slightly. It is interesting to see that even though the phase screen generated from the Zernike method is smooth, the structure of points close together does not diverge much from theoretical calculation. However, points a long distance away experience less variance theoretical values. This is because that high frequency component is missing from the phase screen, due to insufficient number of Zernike modes. The MPI algorithm produces a phase structure very closely matched to theoretical results.

A plot in Figure 82B shows the average maximum amount of phase shift against the strength of turbulence from D/r_0 = 1 to 4, using 50 phase screens generated with the MPI algorithm.

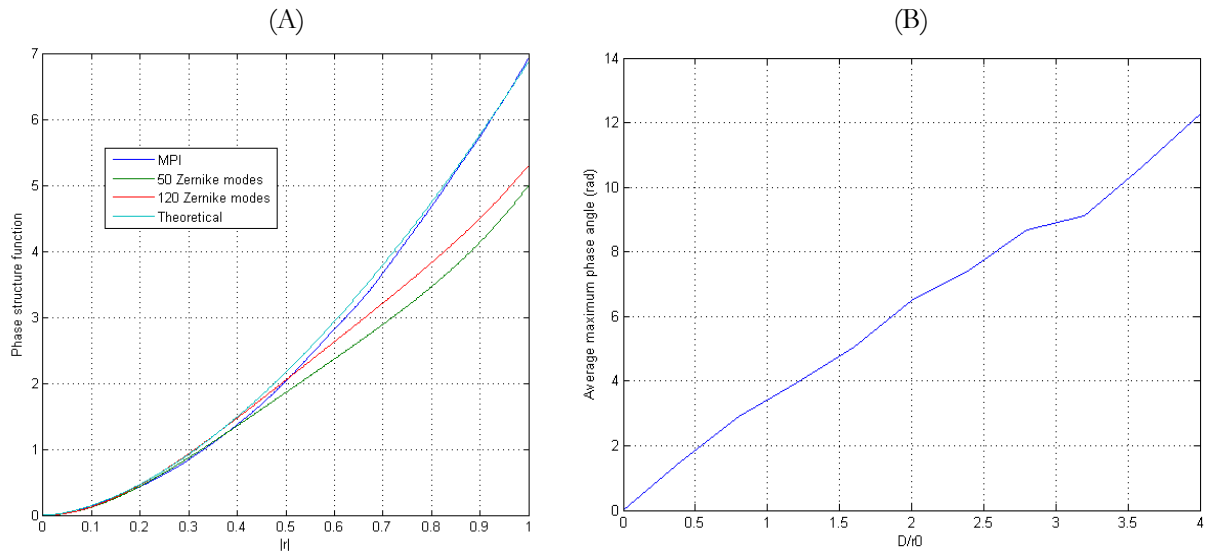

Figure 82. (A) Numerical values of phase structure function for Zernike and MPI methods as a function of point separation. (B) Average maximum phase shifts versus D/r_0.

4.2.3 Binary phase only implementation of phase screen

The MPI algorithm was chosen as the most accurate method of generating a continuous phase distribution with Kolmogorov statistics. A physical representation of this phase distribution has to have enough phase modulation depth to accommodate the range of phase shifts. By using an SLM with modulation range of 2π, it is possible to wrap the phase values to within this range [87]. Because the high Zernike modes needed to accurately simulate a phase screen, deformable mirrors do not have the necessary fidelity for all these modes. They are therefore unsuitable for this application. Therefore, a binary phase only Kolmogorov phase screen on a high resolution liquid crystal SLM was suggested as a possible solution.

Previous studies had shown that using a binary phase hologram, it is possible to generate any continuous phase profile [120] by using the optical system in Figure 83A. This is achieved by using a binary phase only SLM encoded with a tilted phase distribution. A lens is then used to Fourier transform this modulated beam. The first order contains the desired spatial frequency information, which is subsequently filtered using a pinhole. The pinhole acts as a band pass spatial filter, removing unwanted higher spatial frequencies generated by phase binarisation. A second lens is used to transform filtered complex amplitudes back to the desired phase distribution. In this case, the effective phase pattern is located on the second lens.

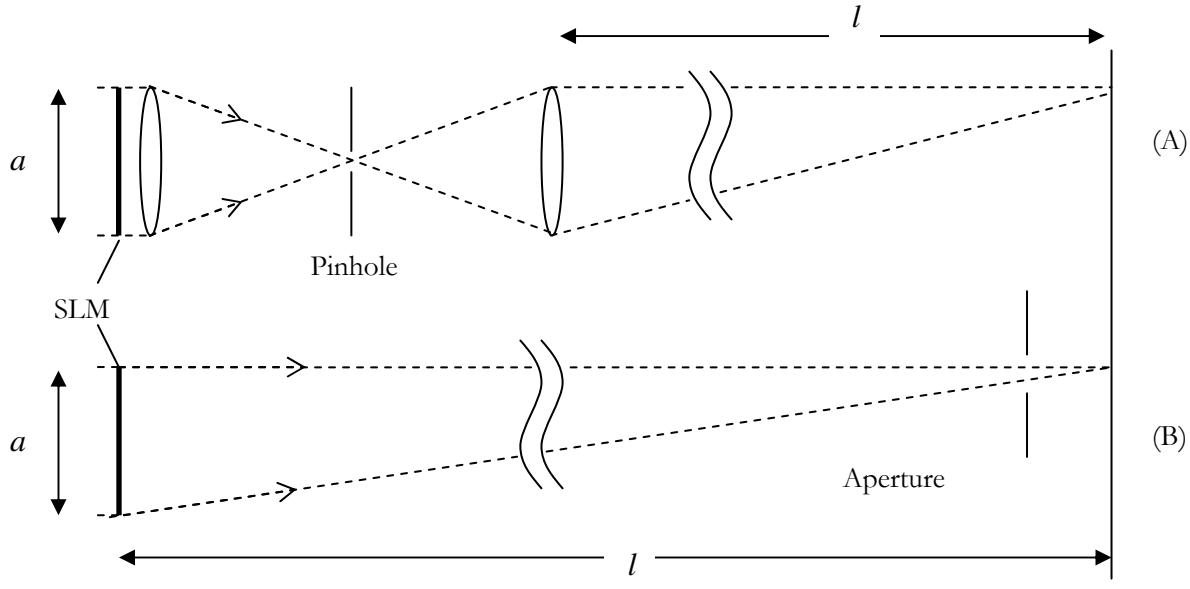

Figure 83. Wavefront generation from binary hologram with (A) spatial filter in Fourier domain (B) spatial filter in Fresnel domain.

A simplified system overcomes the complexity by removing both lenses. Using Fresnel diffraction, the pinhole can be moved to the far field. Figure 83B shows a layout of the proposed optical set up. In this case, the effective phase pattern lies on the SLM plane. The beam then exits the SLM and propagates a further distance l. If l is chosen such that the Fresnel number is greater than one:

$$F = \frac{a^2}{\lambda l} \geq 1 \tag{4.2.18}$$

where a is the size of the SLM, the beam experiences Fresnel diffraction. The complex amplitude $U(x, y, 0)$ after propagation within the Fresnel diffraction distance is given by an integral:

$$U(x, y, l) = \frac{\exp(ikl)}{i\lambda l} \int_{-\infty}^{\infty} \int_{-\infty}^{\infty} U(x', y', 0) \exp\left(\frac{i\pi}{\lambda l} \left((x - x')^2 + (y - y')^2 \right) \right) dx' dy' \tag{4.2.19}$$

Equivalently, this is written in the form of a Fourier transform, with a convolution kernel of a free space impulse response:

$$\begin{aligned} U(x, y, l) = C(x, y) \int_{-\infty}^{\infty} \int_{-\infty}^{\infty} U(x', y', 0) \exp\left(\frac{i\pi}{\lambda l} \left(x'^2 + y'^2 \right) \right) \\ \times \exp\left(\frac{-2i\pi}{\lambda l} (xx' + yy') \right) dx\, dy \end{aligned} \tag{4.2.20}$$

where $C(x, y)$ is a complex phase curvature. If the complex beam amplitude is convolved with a linear phase tilt $\exp(i\phi x')$, and considering only the x axis, the integral becomes:

$$U\left(x - \frac{\phi l}{2\pi}, l \right) = C\left(x - \frac{\phi l}{2\pi} \right) \int_{-\infty}^{\infty} \int_{-\infty}^{\infty} U(x', 0) \exp\left(\frac{i\pi}{\lambda l} x'^2 \right) \exp\left(\frac{-2i\pi}{\lambda l} (xx') \right) dx' \tag{4.2.21}$$

The field is simply translated in the l plane, and the shift does not affect the distribution of the complex amplitude. By expressing binary quantisation of $U(x', 0)$ as a summation of higher order terms [26]:

$$U_B(x, l) = \sum_{n=-\infty}^{\infty} U^n \left(x - \frac{n\phi l}{2\pi}, l \right) \tag{4.2.22}$$

where U^n is self convolution of order n. Phase tilt therefore separates these higher orders spatially, and by appropriately selecting the first order in the far field it is possible to obtain the original distribution. A numerical simulation of Fresnel diffraction of a phase screen was carried out using the Fresnel diffraction

algorithm described in [121]. The flow chart in Figure 84A summarises the algorithm. The algorithm first breaks down the propagating distance into small equidistant segments. This is needed due to limited sampling resolution of a numerical representation of the free-space impulse response. A circular beam is used to simulate a finite extent of a laser beam in a 768x768 pixel array. The path length is set to 3.5 meters. Positioned in the middle is a binary phase hologram consisting of a continuous phase screen tilted with a linear phase shift in the (x, y) = (1,1) direction. These settings are used to simulate the phase screen model of optical turbulence using 40 separate instances of the phase screen. A square aperture 100x100 pixel in extent is used to extract only the first order. Figure 84B compares the intensity distribution of the propagated beam for a continuous and tilted binary phase screen. These show good agreement between the two within the area occupied by the first diffraction order.

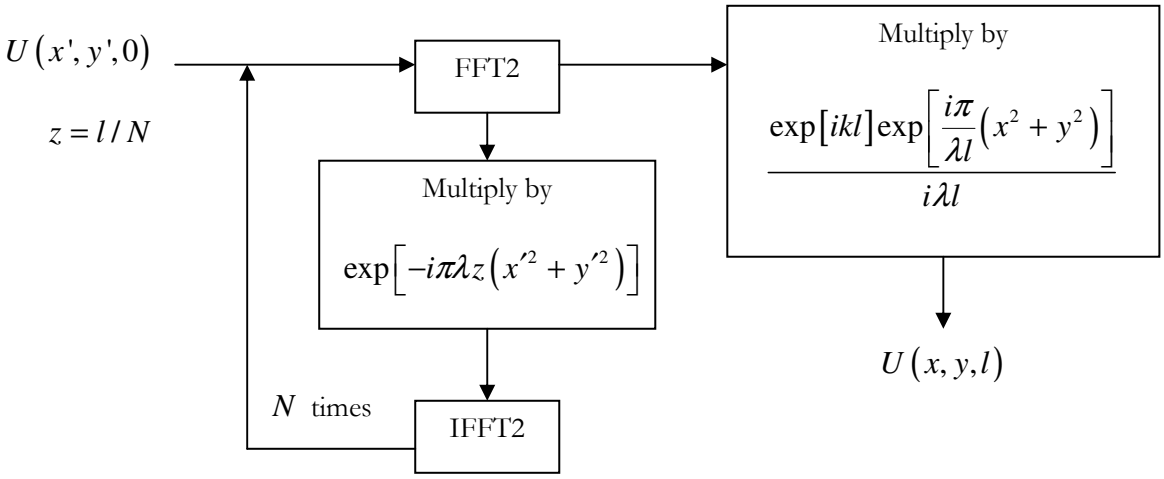

(A)

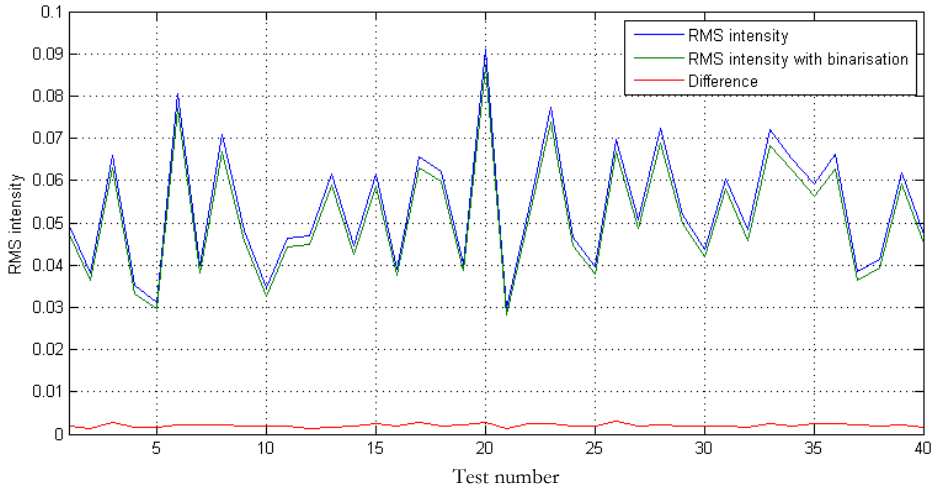

(B)

Figure 84. (A) Fresnel diffraction algorithm. (B) Measured intensity of Fresnel diffracted beam with phase screen, and RMS difference between tilted binary and continuous phase only hologram.

4.3 Optical turbulence simulator

In previous sections, a theoretical review of optical propagation through random medium leads to the development of a phase screen channel model. An MPI phase screen generation algorithm is then compared with Zernike method, giving a good phase screen distribution compared to theoretical results. An optical turbulence simulator (OTS) can now be implemented.

The OTS consists of the optical system in Figure 85. An expanded HeNe laser emitting 10mW was used for the source. A reflective SLM (SLM A) is placed in the beam path, and is used for beam steering and wavefront correction. The SLM can be considered as a mirror for the remainder of this section. The beam is then focused and collimated with two positive lenses, reducing the beam size by 10 times. The output beam can then be closely approximated by a Gaussian shaped beam described in section 4.1.5. The choice of these lenses is critical for obtaining a small collimated beam. The beam propagates a distance L_1 to a second reflective SLM (SLM B) that is used to display the phase screen calculated with MPI algorithm. The beam is then reflected to a detector placed at a distance L_2 from the phase screen. The total path length is $L_1 + L_2 = L$. The system is tilted off-axis with a small tilt angle to save space. This is assumed to have a negligible effect on the system.

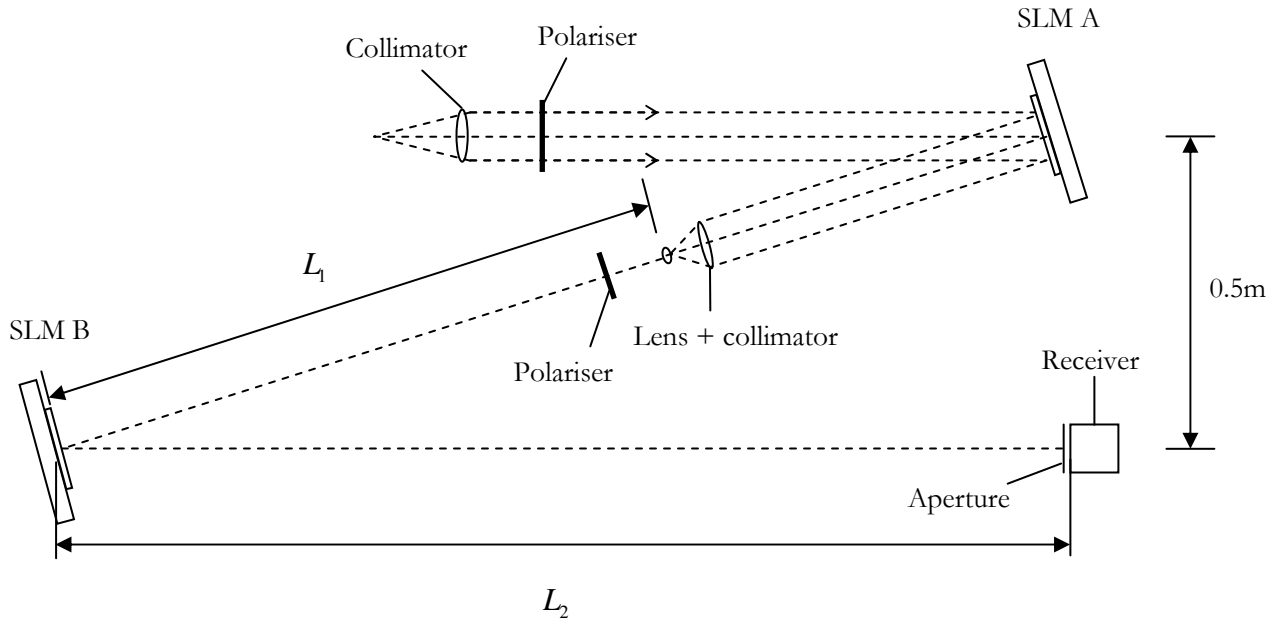

Figure 85. Optical set up for the optical turbulence simulator with a Kolmogorov phase screen on SLM B.

A Zemax simulation of a number of optical configurations were carried out. The optical configuration similar to the retro-reflecting base station in Chapter 2 was reproduced. The collimated beam radius was estimated by using the calculated beam radius at a plane 0.1m from the lens aperture. The distances between the elements were then optimised against spot radius at a distance of 50m. The optical elements consisted of an LA1142 25.4mm diameter positive lens with focal length of 60mm. The focused beam was then collimated with a Comar 03 0L 07 microscope objective. They were mounted co-axially with an SM1 lens tube system. The distance between the two elements was adjusted manually to achieve a collimated beam output, giving a beam radius measuring 1mm.

Using the thin phase screen model, the distance of the phase screen relative to the total path distance is a function of the Gaussian beam parameter [74]:

$$\frac{L-L_1}{L} = 0.67 - 0.17\left[\frac{1}{1+\Lambda_0^{\,2}}\right] \tag{4.3.1}$$

Where L_1 is the distance between the transmitter and the phase screen, and $\Lambda_0 = 2L/kW_0^{\,2}$ is the Gaussian beam diffractive parameter. Fixing L to 3.8m, and the beam diffractive parameter Λ_0 = 0.774, the necessary values for L_1 and L_2 are 1.65m and 2.15m respectively. Using equation (4.1.45), the $\sigma_I^{\,2}/\sigma_R^{\,2}$ ratio for this point was calculated to be to 0.33.

Both SLMs were controlled with a computer. The software and hardware components are shown in Figure 86. SLM A is a 4th Dimension Display FLC panel used in previous systems. SLM B is a vertical aligned nematic liquid crystal display from Cambridge Correlators, operating as a binary phase modulator. The device was masked to a square format, with dimension of 7.5mmx7.5mm at 768×768 pixels. The pixel dimension is 9.7μm×9.7μm.

The OTS system alignment was made by initially aligning the 0th order beam such that the elements are co-axial on the optical axis. A DC balanced hologram was used to generate a 1st order beam, with an angular deviation of 0.0125 radians. SLM B was then readjusted to coincide with the first order beam, and its angle adjusted to steer the reflected beam to the receiver. A phase screen was generated using the MPI algorithm and binarised as described in Section 4.2.3. This resulted in the first order beam that is 20mm away from the optical axis.

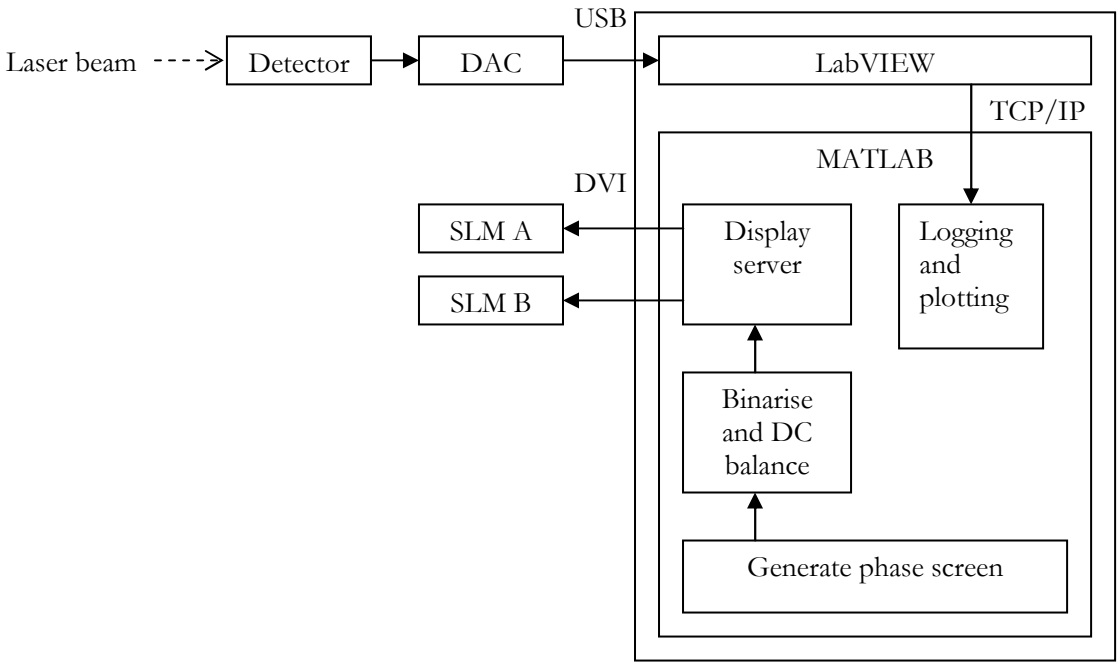

Figure 86. Computing platform for the turbulence simulator.

4.3.1 Detectors

Two different receivers were used to measure the on-axis beam intensity at the receiver. The first was a silicon photodiode detector with a 0.8 mm² active area (DET10A manufactured by Thorlabs). The output was fed to a lowpass DC amplifier with bandwidth of 1 kHz. The voltage output from the amplifier was then digitised by National Instruments USB-6008 USB ADC. The device communicated with the work station using a custom Labview application, which passed the DC value measured to MALAB via an internal TCP socket.

The photodiode operated in reverse bias with a bias voltage of 12V. The peak DC voltage detected was 0.3V using a 10kΩ load resister. High load resistance reduced the detector bandwidth to within 1kHz. The amplifier has a DC gain of approximately -100.

A calibration of the amplified output voltage to optical power was used to correct for the voltage response of the photodiode. Measurements were made using variable power optical source, comparing the output from an optical power meter and the voltage output from the photodiode. Figure 87 shows a plot of the readings with linear and cubic fitting.

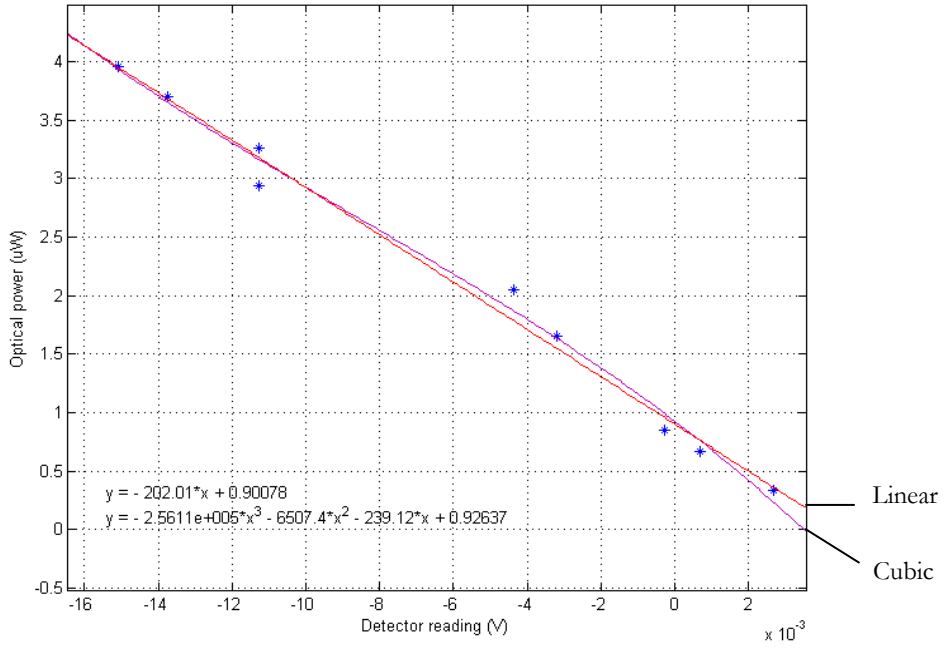

Figure 87. Photodetector output voltage measured against optical power output. Linear and cubit fits are shown.

A Canon EOS 20D digital SLR camera forms a second detector type to simulate a large aperture photodetector. The camera was used with a Tamron 90mm f/2.8 lens, with a lens diameter of 50mm. To avoid saturating the camera sensor, two polarisers were placed in the beam path in a cross polarisation configuration. The camera was calibrated to give a linear intensity response by setting the camera to a linear contrast setting. An USB connection connected the camera to the work station, using the gphoto2 library, controlled within MATLAB. A routine was written to control the camera shutter and data transfer. Only the red pixel values were used, so the camera behaves effectively as an 8bit CMOS sensor. The image pixels are then integrated to obtain pixel values corresponding to the total received intensity.

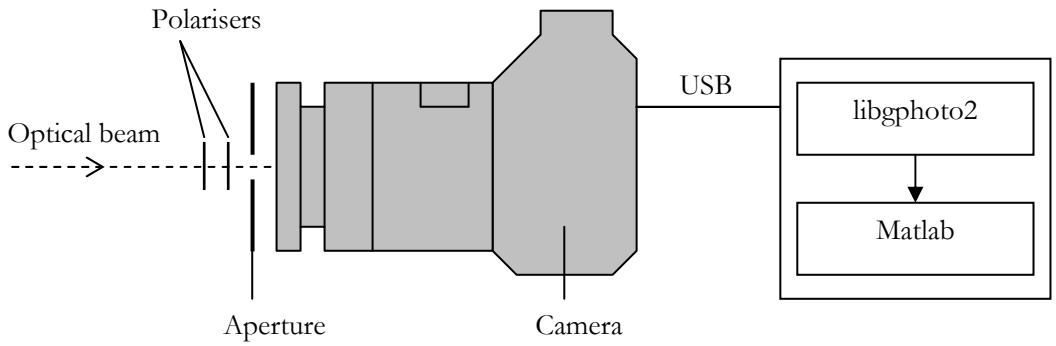

Figure 88. Camera and software for automatic camera shutter activation

For both configurations, an adjustable aperture is placed in the optical axis in front of the detector, ranging from 0.5mm to 15mm. The pin hole was placed in the centre of the 1st order, simulating an on-axis detector configuration. The aperture averaging effect could be measured by varying the diameter of this aperture.

4.4 Turbulence simulation results

The accuracy of the OTS is then tested against theoretical prediction at different turbulence conditions. Later, the receiver apertures are then increased to verify the theoretical calculation for the aperture averaging effect.

The MPI algorithm is used to generate increasing strengths of the Kolmogorov phase screen. The Rytov variances and predicted scintillation indices for a point detector are calculated from equation (4.2.3). The strength of the turbulence is normalised to D/r_0 , where D is the width of the SLM B in Figure 85 and $r_0 = \left(0.16 C_n^2 k^2 L\right)^{-3/5}$ is Fried's parameter. The numerical results are tabulated in Table 12. By using the Gaussian beam parameter Λ_0 = 0.744 and propagating distance of 3.8m, the scintillation index to Rytov variance ratio for this system is $\sigma_I^2 / \sigma_R^2 = 0.330$.

D/r_0	0.5	1.0	1.5	2.0	2.5	3.0	3.5	4.0
C_n^2 (10^{-13})	0.0062	0.0198	0.0390	0.0629	0.0913	0.1237	0.1599	0.1998
σ_R^2 (Rytov Variance)	0.0349	0.1108	0.2177	0.3516	0.5100	0.6912	0.8936	1.1164
σ_I^2 (Scintillation index)	0.0115	0.0365	0.0718	0.1160	0.1683	0.2281	0.2949	0.3684

Table 12. Numerical values of phase structure constant, Rytov variance, and expected scintillation index for a point detector.

The simulated path distance and beam waist radius can be applied to longer propagating distances by using the definition of Λ_0 in equation (4.1.34). The applicable beam waist radius and transmission distance curve is plotted in Figure 89. As an example, the OTS configuration simulates a collimated beam waist radius of 1.75cm, propagating a total distance of 1000m.

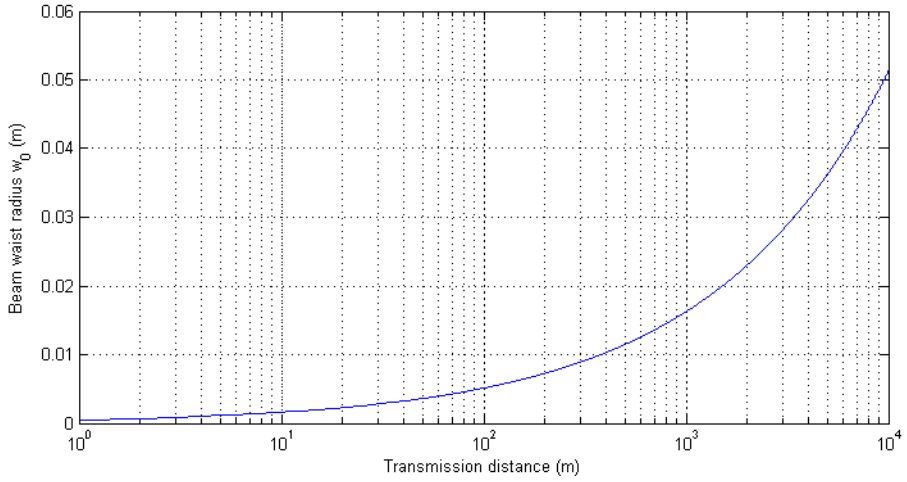

Figure 89. Simulated beam radius as a function of transmission distance corresponding to Λ_0 = 0.744

The statistical measurements are carried out using ensemble mean and variance. The expected intensity for a particular D/r_0 value is calculated using:

$$\langle I \rangle = \frac{\sum_N I_j}{N} \tag{4.4.1}$$

where I_j is the intensity measurement for a phase screen, and N is the total number of phase screens used. The scintillation index is calculated from the unbiased population variance estimate:

$$\sigma_I^2 = \frac{\sum_N \left(I_j - \langle I \rangle\right)^2}{(N-1)\langle I \rangle^2} \tag{4.4.2}$$

The accuracy of the OTS can be estimated by calculating the σ_I^2 / σ_R^2 ratio from the measured scintillation index. By considering the σ_R^2 as a function of D/r_0 for this particular beam waist and propagating distance:

$$\sigma_R^2 = 9.03\left(D/r_0\right)^{5/3} \tag{4.4.3}$$

The σ_I^2 / σ_R^2 ratio is estimated using:

$$\frac{\sigma_I^2}{\sigma_R^2} = 9.03w \tag{4.4.4}$$

where w is the constant of proportionality for a fitted 5/3 power curve of σ_I^2 to D/r_0.

4.4.1 Results for point detector

The theoretical pinhole detector can be closely approximated by choosing the detector aperture diameter to be smaller than the first Fresnel zone of the optical system [79]. The first Fresnel zone size D_p is calculated using the expression:

$$D_p = \sqrt{\frac{L}{k}} \tag{4.4.5}$$

Figure 90 shows a plot of receiver aperture diameter versus the transmission distance that applies to this condition. For propagating distance of 3.8m, the required diameter is 0.64mm or smaller. An aperture diameter of 0.5mm diameter is used to satisfy this requirement. Both the silicon photodiode and the camera are used to compare the measurement results from the two detectors.

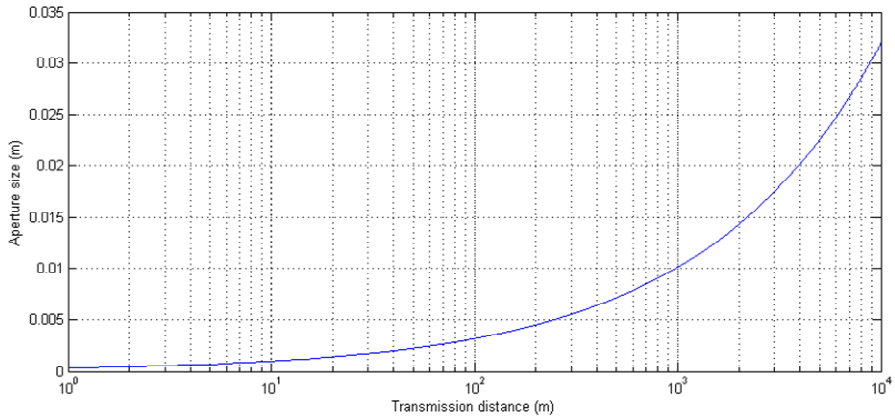

Figure 90. Aperture size corresponding to first Fresnel zone as a function of propagating distance

The scintillation index measurement for the silicon photodetector with 0.5mm diameter aperture is shown in Figure 91A. 500 phase screens were used per data point. The plot is fitted with a 5/3 power curve by using the least square fit. The theoretical prediction from Table 12 is also plotted for comparison. Using the fitted curve, the σ_I^2 / σ_R^2 ratio is then measured to be 0.364. The predicted value of σ_I^2 / σ_R^2 is 0.330, giving a difference of 10%.

The measured mean intensity is plotted with predicted values in Figure 91B. The predicted mean intensity is calculated using equation (4.1.38). It can be seen that the measured and calculated results are in good agreement.

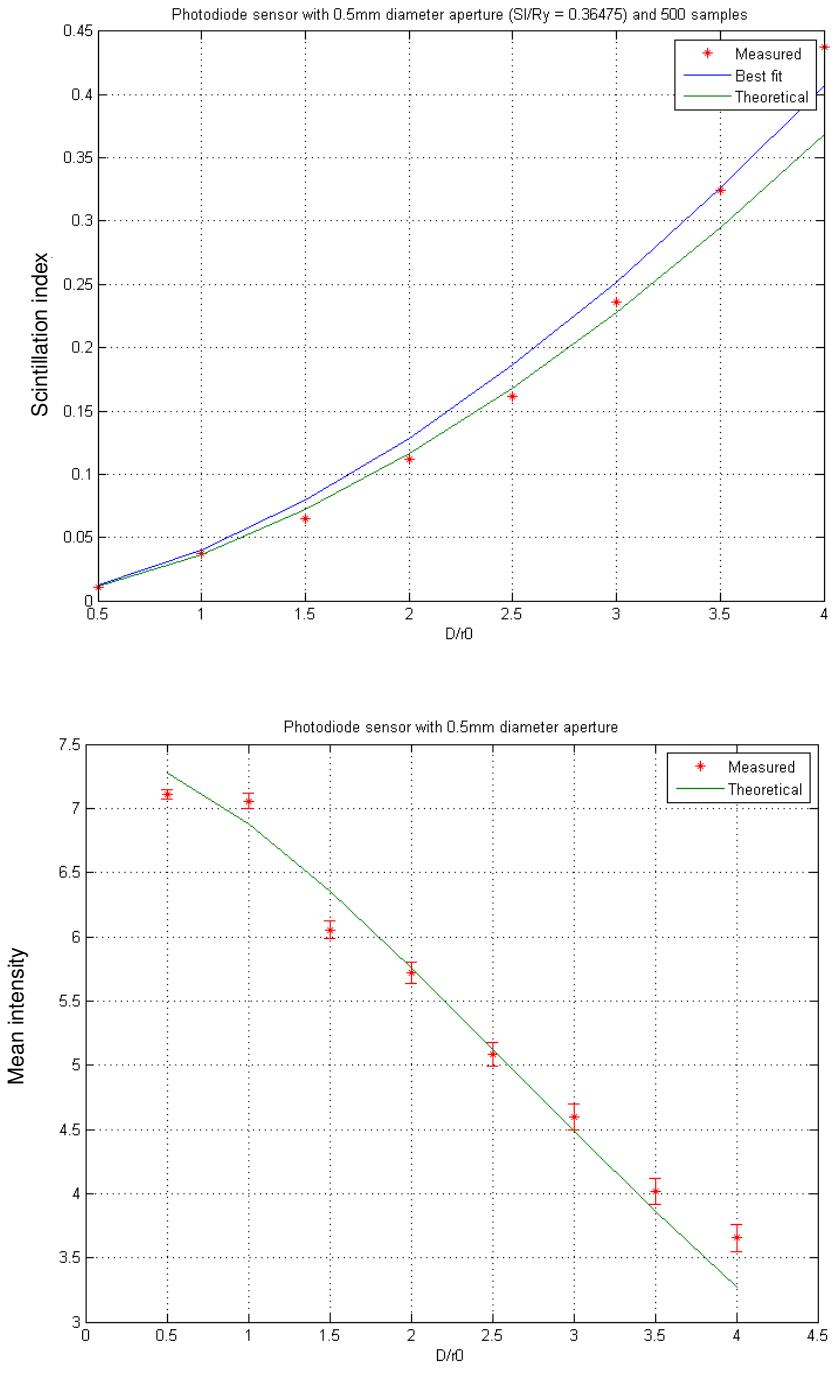

Figure 91. Results of the OTS using 0.5mm diameter aperture and with the photodiode detector

(A) Plot of the measured scintillation versus D/r_0, corresponding to scintillation index result for a point detector. Data is fitted with (5/3) power curve.
(B) Plot of the measured mean detected intensity versus D/r_0 and theoretical prediction. The error bar shows one sample standard deviation.

The OTS was then tested using the same 0.5mm aperture diameter, but with a camera as the photodetector. 120 phase screens were used per data point. Figure 92A shows the measured scintillation index fitted with a 5/3 power curve . The measured scintillation index produces a σ_I^2 / σ_R^2 ratio of 0.334, while the theoretical value is 0.330, giving a difference of 1.2%.

The mean intensity is then plotted in Figure 92B. The results from the camera produces a shallower slope than predicted using equation (4.1.38), although it is within reasonable bounds of experimental error due to fewer number of phase screens. Again, the measured result shows good fit to theoretical prediction.

These results clearly show that the OTS can accurately produce the same statistics as predicted by the weak turbulence theory. Both silicon detector and the camera produce similar scintillation index results, as well as the mean intensity. Measurements for aperture averaging can now be made using a detector that accommodates the larger aperture diameter.

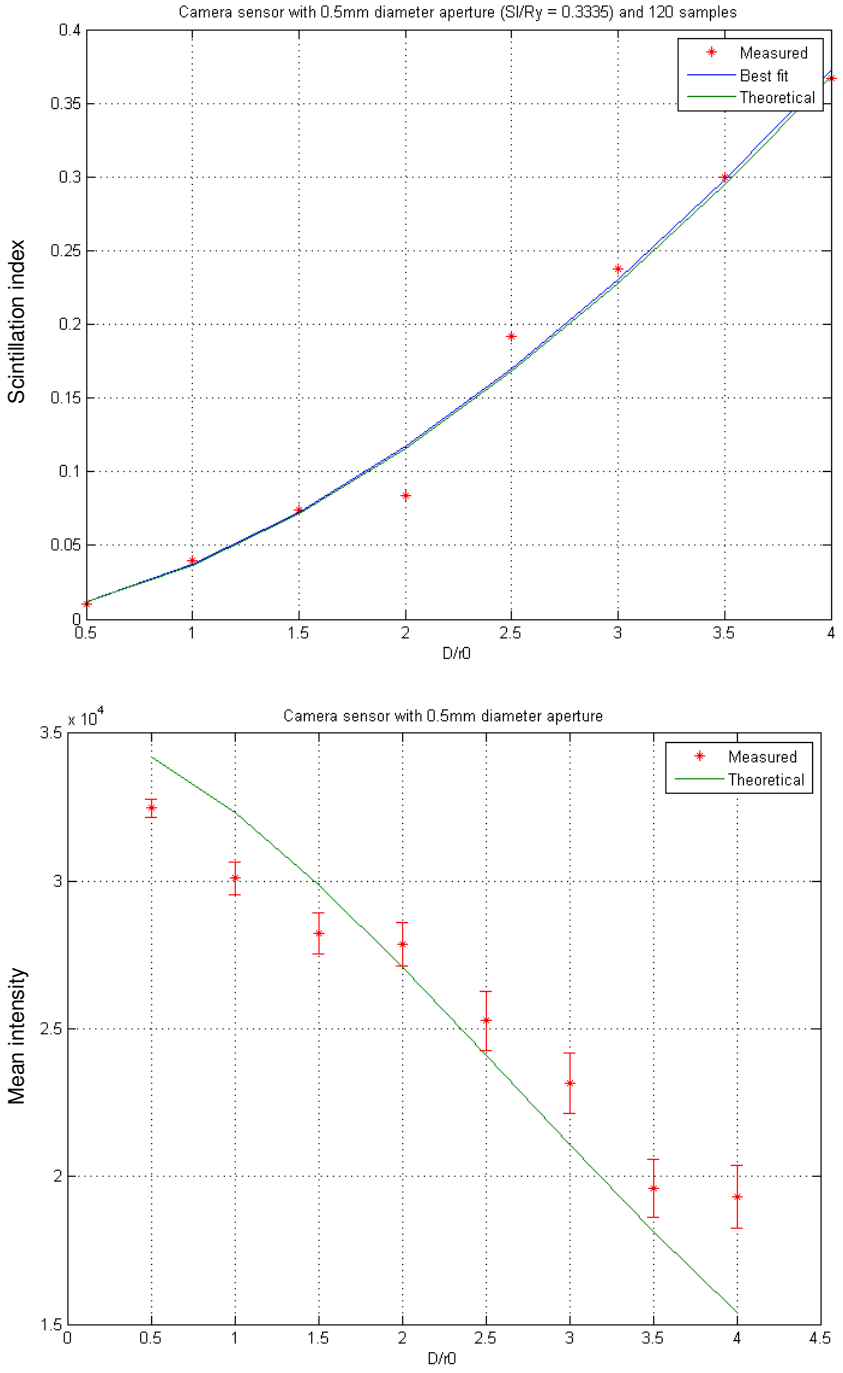

Figure 92. Results of the OTS using 0.5mm diameter aperture and with the camera detector

(A) Plot of the measured scintillation versus D/r_0, corresponding to scintillation index result for a point detector. Data is fitted with (5/3) power curve.

(B) Plot of the measured mean detected intensity versus D/r_0 and theoretical prediction. The error bar shows one sample standard deviation.

4.4.2 Results for aperture averaged detector

The effect of aperture averaging is to reduce the scintillation index, as described in Section 4.1.5. The aperture averaging factor A can be predicted using the circular symmetric covariance function of intensity (Appendix C) and equation (4.1.45). Two aperture sizes of 0.8mm and 2mm were used with the OTS, and compared to the theoretical prediction. Plots in Figure 93A and B show the aperture size versus the transmission distance associated with these apertures.

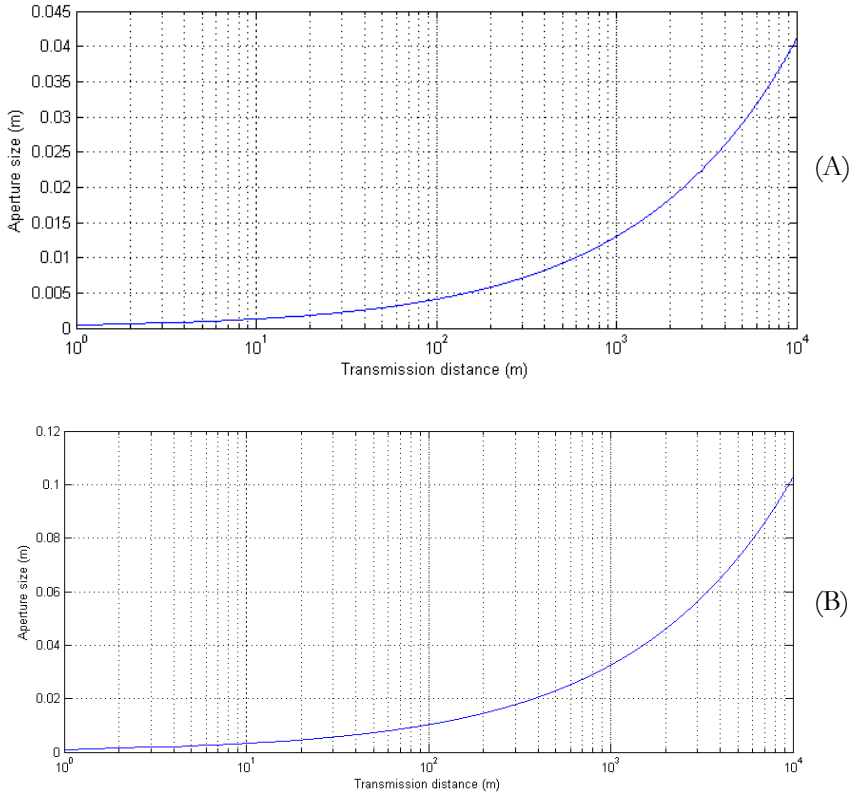

Figure 93. Aperture size as a function of propagating distance
(A) 0.8mm diameter aperture (B) 2mm diameter.

For the case of 0.8mm aperture diameter, the silicon detector was used. The scintillation index is plotted in Figure 94A and fitted with a 5/3 power curve. The measured σ_I^2 / σ_R^2 ratio found to be 0.2126, giving the measured aperture averaging value A of 0.6442. The theoretical value of A was calculated to obtain the value of 0.656. The predicted σ_I^2 / σ_R^2 is therefore 0.2163, corresponding to 3% difference to the measured results. The mean intensity is plotted in Figure 94B.

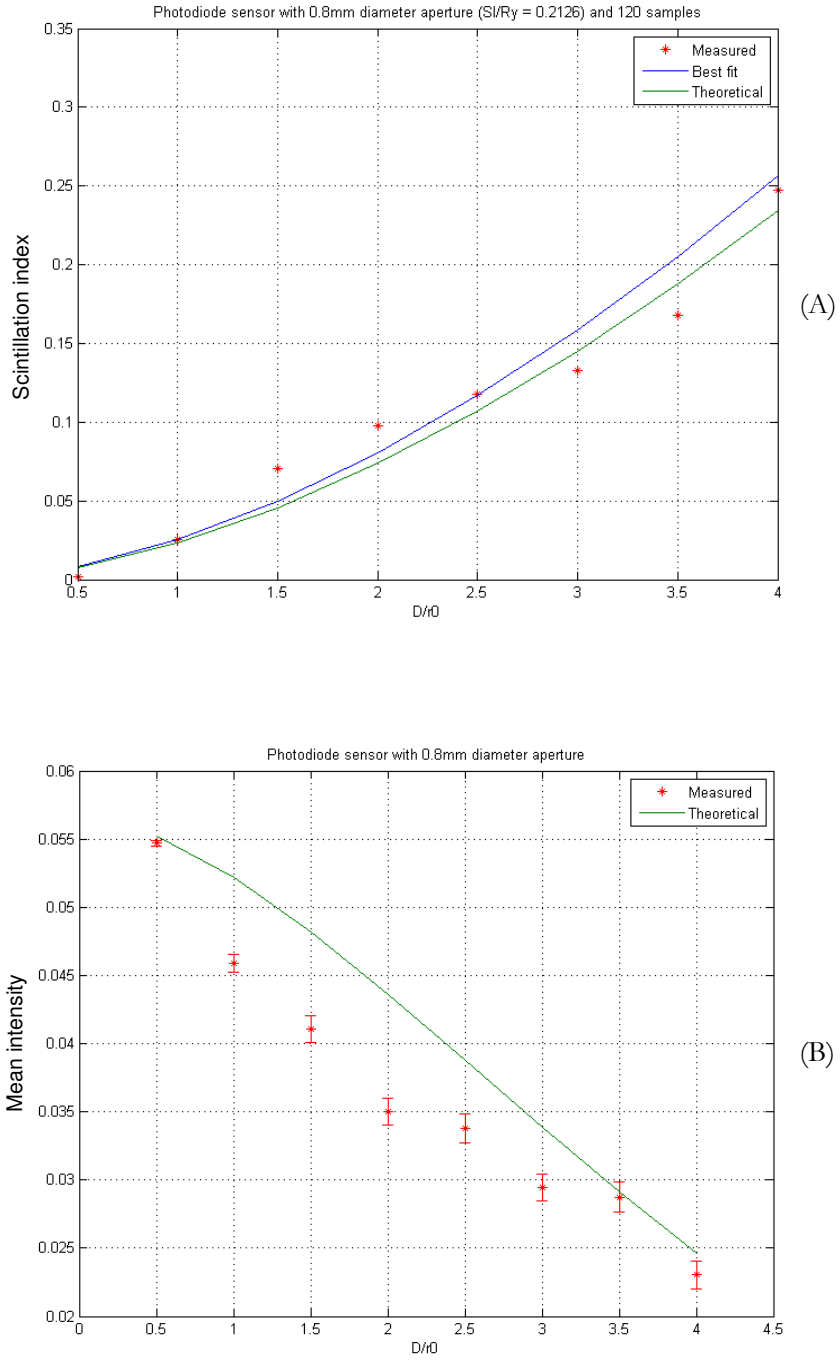

Figure 94. Results of the OTS using 0.8mm diameter aperture and with the photodiode detector

(A) Plot of the measured scintillation versus D/r_0, corresponding to scintillation index result for a point detector. Data is fitted with (5/3) power curve. Aperture factor A is 0.656.
(B) Plot of the measured mean detected intensity versus D/r_0 and theoretical prediction. The error bar shows one sample standard deviation.

For the case of 2mm aperture diameter, the silicon detector was unable to accommodate the whole of the aperture. Instead, the camera was used for the intensity measurements. Figure 95A plots the measured scintillation index, showing the σ_I^2 / σ_R^2 ratio to be 0.0136. The measured value of A is therefore 0.041. The theoretical value of the aperture averaging factor A is 0.136 in this case, giving the predicted σ_I^2 / σ_R^2 ratio of 0.045. The difference between these two is 230%.

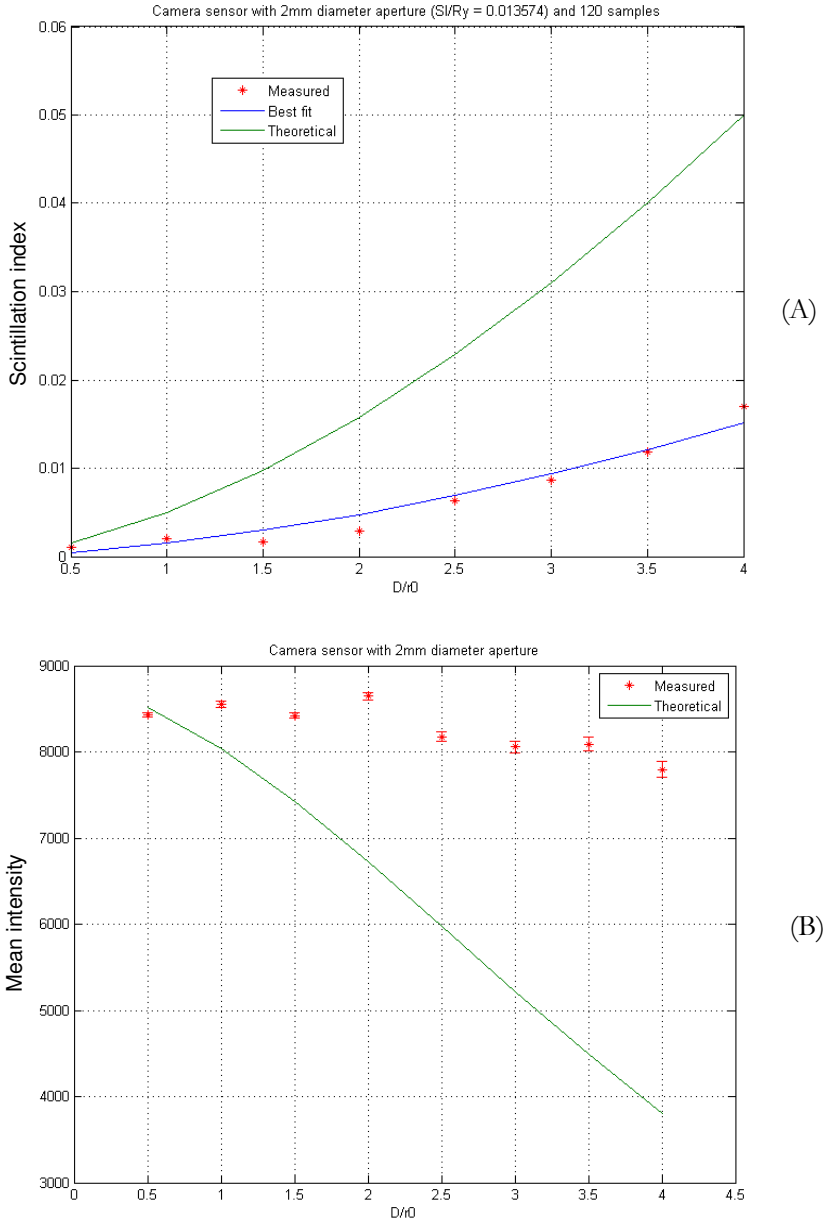

Figure 95. Results of the OTS using 2mm diameter aperture and with the camera detector

(A) Plot of the measured scintillation versus D/r_0, corresponding to scintillation index result for a point detector. Data is fitted with (5/3) power curve. Aperture factor A is 0.136.
(B) Plot of the measured mean detected intensity versus D/r_0 and theoretical prediction. The error bar shows one sample standard deviation.

For the 2mm aperture diameter, it is clear from Figure 95 A and B that the theoretical results do not fit with the scintillation and mean intensity measurements. The measured scintillation index is significantly lower than predicted, while the measured mean intensity is significantly higher. Previous extended medium measurements under real atmospheric conditions have found the theoretical results to agree well with measurement data [122], suggesting that the turbulence simulator cannot be used for large apertures. A likely cause is the finite pixel size of the phase screen, which limits the inner scale l_0 that can be represented. Since small scale structures affect the large scale beam properties, Andrews showed that this can affect the aperture averaging effects [79]. Further aperture averaging measurements were therefore limited to a 0.8mm aperture diameter.

The OTS has been shown to provide an accurate physical simulation of the turbulent conditions. The scintillation index and mean intensity results match well with the theoretical predictions, provided the aperture size is small. Binarisation of the phase screen did not pose a problem with the intensity measurements. The OTS can now be used to develop a novel adaptive optics system designed to reduce the effect of turbulence in the next chapter.

4.5 Wavefront sensor-less adaptive optics

Aperture averaging has been shown to reduce scintillation index significantly. Recently, in addition to aperture averaging, there has been a large interest in using adaptive optics to compensate the phase fluctuations caused by the atmosphere. An adaptive optics (AO) system consists of a wave front detector, a phase compensation device (normally an SLM), and a controller that feeds detected wavefront distortion back to a phase modulator (phase conjugation). Most AO systems are designed to reduce scintillation associated with imaging, for example, phase correction at the receiver aperture to enhance focal plane contrast. In a communication system, the desired AO property is to concentrate optical power within a receiver aperture, and this must be done at the transmitter (Figure 96). By doing so, it is possible to further reduce the scintillation index using multiple transmission beams due to mutually independent paths, and this will be discussed in Section 4.6. A key problem with any AO system is how to measure the phase disturbance at the receiver, while phase is conjugated at the transmitter. The problem can be separated into two parts.

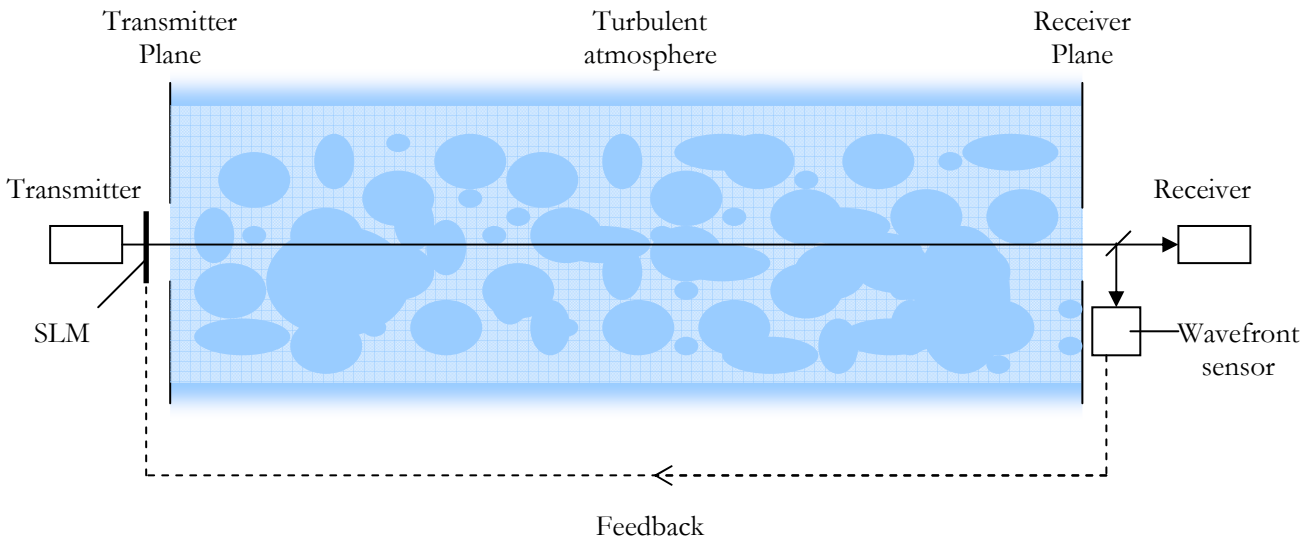

Figure 96. A diagram of a typical AO system with feedback loop

The first is the phase measurement feedback from the receiver to the transmitter. If a channel is severely compromised by fading, it is not possible to send a reliable, high data rate optical signal back to

the transmitter. By keeping the bit rate needed for the feedback loop low, this problem might be alleviated by using a slow and heavily error corrected optical signal.

The second is the limitation of the wavefront phase measurements inside the receiver aperture. At a high scintillation index, the beam is likely to be considerably larger than the receiver aperture; therefore the sensor can not sample the whole extent of the beam. Also, any practical implementation of the sensor has noise and maximum temporal bandwidth that can limit the accuracy of the phase measurements.

A proposed AO system with no wavefront sensor is described in this section. The system uses a sensorless method to estimate Zernike modes present in the random medium. Zernike modes are efficient for interpolating a phase distribution, and only a small number of modes are needed. The method also optimises the whole beam, which could result in larger reduction in scintillation. Using the OTS described in previous section, the system performance is measured in terms of scintillation index reduction, and the mean received intensity. A Bit Error Rate estimation of the channel is then carried out.

4.5.1 Wavefront sensor-less Zernike modes estimation

Up to now, the time dependent component of the phase fluctuation has been assumed to be discretised into separate and discrete manifestations. A continuous time dependent evolution of a phase fluctuation can cause frequency spreading around the carrier frequency. However, this is usually applicable only to acoustic and low frequency radio waves [73][123]. For optical frequencies and moderate turbulence, a quasi-static turbulence model can be used to approximate turbulence processes [124]. This method, or Taylor's frozen flow hypothesis [125], assumes turbulent flow to be virtually static within a specific time scale. The time scale is proportional to the perpendicular component of the bulk fluid's velocity, in this case the wind speed. During this period, the electric field amplitudes are strongly correlated temporally. A typical metric used for this period is Greenwood's time constant [126][127]:

$$\tau \approx \frac{0.53 r_0^{5/6} D^{1/6}}{V_{\perp}} \tag{4.5.1}$$

Where r_0 is Fried's parameter, D is the transmitter diameter and $V_\perp$ is the velocity component perpendicular to propagation path. Typical 1km daytime visible FSO links exhibit a correlation time of 1-2ms [128]. However this can deteriorate to 0.5ms in severe turbulence. An AO system needs to be designed so that phase measurements and compensations occur within this time.

Assuming that turbulence is static, the beam propagation from an AO system can be modelled as shown in Figure 97.

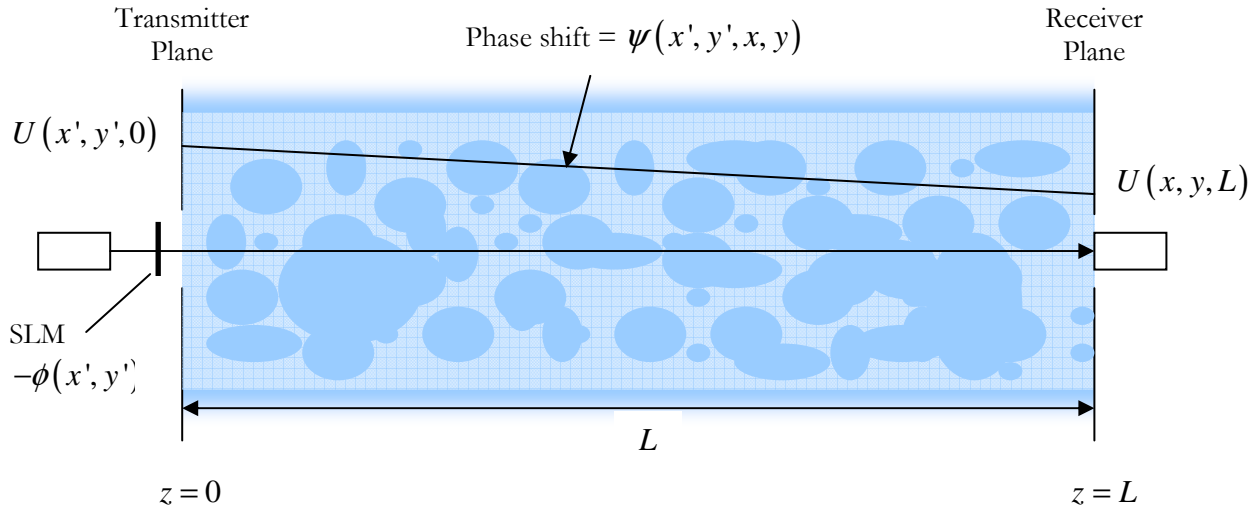

Figure 97. Channel model of wavefront sensorless AO system, with complex amplitudes and phase shifts

The complex field amplitude at the transmitter plane is represented as $U(x', y', 0)$ and at the receiver plane $U(x, y, L)$. The random medium is considered to be static, and therefore it is possible to write a deterministic expression for phase shift as $\psi(x', y', x, y)$. In effect, this function produces phase shifts for a straight line between two points in the transmitter and receiver planes. The SLM modulates the transmitted beam with a spatial phase distribution $-\phi(x', y')$. Assuming that the beam width is much smaller than L, and initially setting $\phi(x', y')$ to zero, the complex amplitudes can be related using the Fresnel diffraction integral (neglecting a constant phase term):

$$U(x, y, L) = \iint U(x', y', 0) \exp\left[i\psi(x', y', x, y)\right] \exp\left[\frac{ik}{2L}\left((x - x')^2 + (y - y')^2\right)\right] dx' dy' \tag{4.5.2}$$

The phase fluctuation term ψ modulates waves traversing a particular straight-line with a phase shift. To reduce the multiplicity of paths available, if a pinhole is placed in front of the receiver only waves that converge to the aperture contribute to the amplitude calculation. The expression then reduces to:

$$U(0,0,L) = \iint U(x',y',0)\exp\left[i\psi(x',y')\right]\exp\left[\frac{ik}{2L}\left(x'^2+y'^2\right)\right]dx'dy' \quad (4.5.3)$$

The transmitted amplitude for a Gaussian beam can be closely approximated using a uniform circular beam radius r_0 and constant amplitude A. With transformation to cylindrical coordinates, the receiver intensity becomes:

$$I = A^2\left|\int_0^{2\pi}\int_0^{r_0}\exp\left[i\psi(r,\theta)\right]\exp\left[\frac{ikr^2}{2L}\right]rdrd\theta\right|^2 \quad (4.5.4)$$

If the SLM phase distribution $-\phi(r,\theta)$ is non-zero, and normalising $r = r/r_0$, the expression becomes:

$$I = A'^2\left|\int_0^{2\pi}\int_0^{1}\exp\left[i\psi'(r,\theta)+i\alpha r^2-i\phi'(r,\theta)\right]rdrd\theta\right|^2 \quad (4.5.5)$$

Where $\alpha = kr_0^{\,2}/2L \simeq \Lambda_0^{-1}$, ψ' and ϕ' are normalised phase distributions with respect to the beam width r_0. Since ψ' and ϕ' are phase only functions, they can be decomposed into orthogonal Zernike modes [129]. The Zernike decomposition of ψ' can be derived by considering the Zernike amplitude covariance given in equation (4.2.12). A spherical wave requires a solution to:

$$\left\langle a_j a_k \right\rangle = \left.\begin{aligned}&\frac{0.0144\sqrt{(n_j+1)(n_k+1)}(-1)^{(n_j+n_k-2n_j)/2}}{\pi}\\ &\times\int_0^1\int k(k^{-11/3})\frac{J_{n_j+1}\left(2\pi k(1-\xi)\right)J_{n_k1}\left(2\pi k(1-\xi)\right)}{k^2(1-\xi)^2}dkd\xi\end{aligned}\right\} m_j = m_k$$
$$= 0 \qquad \text{otherwise} \quad (4.5.6)$$

The solution was found analytically to be a 3/8 factor different from the plane wave solution given by Wang [119] and Roddier [111] (Appendix D). The factor $i\alpha r^2$ can be identified as a Zernike defocus mode without piston. Incorporating this factor into ψ' reduces the expression to:

$$I = A'^2 \left| \int_0^{2\pi} \int_0^1 \exp\left[i\Psi(r,\theta) \right] r dr d\theta \right|^2 \tag{4.5.7}$$

Where the Ψ is the phase residual written as a summation of N Zernike modes:

$$\begin{aligned} \psi'(r,\theta) + \alpha r^2 &= \sum_{n=1}^{N} a_n Z_n(r,\theta) \\ \phi'(r,\theta) &= \sum_{n=1}^{N} b_n Z_n(r,\theta) \\ \Psi(r,\theta) &= \sum_{n=1}^{N} c_n Z_n(r,\theta) = \sum_{n=1}^{N} (a_n - b_n) Z_n(r,\theta) \end{aligned} \tag{4.5.8}$$

Because Zernike polynomials are orthogonal, their amplitudes contribute to the intensity value independently. For a small phase difference, the intensity fall off is given as a function of Zernike amplitudes [129]:

$$I \approx A'^2 \left(1 - \sum_{n=1}^{N} {c_n}^2 \right) \tag{4.5.9}$$

Typically, random phase shifts in the medium causes the intensity to fall below an optimal value. For a mode c_m, adding a correction in ϕ' with positive and negative Zernike amplitude b, the intensity is given by:

$$\begin{aligned} I_{m+} &= A'^2 \left(1 - \sum_{n=1, n\neq m}^{N} {c_n}^2 + (c_m + b)^2 \right) \\ I_{m-} &= A'^2 \left(1 - \sum_{n=1, n\neq m}^{N} {c_n}^2 + (c_m - b)^2 \right) \end{aligned} \tag{4.5.10}$$

The Zernike mode can then be calculated using a quadratic fit to the intensity measurements [130]:

$$c_m = \frac{b(I_{m+} - I_{m-})}{2(I_{m+} - 2I_0 + I_{m-})} \tag{4.5.11}$$

Where I_0 is the intensity measurement without phase correction. The step size b varies with the expected Zernike amplitude given by equation (4.5.6). The flow chart in Figure 98 summarises the procedure. Zernike mode estimation uses three intensity measurements, I_0, I_+ and I_-, which are measured using a constant step size b. The test aberration step size is chosen to be larger than the aberration. For large aberrations, the measured intensity follows a Lorentzian like curve [130] and a

quadratic fit does not perform well. As an example, in Figure 99, two quadratic fits from small and large aberrations produces highly inaccurate fit. A conservative solution was found by choosing only estimates within the bound of two step sizes, as shown in Figure 98.

In contrast with spatially sampled devices such as the Shack-Hartmann wavefront sensor [131], samples are taken in the time domain. A simple point detector such as a fast photodiode can therefore be used for intensity measurements. The number of samples per second required for N modes is $(2N+1)/\tau$, where τ is Greenwood's time constant. If 10 modes are required, and τ = 1ms, the minimum sampling frequency is 21 kHz. Although the quadratic fit is not optimal when compared to the N-dimensional simplex described by Booth [132], which requires only $N+1$ measurements, it does not have to iteratively search for the optimal value of phase distortion and reduces the amount of information sent to the transmitter.

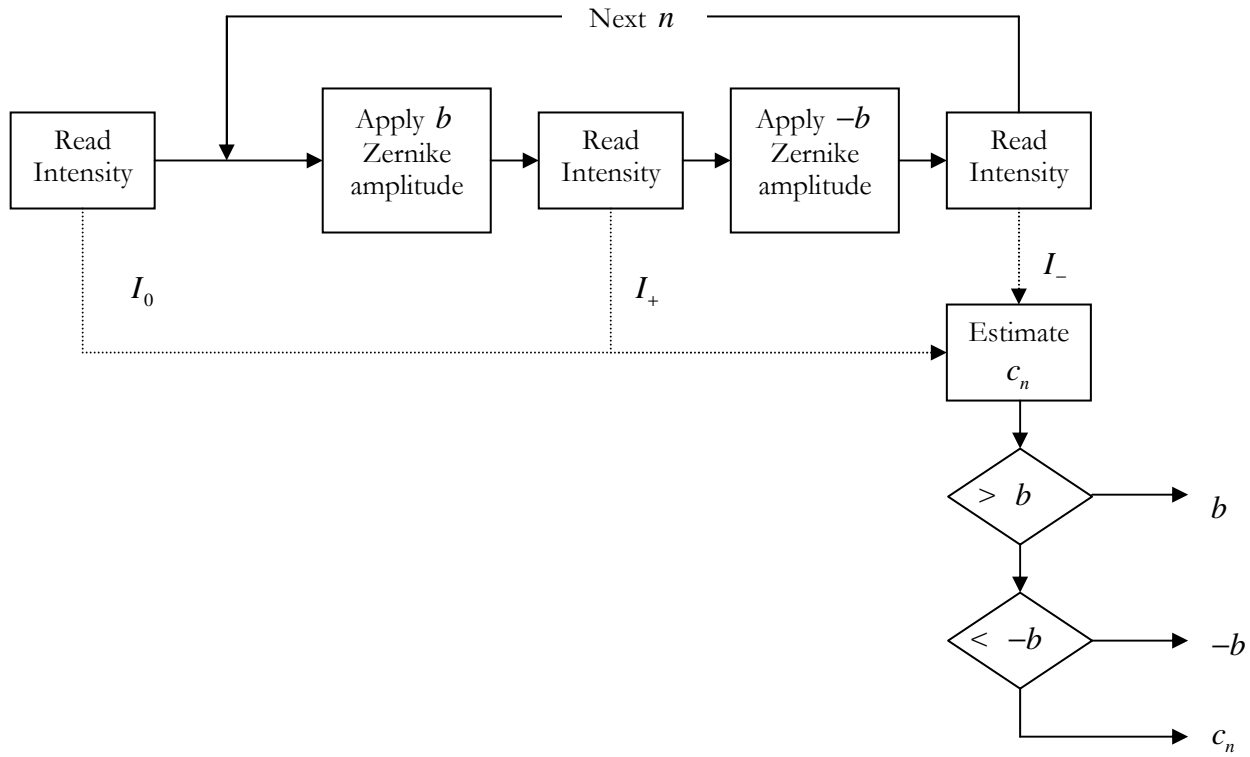

Figure 98. Flow chart of wavefront sensorless Zernike mode estimation.

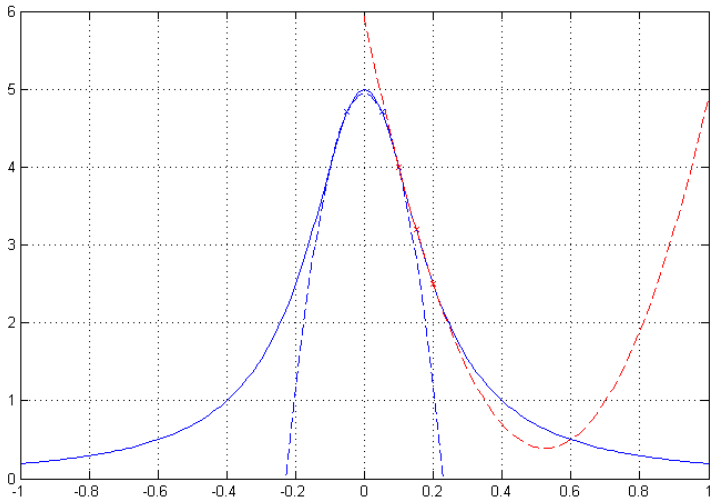

Figure 99. Lorentzian function and fitted quadratic from two sample points locations, showing possible fitting errors.

4.5.2 Optical system layout

Wavefront sensorless correction was implemented in the optical turbulence simulator (OTS) software controller described in the previous section. The flowchart in Figure 101 summarises the software controller. The system was initially tested against single Zernike distortions displayed on SLM B.

During testing of the optical system, it was discovered that a translational beam misalignment at the transmitter can severely disrupt the beam position at the detector. It was expected that due to far-field diffraction, the misalignment would not produce a difference. A computer simulation was carried out to investigate this effect. First, the on-axis diffracted beam intensity at the detector plane is shown in Figure 100, A1, B1 and C1 for the case of a tilted binary phase only hologram. With defocus and astigmatism applied, the intensity centroid remains in the same position. With the misaligned beam in Figure 100 A2, B2 and C2, however, the centroid is clearly translated in the direction of the misalignment. The translation is found to be proportional to Zernike amplitude and inversely proportional to the propagating distance. As distance increases to far-field Fraunhofer regime, the translation becomes negligible.

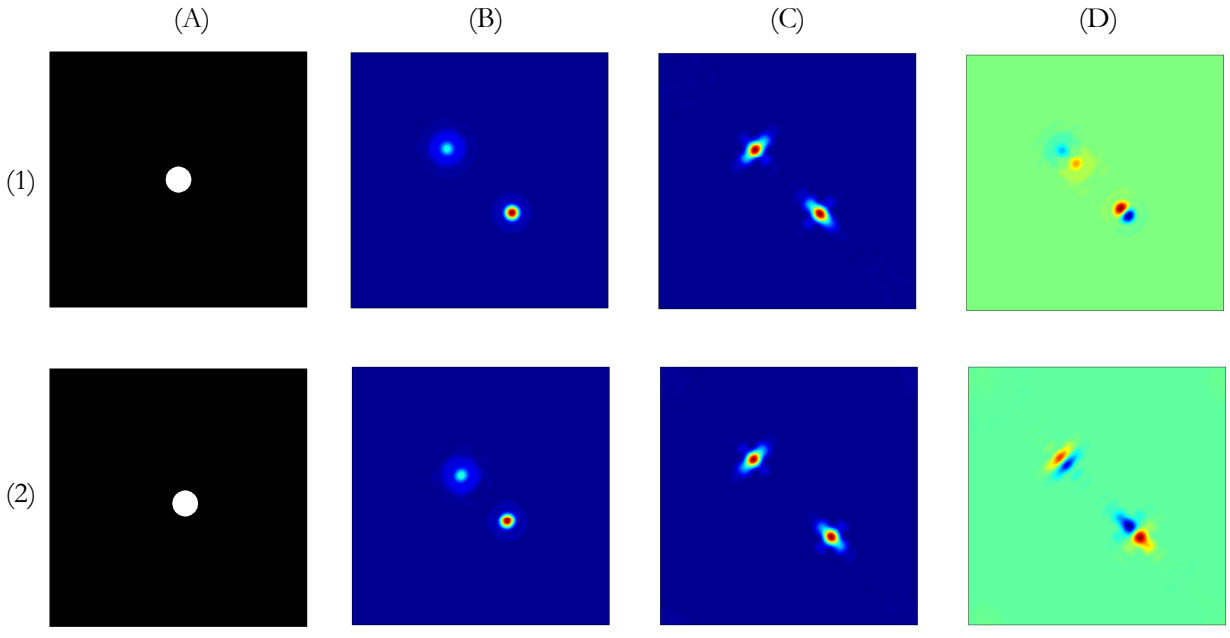

Figure 100. Computed Fresnel diffraction for (A1) on-axis and (A2) off-axis circular beam. Zernike modes applied: (B) defocus (C) astigmatism. Difference for (D1) defocus and (D2) astigmatism.

The optical layout was changed to Figure 102 by including a steerable mirror for fine beam adjustment on SLM B. Manual adjustment was carried out by applying alternating positive and negative Zernike modes on SLM B. The tilt mirror was adjusted to minimise translation at the receiver. For SLM A, spatially shifting the pixels in software was used to align the phase pattern to the beam axis.

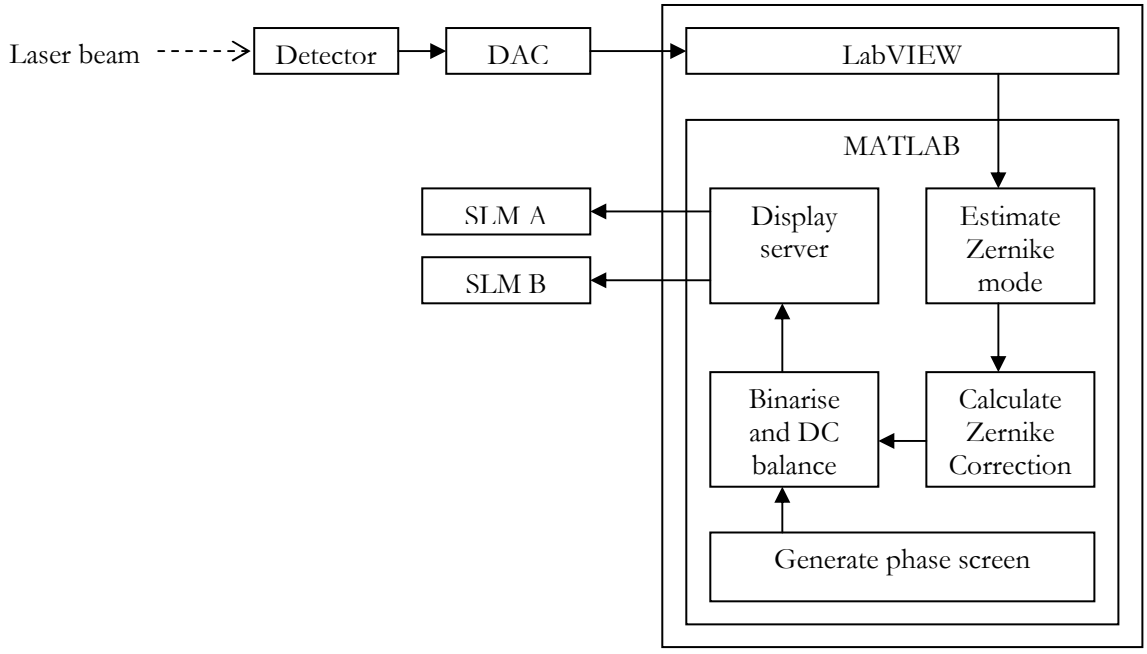

Figure 101. Software controller with wavefront sensorless Zernike estimation.

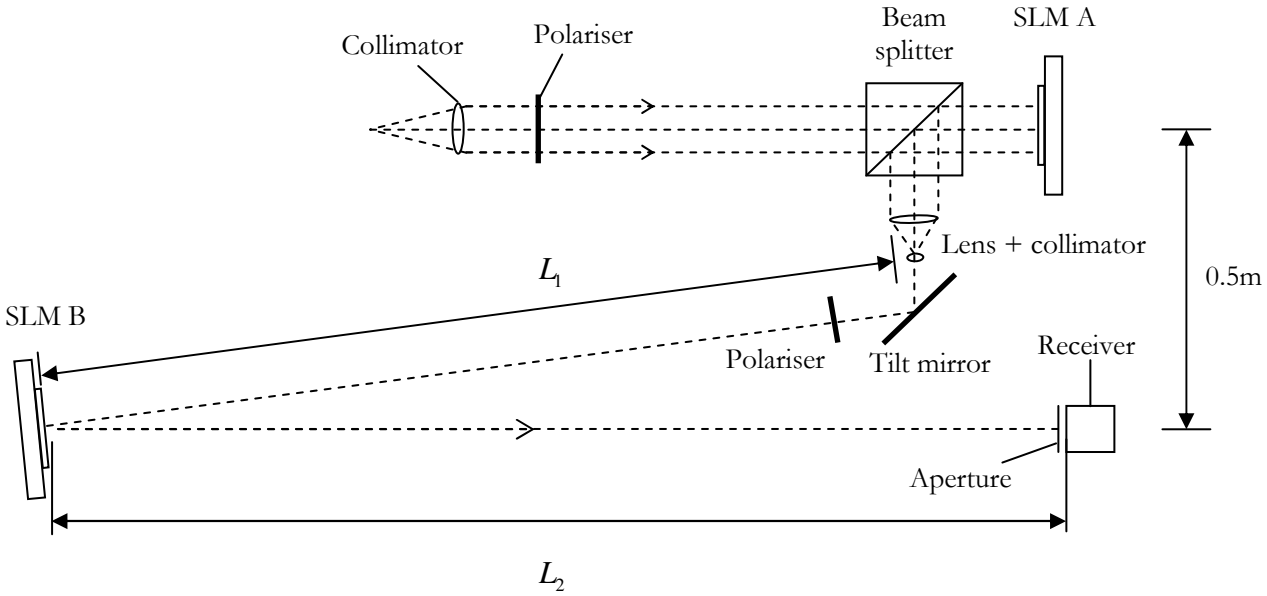

Figure 102. Optical layout of precision beam alignment system for SLM B.

The performance of Zernike correction was measured for modes from $j = 4$ (defocus) to $j = 9$ (coma). Tilt was excluded since the on-axis scintillation index does not improve with beam tracking [74]. Measurements of intensity fall off due to Zernike modes were recorded and plotted in Figure 103. The variation is clearly similar to a Lorentzian curve, with the width varying with the mode number.

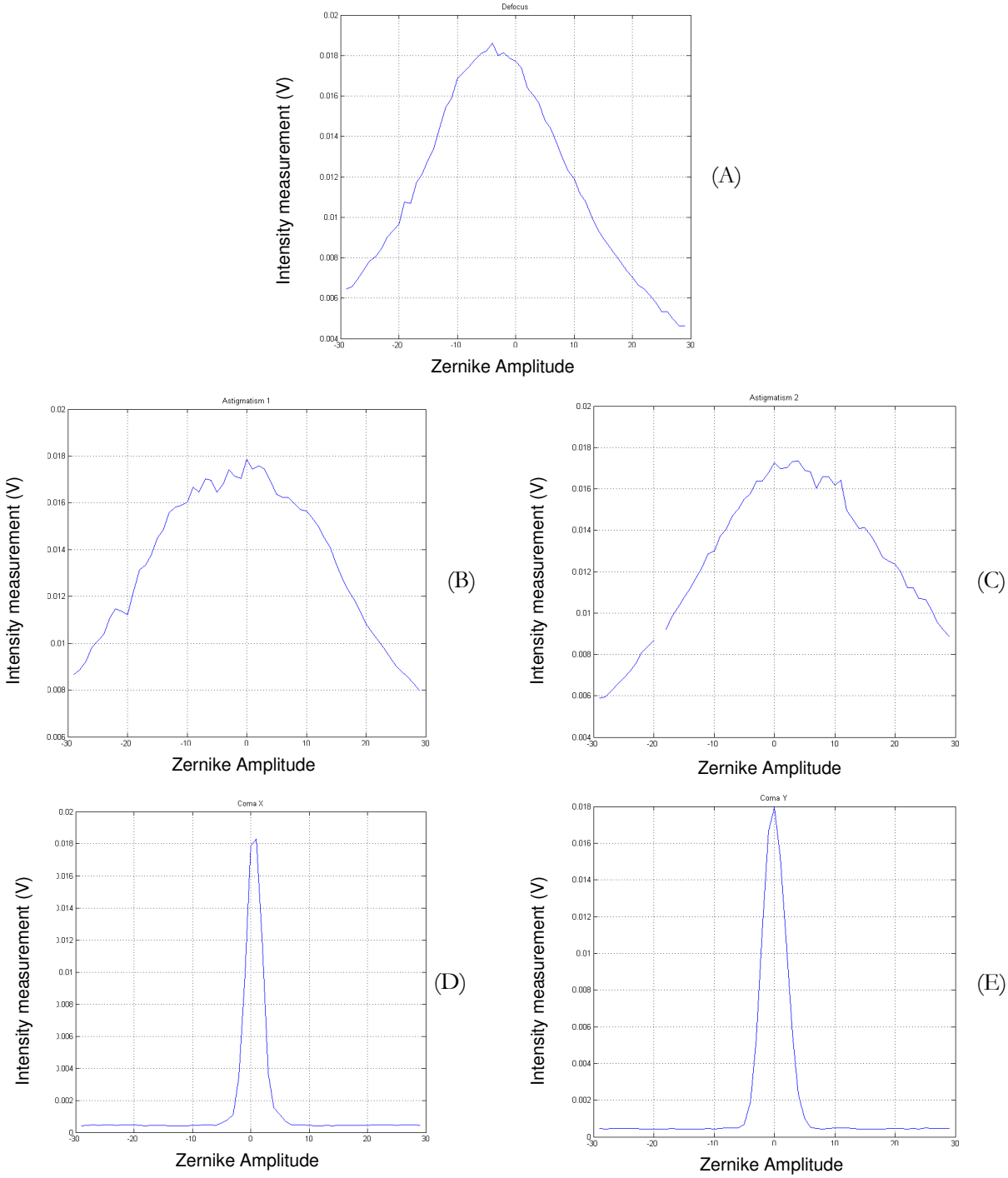

Figure 103. Intensity measurement as a function of Zernike amplitude for: (A) Defocus (B) Astigmatism 1 (C) Astigmatism 2 (D) Coma X-axis (E) Coma Y-axis

In order to assess the Zernike correction performance, a test using an individual Zernike mode correction was carried out. An individual Zernike mode from j = 4 (defocus) to j = 10 was displayed on to SLM B. The Zernike amplitude was normally distributed with a variance of 4. Wavefront sensorless correction was applied using the same Zernike mode on SLM A. Uncorrected and corrected intensities were then recorded along with estimated Zernike amplitudes. Zernike mode estimation performance and corrected intensity for the defocus mode are shown in Figure 104 A and B. The estimated amplitudes closely match the applied amplitudes in most cases. However, due to the large defocus term from free-space propagation only the negative correction is effective. Results for astigmatism 1 and 2 (corresponding to j = 5 and 6) are shown in Figure 105.

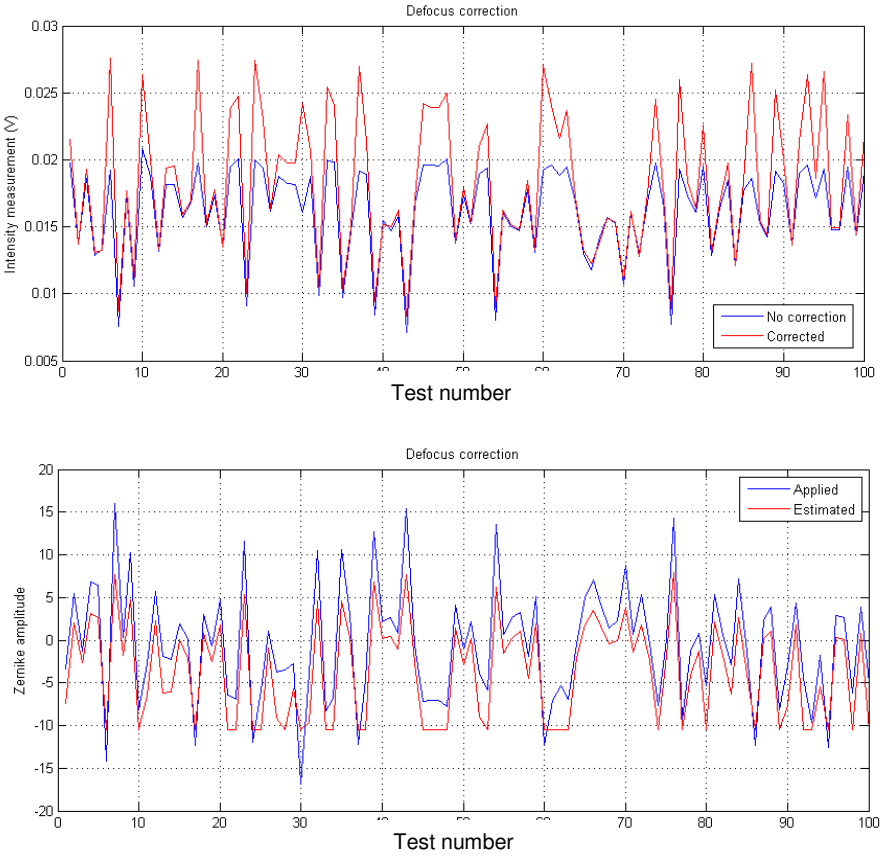

Figure 104. Defocus distortion and correction.
(A) intensity of uncorrected and corrected beam (B) Zernike amplitude estimates.

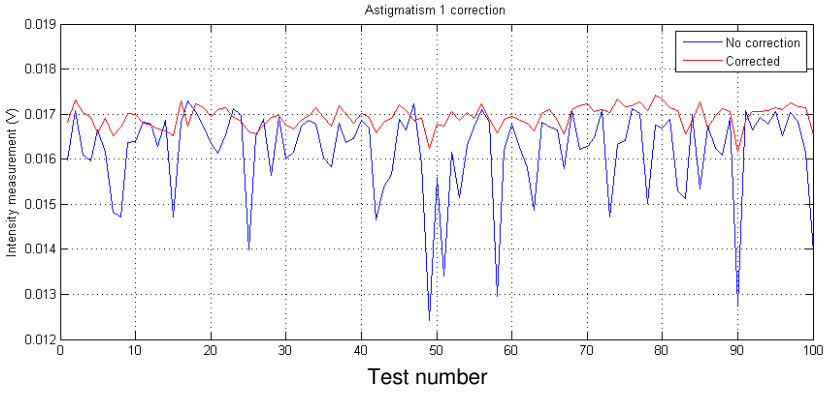

(A)

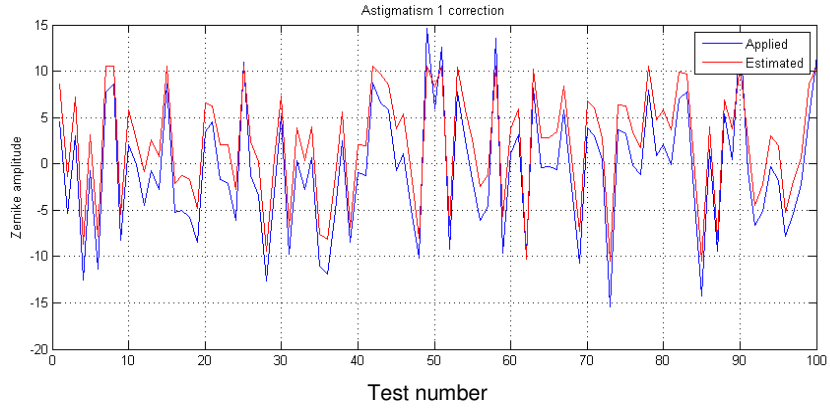

(B)

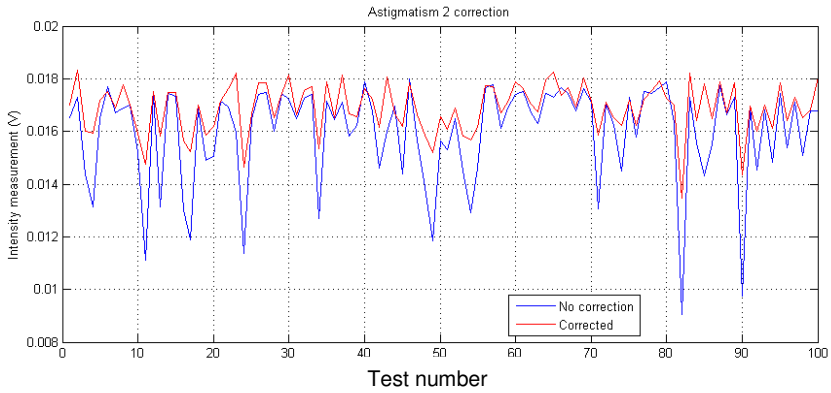

(C)

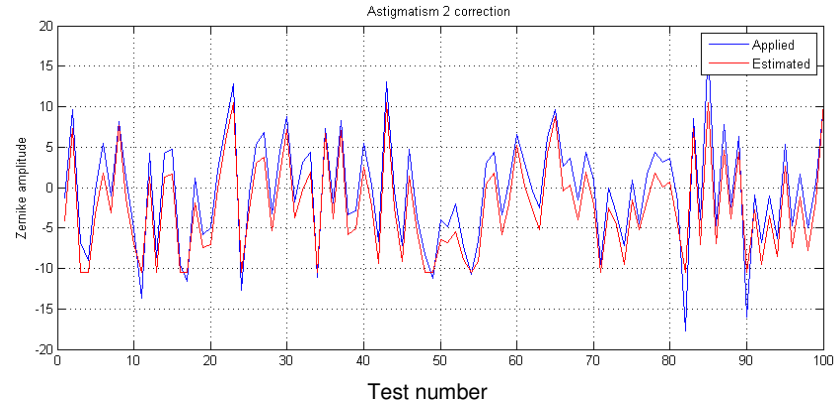

(D)

Figure 105. Astigmatism distortion and correction.
(A) & (C): Uncorrected and corrected intensity measurements for Astigmatism 1 and 2.
(B) & (D): Applied and estimated Zernike amplitudes for Astigmatism 1 and 2.

Correction for astigmatism yields a more consistent performance. Corrected intensity fluctuates significantly less for both modes. The estimated Zernike amplitude matches the applied modes relatively well for the two astigmatisms.

Figure 106 shows the measured results for coma x and y (mode $j = 7$ and 8). The results show no reduction in intensity fluctuation, while the mode amplitudes are not accurately estimated. This is due to the shape of the function of intensity versus coma mode amplitude being very non-parabolic as shown in Figure 103D-E. The fitting error caused is evident from the estimates sometime swinging wildly from negative to positive as seen in Figure 106C and D.

Due to poor coma estimation performance, modes chosen for adaptive optics optimisation are defocus and two astigmatisms. From Table 11 and equation (4.2.13), the lower order Zernike modes are dominant in a Kolmogorov phase screen, which suggest that these three modes are sufficient for a significant scintillation reduction. A Kolmogorov phase screen was then used to measure the performance of the system in real turbulence conditions.

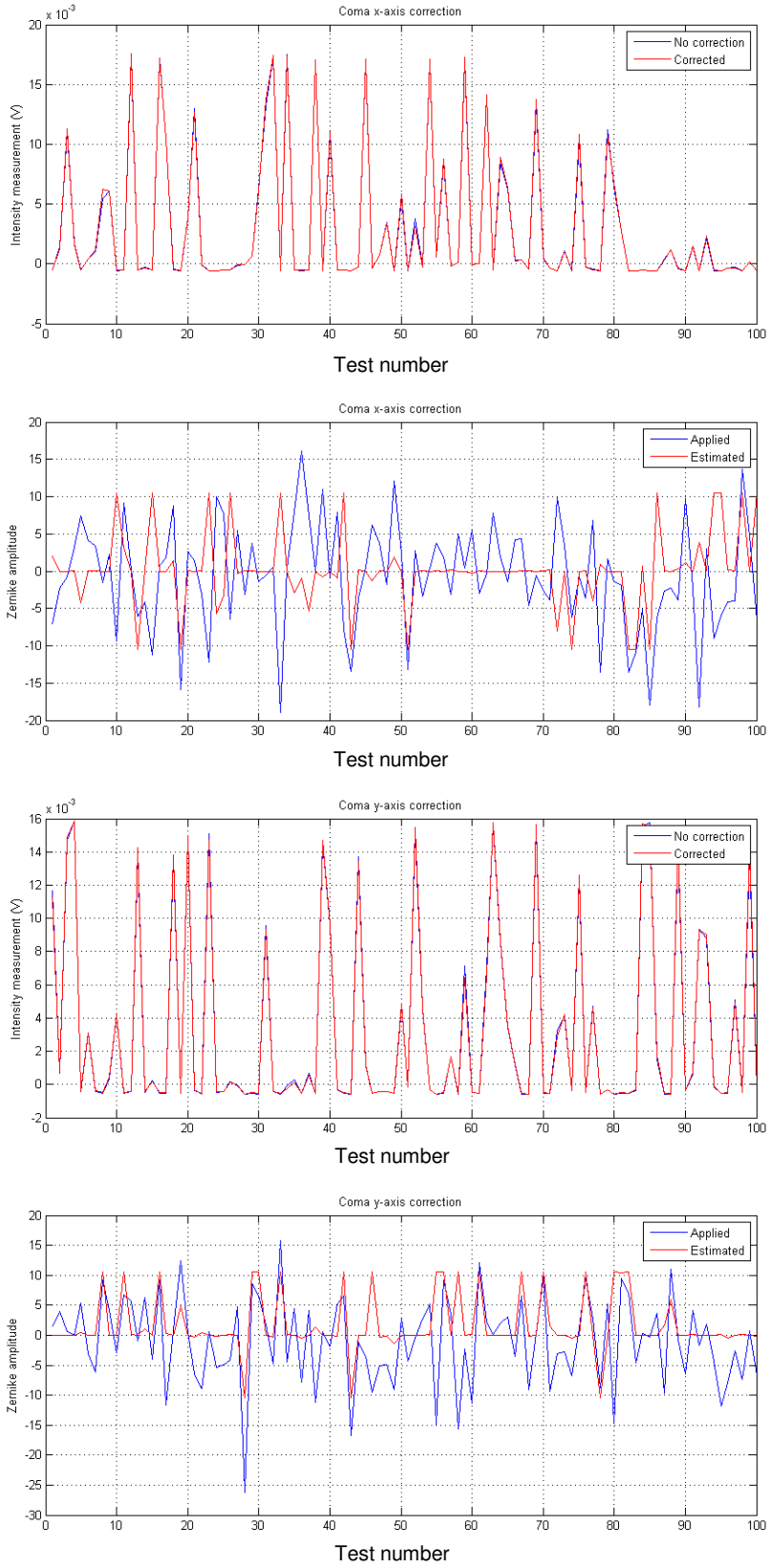

Figure 106. Astigmatism distortion and correction.
(A) & (C): Uncorrected and corrected intensity measurements for Coma x and y
(B) & (D): Applied and estimated Zernike amplitudes of Coma x and y.

4.5.3 Scintillation index results

Turbulence correction was performed on a weak turbulence condition modelled using Kolmogorov phase screens. Turbulence strength ranged from D/r_0 = 0.5 to 4. A 0.5mm pinhole was placed in front of the photodiode detector, which behaves as a point detector. Each phase screen was estimated using wavefront sensorless estimation for defocus, astigmatism 1 and 2, and the correction applied to SLM A. 100 phase screens were used per data point. Figure 107 shows the scintillation index versus D/r_0 with and without correction.

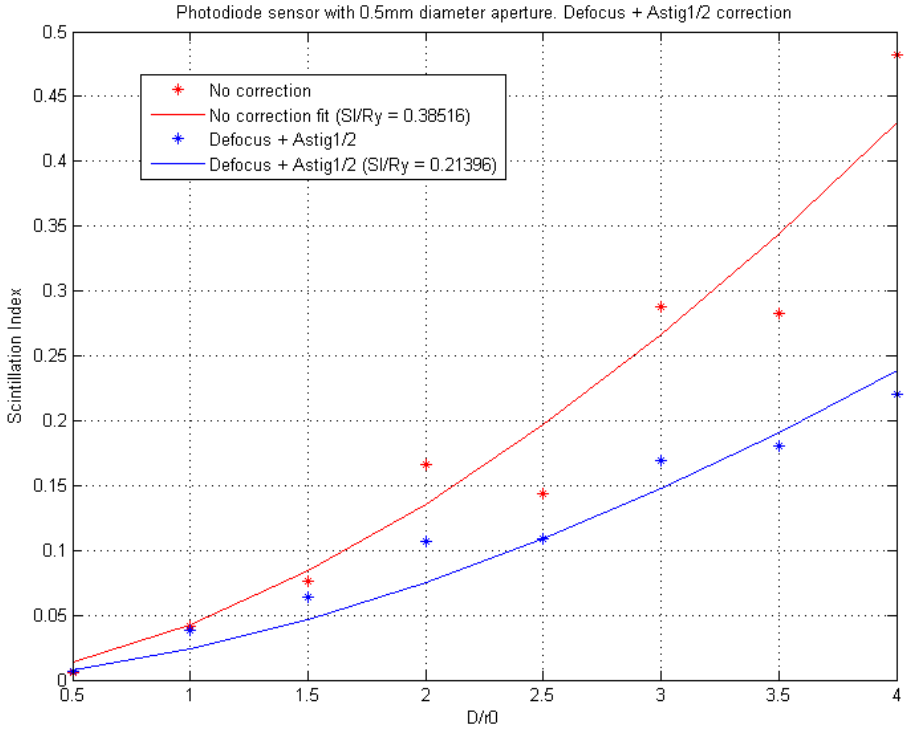

Figure 107. Measured scintillation index with and without defocus + astigmatism 1 and 2.

The scintillation index is again fitted using with a 5/3 power curve, obtaining a σ_I^2/σ_R^2 ratio of 0.214 corrected and 0.385 for uncorrected beams, producing a 44% improvement over the uncorrected beam. The intensity variation is plotted in Figure 108. The AO corrected intensity has been smoothed out, and significantly decreases the deep fading periods.

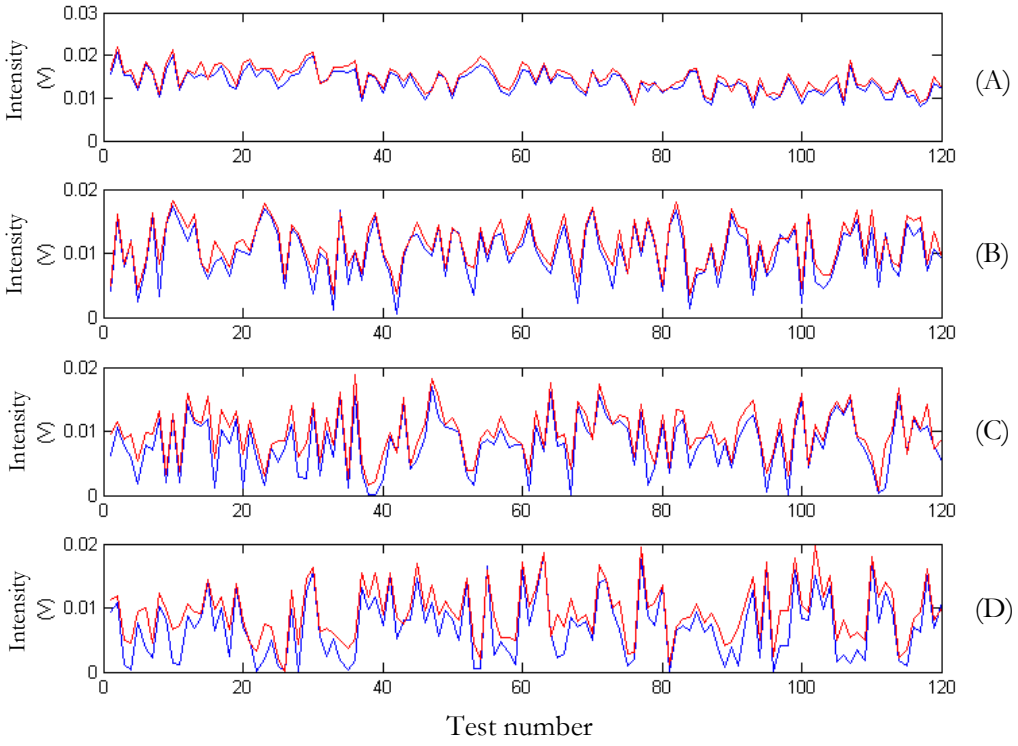

Figure 108. Intensity measurements of uncorrected intensity (blue) and corrected intensity (red) distribution for D/r_0 of 1-4 for (A)-(D) for a 0.5mm aperture.

In reality, an FSO system consists of a finite receiver aperture, and aperture averaging must be taken into account as well as phase correction. A simulation of aperture averaging was achieved by recording the phase screen used to estimate Zernike corrections with the 0.5mm aperture. These were then 'replayed' with and without the phase corrections obtained in the previous experiment. The aperture size is set to 0.8mm. The measured scintillation indices for no correction, correction with point detector, and correction with aperture averaging are shown in Figure 109. They are fitted with a 5/3 power curve. The intensity variations of corrected aperture averaged case are plotted in Figure 110. Again, deep fade periods are reduced with phase correction.

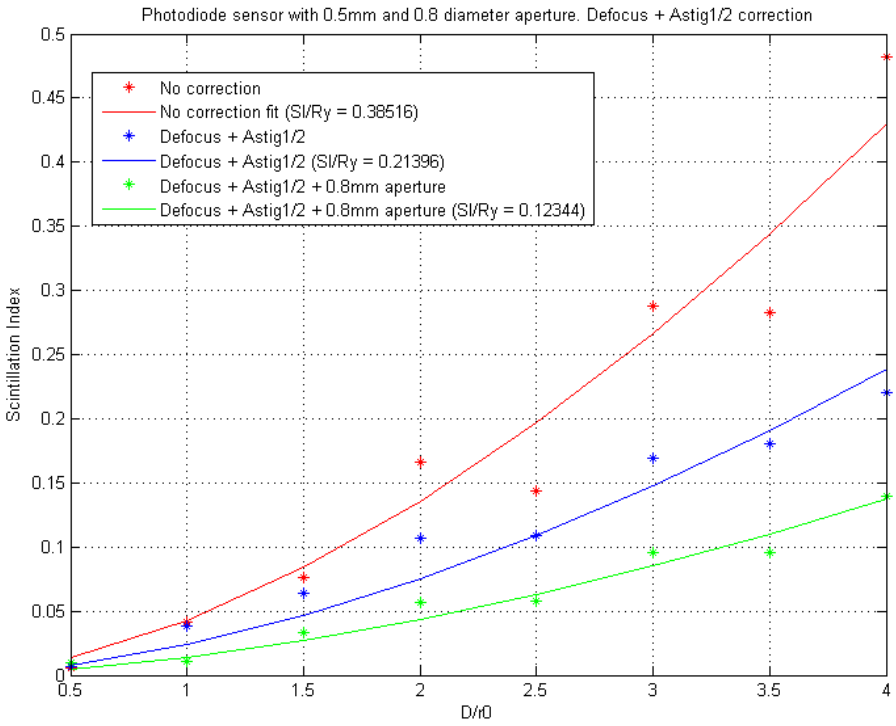

Figure 109. Measured scintillation index with and without defocus and astigmatism 1 and 2, with an aperture of 0.8mm, simulating the aperture averaging effect on the corrected beam.

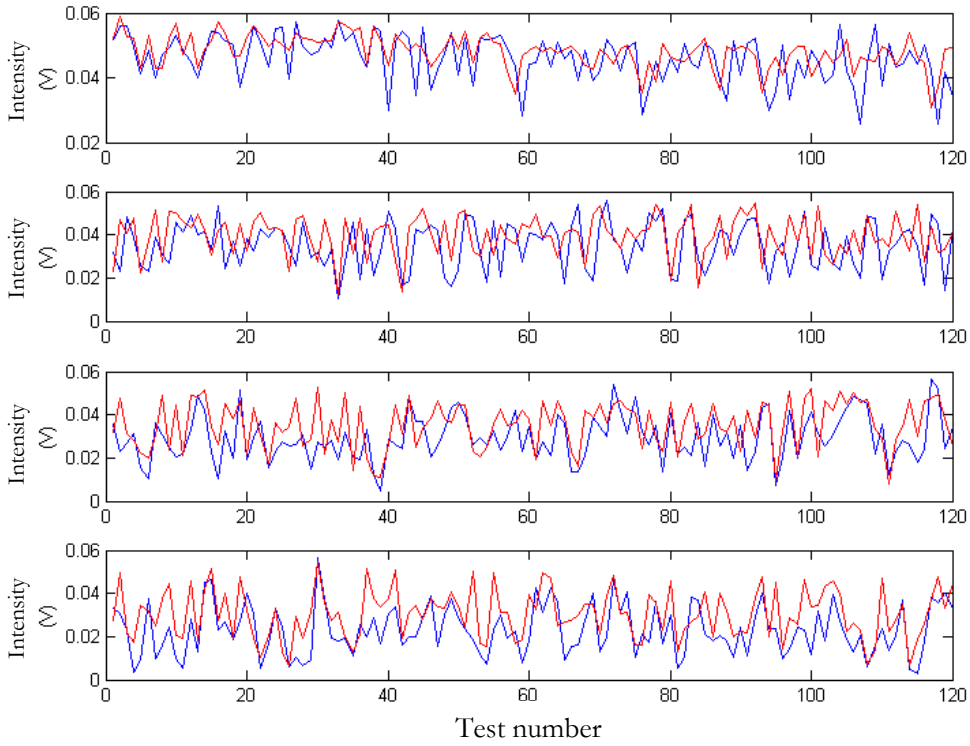

Figure 110. Intensity measurements of uncorrected intensity (blue) and corrected intensity (red) distribution for D/r_0 of 1-4 for (A)-(D) for 0.8mm aperture.

Aperture averaging further reduced the scintillation index to 0.123, or a 68% improvement. Recalling Figure 94, aperture averaging alone provides a 41% reduction along with the AO system providing a 44% reduction. The reductions combined provide a theoretical reduction of 67%. This suggests that the two reduction methods can be considered to provide independent scintillation reduction. The maximum bit error rates for the AO system can be calculated using the intensity PDF from equation (4.1.56) and (4.1.57), using a log-normal distribution. A plot of the maximum bit error rate for OOK in Figure 111 is shown with respect to D/r_0, using Λ_0 = 0.774.

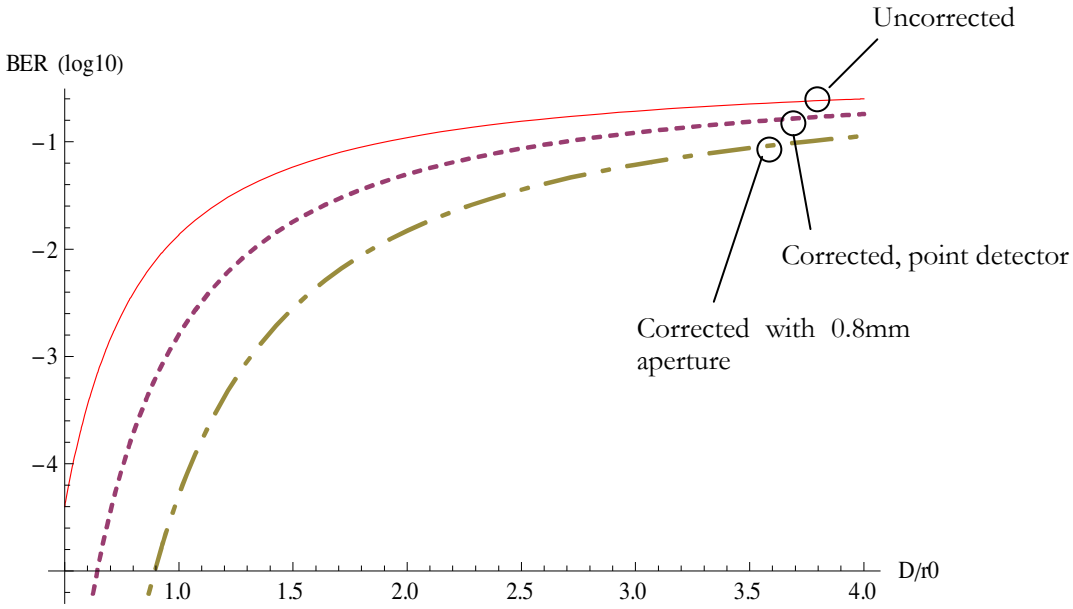

Figure 111. Minimum BER for uncorrected, corrected point receiver, and corrected with aperture averaging using the σ_I^2/σ_R^2 ratios.

The BER improvement is greatest in weak turbulence, providing two orders of magnitude reduction. At stronger turbulence condition the improvements diminishes quickly above D/r_0 of 2, even though results show a large improvement in scintillation index. This is because the intensity follows a log-normal type distribution, thus the difference in the likelihood of a deep fade is small for large scintillation index.

4.6 Multiple Gaussian beams scintillation reduction

An adaptive optics (AO) system relies on dynamic wavefront correction to compensate for phase fluctuations present in the atmosphere. The main assumption for an implementation of AO is the availability of phase measurements either directly from the wavefront, using a sensor such as a Shack-Hartmann, or from indirect Zernike measurement methods described in previous sections. A wavefront sensorless AO system shows a significant reduction in scintillation index and subsequently a significant decrease in calculated bit error rates. In conjunction with aperture averaging at the receiver, it was shown that it is possible to reduce scintillation index even further. However, the atmospheric coherence width r_0 places a limit to the maximum useful aperture diameter. In practice, even larger scintillation reduction is likely to be required for a high availability, long range FSO link.

An interesting development in recent years has been the use of partially coherent beams as a way to reduce effects of turbulence on a propagating optical beam [133][74]. The technique originated from an observation that the expected scintillation index from weak to moderate regime is much greater than in very strong turbulence. Clifford [134] used simplified assumptions of spatial coherence loss to verify experimental results with theoretical calculations. Since then, there has been on going research into using artificially created partially incoherent beams to further reduce the effects of atmospheric effects [135][136][137]. Large reductions are theoretically possible for weak turbulence regime [136].

Two problems are apparent in using this technique. First, a partially incoherent beam is created using a random phase screen at the transmitter as shown in Figure 112A. The phase screen time constant must be smaller than the receiver time constant for scintillation reduction to occur [74]. For high speed optical links, the time constant is in the range of nanoseconds, which is a challenge to create a changing phase screen at this rate. Second, the incoherent nature of the transmitted beam means adaptive optics and other wavefront measurements can not be made. Therefore, only aperture averaging is possible at the receiver.

Many commercial products use a form of partially coherent beam with good results [138]. It was found that using two or more laser sources that are not coherent with respect to one another reduces the

scintillation index. Peleg [139] was able to derive analytical equations for calculating the scintillation index of two mutually incoherent Gaussian beams set up as in Figure 112B. This is achieved in practice using two laser sources with slightly different wavelengths. By placing the beams on parallel paths, significant scintillation reduction was shown theoretically and experimentally [140]. Using a numerical wavefront simulator, Xiao [141] suggests that changing the beam geometrical configuration can have a large and beneficial impact on the scintillation index.

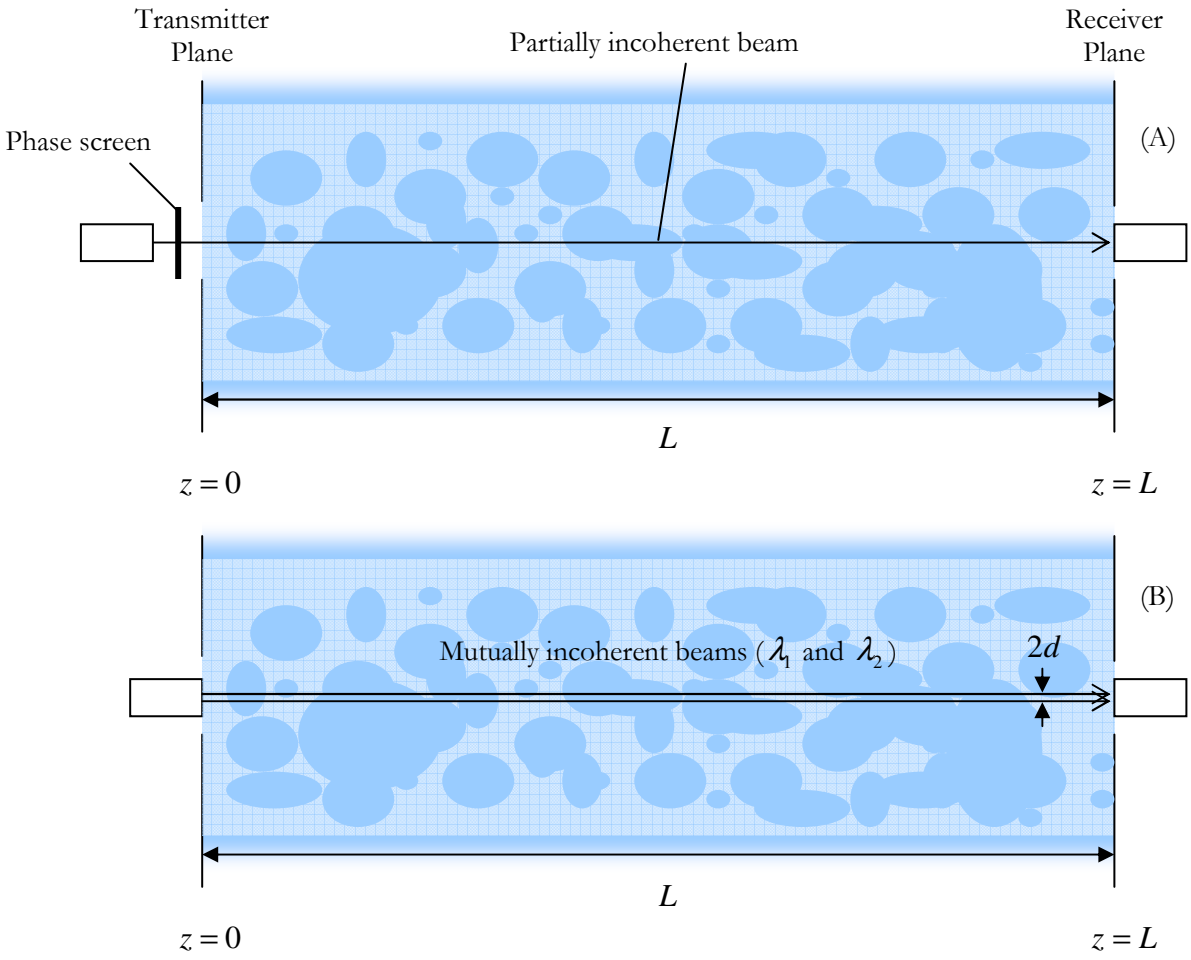

Figure 112. Diagrams of (A) Partially coherent beam using phase screen at the transmitter. (B) Parallel mutually incoherent beams

In this section, the use of multiple Gaussian beams to reduce scintillation index in weak turbulence conditions is investigated. Theoretical derivations are given, based on Peleg [139] for parallel beam configurations. This is then extended to give new sets of analytical equations for scintillation index calculation of converging and diverging Gaussian beams. Numerical integration results are then presented

and compared. Finally, bit error rates are calculated for multiple Gaussian beams, with and without adaptive optics correction described in previous section.

4.6.1 Multiple Gaussian beams

For the configuration in Figure 112B, the total electric field at the transmitter for N multiple Gaussian beams can be written as:

$$U(\mathbf{r},0)=\sum_{j=1}^{N}A_j\exp\left[-\left(\frac{1}{{W_{0j}}^2}+\frac{ik_j}{2F_{0j}}\right)\left|\mathbf{r}-\mathbf{d_j}\right|^2\right] \tag{4.6.1}$$

where $\mathbf{r}$ is the two dimensional positional vector and $\mathbf{d_j}$ is the two dimensional beam displacement vector from the optical axis. W_0, k and F_0 are the beam radius, wave vector and beam curvature as defined in Section 4.1.5. Time dependent components are neglected since the beam frequency differences results in beat frequencies that are much higher than the bandwidth of the receiver. The Gaussian beam parameters Θ and Λ follow the same definition as Section 4.1.5. Using the Rytov approximation, and letting $\mathbf{r_j}=\mathbf{r}-\mathbf{d_j}$, the total field at the receiver is written as perturbed fields:

$$U(\mathbf{r}_j,L)=\sum_{j=1}^{N}U(\mathbf{r}_j,0)\exp\left[\psi_j(\mathbf{r_j},L,k_j)\right] \tag{4.6.2}$$

Because the beams are mutually incoherent, the intensity can be written as a summation of individual intensities since any mutually coherent parts are zero-averaged at the beat frequency. Assuming a receiver with a uniform optical spectral response, the expression becomes:

$$I(\mathbf{r}_j,L)=\sum_{j=1}^{N}I_j(\mathbf{r}_j,L) \tag{4.6.3}$$

The scintillation index can then be written as first and second intensity moments:

$${\sigma_I}^2(\mathbf{r},L)=\frac{\sum_{j=1}^{N}\sum_{m=1}^{N}\left\langle I_j(\mathbf{r},L)I_m(\mathbf{r},L)\right\rangle}{\left(\sum_{j=1}^{N}\left\langle I_j(\mathbf{r},L)\right\rangle\right)^2}-1=\frac{\sum_{j=1}^{N}\left\langle I_j(\mathbf{r},L)^2\right\rangle+2\sum_{j=1}^{N}\sum_{m>j}^{N}\left\langle I_j(\mathbf{r},L)I_m(\mathbf{r},L)\right\rangle}{\left(\sum_{j=1}^{N}\left\langle I_j(\mathbf{r},L)\right\rangle\right)^2}-1 \tag{4.6.4}$$

From the Rytov method in Section 4.1.5, the mean intensity term can be approximated using a Kolmogorov spectrum:

$$\left\langle I_j\left(r,L\right)\right\rangle \simeq \frac{{A_{0j}}^2{W_{0j}}^2}{{W_j}^2}\exp\left[{\sigma_{Rj}}^2{\Lambda_j}^{5/6}\left(2.22\frac{\left|\mathbf{r}_j\right|^2}{{W_j}^2}-1.33\right)\right] \tag{4.6.5}$$

where $W_j=\dfrac{2L}{k_j\Lambda_j}$ is the average beam radius at the receiver and σ_{Rj} is the Rytov variance for specific k_j. For the second moment, self terms that can again be expressed by using results from Section 4.1.5:

$$\left\langle I_j\left(\mathbf{r},L\right)^2\right\rangle=\left\langle I_j\left(\mathbf{r},L\right)\right\rangle^2\exp\left[{\sigma_R}^2\left(\begin{array}{c}3.86\,\mathrm{Re}\left[i^{5/6}\,{}_2F_1\left(-\frac{5}{6},\frac{11}{6};\frac{17}{6};(1-\Theta)+i\Lambda\right)\right]\\ -2.64\Lambda^{5/6}\,{}_1F_1\left(\frac{-5}{6};1;\frac{2r^2}{W^2}\right)\end{array}\right)\right] \tag{4.6.6}$$

Since there is an area of beam overlap, Peleg [139] derived the cross terms using a modification to the standard Rytov approximation, taking into account the differences in position and wave number:

$$\left\langle I_j\left(\mathbf{r},L\right)I_m\left(\mathbf{r},L\right)\right\rangle=\left\langle I_j\left(\mathbf{r},L\right)\right\rangle\left\langle I_m\left(\mathbf{r},L\right)\right\rangle\times\exp\left(\begin{array}{l}E_{2jm}\left(\mathbf{r}_j,\mathbf{r}_m,k_j,k_m\right)\\ +E_{2mj}\left(\mathbf{r}_m,\mathbf{r}_j,k_m,k_j\right)\\ +2\,\mathrm{Re}\left[E_{3jm}\left(\mathbf{r}_j,\mathbf{r}_m,k_j,k_m\right)\right]\end{array}\right) \tag{4.6.7}$$

where E_{2jm}, E_{2mj} and E_{3jm} are complex phase moments given as:

$$\begin{aligned}E_{2jm}\left(\mathbf{r}_j,\mathbf{r}_m,k_j,k_m\right)&=4\pi^2k_jk_mL\int_0^1d\xi\int_0^\infty d\kappa\kappa\Phi_n\left(\kappa\right)J_0\left(\kappa\left|\gamma_j\mathbf{r}_j-{\gamma_m}^*\mathbf{r}_m\right|\right)\\&\quad\times\exp\left[-\frac{i}{2}\kappa^2L\left(\frac{\gamma_j}{k_j}-\frac{{\gamma_m}^*}{k_m}\right)\xi\right]\end{aligned}$$

$$\begin{aligned}E_{2mj}\left(\mathbf{r}_m,\mathbf{r}_j,k_m,k_j\right)&=4\pi^2k_jk_mL\int_0^1d\xi\int_0^\infty d\kappa\kappa\Phi_n\left(\kappa\right)J_0\left(\kappa\left|\gamma_m\mathbf{r}_m-{\gamma_j}^*\mathbf{r}_j\right|\right)\\&\quad\times\exp\left[-\frac{i}{2}\kappa^2L\left(\frac{\gamma_m}{k_m}-\frac{{\gamma_j}^*}{k_j}\right)\xi\right]\end{aligned}$$

$$\begin{aligned}E_{3jm}\left(\mathbf{r}_j,\mathbf{r}_m,k_j,k_m\right)&=4\pi^2k_jk_mL\int_0^1d\xi\int_0^\infty d\kappa\kappa\Phi_n\left(\kappa\right)J_0\left(\kappa\left|\gamma_j\mathbf{r}_j-\gamma_m\mathbf{r}_m\right|\right)\\&\quad\times\exp\left[-\frac{i}{2}\kappa^2L\left(\frac{\gamma_j}{k_j}+\frac{\gamma_m}{k_m}\right)\xi\right]\end{aligned} \tag{4.6.8}$$

where $\gamma_j = 1-\left(\left(1-\Theta_j\right)+i\Lambda_j\right)\xi$, J_0 is Bessel function of the first kind, and $\xi = 1-\frac{z}{L}$ where z is the distance from the transmitter. Numerical results can be obtained by considering two Gaussian beams with separation distance of $2d$ in the y-axis (Figure 112). Using a collimated beam width of 0.01m, L = 1000m, λ_1 = 1000nm, and λ_2 = 1010nm, the scintillation index for a set of turbulence strengths is plotted in Figure 113. It can be seen that a turbulence reduction of 0.6 is obtained at a separation distance of 2.3cm for all turbulence strengths. At large separations, the scintillation index increases rapidly due to the large radial scintillation index from the standard Gaussian beam results.

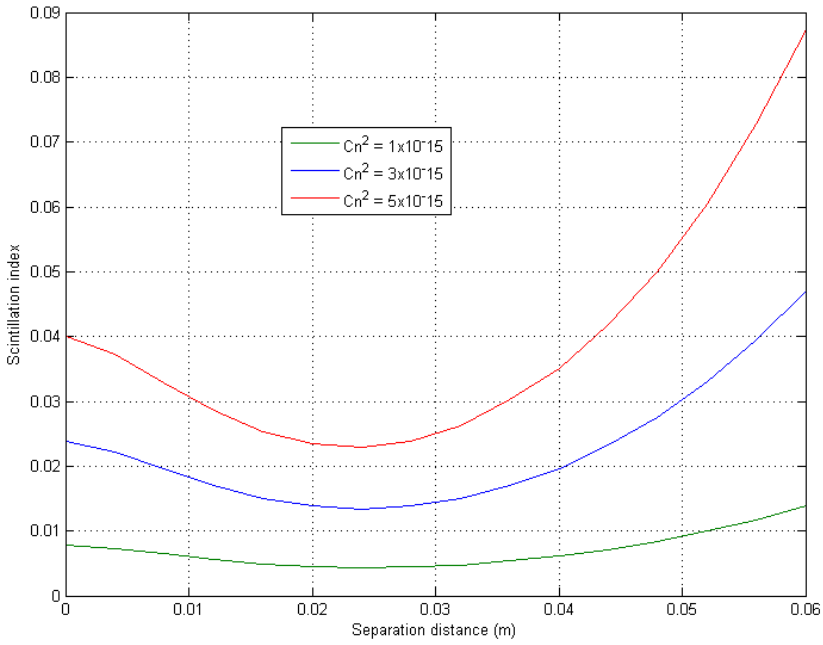

Figure 113. Plot of scintillation index against separation distance between two Gaussian beams for various strengths of turbulence

A modification to the beam geometry was suggested by [141] to point the beams directly into the receiver aperture instead of parallel propagation. Numerical wavefront simulation suggests a reduction in separation distance sensitivity. Figure 114 shows the converging two beam geometry.

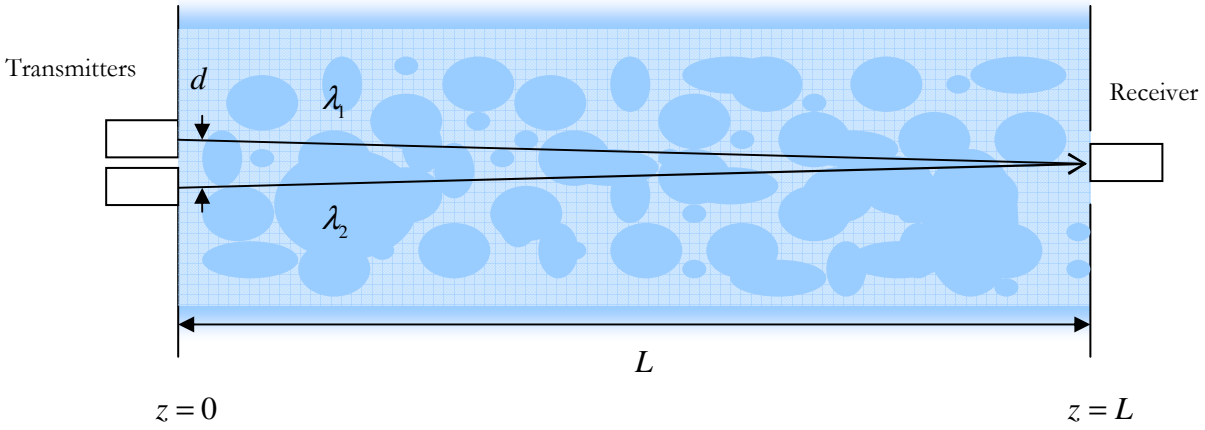

Figure 114. Two Gaussian beams pointing to the receiver (converging beams)

The beams separation distance can be approximated as a function of ξ by using the definition $\xi = 1 - \frac{z}{L}$ in Equation (4.6.8). The complex phase moments for converging Gaussian beams therefore are represented as:

$$E_{2jm_{con}}\left(\mathbf{r}_j, \mathbf{r}_m, k_j, k_m\right) = 4\pi^2 k_j k_m L \int_0^1 d\xi \int_0^\infty d\kappa \kappa \Phi_n\left(\kappa\right) J_0\left(\kappa \left| \gamma_j \mathbf{r}_j - \gamma_m^* \mathbf{r}_m \right| \xi\right) \times \exp\left[-\frac{i}{2}\kappa^2 L \left(\frac{\gamma_j}{k_j} - \frac{\gamma_m^*}{k_m} \right) \xi \right]$$

$$E_{2mj_{con}}\left(\mathbf{r}_m, \mathbf{r}_j, k_m, k_j\right) = 4\pi^2 k_j k_m L \int_0^1 d\xi \int_0^\infty d\kappa \kappa \Phi_n\left(\kappa\right) J_0\left(\kappa \left| \gamma_m \mathbf{r}_m - \gamma_j^* \mathbf{r}_j \right| \xi\right) \times \exp\left[-\frac{i}{2}\kappa^2 L \left(\frac{\gamma_m}{k_m} - \frac{\gamma_j^*}{k_j} \right) \xi \right]$$

$$E_{3jm_{con}}\left(\mathbf{r}_j, \mathbf{r}_m, k_j, k_m\right) = 4\pi^2 k_j k_m L \int_0^1 d\xi \int_0^\infty d\kappa \kappa \Phi_n\left(\kappa\right) J_0\left(\kappa \left| \gamma_j \mathbf{r}_j - \gamma_m \mathbf{r}_m \right| \xi\right) \times \exp\left[-\frac{i}{2}\kappa^2 L \left(\frac{\gamma_j}{k_j} + \frac{\gamma_m}{k_m} \right) \xi \right] \quad (4.6.9)$$

Another beam geometry that can be considered is a diverging beam case, where two beams originate from a single aperture. The beams are tilted off axis such that beams are overlapped over the receiver aperture as shown in Figure 115.

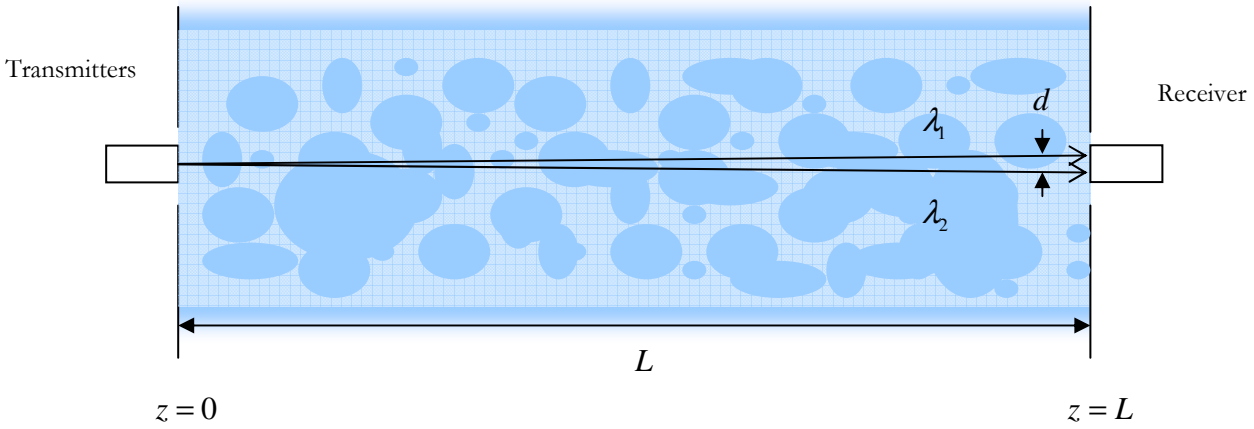

Figure 115. Two Gaussian beams pointing away from the receiver (diverging beams)

A similar expression can be obtained for diverging beams:

$$E_{2\,jm_{div}}\left(\mathbf{r}_j,\mathbf{r}_m,k_j,k_m\right)=4\pi^2k_jk_mL\int_0^1 d\xi\int_0^\infty d\kappa\kappa\Phi_n\left(\kappa\right)J_0\left(\kappa\left|\gamma_j\mathbf{r}_j-\gamma_m{}^*\mathbf{r}_m\right|\left(1-\xi\right)\right)$$
$$\times\exp\left[-\frac{i}{2}\kappa^2L\left(\frac{\gamma_j}{k_j}-\frac{\gamma_m{}^*}{k_m}\right)\xi\right]$$

$$E_{2mj_{div}}\left(\mathbf{r}_m,\mathbf{r}_j,k_m,k_j\right)=4\pi^2k_jk_mL\int_0^1 d\xi\int_0^\infty d\kappa\kappa\Phi_n\left(\kappa\right)J_0\left(\kappa\left|\gamma_m\mathbf{r}_m-\gamma_j{}^*\mathbf{r}_j\right|\left(1-\xi\right)\right)$$
$$\times\exp\left[-\frac{i}{2}\kappa^2L\left(\frac{\gamma_m}{k_m}-\frac{\gamma_j{}^*}{k_j}\right)\xi\right]$$

$$E_{3\,jm_{div}}\left(\mathbf{r}_j,\mathbf{r}_m,k_j,k_m\right)=4\pi^2k_jk_mL\int_0^1 d\xi\int_0^\infty d\kappa\kappa\Phi_n\left(\kappa\right)J_0\left(\kappa\left|\gamma_j\mathbf{r}_j-\gamma_m\mathbf{r}_m\right|\left(1-\xi\right)\right)$$
$$\times\exp\left[-\frac{i}{2}\kappa^2L\left(\frac{\gamma_j}{k_j}+\frac{\gamma_m}{k_m}\right)\xi\right]\qquad(4.6.10)$$

Using numerical integration, it is possible to estimate the scintillation index. Figure 117 shows a plot of the scintillation index for a point receiver for increasing value of beam separation distance d, with a C_n^2 value of $3\text{x}10^{-15}$. The dashed line indicates the lowest possible scintillation index by considering independent paths between the beams, for example when separation distance is large:

$$\sigma_{I_{indep}}{}^2(\mathbf{r},L)=\frac{\sum_{j=1}^{N}\left\langle I_j(\mathbf{r},L)^2\right\rangle-\sum_{j=1}^{N}\left\langle I_j(\mathbf{r},L)\right\rangle^2}{\left(\sum_{j=1}^{N}\left\langle I_j(\mathbf{r},L)\right\rangle\right)^2} \tag{4.6.11}$$

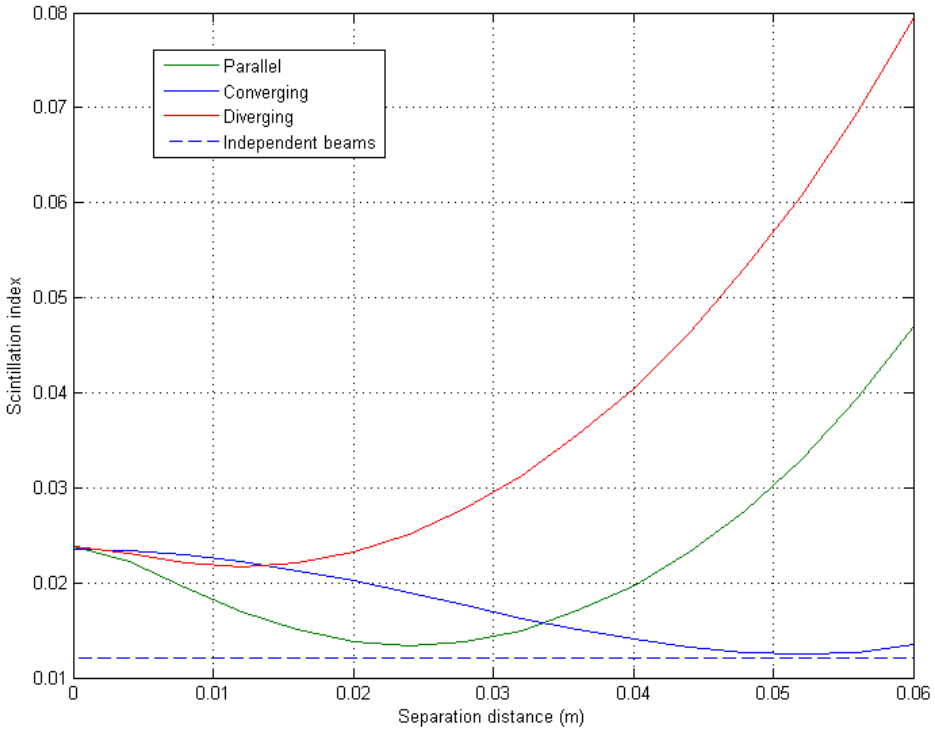

Figure 116. Plot of scintillation index against separation distance between two Gaussian beams with parallel, convergent and divergent different beam geometries.

The curve for converging beams matches results published using numerical wavefront simulation [141] for beam separation of 5cm or less. The scintillation index is found to be less sensitive from changes in separation distance compared to parallel beams, while requiring twice as large a separation distance, at 5.1cm. A larger distance is found to increase the scintillation. This is possibly due to the break down of the approximation used to obtain equation (4.6.9) at large beam distances, and the effect is not present in [141]. The minimum scintillation indexes for both cases are approximately the same as statistically independent beams. Divergent beams are found to produce little scintillation index reduction, however a small minimum is observed at separation distance of 1.2cm.

The beam configuration can be extended to more than 2 beams. The scintillation index for parallel, convergent and divergent 4 beams symmetrically distributed around the optical axis with wavelengths of 1.00, 1.01, 1.02 and 1.03 μm are plotted in Figure 117.

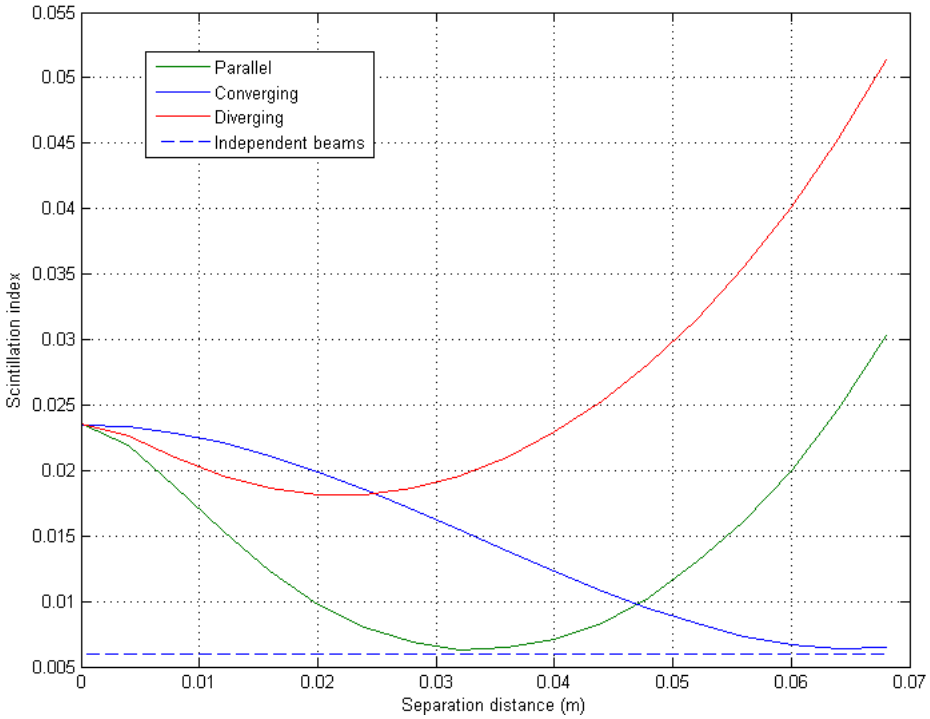

Figure 117. Plot of scintillation index against separation distance between four Gaussian beams with parallel, convergent and divergent beam geometries.

With four beams, all configurations obtain reduction in scintillation index relative to two beams. Again, the minimum scintillation indexes for parallel and convergent beams are approximately the same as independent beams. The separation distance for minimum scintillation with parallel beams has been increased to 3.2cm, and for convergent beams to 6.4cm.

4.6.2 Bit Error Rates for multiple beams

For a greater number of beams, the integration for cross terms grows as a function of number of beams squared. The computation time can therefore increase quickly. A lower bound for converging beams using independent beam paths using Equation (4.6.11) can then be used to estimate the scintillation index. Assuming that the effect of differences in beam wavelengths is negligible, the expression for scintillation index is reduced to having zero covariance:

$$\sigma_{I_N}{}^2(\mathbf{r},L,N)=\frac{\left\langle I(\mathbf{r},L)^2\right\rangle-\left\langle I(\mathbf{r},L)\right\rangle^2}{N\left\langle I(\mathbf{r},L)\right\rangle^2} \tag{4.6.12}$$

where N is the number of beams.

The separation distance d needed to produce independent beams can be estimated by considering the minimum a distance between adjacent beams as the transmitters are packed uniformly around a circle with radius d:

$$a=d\sin\left(\frac{\pi}{N}\right) \tag{4.6.13}$$

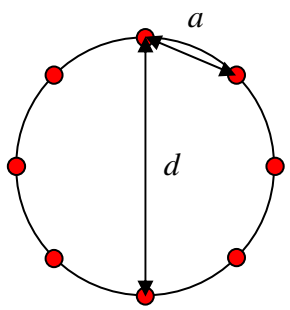

Figure 118. Radially arranged transmitters centred on the optical axis and their relative distances.

a can be approximated to be the separation distance for two converging Gaussian beams to produce scintillation index close to $\sigma_{I_{indep}}{}^2$, which is found to be 0.05m for the beam diameter and propagating distance considered in Section 4.6.1. Figure 119 shows a plot of d as a function of N.

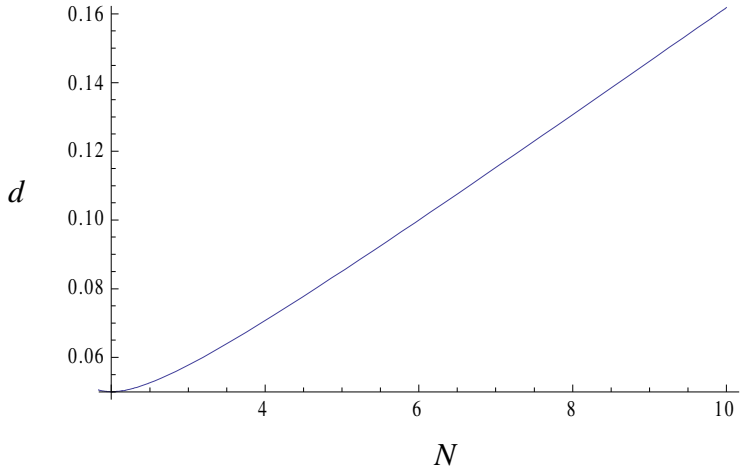

Figure 119. Plot of separation distance d for a radially uniformly distributed transmitters around a circle radius d .

The minimum BER can then be estimated using (4.1.56), (4.1.57) and a Log-normal distribution using the number of independent optical beams as shown in Figure 120. The optical turbulence simulator in Section 4.5.3 demonstrated the AO system's ability to independently reduce scintillation index with respect to aperture averaging. Using this result, a further scintillation index reduction by a factor of 3 (Section 4.5.3) can also be applied to each beam independently.

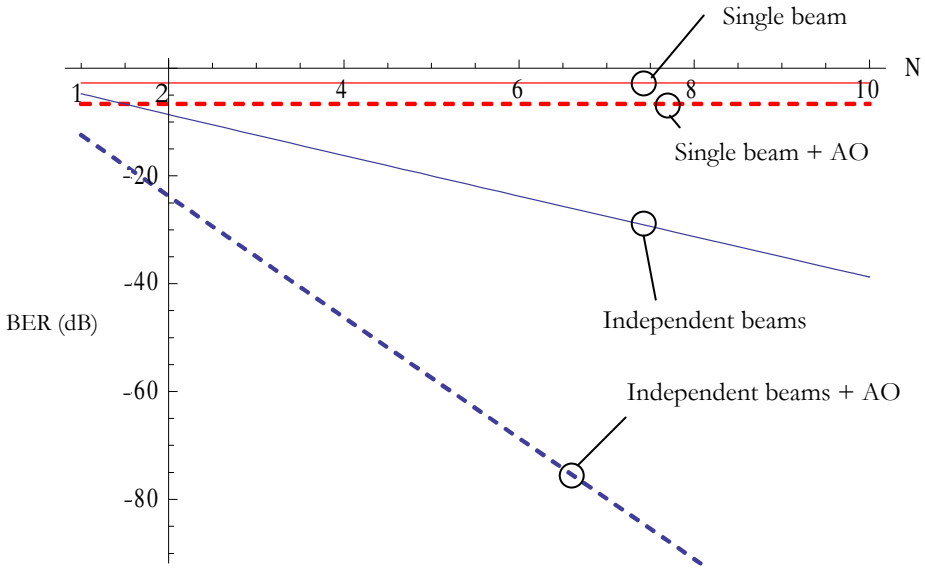

Figure 120. Minimum BER using independent beams with and with out AO correction as a function of the number of converging beams (N).

The minimum BER is reduced significantly by using an AO correction since the number of corrections increases with the number of beams. However, this might be unfeasible in reality since all corrections must be performed within the turbulence time scale.

4.7 Conclusion

A brief overview of Rytov weak fluctuation theory and relevant results has been presented. Numerical calculations for scintillation index and mean intensity for collimated beam gave very high bit error rates. An optical turbulence simulator consisting of a binary SLM has been implemented. The measured scintillation index and mean intensity due to Kolmogorov phase screen agree well with the weak fluctuation theory. The simulator also showed good aperture averaging factor agreement for smaller aperture diameters, but at a large diameter the scintillation index is found to be much smaller than predicted.

A wavefront sensorless adaptive optics system has been described and tested. By breaking down Kolmogorov phase screen into Zernike modes, the system was able to correct astigmatism and performed reasonably well for defocus distortion. The system was subjected to simulated turbulence and found to reduce scintillation by 44%. With aperture averaging, the performance increased to 68%. Bit error rates were calculated to give two orders of magnitude increase in performance for low turbulence strength. At high turbulence strengths, the BER improvement has been found to be roughly a factor of two.

Using multiple Gaussian beams, scintillation index expression for parallel, convergent and divergent beams were described as a function of their separation distances. Numerical results show that for parallel and convergent beams, significant scintillation index reduction was observed. At large separation, convergent beams were found to be statistically independent and the scintillation index expression can be greatly simplified. Bit error rates were found to be reduced by multiple beams, and can be improved significantly in conjunction when used with AO system. It is therefore evident that multiple methods are needed to reduce the bit error rates to suitable levels.

5 Conclusion and future work

5.1 Conclusion

A high resolution ferro-electric liquid crystal display (FLC) device has been shown to function as a spatial light modulator for various free-space optical applications. These include holographic beam steering and forming, optical aberration compensation for transmitted beam, turbulent atmosphere simulation adaptive optics turbulence compensation system. The majority of the initial work revolved around binary phase modulation of FLC devices. Traditional binary hologram generation algorithms do not take DC balancing of the liquid crystal cells in to account, which can deteriorate the cell's optical switching performance. By multiple small phase shifts during hologram generation stage, the cells can be DC balanced while producing very small intensity drop during balancing process. This is a key property for allowing complex phase patterns to be used on the FLC.

Numerical and physical demonstration of the DC balancing method's effectiveness was carried out for single and multiple steered beams, achieving intensity drops of less than 11 percent between hologram frames. A free-space broadcast to two receivers was also demonstrated for communications bitrates.

By using the new DC balancing algorithm, a holographic beam steerer was designed and implemented for image based retro-reflecting target acquisition system. The beam steerer was used as a novel approach to correct for aberrations in beam angle magnifier, resulting in an increase in the transmitted beam power density. A software control system for acquisition and beam coordinate transform was also described. A software image processing routine that uses morphological filters to decrease the effects of ambient light was implemented and tested. The accuracy of the acquisition system was tested using an array of retro-reflectors, resulting in a measured mean acquisition error of 4.0×10^{-4} radians.

The effects of atmospheric turbulence were then investigated for Gaussian beam transmission in weak turbulent condition using Rytov approximation and Kolmogorov spectrum. A novel optical

turbulence simulator was described. A binary phase screen was used with the conjunction of a receiver aperture to produce the same beam intensity as a continuous phase distribution. Scintillation index and intensity measurements were made which agreed well with theoretical prediction.

An adaptive optics turbulence compensation method was then described. It used wavefront sensorless Zernike modes estimation to simplify the phase aberration measurements. This allowed very simple point receiver to be used instead of more a complex wavefront sensing scheme. The optical turbulence simulator was then tested with the new adaptive optics system under various turbulence strengths. It showed a significant reduction in scintillation index. With aperture averaging effect, the scintillation index was reduced even further. The result indicated that the two methods for scintillation reduction can be regarded as independent. The minimum bit error rates were then calculated for these conditions.

Finally, multiple transmitted beam configurations were described. By using beams with different wavelengths, the expression for parallel was derived, and then extended to give new analytical expressions for the converging and diverging beams. The scintillation indices for all cases were found to depend on the separation distance, with different minima corresponding to their geometry. In the converging beams case, it was further found that the beams could be approximated to follow independent beam paths at a large separation distance. This reasoning was backed by the beams to have independent statistics, and therefore they could be independently corrected with an adaptive optics system. A numerical estimate of such system shows the reduction of the bit error rates to be significant. The combination of adaptive optics system and multiple mutually incoherent beams is therefore potentially a powerful technique to achieve higher link capacity.

5.2 Future work

5.2.1 Binary phase hologram

Currently the computation time for the holograms is too long, leading to unacceptable beam steering performance for a real FSO system. In the case of the Iterative Fourier Transform algorithm, the speed of the Fast Fourier Transform is the bottle neck. Preliminary work has been done to use a Graphics Processing Unit (GPU) to accelerate FFT and optimising the memory access pattern such that all computation can be done on the GPU. The computation time was reduced to less than one second, compared to 17s on dual core CPU, using NVIDIA 8800GT and CUDA 2.2 library. A higher performing FFT on GPU implementation has now been published [142], which should lead to even faster calculation using IFT. The Direct Binary Search holds a promising future as the best algorithm for generating binary holograms [143]. Therefore, a GPU accelerated version will enable higher efficiencies at reasonable computation time.

A higher bit rate transmission test may be necessary to demonstrate the DC balancing scheme's efficiency, by using higher a speed laser source and modulator.

Binary holograms generate unwanted orders that can compromise the secrecy of the communication link. Suppression of unwanted orders may be necessary by using a FLC SLM in conjunction with a passive phase screen [144].

5.2.2 Retro-reflecting location acquisition

In order to decrease the acquisition error using retro-reflector targets, and reduce confusion from illuminated retro-reflecting materials such as road signs in an outdoor environment, a real FSO system using retro-reflecting location acquisition will require a retro-reflector design that can be distinguished using spatial information alone. In Chapter 3, a morphological filter was developed to reduce the effect of background illumination from ambient lighting by selectively subtract large areas of illumination. An extension may be used to place the retro reflectors in a pattern that can be recognised by software. An

example might be a circular ring of constant size as shown in Figure 121. This extra spatial information may reduce the likelihood of false positive and the acquisition error.

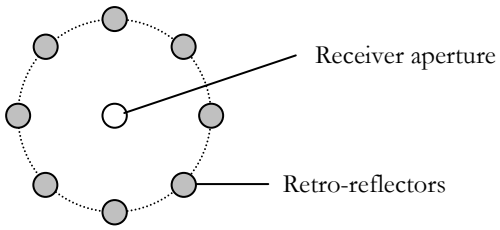

Figure 121. Possible retro-reflector arrangement to reduce probability of false positives and reduction in acquisition error

The aberration correction in the transmitter's optics could be calculated automatically by using Zernike mode estimation used in Chapter 4. Higher Zernike modes should improve the optical power density of the out going beam.

The gradient search algorithm used for measuring the steering error may be adapted to the controller for dynamic beam tracking. Currently the gradient search feedback loop is not optimised as a tracking controller.

5.2.3 Optical turbulence simulator

Currently, the optical turbulence simulator requires a calculation time in the range of seconds per manifestation of a phase screen. As reported in Chapter 4, real time phase screen calculation has been achieved by using inferior Zernike mode decomposition. A GPU accelerated MPI algorithm is technically possible, allowing accurate and fast implementation. With the fast switching time offered by FLC SLM, accurate real time turbulence simulator may be used in conjunction with a transmitter-receiver pair to test bit error rates under wide ranging turbulent conditions.

The weak phase fluctuation model of the turbulent atmosphere limits the range of the applicability for the calculations used in Chapter 4. A strong fluctuation model exists that predicts lower scintillation index than Rytov theory at large Rytov variance; however, spatial coherence reduction needs to be considered as well. This affects the accuracy phase screen approximation, such as the one used in

the optical turbulence simulator. An improved system must therefore incorporate the reduction in the beam coherence [79].

Time evolution of turbulence eddies has largely been ignored by considering only individual manifestations of phase screens. Although this would give the worst case scenario which is sufficient for bit error rates calculation, time evolution might be useful of frequency domain signal analysis and filter design. Some work has been done in this area, by using Taylor's frozen flow analysis to approximate crosswind flow in conjunction with Zernike mode decomposition. An MPI based approach may give more accurate phase screen that improves on the existing solution.

5.2.4 Wavefront sensorless adaptive optics

The wavefront sensorless adaptive optics system described in Chapter 4 requires a feedback link from the receiver to the transmitter. For a completely wireless optical solution, a protocol is necessary to transmit this feedback data in timely manner. The development would need to consider error correction codes that can be processed within the turbulence timescale, despite large scintillation index.

The Zernike mode estimation does not take time evolution of the phase fluctuation, which may allow lower number of mode estimation to be made. This would require the development of a time dependent optical turbulence simulator as previously described.

The aperture averaging effect was demonstrated to offer independent reduction in scintillation index from the adaptive optics. However, further reduction in scintillation in necessary to meet the bit error rates of a typical requirement of 10^{-9} or better. Time diversity error correction codes have been used to further reduce the effect of scintillation index even further in simulation. Further investigation is needed to assess the effectiveness of coding with an adaptive optics system and aperture averaging.

For a practical implementation of the adaptive optics system, the optical beam needed to estimate the Zernike modes must be separate from the data carrying beam. The beams have to be aligned co-linearly such that they both experience the same path. A possible solution is to use different polarisation states for the beams. A possible arrangement of this system is shown in Figure 122. The two FLC SLMs

controls the polarisation state independently. The modulated beam is then recombined to form a single beam as it leaves the transmitter.

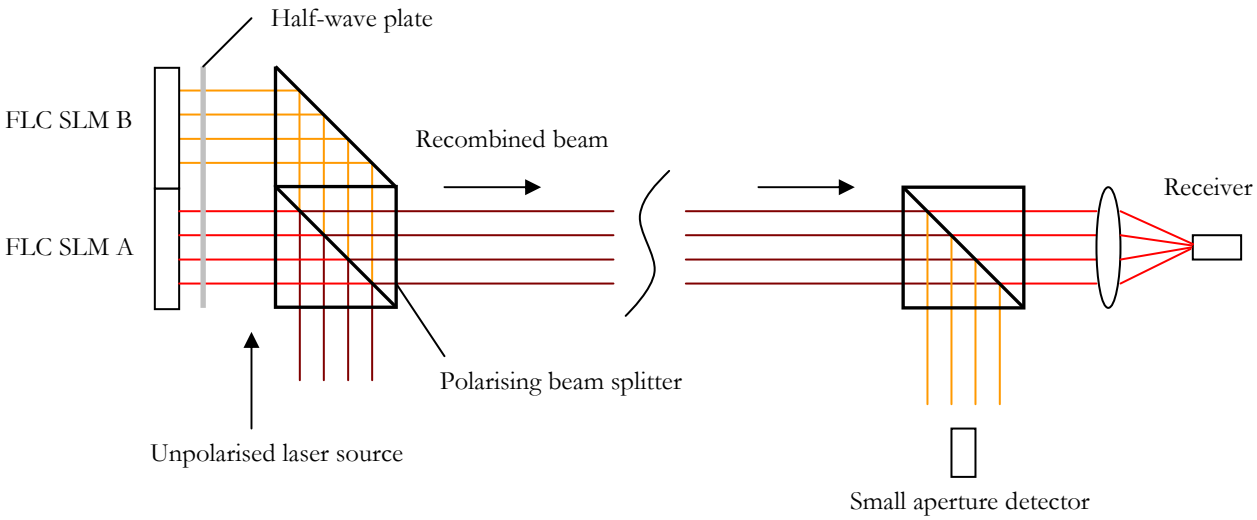

Figure 122. A possible co-linear arrangement of Zernike mode estimation and data carrying beams

5.2.5 Multiple Gaussian beams

The use of multiple beams shows substantial reduction in the predicted scintillation index. By applying an adaptive optics system per individual beam, it is possible to reduce scintillation index even further. Since there is a practical limit of the number of beams, other ways of exploiting the spatial diversity in a multiple beam configuration should allow even lower bit error rates. An example is to use multiple emitters and multiple receivers, or MIMO, in conjunction with temporal diversity to produce efficient coding schemes.

6 Bibliography

[1] H. Willebrand and B. Ghuman, *Free Space Optics: Enabling Optical Connectivity in Today's Networks*, Sams, 2001.

[2] D. O'Brien, G. Faulkner, H. Minh, O. Bouchet, M. Tabach, M. Wolf, J. Walewski, S. Randel, S. Nerreter, M. Franke, K. Langer, J. Grubor, and T. Kamalakis, "Home access networks using optical wireless transmission," *IEEE International Symposium on Personal, Indoor and Mobile Radio Communications, PIMRC*, 2008.

[3] S. Cherry, "Special report: Wireless networking: the wireless last mile," *IEEE Spectr.*, vol. 40, 2003, pp. 18-22.

[4] E. Leitgeb, M. Gebhart, and U. Birnbacher, "Optical networks, last mile access and applications," *Journal of Optical and Fiber Communications Reports*, vol. 2, 2005, pp. 56-85.

[5] R. Low, "What's next after DSL - Passive optical networking?," *Journal of the Communications Network*, vol. 4, 2005, pp. 49-52.

[6] S. Appathurai, R. Davey, and D. Nesset, "Next generation fibre-to-the-home solutions," *5th International Conference on Broadband Communications, Networks, and Systems, BROADNETS 2008*, 2008, pp. 232-235.

[7] T. Nakazato, "Sewer optical fibre network in Tokyo," *Water Quality International*, vol. Jan-Feb, 1997, pp. 16-18.

[8] P. Green, "Fiber to the home: the next big broadband thing," *Communications Magazine, IEEE*, vol. 42, 2004, pp. 100-106.

[9] K. Munasinghe and A. Jamalipour, "Interworked WiMAX-3G cellular data networks: An architecture for mobility management and performance evaluation," *IEEE Transactions on Wireless Communications*, vol. 8, 2009, pp. 1847-1853.

[10] O. Bouchet, H. Sizun, C. Boisrobert, and F. Fornel, *Free-Space Optics: Propagation and Communication*, Wiley-ISTE, 2006.

[11] C. Colvero, M. Cordeiro, and J. Von Der Weid, "FSO systems: Rain, drizzle, fog and haze

attenuation at different optical windows propagation," *SBMO/IEEE MTT-S International Microwave and Optoelectronics Conference Proceedings*, 2007, pp. 563-568.

[12] R. Sasiela, *Electromagnetic wave propagation in turbulence*, SPIE Press, 2007.

[13] I.I. Kim, M. Mitchell, and E. Korevaar, "Measurement of scintillation for free-space laser communication at 785 nm and 1550 nm," *Proceedings of SPIE - The International Society for Optical Engineering*, 1999, pp. 49-62.

[14] J. Beckers, "Adaptive optics for astronomy: Principles, performance, and applications," *Annual Review of Astronomy and Astrophysics*, vol. 31, 1993, pp. 13-62.

[15] S. Broomfield, M. Neil, E. Paige, and G. Yang, "Programmable binary phase-only optical device based on ferroelectric liquid crystal SLM," *Electronics Letters*, vol. 28, 1992, pp. 26-28.

[16] W. Crossland, T. Clapp, T. Wukinson, I. Manolis, A. Georgiou, and B. Robertson, "Liquid crystals in telecommunications systems," *Molecular Crystals and Liquid Crystals*, vol. 413, 2004.

[17] C. Tee, W. Crossland, T. Wilkinson, and A. Davey, "Binary phase modulation using electrically addressed transmissive and silicon backplane spatial light modulators," *Optical Engineering*, vol. 39, 2000, pp. 2527-2534.

[18] N. Savage, "Digital spatial light modulators," *Nat Photon*, vol. 3, Mar. 2009, pp. 170-172.

[19] C. Stolz, L. Bigue, and P. Ambs, "Implementation of High-Resolution Diffractive Optical Elements on Coupled Phase and Amplitude Spatial Light Modulators," *Applied Optics*, vol. 40, Dec. 2001, pp. 6415-6424.

[20] V. Arrizon, L. Gonzalez, R. Ponce, and A. Serrano-Heredia, "Computer-generated holograms with optimum bandwidths obtained with twisted-nematic liquid-crystal displays," *Applied Optics*, vol. 44, Mar. 2005, pp. 1625-1634.

[21] S. Osten, S. Kruger, and A. Steinhoff, "Spatial Light Modulators Based on Reflective Micro-Displays," *Technisches Messen*, vol. 73, 2006, pp. 149-156.

[22] J. Liesener and W. Osten, "Wavefront Optimization using Piston Micro Mirror Arrays," *Fringe 2005*, 2006, pp. 150-157.

[23] T. Kurokawa and S. Fukushima, "Spatial light modulators using ferroelectric liquid crystal," *Optical and Quantum Electronics*, vol. 24, Oct. 1992, pp. 1151-1163.

[24] C. Henderson, D. Leyva, and T. Wilkinson, "Free space adaptive optical interconnect at 1.25 Gb/s, with beam steering using a ferroelectric liquid-crystal SLM," *Journal of Lightwave Technology*, vol. 24, 2006, pp. 1989-1997.

[25] C. Uche, "Development of high capacity and low crosstalk 2-D holographic switches for deployment in optical transport networks," DPhil Thesis, University of Cambridge, 2003.

[26] M. Neil, M.J. Booth, and T. Wilson, "Dynamic wave-front generation for the characterization and testing of optical systems," *Optics Letters*, vol. 23, Dec. 1998, pp. 1849-1851.

[27] J. Goodman, *Introduction To Fourier Optics*, McGraw-Hill Science/Engineering/Math, 1996.

[28] M. Seldowitz, J. Allebach, and D. Sweeney, "Synthesis of digital holograms by direct binary search," *Applied Optics*, vol. 26, Jul. 1987, pp. 2788-2798.

[29] M. Clark, "Enhanced direct-search method for the computer design of holograms using state variables," *Proceedings of SPIE*, San Jose, CA, USA: 1996, pp. 24-34.

[30] C.L. Andrews and R. Weiss, "Demonstration of Babinet's Principle," *American Journal of Physics*, vol. 39, Jan. 1971, pp. 122-123.

[31] J. Gustafson, "Reevaluating Amdahl's law," *Commun. ACM*, vol. 31, 1988, pp. 532-533.

[32] R. Chandra, R. Menon, L. Dagum, D. Kohr, D. Maydan, and J. McDonald, *Parallel Programming in OpenMP*, Morgan Kaufmann, 2000.

[33] J. Reinders, *Intel Threading Building Blocks: Outfitting C++ for Multi-core Processor Parallelism*, O'Reilly Media, Inc., 2007.

[34] D. Butenhof, *Programming with POSIX Threads*, Addison Wesley, 1997.

[35] R. Shonkwiler and L. Lefton, *An Introduction to Parallel and Vector Scientific Computing*, Cambridge University Press, 2006.

[36] X. Tian, M. Girkar, A. Bik, and H. Saito, "Practical compiler techniques on efficient multithreaded code generation for OpenMP programs," *Computer Journal*, vol. 48, 2005, pp. 588-601.

[37] J. Kepner and S. Ahalt, "MatlabMPI," *Journal of Parallel and Distributed Computing*, vol. 64, 2004, pp. 997-1005.

[38] P. Després, M. Sun, B. Hasegawa, and S. Prevrhal, "FFT and cone-beam CT reconstruction on graphics hardware," *Progress in Biomedical Optics and Imaging - Proceedings of SPIE*, 2007.

[39] K.L. Tan, S.T. Warr, I.G. Manolis, T.D. Wilkinson, M.M. Redmond, W.A. Crossland, R.J. Mears, and B. Robertson, "Dynamic holography for optical interconnections. II. Routing holograms with predictable location and intensity of each diffraction order," *Journal of the Optical Society of America A*, vol. 18, Jan. 2001, pp. 205-215.

[40] T. Wilkinson, C. Henderson, D. Leyva, and W. Crossland, "Phase modulation with the next generation of liquid crystal over silicon technology," *Journal of Materials Chemistry*, vol. 16, 2006, pp. 3359-3365.

[41] M. Johansson, S. Hard, B. Robertson, I. Manolis, T. Wilkinson, and W. Crossland, "Adaptive Beam Steering Implemented in a Ferroelectric Liquid-Crystal Spatial-Light-Modulator Free-Space, Fiber-Optic Switch," *Applied Optics*, vol. 41, 2002, pp. 4904-4911.

[42] O. Ripoll, V. Kettunen, and H. Herzig, "Review of iterative Fourier-transform algorithms for beam shaping applications," *Optical Engineering*, vol. 43, Nov. 2004, pp. 2549-2556.

[43] S. Tao and X. Yuan, "Practical Implementation of the Phase-Quantization Technique in an Iterative Fourier-Transform Algorithm," *Applied Optics*, vol. 43, Apr. 2004, pp. 2089-2092.

[44] R. Gerchberg and W. Saxton, "Practical Algorithm For The Determination Of Phase From Image And Diffraction Plane Pictures.," *Optik (Stuttgart)*, vol. 35, 1972, pp. 237-250.

[45] V. Sidorovich, "Optical counter-measures and security of free-space optical communication links," *Proceedings of SPIE - The International Society for Optical Engineering*, 2004, pp. 97-108.

[46] D. O'Brien, W. Wei, J. Jing, G. Faulkner, S. Elston, S. Collins, and L. Parry-Jones, "Optical wireless communications for micro-machines," *Proceedings of SPIE - The International Society for Optical Engineering*, 2006.

[47] D. O'Brien, J. Liu, W. Yuan, G. Faulkner, S. Elston, and S. Collins, "Optical wireless communications with low voltage self-powered sensor motes," *Proceedings of SPIE - The International Society for Optical Engineering*, 2007.

[48] Y. Shim, S. Milner, and C. Davis, "A precise pointing technique for free space optical networking," *Proceedings - IEEE Military Communications Conference MILCOM*, 2007.

[49] P. Kai, D. Tianping, L. Yimin, and L. Gang, "Research of signal tracking technology in FSO communication," *2nd International Conference on Space Information Technology, November 10, 2007 -*

November 11, 2007, Wuhan, China: SPIE, 2007, p. Huazhong University of Science and Technology; The Second Academy of China Aerospace Sci. Ind. Corp.; The National Natural Science Foundation of China; Chinese Academy of Space Technology; China Aerospace Science and Industry Corporation.

[50] Tzung-Hsien Ho, S. Milner, and C. Davis, "Fully optical real-time pointing, acquisition, and tracking system for free space optical link," *Free-Space Laser Communication Technologies XVII, 26 Jan. 2005*, USA: SPIE-Int. Soc. Opt. Eng, 2005, pp. 81-92.

[51] E. Leitgeb, K. Zettl, S. Muhammad, N. Schmitt, and W. Rehm, "Investigation in Free Space Optical Communication Links Between Unmanned Aerial Vehicles (UAVs)," *Transparent Optical Networks, 2007. ICTON '07. 9th International Conference on*, 2007, pp. 152-155.

[52] W. Klaus, "Development of LC optics for free-space laser communications," *AEU-Archiv fur Elektronik und Ubertragungstechnik*, vol. 56, 2002, pp. 243-253.

[53] B. Epple, "Using a GPS-aided inertial system for coarse-pointing of free-space optical communication terminals," *Proceedings of SPIE - The International Society for Optical Engineering*, 2006.

[54] P. Kai, D. Tianping, L. Yimin, and L. Gang, "Research of signal tracking technology in FSO communication," *Proceedings of SPIE - The International Society for Optical Engineering*, 2007.

[55] J. Wang, J. Kahn, and K. Lau, "Minimization of acquisition time in short-range free-space optical communication," *Applied Optics*, vol. 41, Dec. 2002, pp. 7592-7602.

[56] W. Monaco and F. Barker 2nd., "Laser hazards and safety.," *Optometry clinics : the official publication of the Prentice Society*, vol. 4, 1995, pp. 1-15.

[57] J. Semple and G. Kneebone, *Algebraic Projective Geometry*, Oxford University Press, USA, 1998.

[58] D. Poole, *Linear Algebra: A Modern Introduction*, Brooks Cole, 2005.

[59] M. Waeny and P. Schwider, "CMOS megapixel digital camera with CameraLink™ interface," *Proceedings of SPIE - The International Society for Optical Engineering*, 2002, pp. 137-144.

[60] D. Wick, T. Martinez, J. Baker, D. Payne, B. Stone, and S. Restaino, "Wide field-of-view, foveated imaging system using a liquid crystal spatial light modulator," *Proceedings of SPIE - The International Society for Optical Engineering*, 2002, pp. 58-62.

[61] T. Martinez, D. Wick, and S. Restaino, "Foveated, wide field-of-view imaging system using a liquid

crystal spatial light modulator," *Optics Express*, vol. 8, 2001, pp. 555-560.

[62] T. Hui, B. Fowler, and A. Gamal, "Analysis of temporal noise in CMOS photodiode active pixel sensor," *Solid-State Circuits, IEEE Journal of*, vol. 36, 2001, pp. 92-101.

[63] P. Maragos and R. Schafer, "Morphological filters--Part II: Their relations to median, order-statistic, and stack filters," *Acoustics, Speech and Signal Processing, IEEE Transactions on*, vol. 35, 1987, pp. 1170-1184.

[64] P. Maragos and R. Schafer, "Morphological filters--Part I: Their set-theoretic analysis and relations to linear shift-invariant filters," *Acoustics, Speech and Signal Processing, IEEE Transactions on*, vol. 35, 1987, pp. 1153-1169.

[65] Lai Wai Kuen, Cham Wai Kuen, and J. Siu, "A graphical reconstruction of FIR filter from its morphological kernel," *TENCON '93. Proceedings. Computer, Communication, Control and Power Engineering.1993 IEEE Region 10 Conference on*, 1993, pp. 584-586 vol.3.

[66] S. Mitra and G. Sicuranza, *Nonlinear Image Processing*, Academic Press, 2000.

[67] R. Haralick and L. Shapiro, *Computer and Robot Vision, Vol. 1*, Addison-Wesley, 1991.

[68] N. Barnes and P. Walsh, "Loss of Gaussian beams through off-axis circular apertures," *Applied Optics*, vol. 27, Apr. 1988, pp. 1230-1232.

[69] Kreyzig, *Kreyzig: Advanced Engineering Mathematics*, John Wiley & Sons Inc, .

[70] D. Tse and P. Viswanath, *Fundamentals of wireless communication*, Cambridge University Press, 2005.

[71] L. Mundie and H. Bailey, "Effects of atmospheric scattering and absorption on the performance of optical sensors," *Optical Instruments and Techniques 1969, Proc Conf*, 1970, pp. 538-545.

[72] V. Tatarskii, *The effects of the turbulent atmosphere on wave propagation*, Jerusalem: Israel Program for Scientific Translations, 1971, 1971.

[73] V.I. Tatarski, *Wave Propagation In A Turbulent Medium*, McGraw Hill, 1961.

[74] L. Andrews and R. Phillips, *Laser Beam Propagation through Random Media, Second Edition*, SPIE Publications, 2005.

[75] J. Kerr, P. Titterton, A. Kraemer, and C. Cooke, "Atmospheric Optical Communications System," *Proceedings of the IEEE*, vol. 58, 1970, pp. 1691-1709.

[76] A. Maitra and M. Dan, "Propagation of pulses at optical wavelengths through fog-filled medium,"

Radio Science, vol. 31, 1996, pp. 469-475.

[77] W. Binbin, B. Marchant, and M. Kavehrad, "Optical scattering in battlefield obscurants: Analysis of channel spatial, angular and temporal dispersion," *Proceedings - IEEE Military Communications Conference MILCOM*, 2007.

[78] J.W. Strohbehn and S.F. Clifford, *Laser beam propagation in the atmosphere*, Springer-Verlag, 1978.

[79] L. Andrews, R. Phillips, and C. Hopen, *Laser beam scintillation with applications*, 2001.

[80] F. Zocchi, "A simple analytical model of adaptive optics for direct detection free-space optical communication," *Optics Communications*, vol. 248, 2005, pp. 359-374.

[81] R. Khandekar, V. Nikulin, and J. Sofka, "Mitigation of optical turbulence effects using a modified simplex optimization approach: Experimental study," *Proceedings of SPIE - The International Society for Optical Engineering*, 2007.

[82] A.N. Kolmogorov, "The local structure of turbulence in incompressible viscous fluid for very large Reynolds numbers," *Soviet Physics Uspekhi*, vol. 10, 1968, pp. 734-746.

[83] A.M. Obukhov, "Some Specific Features of Atmospheric Turbulence," *Journal of Geophysical Research*, vol. 67.

[84] A.M. Obukhov, "The effect of weak inhomogeneities in the atmosphere on propagation of sound and light.," *Izv. AN SSSR, Ser. Geophys. Geogr.*, vol. 2, 1953, pp. 155–165.

[85] A. Prokhorov, F. Bunkin, K. Gochelashvily, and V. Shishov, "Laser irradiance propagation in turbulent media," *Proceedings of the IEEE*, vol. 63, 1975, pp. 790-811.

[86] A. Ishimaru, *Wave Propagation and Scattering in Random Media*, Wiley-IEEE Press, 1999.

[87] L. Hu, L. Xuan, Z. Cao, Q. Mu, D. Li, and Y. Liu, "A liquid crystal atmospheric turbulence simulator," *Optics Express*, vol. 14, Dec. 2006, pp. 11911-11918.

[88] C. Wilcox, T. Martinez, F. Santiago, J. Andrews, S. Restaino, S. Teare, and D. Payne, "Atmospheric simulator for testing adaptive optics systems," *Proceedings of SPIE - The International Society for Optical Engineering*, 2008.

[89] L. Hu, L. Xuan, D. Li, Z. Cao, Q. Mu, Y. Liu, Z. Peng, and X. Lu, "Real-time liquid-crystal atmosphere turbulence simulator with graphic processing unit," *Optics Express*, vol. 17, Apr. 2009, pp. 7259-7268.

[90] J. Owens, "Optical Refractive Index of Air: Dependence on Pressure, Temperature and Composition," *Applied Optics*, vol. 6, Jan. 1967, pp. 51-59.

[91] A. Fung, "A note on the Wiener-Khintchine theorem for autocorrelation," *Proceedings of the IEEE*, vol. 55, 1967, pp. 594-595.

[92] R. Roth, "On the existence of a relation between the Kolmogoroff and von Kármán constants," *Boundary-Layer Meteorology*, vol. 1, 1970, pp. 131-136.

[93] R. Hill, "Models of the Scalar Spectrum for Turbulent Advection," *Journal of Fluid Mechanics Digital Archive*, vol. 88, 1978, pp. 541-562.

[94] R. Hill and S. Clifford, "Modified spectrum of atmospheric temperature fluctuations and its application to optical propagation," *Journal of the Optical Society of America*, vol. 68, Jul. 1978, pp. 892-899.

[95] P. Moon, *Field theory handbook: Including coordinate systems, differential equations, and their solutions*, Springer-Verlag, 1988.

[96] T. Wu and T. Ohmura, *Quantum Theory of Scattering*, Prentice Hall, 1962.

[97] A. Wheelon, *Electromagnetic Scintillation: Volume 2, Weak Scattering*, Cambridge University Press, 2006.

[98] M.E. Gracheva and A.S. Gurvich, "Strong fluctuations in the intensity of light propagated through the atmosphere close to the earth," *Radiophysics and Quantum Electronics*, vol. 8, Jul. 1965, pp. 511-515.

[99] W.B. Miller, J.C. Ricklin, and L.C. Andrews, "Log-amplitude variance and wave structure function: a new perspective for Gaussian beams," *Journal of the Optical Society of America A*, vol. 10, Apr. 1993, pp. 661-672.

[100] G. Fikioris, "Integral Evaluation Using the Mellin Transform and Generalized Hypergeometric Functions: Tutorial and Applications to Antenna Problems," *Antennas and Propagation, IEEE Transactions on*, vol. 54, 2006, pp. 3895-3907.

[101] H. Yuksel and C. Davis, "Aperture averaging experiment for optimizing receiver design and analyzing turbulence on free space optical communication links," *Lasers and Electro-Optics, 2005. (CLEO). Conference on*, 2005, pp. 743-745 Vol. 1.

[102] E. Jakeman and K. Ridley, *Modeling fluctuations in scattered waves*, CRC Press, 2006.

[103] M. Uysal and J. Li, "Error rate performance of coded free-space optical links over gamma-gamma turbulence," *Communications, 2004 IEEE International Conference on*, 2004, pp. 3331-3335 Vol.6.

[104] R. Tyson, "Bit-error rate for free-space adaptive optics laser communications," *Journal of the Optical Society of America A*, vol. 19, Apr. 2002, pp. 753-758.

[105] J. Shapiro, "Imaging and optical communication through atmospheric turbulence," *Laser Beam Propagation in the Atmosphere*, 1978, pp. 171-222.

[106] L. Mayhew, H. Willebrand, and E. Kube, "Scintillation bit error rate-reduction for free space optical communications systems," *Current Developments in Lens Design and Optical Engineering II*, San Diego, CA, USA: SPIE, 2001, pp. 163-170.

[107] F. Xu, A. Khalighi, P. Caussé, and S. Bourennane, "Channel coding and time-diversity for optical wireless links," *Optics Express*, vol. 17, 2009, pp. 872-887.

[108] F. Davidson and Y. Koh, "Interleaved convolutional coding for the turbulent atmospheric optical communication channel," *Communications, IEEE Transactions on*, vol. 36, 1988, pp. 993-1003.

[109] X. Zhu and J. Kahn, "Free-space optical communication through atmospheric turbulence channels," *IEEE Transactions on Communications*, vol. 50, 2002, pp. 1293-1300.

[110] C. Harding, R. Johnston, and R. Lane, "Fast Simulation of a Kolmogorov Phase Screen," *Applied Optics*, vol. 38, Apr. 1999, pp. 2161-2170.

[111] N. Roddier, "Atmospheric wavefront simulation using Zernike polynomials," *Optical Engineering*, vol. 29, Oct. 1990, pp. 1174-1180.

[112] R.J. Noll, "Zernike polynomials and atmospheric turbulence," *Journal of the Optical Society of America*, vol. 66, Mar. 1976, pp. 207-211.

[113] O. Keskin, L. Jolissaint, and C. Bradley, "Hot-air optical turbulence generator for the testing of adaptive optics systems: principles and characterization," *Applied Optics*, vol. 45, Jul. 2006, pp. 4888-4897.

[114] O. Keskin, L. Jolissaint, C. Bradley, S. Dost, and I. Sharf, "Hot Air Turbulence Generator for Multi-Conjugate Adaptive Optics," *Proceedings of SPIE - The International Society for Optical Engineering*, 2003, pp. 49-57.

[115] S. Hippler, F. Hormuth, D. Butler, W. Brandner, and T. Henning, "Atmosphere-like turbulence

generation with surface-etched phase-screens," *Optics Express*, vol. 14, Oct. 2006, pp. 10139-10148.

[116] L.C. Andrews, R.L. Phillips, and A.R. Weeks, "Propagation of a Gaussian-beam wave through a random phase screen," *Waves in Random and Complex Media*, vol. 7, 1997, p. 229.

[117] D.L. Fried, "Optical Resolution Through a Randomly Inhomogeneous Medium for Very Long and Very Short Exposures," *Journal of the Optical Society of America*, vol. 56, Oct. 1966, pp. 1372-1379.

[118] R. Lane, A. Glindemann, and J. Dainty, "Simulation of a Kolmogorov phase screen," *Waves in Random Media*, vol. 2, Jul. 1992, pp. 209-224.

[119] J.Y. Wang and J.K. Markey, "Modal compensation of atmospheric turbulence phase distortion," *Journal of the Optical Society of America*, vol. 68, Jan. 1978, pp. 78-87.

[120] M. Neil, T. Wilson, and Juskaitis, "A wavefront generator for complex pupil function synthesis and point spread function engineering," *Journal of Microscopy*, vol. 197, Mar. 2000, pp. 219-223.

[121] M. Sypek, "Light propagation in the Fresnel region. New numerical approach," *Optics Communications*, vol. 116, 1995, pp. 43-48.

[122] N. Perlot and D. Fritzsche, "Aperture averaging: theory and measurements," *Free-Space Laser Communication Technologies XVI*, San Jose, Ca, USA: SPIE, 2004, pp. 233-242.

[123] S.F. Clifford, "Temporal-Frequency Spectra for a Spherical Wave Propagating through Atmospheric Turbulence," *Journal of the Optical Society of America*, vol. 61, Oct. 1971, pp. 1285-1292.

[1] T. Burghelea, E. Segre, and V. Steinberg, "Validity of the Taylor hypothesis in a random spatially smooth flow," *Physics of Fluids*, vol. 17, Oct. 2005, pp. 103101-8.

[125] M. Roggemann, B. Welsh, D. Montera, and T. Rhoadarmer, "Method for simulating atmospheric turbulence phase effects for multiple time slices and anisoplanatic conditions," *Applied Optics*, vol. 34, Jul. 1995, pp. 4037-4051.

[126] D. Greenwood, "Bandwidth specification for adaptive optics systems," *Journal of the Optical Society of America*, vol. 67, Mar. 1977, pp. 390-393.

[127] X.J. Gan, J. Guo, and Y.Y. Fu, "The Simulating Turbulence Method of Laser Propagation in the Inner Field," *Journal of Physics: Conference Series*, vol. 48, 2006, pp. 907-910.

[128] "BD5DCE66-BDB9-137E-C7548BA3D54AE9B3_56506.pdf."

[129] M. Booth, "Wave front sensor-less adaptive optics: a model-based approach using sphere

packings," *Optics Express*, vol. 14, Feb. 2006, pp. 1339-1352.

[130] D. Debarre, M. Booth, and T. Wilson, "Image based adaptive optics through optimisation of low spatial frequencies," *Optics Express*, vol. 15, 2007, pp. 8176-8190.

[131] W. Jiang and H. Li, "Hartmann-Shack wavefront sensing and wavefront control algorithm," *Proceedings of SPIE - The International Society for Optical Engineering*, 1990, pp. 82-93.

[132] M. Booth, "Wavefront sensorless adaptive optics for large aberrations," *Optics Letters*, vol. 32, Jan. 2007, pp. 5-7.

[133] B. Yahya, H. Eyyuboglu, and C. Yangjian, "Scintillations of partially coherent multiple Gaussian beams in turbulence," *Applied Optics*, vol. 48, 2009, pp. 1943-1954.

[134] S. Clifford, G. Ochs, and R. Lawrence, "Saturation Of Optical Scintillation By Strong Turbulence.," *J Opt Soc Am*, vol. 64, 1974, pp. 148-154.

[135] J. Goodman, *Statistical Optics*, Wiley-Interscience, 2000.

[136] R. Fante, "Intensity Fluctuations of an Optical Wave in a Turbulent Medium Effect of Source Coherence," *Journal of Modern Optics*, vol. 28, Sep. 1981, pp. 1203-1207.

[137] J. Ricklin and F. Davidson, "Atmospheric optical communication with a Gaussian Schell beam," *Journal of the Optical Society of America A*, vol. 20, May. 2003, pp. 856-866.

[138] H. Willebrand and B. Ghuman, *Free space optics: enabling optical connectivity in today's networks*, Sams Publishing, 2002.

[139] A. Peleg and J. Moloney, "Scintillation index for two Gaussian laser beams with different wavelengths in weak atmospheric turbulence," *Journal of the Optical Society of America A*, vol. 23, Dec. 2006, pp. 3114-3122.

[140] P. Polynkin, A. Peleg, L. Klein, T. Rhoadarmer, and J. Moloney, "Optimized multiemitter beams for free-space optical communications through turbulent atmosphere," *Optics Letters*, vol. 32, Apr. 2007, pp. 885-887.

[141] X. Xiao, J. Aluguri, and D. Voelz, "Wave optics simulation study of multiple Gaussian beam transmitters for free space optical transmission through turbulence," *Proceedings of SPIE - The International Society for Optical Engineering*, 2009.

[142] D. Lloyd, C. Boyd, and N. Govindaraju, "Fast computation of general fourier transforms on

GPUs," *2008 IEEE International Conference on Multimedia and Expo, ICME 2008 - Proceedings*, 2008, pp. 5-8.

[143] A. Georgiou, T. Wilkinson, N. Collings, and W. Crossland, "An algorithm for computing spot-generating holograms," *Journal of Optics A: Pure and Applied Optics*, vol. 10, 2008, p. 015306.

[144] C. Maurer, A. Schwaighofer, A. Jesacher, S. Bernet, and M. Ritsch-Marte, "Suppression of undesired diffraction orders of binary phase holograms," *Applied Optics*, vol. 47, 2008, pp. 3994-3998.

7 Appendix A: Binarisation of phase holograms

Consider a binary amplitude-only filter that approximates a continuous complex function $H(u)$ (the following derivation is done only in one dimension, but would equally apply to two dimensions.)

$$H_B(u) = \begin{cases} 1 & when\ \cos(\xi) > 0 \\ 0 & otherwise \end{cases} \tag{7.1.1}$$

where $\xi = \arg\left[H(u)\right]$. This is equivalent to assigning a 1 if a real part of function is greater than zero, and 0 otherwise. Generally this is the same form as a step function

$$g(x) = \begin{cases} 1 & when\ x > 0 \\ 0 & when\ x \le 0 \end{cases} \tag{7.1.2}$$

Laplace transforming this function gives rise to $G(s) = \frac{1}{s}$.

Substituting $x = \cos(\xi)$ and apply inverse Laplace transform

$$H_B(u) = \frac{1}{2\pi j}\int_{\delta - j\infty}^{\delta + j\infty} \exp(s\cos\xi).\frac{1}{s}ds \tag{7.1.3}$$

Expanding the exponential into infinite series, it is possible to obtain an exact solution to the integral

$$H_B(u) = \frac{1}{2} + \sum_{n=odd}^{\infty} A_n \cos(n\xi) \tag{7.1.4}$$

where $A_n = \frac{2(-1)^{\frac{n-1}{2}}}{n\pi}$. Recognising that binary phase is related the binary amplitude quantisation by

$$H_{BP}(u) = 2\left[H_B(u) - 1\right] \tag{7.1.5}$$

The expression for binary phase becomes

$$H_{BP}(u) = 2\sum_{n=odd}^{\infty} A_n \cos(n\xi) \tag{7.1.6}$$

And finally expanding the cos terms into their sums of exponentials

$$H_{BP}(u) = 2\sum_{n=odd}^{\infty} A_n \left(e^{jn\xi} + e^{-jn\xi} \right) \tag{7.1.7}$$

It clearly shows that the phase quantisation results in a superposition of various orders of *continuous phase* of the function. It also shows that there is an equal component of the complex conjugate of the phase function, which causes binary holograms to duplicate an image with 180° rotation around the origin.

8 Appendix B: Hypergeometric functions

Recently, due to the increasing popularity of computer assisted analytical integration methods, hypergeometrical functions are becoming more popular as a standard solution. This is particularly due to the use of Mellin transform based decomposition [100]. A hypergeometric function is defined by the algebraic series, where the coefficients are the parameters of the function. Many elementary functions are special cases of these functions, and fast algorithms exist for calculating hypergeometric functions. Two functions are used in this thesis, the confluent hypergeometric function and Gauss hypergeometrical function.

8.1 Confluent hypergeometric function

The confluent hypergeometric function ${}_1F_1$ is defined as:

$$ {}_1F_1\left(a;c;z\right)=\sum_{n=0}^{\infty}\frac{\left(a\right)_n z^n}{\left(c\right)_n n!} \quad \text{where } \left|z\right|<\infty \tag{8.1.1}$$

and $\left(a\right)_n$ is the Pochhammer symbol:

$$ \left(a\right)_n=\frac{\Gamma\left(a+n\right)}{\Gamma\left(a\right)} \tag{8.1.2}$$

8.2 Gauss hypergeometrical function

The Gauss hypergeometrical function ${}_2F_1$ is defined as:

$$ {}_2F_1\left(a,b;c;z\right)=\sum_{n=0}^{\infty}\frac{\left(a\right)_n\left(b\right)_n z^n}{\left(c\right)_n n!} \quad \text{where } \left|z\right|<1$$

$$ \begin{aligned} {}_2F_1\left(a,b;c;z\right)=&\frac{\Gamma\left(c\right)\Gamma\left(b-a\right)}{\Gamma\left(b\right)\Gamma\left(c-a\right)}\left(-z\right)^{-a}F_1\left(a,1-c+a;1-b+a;\frac{1}{z}\right)\\ &+\frac{\Gamma\left(c\right)\Gamma\left(a-b\right)}{\Gamma\left(a\right)\Gamma\left(c-b\right)}\left(-z\right)^{-a}F_1\left(b,1-c+b;1-a+b;\frac{1}{z}\right) \quad \text{otherwise} \end{aligned} \tag{8.1.3}$$

9 Appendix C: Covariance function of Intensity

The fourth order cross coherence function is defined by Andrews as [74]:

$$\begin{aligned}\left\langle U(\mathbf{r}_1,L)U^*(\mathbf{r}_2,L)U(\mathbf{r}_3,L)U^*(\mathbf{r}_4,L)\right\rangle = \\ \left\langle U(\mathbf{r}_1,L)U^*(\mathbf{r}_2,L)\right\rangle\left\langle U(\mathbf{r}_3,L)U^*(\mathbf{r}_4,L)\right\rangle \\ \times\exp\left(E_2(\mathbf{r}_1,\mathbf{r}_4,L)+E_2(\mathbf{r}_3,\mathbf{r}_2,L)+E_3(\mathbf{r}_1,\mathbf{r}_3,L)+E_3^*(\mathbf{r}_2,\mathbf{r}_4,L)\right)\end{aligned} \tag{9.1.1}$$

where $U(\mathbf{r},L)$ is the electric field amplitude, and $\mathbf{r}$ is the 2D position vector from the beam axis. The quantity E_2 and E_3 are defined as:

$$\begin{aligned}E_2(\mathbf{r}_1,\mathbf{r}_2,L) &= 4\pi^2k^2L\int_0^1\int_0^\infty \kappa\Phi_n(\kappa)J_0\left[\kappa\left|(1-(1-\Theta)\xi)(\mathbf{r}_1-\mathbf{r}_2)-i\Lambda\xi(\mathbf{r}_1+\mathbf{r}_2)\right|\right] \\ &\quad\times\exp\left[-\frac{\Lambda L\kappa^2\xi^2}{k}\right]d\kappa d\xi \\ E_3(\mathbf{r}_1,\mathbf{r}_2,L) &= -4\pi^2k^2L\int_0^1\int_0^\infty \kappa\Phi_n(\kappa)J_0\left[\kappa\left|1-(1-\Theta)\xi-i\Lambda\xi\right|.\left|\mathbf{r}_1-\mathbf{r}_2\right|\right] \\ &\quad\times\exp\left[-\frac{\Lambda L\kappa^2\xi^2}{k}\right]\times\exp\left[-\frac{iL\kappa^2}{k}\xi(1-(1-\Theta)\xi)\right]d\kappa d\xi\end{aligned} \tag{9.1.2}$$

A simplification can be made by assuming that only the intensity of the field is needed. For a circular symmetric case, the covariance function of intensity is written as a function of the radial distance from the optical axis:

$$\left\langle I(0,L)I(r,L)\right\rangle = \left\langle U(0,L)U^*(0,L)U(r,L)U^*(r,L)\right\rangle \tag{9.1.3}$$

Substituting equation (9.1.3) into equation (9.1.1) and (9.1.2) gives:

$$\left\langle I(0,L)I(r,L)\right\rangle = \left\langle I(0,L)\right\rangle\left\langle I(r,L)\right\rangle\exp\left[2E_2(0,r,L)+2\,\mathrm{Re}\left\{E_3(0,r,L)\right\}\right] \tag{9.1.4}$$

where E_2 and E_3 are now simplified to:

$$E_2(r,L) = 4\pi^2 k^2 L \int_0^1 \int_0^\infty \kappa \Phi_n(\kappa) J_0\left[\kappa r \left|\left(1-(1-\Theta)\xi\right) - i\Lambda\xi\right|\right] \times \exp\left[-\frac{\Lambda L \kappa^2 \xi^2}{k}\right] d\kappa d\xi$$

$$E_3(r,L) = -4\pi^2 k^2 L \int_0^1 \int_0^\infty \kappa \Phi_n(\kappa) J_0\left[\kappa r \left|1-(1-\Theta)\xi - i\Lambda\xi\right|\right] \times \exp\left[-\frac{\Lambda L \kappa^2 \xi^2}{k}\right] \times \exp\left[-\frac{iL\kappa^2}{k}\xi\left(1-(1-\Theta)\xi\right)\right] d\kappa d\xi \quad (9.1.5)$$

10 Appendix D: Zernike modes covariance matrix for Kolmogorov spectrum

Zernike modes are orthogonal polynomials within a unit circle. They can be used to describe optical phase aberrations in polar coordinates. The modes can be written as a function of mode number j:

$$\begin{aligned}
&Z_{even\ j} = \sqrt{n+1}\,R_n^m(r)\sqrt{2}\cos(m\theta)\Big\} \quad m \neq 0\\
&Z_{odd\ j} = \sqrt{n+1}\,R_n^m(r)\sqrt{2}\sin(m\theta)\Big\}\\
&Z_j = \sqrt{n+1}R_n^0(r) \qquad\qquad m = 0\\
&R_n^m(r) = \sum_{s=0}^{(n-m)/2} \frac{(-1)^s (n-s)!}{s!\left[(n+m)/2-s\right]!\left[(n-m)/2-s\right]!} r^{n-2s}
\end{aligned} \tag{10.1.1}$$

where n and m are related to j using:

$$\begin{aligned}
n &= ceil\left[\frac{\sqrt{8j-1}-1}{2}\right]-1\\
m &= ceil\left[j-\frac{n(n+1)+(n+1)(\mathrm{mod}\,2)}{2}\right]\times 2-1-(n+1)(\mathrm{mod}\,2)
\end{aligned} \tag{10.1.2}$$

The Fourier transform Q can be written as [112]:

$$\begin{aligned}
&Q_{even\ j}(\kappa,\phi) = (-1)^{(n-m)/2}\, i^m \sqrt{2}\cos(m\phi)\,S(n,\kappa)\Big\} \quad m \neq 0\\
&Q_{odd\ j}(\kappa,\phi) = (-1)^{(n-m)/2}\, i^m \sqrt{2}\sin(m\phi)\,S(n,\kappa)\Big\}\\
&Q_j(\kappa,\phi) = (-1)^{n/2} \qquad\qquad m = 0\\
&S(n,\kappa) = \sqrt{n+1}\,\frac{J_{n+1}(2\pi\kappa)}{\pi\kappa}
\end{aligned} \tag{10.1.3}$$

In a turbulent atmosphere, and considering plane wave propagation, the covariance between the Zernike modes are calculated with:

$$\left\langle a_j a_k \right\rangle = \int_0^{2\pi}\int_0^{2\pi}\int_0^{1}\int_0^{1} Z_j(\rho,\theta)\,Z_m(\rho',\theta')\,B(D\rho, D\rho')\,d\rho\,d\rho'\,d\theta\,d\theta' \tag{10.1.4}$$

where $B(D\rho, D\rho')$ is the phase covariance function defined in Equation (4.1.4). Noll showed [112] this can be calculated in Fourier space by rewriting the covariance to:

$$\langle a_j a_k \rangle = \int_0^{2\pi}\int_0^{2\pi}\int_0^{1}\int_0^{1} Q_j(\kappa,\phi) Q_k^*(\kappa',\phi') \Phi(\kappa,\kappa') dk dk' d\phi d\phi' \tag{10.1.5}$$

where $\Phi(\kappa,\kappa')$ is a delta-correlated Kolmogorov spectrum:

$$\Phi(\kappa,\kappa') = 0.023\left(\frac{R}{r_0}\right)^{5/3} \kappa^{-11/3}\delta(\kappa-\kappa') \tag{10.1.6}$$

where R is the diameter of the phase screen in consideration, and r_0 is Fried's parameter. The integral can be further simplified by considering the orthogonality of $\sin(m\phi)$ and $\cos(m\phi)$ terms, and substitution of (10.1.3) into (10.1.5) [119]:

$$\left.\begin{aligned}\langle a_j a_k \rangle = &\frac{0.0114\sqrt{(n_j+1)(n_k+1)}(-1)^{(n_j+n_k-2n_j)/2}}{\pi} \\ &\times\int k(k^{-11/3})\frac{J_{n_j+1}(2\pi k) J_{n_k 1}(2\pi k)}{k^2} dk\end{aligned}\right\} m_j = m_k$$
$$= 0 \qquad \text{otherwise} \tag{10.1.7}$$

The solution is found to be:

$$\langle a_j a_k \rangle = \begin{cases} \dfrac{0.0072\pi^{8/3}\Gamma[14/3]\Gamma\left[\frac{1}{6}(-5+3n_j+3n_k)\right]\left(\frac{R}{r_0}\right)^{5/3}}{\Gamma\left[\frac{1}{6}(17+3n_j-3n_k)\right]\Gamma\left[\frac{1}{6}(17-3n_j+3n_k)\right]\Gamma\left[\frac{1}{6}(23+3n_j+3n_k)\right]} \text{even}(j-k) \\ 0 \qquad \text{otherwise} \end{cases} \tag{10.1.8}$$

For spherical wave propagation, the integral is replaced with [79][12]:

$$\left.\begin{aligned}\langle a_j a_k \rangle = &\frac{0.0144\sqrt{(n_j+1)(n_k+1)}(-1)^{(n_j+n_k-2n_j)/2}}{\pi} \\ &\times\int_0^1\int k(k^{-11/3})\frac{J_{n_j+1}(2\pi k(1-\xi)) J_{n_k 1}(2\pi k(1-\xi))}{k^2(1-\xi)^2} dk d\xi\end{aligned}\right\} m_j = m_k$$
$$= 0 \qquad \text{otherwise} \tag{10.1.9}$$

This is accounted by considering the propagation of a Gaussian beam and setting the beam parameters to the spherical case. The solution is found to be:

$$\left\langle a_j a_k \right\rangle = \begin{cases} \dfrac{0.0264\pi^{8/3}\Gamma[8/3]\Gamma\left[\dfrac{1}{6}\left(-5+3n_j+3n_k\right)\right]\left(\dfrac{R}{r_0}\right)^{5/3}}{\Gamma\left[\dfrac{1}{6}\left(17+3n_j-3n_k\right)\right]\Gamma\left[\dfrac{1}{6}\left(17-3n_j+3n_k\right)\right]\Gamma\left[\dfrac{1}{6}\left(23+3n_j+3n_k\right)\right]} \text{even}\left(j-k\right) \\ 0 \qquad \text{otherwise} \end{cases}$$

(10.1.10)

Dividing Equation (10.1.10) by (10.1.8) give the ratio of $3/8$ between parallel and spherical beams exactly.